Universidad Nacional Autónoma de México
Posgrado en Ciencias de la Tierra
Instituto de Geología

Origen y evolución del basamento metamórfico de la Sierra de Chuacús, Guatemala y sus implicaciones tectónicas

Origin and evolution of the metamorphic basement of the Sierra de Chuacús, Guatemala and their tectonic implications

Tesis
que para optar por el grado de
Doctor en Ciencias de la Tierra

Presenta:

Roberto Maldonado Villanueva

Director de tesis:

Dr. Fernando Ortega Gutiérrez, Instituto de Geología, UNAM

Comité tutor:

Dr. Fernando Ortega Gutiérrez, Instituto de Geología, UNAM
Dr. Peter Schaaf, Instituto de Geofísica, UNAM
Dr. Luigi Solari, Centro de Geociencias, UNAM

Ciudad Universitaria, CDMX
Junio de 2018

Comité de examen predoctoral:

Dr. Dante J. Morán Zenteno, Instituto de Geología, UNAM
Dr. Jesús Solé Viñas, Instituto de Geología, UNAM
Dr. Bodo Weber, Centro de Investigación Científica y Estudios Superiores de Ensenada
Dr. Ricardo Vega Granillo, Universidad de Sonora
Dr. Fernando Ortega Gutiérrez, Instituto de Geología, UNAM

Comité de examen de grado:

Dr. Jesús Solé Viñas, Instituto de Geología, UNAM
Dr. Antonio García Casco, Universidad de Granada
Dra. Yamirka Rojas Agramonte, Universidad de los Andes
Dr. Fernando Ortega Gutiérrez, Instituto de Geología, UNAM
Dr. Luigi Solari, Centro de Geociencias, UNAM

Agradecimientos

Este trabajo fue financiado a través del Programa de Apoyo a Proyectos de Investigación e Innovación Tecnológica (PAPIIT), DGAPA-UNAM, número IN104914.

Agradezco la beca que recibí por parte del Consejo Nacional de Ciencia y Tecnología (CONACYT) y la beca de apoyo para la terminación de la tesis otorgada por el Instituto de Geología.

Agradezco a Fernando Ortega Gutiérrez su confianza en este proyecto y el apoyo que me brindó durante estos años. Un agradecimiento especial a los miembros de mi comité tutor: Peter Schaaf y Luigi Solari por su apoyo y disposición constantes a lo largo del proceso. Le agradezco a Sergio Morán Ical (Universidad de San Carlos de Guatemala) el haberme introducido en la geología de la Sierra de Chuacús y por su apoyo logístico para la realización del trabajo de campo. De igual modo, les agradezco a David Hernández Uribe (Colorado School of Mines) y a Guillermo A. Ortiz Joya su esfuerzo y compañía en las campañas de trabajo en Guatemala.

Le agradezco a Bodo Weber (CICESE) por abrirme las puertas de su laboratorio y por la oportunidad de colaborar académicamente en mi proyecto.

Gracias a Y. Tatiana Valencia Morales (Servicio Geológico Colombiano) quien me brindó aliento y compañía inagotables. Agradezco también a Guillermo Espejo Bautista, Daniel Villanueva Lascurain (The University of Texas) y Alejandro Cisneros de León (Universität Heidelberg) por todas las discusiones y el compañerismo de estos años.

El jurado de examen estuvo integrado por: Yamirka Rojas Agramonte (Universidad de los Andes), Antonio García Casco (Universidad de Granada), Jesús Solé Viñas, Luigi Solari y Fernando Ortega Gutiérrez, a quienes agradezco sus observaciones y comentarios enriquecedores sobre mi trabajo. Agradezco también a quienes formaron parte de mi jurado de examen de candidatura: Dante Morán Zenteno, Jesús Solé Viñas, Bodo Weber, Ricardo Vega Granillo (Universidad de Sonora) y Fernando Ortega Gutiérrez por su evaluación constructiva de mi proyecto.

Los artículos derivados des este trabajo fueron revisados por Tatsuki Tsujimori (Tohoku University), Hans Peter Schertl (Ruhr-Universität Bochum), Kennet Flores (City University of New York), Hans Joachim Massonne (Universität Stuttgart), Samuel Angiboust (Institut de Physique du Globe de Paris) y dos revisores anónimos, a quienes les doy las gracias por sus revisiones críticas y constructivas.

Agradezco a Consuelo Macías Romo, Teodoro Hernández Treviño y Claudia Bautista Reyes (Instituto Politécnico Nacional) por su apoyo durante el procesamiento de las muestras. El trabajo de microscopía electrónica y microanálisis se realizó con el apoyo de Carlos Linares López, Margarita Reyes Salas, Sonia Ángeles García, Oscar Talavera Mendoza (Universidad Autónoma de Guerrero) y Jazmín López Díaz (Universidad Autónoma de Guerrero). Los procedimientos isotópicos fueron posibles gracias al apoyo de Carlos Ortega Obregón, Sergio Padilla Ramírez (CICESE), Daniela Tazzo Rangel (CICESE), Alejandro Cisneros de León, Gerardo Arrieta García y Gabriela Solís Pichardo. Les doy las gracias también a otras personas que colaboraron amablemente en distintas etapas del proyecto: Douglas Tinkham (Laurentian University), Julie Chouinard (University of Oregon), Juliana Estrada Carmona, Reneé González Guzmán (CICESE), Lidia Butjosa (Universitat de Barcelona), Marta Lagunas, Juan Tomás Vázquez Ramírez, Joaquín Aparicio Aparicio, Jaime Díaz Ortega, Leticia Alba Aldave, Teresa Pi Puig, Patricia Girón, Ofelia Pérez Arvizu, Emiliano Campos Madrigal, Nora Ahuatzín Zárraga, Elena Centeno García, Rosa Bill Guevara, Juan Carlos Cruz Ocampo, Ma. Guadalupe Quintino Cintora, Alicia Pérez Mójica, María Luisa Reyes Ochoa y Gloria Benítez Alba.

Tabla de contenido

Resumen

El Complejo Chuacús, en la cordillera central de Guatemala, es un basamento polimetamórfico mesoproterozoico a triásico tardío que se encuentra emplazado en el límite actual de las placas de Norteamérica y el Caribe. La historia pre-caribeña (>140 Ma) de este basamento incluye distintos episodios de magmatismo y metamorfismo ocurridos durante los periodos Esténico (1.1-1.0 Ga), Ordovícico (ca. 450 Ma), Silúrico-Devónico (420-400 Ma) y Triásico Tardío (ca. 220 Ma), así como también periodos intermitentes de sedimentación marina durante el Neoproterozoico y el Paleozoico. Esta cronología de eventos es análoga tanto al bloque Maya como a los terrenos del norte de los Andes en Sudamérica, e implica una afinidad con un basamento tipo Rodinia y una evolución paleozoica peri-Gondwánica. En el Cretácico Temprano (ca. 100 Ma), este basamento fue inhumado a través de un gradiente geotérmico bajo de ~9 °C/km, experimentando así un metamorfismo prógrado a 18-20 kbar y 530-580 °C, que alcanzaría condiciones pico de 23-25 kbar y 630-690 °C. La naturaleza del basamento, así como la edad y las condiciones *P-T* del metamorfismo cretácico temprano, son consistentes con una etapa temprana de metamorfismo de subducción, donde el basamento continental de la placa de Norteamérica habría subducido a una profundidad de ~80 km por debajo de un bloque cortical meridional, probablemente el Arco de las Antillas Mayores, durante la evolución de la placa del Caribe. Los datos petrológicos sugieren que el Complejo Chuacús habría subducido como una unidad coherente, aunque una discrepancia en presión de ~7 kbar entre las rocas de composición granítica y otros tipos de roca de la región debe ser todavía reevaluada. Durante una fase inicial de exhumación, el complejo experimentó una descompresión casi isotérmica de ~13 kbar, reequilibrándose localmente a ~12 kbar y ~640 °C. Un reequilibrio extenso en facies de anfibolita a 7-8 kbar y 590-620 °C ocurrió en el Cretácico Tardío (ca. 74 Ma) durante una etapa colisional subsecuente.

Abstract

The Chuacús Complex, in the central cordillera of Guatemala, is a Mesoproterozoic to Late Triassic polymetamorphic basement located at the current North American-Caribbean plate boundary. The pre-Caribbean history of this basement comprises several episodes of magmatism and metamorphism, which occurred during the Stenian (1.1-1.0 Ga), Ordovician (ca. 450 Ma), Silurian-Devonian (420-400 Ma) and Late Triassic (ca. 220 Ma), as well as intermittent periods of marine sedimentation during the Neoproterozoic and Paleozoic. This chronology of events is analogous to both the Maya block and the terranes of the northern Andes in South America, implying a Rodinia-type basement affinity and a peri-Gondwanan Paleozoic evolution. During the Early Cretaceous (ca. 100 Ma), this basement was buried along a low geothermal gradient of ~9 °C/km, such that it experienced prograde metamorphism at 18-20 kbar and 530-580 °C, and peak metamorphic conditions at 23-25 kbar and 630-690 °C. The nature of the basement, along with the age and the *P-T* conditions of Early Cretaceous metamorphism, are consistent with an early stage of subduction-zone metamorphism, where the North American continental basement would have subducted to ~80 km beneath a southern crustal block, probably the Greater Antilles Arc, during the Caribbean plate evolution. Petrological data suggest that the Chuacús Complex would have subducted as a coherent unit, although a pressure discrepancy of ~7 kbar between granitic rocks and other rock types from the region still require a re-evaluation. During an initial exhumation stage, the complex experienced an almost isothermal decompression of ~13 kbar, which resulted in local reequilibration at ~12 kbar y ~640 °C. A pervasive reequilibration under amphibolite-facies conditions at 7-8 kbar y 590-620 °C occurred at Late Cretaceous time (ca. 74 Ma) during a subsequent collisional stage.

1

Introducción

1.1. ANTECEDENTES

La geología de la cordillera central de Guatemala, entre los valles de Polochic y Motagua, representa una pieza clave en el complejo rompecabezas tectónico de la región de Centroamérica y el Caribe. La importancia de dicha área se debe, sobre todo, a que se encuentra ubicada en el límite actual de las placas de Norte América y del Caribe (Fig. 1.1a). La Zona de Sutura de Guatemala (Brueckner *et al*., 2009; Flores *et al*., 2013), como se le conoce, ha registrado tanto en la estratigrafía, como en la estructura y naturaleza petrológica de sus unidades, una serie de procesos incluidos subducción, cierre oceánico, colisión, exhumación y transporte tectónico lateral, que se relacionan con la evolución de la placa del Caribe desde el periodo Jurásico hasta el presente (*evento caribeño* en adelante). Si bien el trabajo geológico en esta área se inició hace poco más de 150 años, con los trabajos pioneros de Dollfus & Montserrat (1868) y Sapper (1899), los primeros estudios detallados no se llevaron a cabo sino hasta un siglo después (e.g. McBirney, 1963; Kesler *et al*., 1970). Desde entonces y de forma más o menos continua, con algunos episodios de interés renovado, el conocimiento geológico de la región ha ido en aumento, a la par del establecimiento de nuevos paradigmas geológicos y el desarrollo de distintas metodologías analíticas (e.g. Donnelly *et al*., 1990; Harlow, 1994; Harlow *et al*., 2004; Ortega-Gutiérrez *et al*., 2004; Tsujimori *et al*., 2006; Brueckner *et al*, 2009; Ratschbacher *et al*., 2009; Solari *et al*., 2011; Martens *et al*., 2012; Flores *et al*., 2013).

Pocos lugares en la Zona de Sutura de Guatemala poseen un registro geológico tan extenso e intrincado como el complejo metamórfico expuesto en la Sierra de Chuacús (Fig. 1.1a, recuadro). Este basamento metamórfico es hoy conocido como "Complejo Chuacús" (Ortega-Gutiérrez *et al*., 2004), un nombre que reemplaza otras denominaciones empleadas en estudios anteriores de la misma zona y de otras áreas de la cordillera (McBirney, 1963; Kesler *et al*., 1970). Lo primero que hace relevante al Complejo Chuacús es que, mientras el *evento caribeño* en otras áreas de la cordillera se manifiesta en aspectos como el registro sedimentológico, el desarrollo de zonas de cizalla regionales o el emplazamiento tectónico de fragmentos ofiolíticos (e.g. Donnelly *et al*., 1990; Harlow *et al*., 2004; Ratschbacher *et al*.,

2009; Martens *et al*., 2012), este basamento manifiesta en sí mismo el proceso de subducción/colisión entre el margen continental de la placa de Norteamérica y un bloque cortical meridional, probablemente el Arco de las Antillas Mayores (e.g. Pindell *et al*., 2012; Fig. 1.1b). Como resultado de este proceso, el basamento de la placa de Norteamérica habría sido inhumado a una profundidad de al menos 80 km (Martens *et al*., 2012), experimentando un metamorfismo eclogítico que probablemente alcanzaría condiciones de presión ultra alta (Ortega-Gutiérrez *et al*., 2004). Sin embargo, los estudios previos enfocados en dicho evento han dejado abiertos a discusión varios temas, relacionados no solo con aspectos regionales sino también con aspectos propios del proceso metamórfico y su interpretación tectónica inherente. Una interrogante importante de carácter regional, por ejemplo, se refiere a la extensión misma del metamorfismo de alta presión relacionado con el proceso de subducción/colisión continental. Dicho metamorfismo ha sido reconocido únicamente en el flanco sur de la Sierra de Chuacús (e.g. Martens *et al*., 2012) y sus límites, sean tectónicos o transicionales, se encuentran escasamente documentados. A su vez, este ha sido documentado principalmente con base en la presencia de cuerpos de eclogita intercalados en una secuencia mayoritariamente gnéisica, sin que la extensión de un metamorfismo cofacial hacia otras litologías, relacionadas espacialmente, haya sido corroborada y evaluada en profundidad.

Con respecto al proceso metamórfico, es muy poco lo que se conoce sobre la evolución presión-temperatura-tiempo (*P*-*T*-*t*) del complejo. La información *P*-*T* se limita a un número de estimaciones termobarométricas (e.g. Ortega-Gutiérrez *et al*., 2004; Ratschbacher *et al*., 2009; Martens *et al*., 2012), que si bien proporcionan un estimación razonable de las condiciones máximas alcanzadas, son insuficientes para evaluar la trayectoria metamórfica en términos del gradiente geotérmico imperante durante la inhumación (etapa prógrada), de las condiciones pico registradas por litologías contrastantes o de las características y el estilo de la exhumación (etapa retrógrada). ¿Experimentó el Complejo Chuacús un metamorfismo de subducción o de colisión?, ¿se equilibró en condiciones de presión ultra alta?, ¿durante el metamorfismo se comportó como una secuencia coherente o fue amalgamado durante la exhumación?. Por otro lado, en relación con la edad del metamorfismo, se ha documentado ampliamente un pico de edades (U-Pb en zircón) de ca. 75 Ma, el cual ha sido atribuido a la perturbación térmica que habría resultado del *evento caribeño*. Sin embargo, las distintas edades metamórficas disponibles, interpretadas ya sea como de pico metamórfico o de retrogresión, son indistinguibles dentro de las incertidumbres analíticas (e.g. Martens *et al*., 2012). ¿Fue el ciclo metamórfico lo suficientemente acelerado para impedir que se discrimine en términos geocronológicos las etapas de inhumación y exhumación?, ¿Cuánto duró dicho ciclo y cuál es la correlación espacio-temporal de la edad de pico metamórfico con otras áreas del Caribe?

No obstante el *evento caribeño* significa un parteaguas en la historia geológica del Complejo Chuacús, este episodio representa tan solo la etapa más reciente en la cronología de un basamento cuya

historia geológica puede rastrearse hasta el Mesoproterozoico. Estudios geocronológicos recientes han demostrado que los protolitos ígneos en el Complejo Chuacús cristalizaron principalmente durante un pulso magmático del Triásico Tardío (ca. 220 Ma; Ratschbacher *et al*., 2009; Solari *et al*., 2011; Martens *et al*., 2012), pero otras edades más antiguas, del Ordovícico (ca. 450 Ma; Solari *et al*., 2011) al Cámbrico-Ediacárico (Ratschbacher *et al*., 2009) han sido también reportadas. Por otro lado, estos mismos estudios, y otros más a lo largo del bloque Maya (e.g. Solari *et al*., 2009; Martens *et al*., 2010; Solari *et al*., 2013; Fig. 1.1a), coinciden en encontrar, tanto en rocas metaígneas como metasedimentarias, un componente constante heredado/detrítico del Mesoproterozoico. ¿Existe un basamento precámbrico en la Zona de Sutura de Guatemala? Adicionalmente, también de la mano de estudios geocronológicos, se ha reconocido la posible ocurrencia de dos eventos de metamorfismo paleozoico de alto grado (Solari *et al*., 2011); de ahí que la existencia de episodios repetidos de magmatismo y metamorfismo sugiera una evolución polimetamórfica pre-caribeña. ¿En qué contexto tectónico-temporal estaría situado cada evento? A pesar de estos hallazgos, el origen de las distintas unidades del complejo, la naturaleza de sus relaciones espacio-temporales pre-Mesozoicas y los escenarios tectónico-temporales correspondientes se encuentran todavía poco entendidos, sobre todo ante la necesidad de un mayor trabajo cartográfico y la carencia de una base de datos geocronológica y geoquímica sistemática que permitan además correlacionar el Complejo Chuacús con otras regiones de México, Centro-Sudamérica y el Caribe.

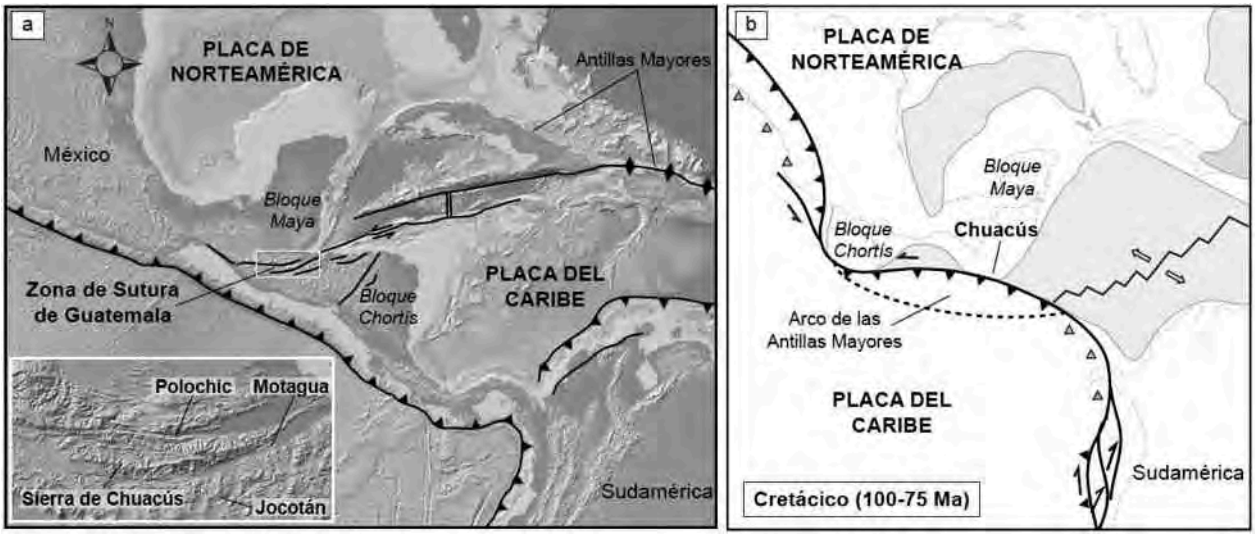

Figura 1.1. (a) Contexto tectónico de la Zona de Sutura de Guatemala (Brueckner *et al*., 2009; Flores *et al*., 2013) mostrando la ubicación de la Sierra de Chuacús en la cordillera central de Guatemala (recuadro). Las líneas representan las zonas de falla principales y en el recuadro se señala la ubicación de las fallas Polochic, Motagua y Jocotán. (b) Esquema paleogeográfico simplificado (modificado de Pindell *et al*., 2012) que muestra la configuración tectónica inferida de la zona del Caribe durante el periodo Cretácico. El modelo de elevación fue obtenido con GeoMapApp versión 3.5.2 (http://www.geomapapp.org).

1.2. PROPUESTA Y OBJETIVOS

Este trabajo surge en gran medida del planteamiento de las interrogantes anteriores y se desarrolla sobre la base de un enfoque multidisciplinario en un esfuerzo por dilucidar aspectos relacionados tanto con el evento tectonotérmico caribeño como con el origen y la evolución previa del basamento. Se busca integrar la información existente con un nuevo cuerpo de datos derivados de tres fuentes distintas: 1) de campo, 2) analíticos y 3) de modelación teórica. Un análisis exhaustivo de campo fue el primer paso crucial para la colección oportuna de muestras de roca, mientras que una descripción petrográfica detallada fue crítica para la identificación y selección de muestras adecuadas para los procedimientos analíticos subsecuentes. Los métodos analíticos fueron empleados para obtener información mineralógica (identificación a través de difracción de rayos X y espectroscopia Raman), petrológica (textural y químico-mineral a través de microscopía electrónica), geoquímica (elementos mayores, traza e isótopos en roca total) y geocronológica (métodos isotópicos *in situ* y por dilución). La modelación teórica se utilizó para evaluar las observaciones petrográficas y obtener información cuantitativa sobre las condiciones del metamorfismo. Para tal efecto, se emplearon distintos programas de cómputo (e.g. TWQ, Perplex, Theriak-Domino) que integran bases de datos termodinámicos (propiedades termodinámicas y modelos de solución) y permiten investigar equilibrios minerales en el espacio *P*-*T*-composición. La metodología empleada para la investigación de cada tópico específico se detalla en los capítulos subsecuentes.

El objetivo del estudio fue investigar y tratar de dar respuesta a los siguientes problemas particulares:

1) ¿Cuáles fueron las condiciones *P*-*T* máximas alcanzadas durante el metamorfismo de alta presión del Complejo Chuacús?, ¿experimentaron otros tipos de roca asociados las mismas condiciones *P*-*T* que los cuerpos de eclogita?

2) ¿Cuál es la extensión del metamorfismo de alta presión en el Complejo Chuacús y de qué forma está relacionada con la estructura interna del mismo?

3) ¿Se comportó el Complejo Chuacús como una secuencia coherente durante dicho metamorfismo?

4) ¿Se preservaron evidencias de la evolución prógrada?, ¿en qué régimen geotérmico ocurrió?

5) ¿Cuáles fueron las características de la exhumación?

6) ¿Puede distinguirse la temporalidad de las distintas etapas del metamorfismo de alta presión?, ¿qué relación tiene con la cronología aparentemente variable de dicho evento en otras regiones del Caribe?

7) ¿Cuál es el intervalo de edad y el origen del basamento del Complejo Chuacús?

8) ¿En qué escenarios tectónico-temporales evolucionó dicho basamento y cuáles son sus posibles conexiones con otras áreas del continente americano?

1.3. ESTRUCTURA DE LA TESIS

Lo temas relacionados con el *evento caribeño* (preguntas 1 a 6) representan en conjunto uno de los objetivos centrales de este trabajo y como tal subyacen el contenido de los tres capítulos centrales de la tesis (Capítulos 2, 3 y 4), mientras que lo referente al origen y evolución pre-caribeña (últimas y no por ello menos importantes cuestiones) es abordado en los capítulos 3 y 4. Dichos capítulos adoptan el formato de tres artículos publicados en revistas especializadas de circulación internacional.

El **Capítulo 2** consiste en un estudio petrológico basado en la cartografía detallada de un área relativamente pequeña ubicada a <5 km al sur de la zona de cizalla de Baja Verapaz (Ortega-Obregón *et al.*, 2008). Se investiga la ocurrencia de una secuencia metasedimentaria con evidencias de metamorfismo de alta presión, en un sector donde los trabajos previos habían documentado únicamente asociaciones metamórficas en facies de esquisto verde y anfibolita (e.g. McBirney, 1963; van den Boom, 1972). Como resultado, este estudio permite documentar la extensión del metamorfismo de alta presión (~20 kbar) hacia el sector septentrional de la Sierra de Chuacús, al menos 10 km más al norte de lo que previamente se suponía. Otra conclusión importante se refiere a las características petrográficas que, en conjunto con la predicción termodinámica, sugieren la ocurrencia de un solo ciclo metamórfico a través de un gradiente geotérmico considerablemente bajo (7-9 °C/km), típico de zonas de subducción. Se discuten las posibles implicaciones tectónicas de estos resultados, considerando la posición estructural de esta zona dentro del complejo y de sus características petrológicas en relación con otras localidades de la zona de estudio aparentemente más profundas. Este artículo se encuentra publicado en el *European Journal of Mineralogy* y fue revisado por los Prof. Hans-Peter Schertl de la *Ruhr-Universität Bochum*, Alemania y Tatsuki Tsujimori de la *Tohoku University*, Japón, así como por un revisor anónimo.

En el **Capítulo 3** se presenta un estudio petrológico y geocronológico exhaustivo que busca, en primera instancia, precisar la evolución metamórfica cretácica del complejo y, adicionalmente, indagar acerca del origen de los precursores, tanto ígneos (básicos) como sedimentarios (pelíticos). Para ello, se llevó a cabo un trabajo de campo extenso donde se verificó la ocurrencia de varias localidades nuevas de eclogita y de esquisto pelítico con granate-cianita. Se estudiaron dos variedades representativas de eclogita provenientes del sector central de la Sierra de Chuacús, donde Ortega-Gutiérrez *et al*. (2004) y Martens *et al*. (2012) habían reportado rocas similares y aportado los primeros datos termobarométricos y geocronológicos. Adicionalmente, se estudió un esquisto pelítico, expuesto en el sector oriental del área de estudio y asociado espacialmente con cuerpos de eclogita. Rocas similares habían sido descritas también en trabajos previos (Ortega-Gutiérrez *et al*., 2004; Solari *et al*., 2011), pero sin que se reportara información sobre las condiciones o la edad del metamorfismo. Se examinaron en detalle las características relacionadas con la evolución prógrada de dichos tipos de roca y se evaluaron las

condiciones *P-T* del pico metamórfico con la finalidad de detectar posibles contrastes o, en su caso, corroborar si la secuencia experimentó una misma evolución metamórfica. La edad del metamorfismo se investigó teniendo como base el contexto petrológico y utilizando un enfoque isotópico multi-mineral: 1) el sistema U-Pb en zircón, monacita y titanita, y 2) el sistema Lu-Hf en granate (y roca total). Finalmente, se utilizó un conjunto de muestras para investigar la edad y proveniencia de los protolitos a partir de geocronología por el método U-Pb en zircón, así como su origen probable con base en las composiciones químicas de elementos mayores y traza en roca total. Se discute el posible significado tectónico de una discrepancia de ca. 25 Ma en las edades metamórficas obtenidas y se propone un modelo que busca explicar cómo se habría registrado el *evento caribeño* en el Complejo Chuacús. Asimismo, se proponen distintos escenarios tectónico-temporales y posibles correlaciones regionales para los protolitos en cuestión. Este trabajo está publicado en el *Journal of Metamorphic Geology* y fue arbitrado por el Prof. Kennet E. Flores de la *City University of New York*, EUA y un revisor anónimo.

En el **Capítulo 4** se llevó a cabo un trabajo petrológico, geocronológico y geoquímico enfocado en el análisis de las rocas metaígneas graníticas de la Sierra de Chuacús. A pesar de que este tipo de roca es el más abundante en la zona de estudio, había recibido poca atención en estudios previos. El trabajo de campo reveló que la estructura de dichas rocas es considerablemente variable a escala meso y macroscópica, variando desde gneises hasta cuerpos no deformados, por lo que se realizó un muestreo sistemático basado en criterios estructurales y de sus relaciones con otros tipos de roca. Por un lado, se consideró indispensable determinar si dichos metagranitos, que comúnmente hospedan lentes de eclogita, habrían experimentado una evolución *P-T* en común; lo cual era probable de acuerdo con Ortega-Gutiérrez *et al*. (2004) y Ratschbacher *et al* (2009), quienes reportaron petrográficamente relictos de onfacita en rocas de este tipo. Numerosos estudios en otros orógenos colisionales, sin embargo, han mostrado que los contrastes *P-T* entre las rocas félsicas y los cuerpos asociados de eclogita son relativamente comunes (e.g. Massonne, 2016 y referencias citadas), lo cual representa un aspecto crucial en la interpretación de los mecanismos de inhumación y exhumación. Para evaluarlo, se estudiaron en detalle las características petrográficas y químico-minerales de tres tipos de metagranito con un grado bajo de retrogresión, y se siguió un método que combina calibraciones termobarométricas experimentales (barometría de Si en fengita y termometría de Zr en rutilo) con modelación termodinámica, para obtener información sobre las condiciones *P-T*. Se revisa la discrepancia considerable encontrada entre las condiciones *P-T* obtenidas y las calculadas en el Capítulo 3 para otros tipos de roca relacionados, asimismo se discuten los posibles escenarios tectónicos/conceptuales que pudieran explicar dicho fenómeno. Con la finalidad de investigar el posible origen de los protolitos, se estudiaron diez localidades para determinar la edad de cristalización de los magmas graníticos precursores, empleando el método U-Pb en zircón, así como para determinar el ambiente tectónico en que podrían haberse generado, con base

en las composiciones químicas de elementos mayores y traza en roca total. Lo más relevante en términos geocronológicos es el hallazgo de tres localidades con edades de cristalización de entre 1.1 y 1.0 Ga, lo que demuestra la existencia de fragmentos de un basamento Mesoproterozoico en la Sierra de Chuacús. Por otro lado, se discute el posible significado tectónico de un magmatismo bimodal del Triásico Tardío, cuya base no solo son los datos de este capítulo sino también los presentados en el Capítulo 3 y en otros estudios previos (Solari *et al*., 2011; Martens *et al*., 2012). Adicionalmente, las evidencias petrológicas de un metamorfismo de alta presión en dichos granitoides, implicaría que dicho basamento antiguo se habría subducido y exhumado eventualmente durante el *evento caribeño*. Este trabajo está publicado en la revista *Lithos* y fue arbitrado por los Prof[es]. Hans Joachim Massonne, de la *Universität Stuttgart*, Alemania y Samuel Angiboust, del *Institut de Physique du Globe de Paris*, Francia.

Referencias

Brueckner, H. K., Avé Lallemant, H. G., Sisson, V. B., Harlow, G. E., Hemming, S. R., Martens, U., Tsujimori, T., Sorensen, S.S. (2009): Metamorphic reworking of a high pressure–low temperature mélange along the Motagua fault, Guatemala: a record of Neocomian and Maastrichtian transpressional tectonics. *Earth and Planetary Science Letters*, 284, 228–235.

Dollfus, A., Montserrat, E., 1868, Voyage géologique dans les Républiques de Guatemala et de Salvador, Mission scientifique au Mexique et dans l'Amerique céntrale, Géologie. *Paris, Imprimerie Impériale*, 539.

Donnelly, T. M., Horne, G. S., Finch, R. C., & Ramos, E. L. (1990). Northern Central America: The Maya and Chortis Blocks: in The Geology of North America, H: The Caribbean Region,(Dengo, G. and JE Case, eds.), 37-76. *Geological Society of America, Boulder, CO USA*.

Flores, K. E., Martens, U. C., Harlow, G. E., Brueckner, H. K., & Pearson, N. J. (2013). Jadeitite formed during subduction: In situ zircon geochronology constraints from two different tectonic events within the Guatemala Suture Zone. *Earth and Planetary Science Letters*, *371*, 67-81.

Harlow, G. E. (1994). Jadeitites, albitites and related rocks from the Motagua Fault Zone, Guatemala. *Journal of Metamorphic Geology*, *12*(1), 49-68.

Harlow, G. E., Hemming, S. R., Lallemant, H. G. A., Sisson, V. B., & Sorensen, S. S. (2004). Two high-pressure–low-temperature serpentinite-matrix mélange belts, Motagua fault zone, Guatemala: a record of Aptian and Maastrichtian collisions. *Geology*, *32*(1), 17-20.

Kesler, S. E., Josey, W. L., & Collins, E. M. (1970). Basement rocks of western nuclear Central America: the western Chuacús Group, Guatemala. *Geological Society of America Bulletin*, *81*(11), 3307-3322.

Massonne, H. J., 2016. Hydration of the lithospheric mantle by the descending plate in a continent–continent collisional setting and its geodynamic consequences. *Journal of Geodynamics*, 96, 50-61.

Martens, U. C., Brueckner, H. K., Mattinson, C. G., Liou, J. G., & Wooden, J. L. (2012). Timing of eclogite-facies metamorphism of the Chuacús complex, Central Guatemala: record of Late Cretaceous continental subduction of North America's sialic basement. *Lithos*, *146*, 1-10.

Martens, U., Weber, B., & Valencia, V. A. (2010). U/Pb geochronology of Devonian and older Paleozoic beds in the southeastern Maya block, Central America: Its affinity with peri-Gondwanan terranes. *Geological Society of America Bulletin*, *122*(5-6), 815-829.

McBirney, A.R. (1963): Geology of a part of the central Guatemalan cordillera. *California University Publications in Geological Sciences*, 38, 177–242.

Ortega-Gutiérrez, F., Solari, L.A., Sole, J., Martens, U., Gomez-Tuena, A., Morán-Ical, S., Reyes-Salas, M., Ortega-Obregón, C. (2004): Polyphase, high-temperature eclogite facies metamorphism in the Chuacus Complex, central Guatemala; petrology, geochronology, and tectonic implications. *International Geology Review*, 46, 445–470.

Ortega-Obregón, C., Solari, L.A., Keppie, J.D., Ortega-Gutiérrez, F., Solé, J., Morán-Ical, S. (2008): Middle-Late Ordovician magmatism and Late Cretaceous collision in the southern Maya block, Rabinal-Salamá area, central Guatemala: implications for North America–Caribbean plate tectonics. *Geological Society of America Bulletin*, 120(5-6), 556-570.

Pindell, J., Maresch, W. V., Martens, U., & Stanek, K. (2012). The Greater Antillean Arc: Early Cretaceous origin and proposed relationship to Central American subduction mélanges: implications for models of Caribbean evolution. *International Geology Review*, *54*(2), 131-143.

Ratschbacher, L., Franz, L., Min, M., Bachmann, R., Martens, U., Stanek, K., Stübner, K., Nelson, B.K., Herrmann, U., Weber, B., López-Martínez, M., Jonckheere, R., Sperner, B., Tichomirowa, M., Mcwilliams, M.O., Gordon, M., Meschede, M., Bock, P. (2009): The North American–Caribbean Plate boundary in Mexico–Guatemala–Honduras. *Geological Society of London Special Publication*, 328, 219–293.

Sapper, K.T., 1899. Ueber Gebirgsbau und Boden des noerdlichen Mittelamerika. *Petermanns Geographische Mitteilungen*, 119.

Solari, L. A., Gómez-Tuena, A., Ortega-Gutiérrez, F., & Ortega-Obregón, C. (2011). The Chuacús Metamorphic Complex, central Guatemala: geochronological and geochemical constraints on its Paleozoic-Mesozoic evolution. *Geologica Acta*, *9*(3-4), 329-350.

Solari, L. A., Ortega-Gutiérrez, F., Elías-Herrera, M., Schaaf, P., Norman, M., Ortega-Obregón, C., & Chiquín, M. (2009). U-Pb zircon geochronology of Palaeozoic units in western and central Guatemala: Insights into the tectonic evolution of Middle America. *Geological Society, London, Special Publications*, *328*(1), 295-313.

Solari, L., Garcia-Casco, A., Martens, U., Lee, J.K.W., Ortega-Rivera, A. (2013): Late cretaceous subduction of the continental basement of the Maya Block (Rabinal granite, Central Guatemala): Tectonic implications for the geodynamic evolution of Central America. *Geological Society of America*, 125, 625-639.

Tsujimori, T., Sisson, V.B., Liou, J.G., Harlow, G.E., Sorensen, S.S. (2006): Petrologic characterization of Guatemalan lawsonite eclogite; eclogitization of subducted oceanic crust in a cold subduction zone. *Geological Society of America Special Paper*, 403,147–168.

van den Boom, G. (1972). Petrofazielle Gliederung des metamorphen Grungebirges in der Sierra de Chuacús, Guatemala. *Beihefte Geologisches Jahrbuch*, *122*, 5-49.

2

La extensión del metamorfismo de alta presión en el Complejo Chuacús y sus implicaciones tectónicas en el límite de placas Norte América-Caribe

---

Maldonado, R., Ortega-Gutiérrez, F., & Hernández-Uribe, D. (2016). Garnet–chloritoid–paragonite metapelite from the Chuacús Complex (Central Guatemala): new evidence for continental subduction in the North America–Caribbean plate boundary. *European Journal of Mineralogy*, 28(6), 1169-1186.

CONTRIBUCIÓN DE LOS COAUTORES

Roberto Maldonado: planeación del proyecto, trabajo de campo, obtención, procesamiento e interpretación de los datos, redacción del artículo.

Fernando Ortega Gutiérrez: planeación del proyecto, supervisión del trabajo, revisión del borrador del artículo.

David Hernández Uribe: trabajo de campo, procesamiento e interpretación de los datos, revisión del borrador del artículo.

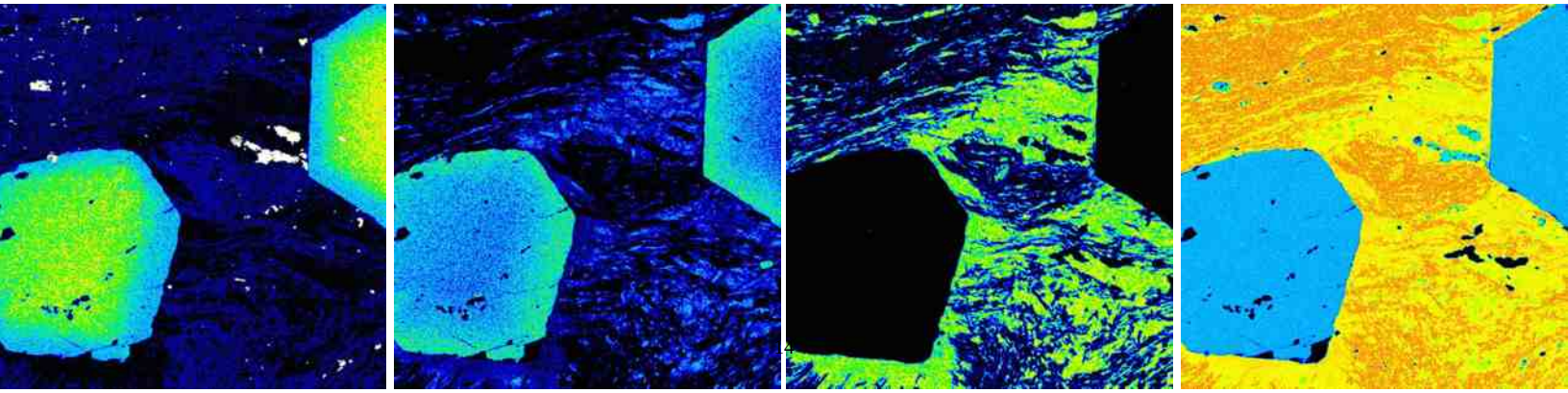

Eur. J. Mineral.
2016, **28**, 1169–1186
Published online 14 October 2016

Paper presented at the XI Eclogite Conference, Dominican Republic, 2–5 February 2015

Garnet–chloritoid–paragonite metapelite from the Chuacús Complex (Central Guatemala): new evidence for continental subduction in the North America–Caribbean plate boundary

ROBERTO MALDONADO[1,*], FERNANDO ORTEGA-GUTIÉRREZ[1] and DAVID HERNÁNDEZ-URIBE[2]

[1] Instituto de Geología, Universidad Nacional Autónoma de México, Ciudad Universitaria, México, D.F. 04510, Mexico
*Corresponding author, e-mail: roberto_maldonado@ciencias.unam.mx
[2] Facultad de Ingeniería, Universidad Nacional Autónoma de México, Ciudad Universitaria, México, D.F. 04510, Mexico

Abstract: We describe for the first time the presence of high-pressure metapelites in the northern Chuacús Complex of Central Guatemala. Garnet–chloritoid–paragonite-bearing pelitic schist occurs in a predominantly metasedimentary sequence consisting of intercalated garnet paragneisses, pelitic schists, impure marbles, granitic orthogneisses and minor garnet amphibolites, an association that denotes a passive continental margin origin. The metapelite we have studied is mainly composed of almandine-rich garnet porphyroblasts in a schistose matrix consisting of phengite, paragonite, quartz, chloritoid and rutile, with minor amounts of chlorite, epidote, Fe–Ti oxides and sporadic kyanite. The metapelite also includes fine-grained paragonite + quartz and paragonite + epidote aggregates, which resemble jadeite and lawsonite pseudomorphs, respectively. A late staurolite-bearing assemblage overprints the high-pressure paragenesis. We have used a phase-equilibria modeling approach to constrain the *P–T* conditions of metamorphism. Equilibrium phase diagrams were calculated in the system MnNCKFMASHTO ($MnO–Na_2O–CaO–K_2O–FeO–MgO–Al_2O_3–SiO_2–H_2O–TiO_2–Fe_2O_3$) for three hypothetical effective bulk-compositions. The compositions of garnet, chloritoid and phengite cores indicate they crystallized during an early stage of prograde high-pressure metamorphism at 20–21 kbar and 500–540 °C. The composition of garnet rims constrains the *P–T* peak conditions to ~19.5–20 kbar and 580–600 °C. Both the zoning pattern of the garnet and the calculated *P–T* path indicate that the studied metapelite could be formed during a single progressive metamorphic event along a subduction geothermal gradient of 7–9 °C/km. The retrograde path is less well constrained, although decreasing pressure coupled with a slight drop of temperature are indicated by the absence of biotite and the growth of post-peak chlorite and epidote. Moreover, a late-stage heating event is required, in order for the metapelite to reach the stability field of staurolite at 7–8 kbar and 590–620 °C. The occurrence of this high-pressure metapelite implies that high-pressure metamorphism in the Chuacús Complex must have extended at least 10 km further to the north than previously thought. We propose that both Chuacús Complex and Rabinal Granite show a succession of decreasing *P–T* peak conditions towards the north, which may preserve in part the original thermal structure of the subduction zone in the southern margin of North America during the Cretaceous.

Key-words: metapelite; high-pressure metamorphism; equilibrium phase diagram; continental subduction; Guatemala Suture Zone; Chuacús Complex.

1. Introduction

Petrological studies of high-pressure (HP) metamorphic belts have revealed that mineral assemblages of metapelitic lithologies provide valuable information about the pressure–temperature (*P–T*) evolution of both subducted continental and oceanic crust (*e.g.*, Compagnoni, 1977; Holland, 1979; El-Shazly & Liou, 1991; Meyre *et al.*, 1999; Okay, 2002; Ko *et al.*, 2005; Le Bayon *et al.*, 2006; Negulescu *et al.*, 2009; Smye *et al.*, 2010; López-Carmona *et al.*, 2013). However, in many cases HP metapelites are strongly affected by late-stage metamorphism, which partially or completely overprints primary mineral assemblages, making it difficult to recognize earlier metamorphic conditions (*e.g.*, Compagnoni *et al.*, 1995; Guillot *et al.*, 1997; Hoschek *et al.*, 2010; Cruciani *et al.*, 2013). In these cases, relic minerals or mineral assemblages from earlier *P–T* conditions are most likely to be preserved either as inclusions within refractory phases or as pseudomorphs (*e.g.*, Liou *et al.*, 1997; Groppo *et al.*, 2006; Song *et al.*, 2007). In particular, the common occurrence of mineral assemblages containing garnet + chloritoid + paragonite + phengite (±jadeite ± lawsonite ± glaucophane ± chlorite) not only in continental-type HP rocks but also in the oceanic-type ones (*e.g.*, Bosse *et al.*, 2002; Song *et al.*, 2007), has proven to be a good

DOI: 10.1127/ejm/2016/0028-2578
0935-1221/16/0028-2578 $ 8.10

indicator of paleo-subduction zones, just like the mineral assemblage garnet + kyanite + chloritoid (Smye *et al.*, 2010).

Eclogite-facies metamorphism in the Chuacús Complex (Central Guatemala) has previously been recognized in metabasic lenses hosted by granitic orthogneisses although there are a few descriptions of other HP lithologies, including metapelitic rocks (Ortega-Gutiérrez *et al.*, 2004; Solari *et al.*, 2011; Martens *et al.*, 2012). These previous studies were concentrated in the southern slope of the Sierra de Chuacús, whereas other areas within the complex have remained almost unknown. This has prevented to determine whether or not the HP metamorphism extends to other areas into the Chuacús Complex, in particular to the north, where the Baja Verapaz shear zone diffusely separates the Chuacús Complex from the Rabinal Granite (Ortega-Obregón *et al.*, 2008). On the other hand, the metamorphic evolution of the Chuacús Complex has been poorly constrained because estimates of the *P–T* conditions have been determined only in restricted areas of the complex by conventional thermobarometric methods. In this study we report, for the first time, the occurrence of HP medium-temperature metapelites in the northern Chuacús Complex. We present detailed petrographic and microchemical descriptions, and undertake phase equilibria modeling to constrain the conditions of metamorphism and the metamorphic evolution of this continental-affinity metapelite. Our results contribute to an understanding of the geologic evolution of the northern Guatemala Suture Zone, and the relationship between the Chuacús Complex and adjacent blocks during Late Cretaceous subduction of the southernmost edge of North America.

2. Geological setting

2.1. The Guatemala Suture Zone

The Guatemala Suture Zone (Brueckner *et al.*, 2009) consists of a complex array of crustal blocks assembled along the Polochic-Motagua-Jocotán left-lateral strike-slip system, which represents the current North American–Caribbean plate boundary in Central America (Fig. 1). This zone forms an east-west trending belt *ca.* 350 km long that extends from western Guatemala to the Caribbean Sea (McBirney, 1963; Ratschbacher *et al.*, 2009), juxtaposing two different continental blocks known as Maya block (North American plate) and Chortis block (Caribbean plate; Dengo, 1969).

The units in the Maya block include the Chuacús metamorphic complex (Ortega-Gutiérrez *et al.*, 2004), which records two main magmatic episodes during the Ordovician and the Triassic, respectively (Solari *et al.*, 2011), the Early Ordovician S-type Rabinal Granite (Ortega-Obregón *et al.*, 2008; Solari *et al.*, 2011), and Paleozoic sedimentary rocks of the Santa Rosa Group. The Chortís block contains the greenschist-facies San Diego phyllite, the amphibolite-facies Las Ovejas complex, and relatively undeformed granitoids. The Guatemala Suture Zone also incorporates a composite unit consisting of serpentinite mélanges associated with low-grade metasediments (*e.g.*, El Tambor complex), which represents obducted fragments of a Jurassic-Cretaceous oceanic crust (Rosenfeld, 1981; Chiari *et al.*, 2006) with proto-Caribbean affinity (*e.g.* Pindell & Barrett, 1990; Mann, 2007). These anachronous units record subduction, collision, lateral tectonic transport and exhumation of both oceanic and continental crust (*e.g.*, Harlow *et al.*, 2004; Ortega-Gutiérrez *et al.*, 2004; Tsujimori *et al.*, 2006; Brueckner *et al.*, 2009; Martens *et al.*, 2012; Solari *et al.*, 2013). Major structures associated with the Polochic-Motagua-Jocotán fault system are shown in Fig. 1b. They consist of a series of arcuate E-W-trending faults, which are the continental extension of the Cayman Trough system (Fig. 1a). The currently active structure is considered to be the Cabañas fault (*e.g.* Martens *et al.*, 2012). Although the total displacement since the early Eocene is estimated to be ≥1100 km (Rosencrantz & Mann, 1991), the manner in which the Polochic-Motagua-Jocotán fault system has accommodated this movement is poorly known.

2.2. High-pressure (HP) rocks in the Guatemala Suture Zone

The HP rocks in the Guatemala Suture Zone (Fig. 1b) consist of two main groups according to the crustal affinity of their protoliths: (1) eclogites and associated basic HP rocks derived from subducted oceanic crust and (2) eclogites and HP gneisses of subducted continental crustal origin.

Eclogitic rocks with oceanic crust affinity occur as exotic blocks within serpentinite mélanges along the Motagua fault zone (*e.g.*, El Tambor complex). These exotic blocks show petrographic variations according to their geographical position with respect to the Cabañas fault (*e.g.*, Tsujimori *et al.*, 2004). To the south of the Cabañas fault, the serpentinite mélange contains blocks of lawsonite eclogite and garnet blueschist with peak mineral assemblages consisting of garnet + omphacite + lawsonite + rutile ± jadeite ± glaucophane ± phengite (Harlow *et al.*, 2004; Tsujimori *et al.*, 2005, 2006; Endo *et al.*, 2012). These HP–LT (low-temperature) eclogites underwent maximum *P–T* conditions at 480–520 °C and 25–26 kbar (Tsujimori *et al.*, 2006; Endo *et al.*, 2012). On the other hand, north of the Cabañas fault, extensive serpentinite bodies contain blocks mainly of garnet amphibolite and clinozoisite eclogite with a peak assemblage of garnet + omphacite + phengitic muscovite + rutile + clinozoisite ± Ca–Na amphibole ± quartz (Tsujimori *et al.*, 2004; Brueckner *et al.*, 2009). This eclogitic assemblage is moderate to strongly overprinted by an amphibolite- to greenschist-facies assemblage. The primary mineralogy of this type of eclogite suggests higher temperatures of 500–650 °C at 20–22 kbar (Tsujimori *et al.*, 2004; Harlow *et al.*, 2004). Equivalent metamorphic ages of 144–126 Ma were obtained from Sm-Nd mineral isochrons of eclogites from both the southern and northern serpentinite mélanges indicating

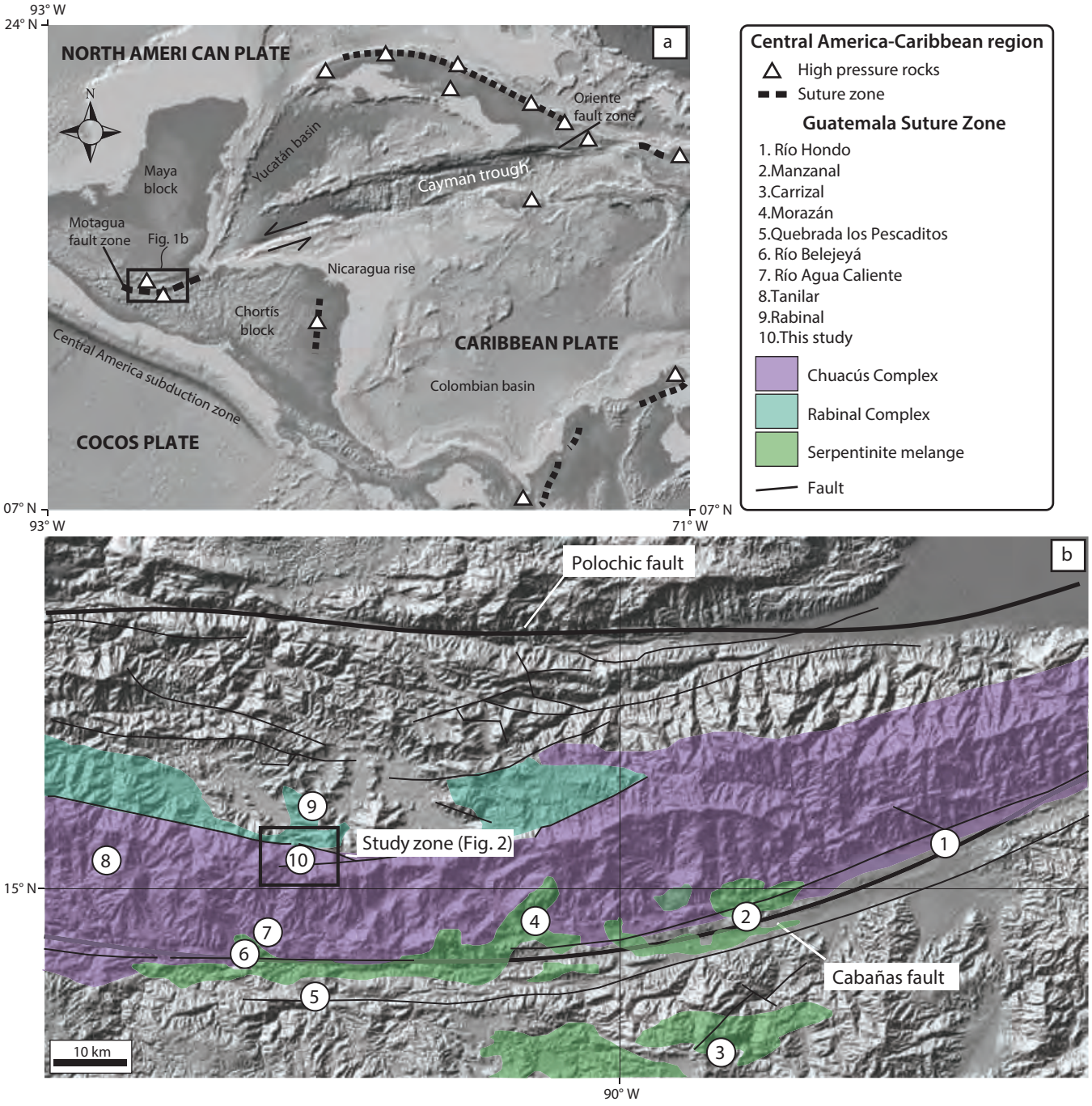

Fig. 1. (a) Tectonic setting of the Central America–Caribbean region modified from Martens *et al.* (2012). Open triangles and dotted lines denote where high-pressure rocks and suture zones have been reported, respectively; notice the location of the Guatemala Suture Zone (rectangle); (b) generalized geologic map of the Guatemala Suture Zone modified from Ratschbacher *et al.* (2009; and references therein) showing the main high-pressure rocks localities after Harlow *et al.* (2004), Ortega-Gutiérrez *et al.* (2004), Tsujimori *et al.* (2006), Martens *et al.* (2012) and Solari *et al.* (2013). Base relief map was obtained from GeoMapApp version 3.5.2 (http://www.geomapapp.org).

coeval HP metamorphism during oceanic subduction (Brueckner *et al.*, 2009). Differences in metamorphic peak conditions imply different *P–T* paths within the same, laterally extensive, subduction system. Meanwhile, Harlow *et al.* (2004) obtained amphibole-white mica Ar/Ar ages of 125–113 Ma and 77–65 Ma for southern and northern eclogites, respectively. These considerably different cooling ages suggest that these belts also underwent separate exhumation histories and thus, different retrogression processes, until they were juxtaposed by strike slip movement along the Motagua fault zone (Brueckner *et al.*, 2009). However, the relative displacement between these belts up to reach their current position is poorly constrained.

Eclogites with continental crust affinity occur as discontinuous bands and lenses widely distributed within the granitic gneisses of the Chuacús Complex (Ortega-Gutiérrez *et al.*, 2004), about 10 km north of the Motagua fault zone (Fig. 1b). The primary eclogitic mineral assemblage, consisting of omphacite + garnet + rutile + quartz ± phengite ± zoisite ± Ca–Na amphibole, yielded *P–T* peak conditions of 660–750 °C and 21–24 kbar (Ortega-Gutiérrez *et al.*, 2004; Ratschbacher *et al.*, 2009; Martens *et al.*, 2012). These near ultra-HP (UHP) conditions were followed by isothermal decompression at 660 °C and 13 kbar (Ratschbacher *et al.*, 2009) producing widespread partial melting and subsequent emplacement of late- to post-tectonic pegmatites (Van den Boom, 1972; Ortega-Gutiérrez *et al.*, 2004; Martens *et al.*, 2012). A regional amphibolite-facies overprint of albite + Ca–Na to Ca amphibole ± biotite ± garnet ± titanite partially replaced the eclogitic mineralogy at 450–550 °C and 7–8 kbar (Ratschbacher *et al.*, 2009). However, recent geochronological data (see below) suggest that this later overprint represents a continuous retrograde process, rather than a post-eclogitic discrete tectonothermal event. One relevant characteristic of the Chuacús Complex is its wide diversity of HP rocks, in addition to eclogites *sensu stricto* and host HP orthogneisses, including garnet–kyanite pelitic schists, garnet paragneisses and impure marbles. For instance, eclogite-facies assembages in mafic rocks are equivalent to garnet + kyanite + phengite + rutile + quartz ± staurolite ± chloritoid ± zoisite assemblages in pelitic rocks, and amphibole + calcite/dolomite + rutile + quartz + zoisite ± chlorite ± diopside in marbles (Ortega-Gutiérrez *et al.*, 2004). U-Pb zircon dating of eclogites and related host orthogneisses yielded a metamorphic age of *ca.* 75 Ma, interpreted as the age of the eclogite-facies metamorphism of the Chuacús Complex (Martens *et al.*, 2012). This age is supported by rare-earth elements patterns of zircon, showing depletions in HREE and lacking Eu anomalies, which suggest zircon growth in a garnet-rich, plagioclase-free, eclogitic assemblage. In addition, a Sm-Nd mineral-whole rock isochron yielded a consistent age of *ca.* 77 Ma. Martens *et al.* (2012) also interpreted an age of *ca.* 74 Ma to be the time of the amphibolite-facies overprinting, which indicates a successive eclogite- to amphibolite facies transition during retrogression instead of two separated tectonothermal events (*e.g.*, Ratschbacher *et al.*, 2009).

Adjacent to, but north of the Chuacús Complex, the Rabinal Granite (Fig. 1b) also records a process of continental subduction (Solari *et al.*, 2013), becoming another locality with HP metamorphism in the Guatemala Suture Zone. This variably deformed pluton has a mineral assemblage of quartz + K-feldspar + plagioclase + phengite ± chlorite ± biotite that overprints the original magmatic mineralogy. Phengite barometry combined with two-feldspar thermometry suggests minimal *P–T* conditions of *ca*. 8 kbar at 280–330 °C (Solari *et al.*, 2013), indicating low blueschist-facies metamorphism. Ar–Ar dating of phengite yielded a mean age of 70.1 ± 0.55 Ma interpreted as the time of recrystallization at HP conditions (Solari *et al.*, 2013), which coincides with the Late-Cretaceous eclogitic metamorphism documented in other localities of the Guatemala Suture Zone.

3. Petrography and mineral chemistry

3.1. Analytical techniques

Two samples from the metasedimentary sequence exposed along Río Pachirax, about 4 km south of Rabinal (Figs. 2 and 3), were analyzed. Representative photomicrographs of microstructural features and assemblages are shown in Fig. 4, and representative compositions for suitable minerals are given in Table 1. X-ray compositional maps and the chemistry of garnet, white mica and chloritoid are displayed in Fig. 5. Mineral abbreviations in figures and tables follow Whitney & Evans (2010).

Mineral assemblages and microstructures were evaluated by petrographic analysis of eight thin sections. Mineral chemical data were acquired at the CAMCOR facility, University of Oregon, using a Cameca SX100 electron microprobe with an accelerating voltage of 15 kV, a beam current of 12 nA, and a beam diameter of 2 μm. Microprobe X-ray images were acquired at the Laboratory of Petrology, National Autonomous University of Mexico, using a JEOL JXA-8900R Superprobe with an accelerating voltage of 20 kV, a beam current of 15 nA, and a beam diameter of 2 μm.

All mineral cations were calculated using the program AX (Holland, 2009; September 2014 update). Anhydrous mineral compositions were calculated to standard numbers of oxygen per formula unit (pfu); whereas white mica analyses were calculated to a total of 11, chloritoid to 6 and epidote to 12.5 oxygens pfu.

3.2. Petrography

A simplified geological map of the northern Chuacús metamorphic complex is shown in Fig. 2. The garnet–chloritoid–paragonite metapelite belongs to a predominantly metasedimentary sequence of alternating garnet–phengite paragneisses, garnet–chlorite micaschists, clinoamphibole–epidote marbles, two-mica granitic orthogneisses and garnet amphibolites. Granitic orthogneisses and amphibolites are part of a metaigneous sequence that crops out widely in other southern localities of the Chuacús Complex (*e.g.*, El Chol area).

The studied pelitic schists occur as centimeter- to meter-size layers intercalated with garnet–phengite paragneisses, and locally with garnet–staurolite micaschists (Fig. 3). In thin section they are seen to be composed of garnet porphyroblasts in a schistose matrix mainly consisting of phengite/muscovite, paragonite, quartz, chloritoid and rutile, with minor amounts of epidote, chlorite, Fe–Ti oxides, apatite, zircon and sporadic kyanite (Fig. 4).

Garnet occurs as small porphyroblasts (<5 mm), sometimes with mineral inclusion-rich cores (Fig. 4a and e). The main minerals included in the garnet are rutile, ilmenite, epidote, chloritoid, white mica and quartz.

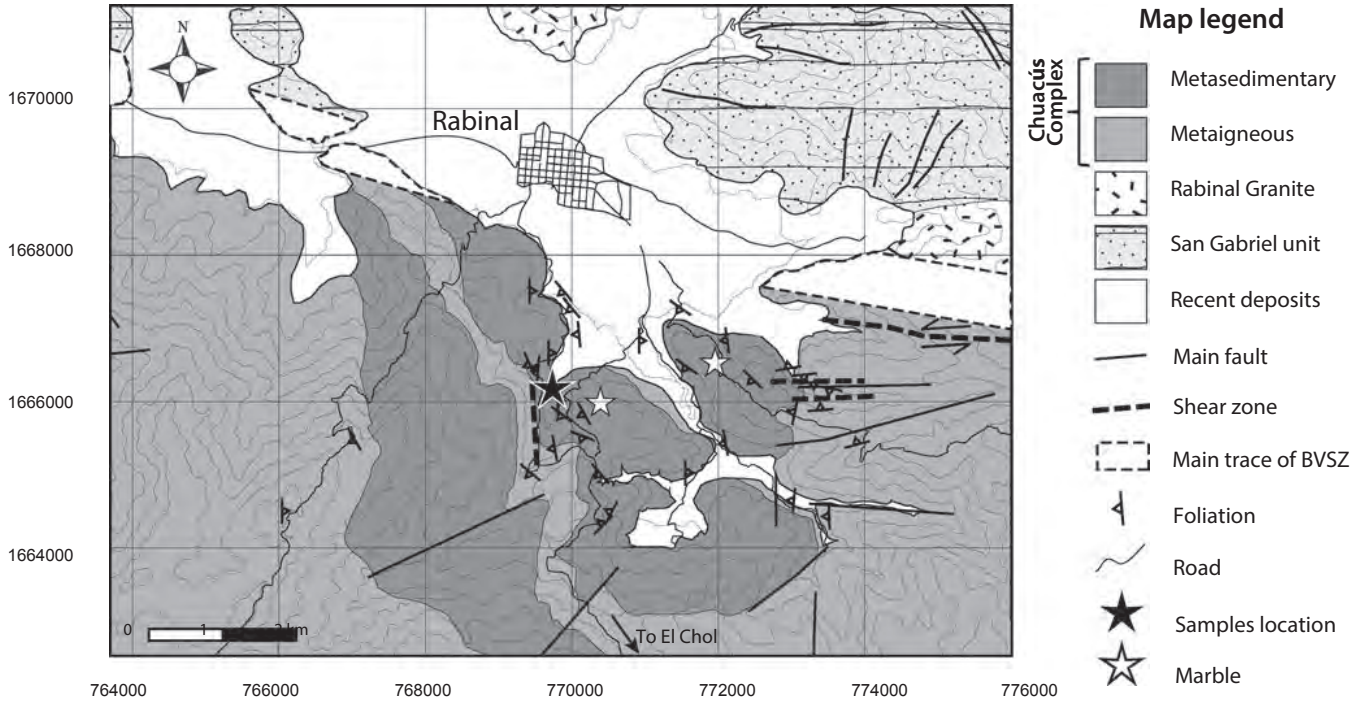

Fig. 2. Simplified geologic map of the study area. Sample location is indicated by black star. Outcrops of Rabinal Granite and San Gabriel unit modified from Ortega-Obregón *et al.* (2008). BVSZ: Baja Verapaz shear zone.

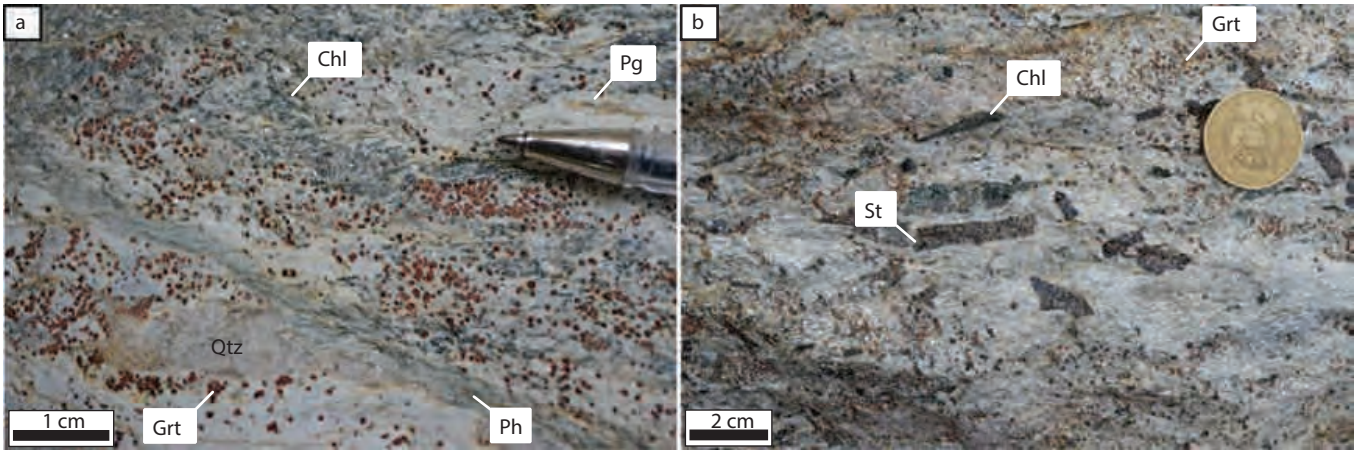

Fig. 3. Outcrop details of the studied metapelite; notice the scale. (a) Millimeter-sized garnet crystals in matrix of white mica, chlorite, quartz and chloritoid (sample CH24). (b) Centimeter-sized staurolite porphyroblasts (center) in a matrix of white mica, garnet, chlorite, quartz and chloritoid (sample CH35).

Chloritoid is found as (i) inclusions within the garnet (Figs. 4e and 5a), (ii) subhedral porphyroblasts (Fig. 5a), and (iii) small anhedral grains within the rock matrix where it is mainly concentrated in quartz-rich domains (Fig. 4a). The cores of both garnet and chloritoid appear to have crystallized simultaneously overgrowing a relic S_{n+1} foliation, which is probably related to an early stage of prograde metamorphism. Kyanite is very rare in the studied samples but in one thin section we observed a small anhedral kyanite crystal partially replaced by phengite.

In the rock matrix, aligned phengite/muscovite, paragonite, chlorite and elongate aggregates of both epidote–paragonite and rutile–ilmenite, all wrap both chloritoid and garnet, and define a S_{n+2} metamorphic foliation (Fig. 4a). This structure appears to be contemporaneous with the growth of both garnet and chloritoid. Phengite is commonly found as coarse-grained aggregates, which irregularly alternate with millimeter- to centimeter-thick quartz-rich domains. Paragonite commonly forms fine-grained lenticular aggregates (Fig. 4b, c), but also is associated with quartz or epidote, forming tabular-shaped intergrowths (Fig. 4e). Coarse-grained flakes of chlorite are aligned with phengite and paragonite; however, these aligned crystals appear to be overgrowing the foliation and partially replacing some garnet crystals (Fig. 4a). So, probably chlorite is not part of the peak metamorphic assemblage. Most epidote grains in the matrix are

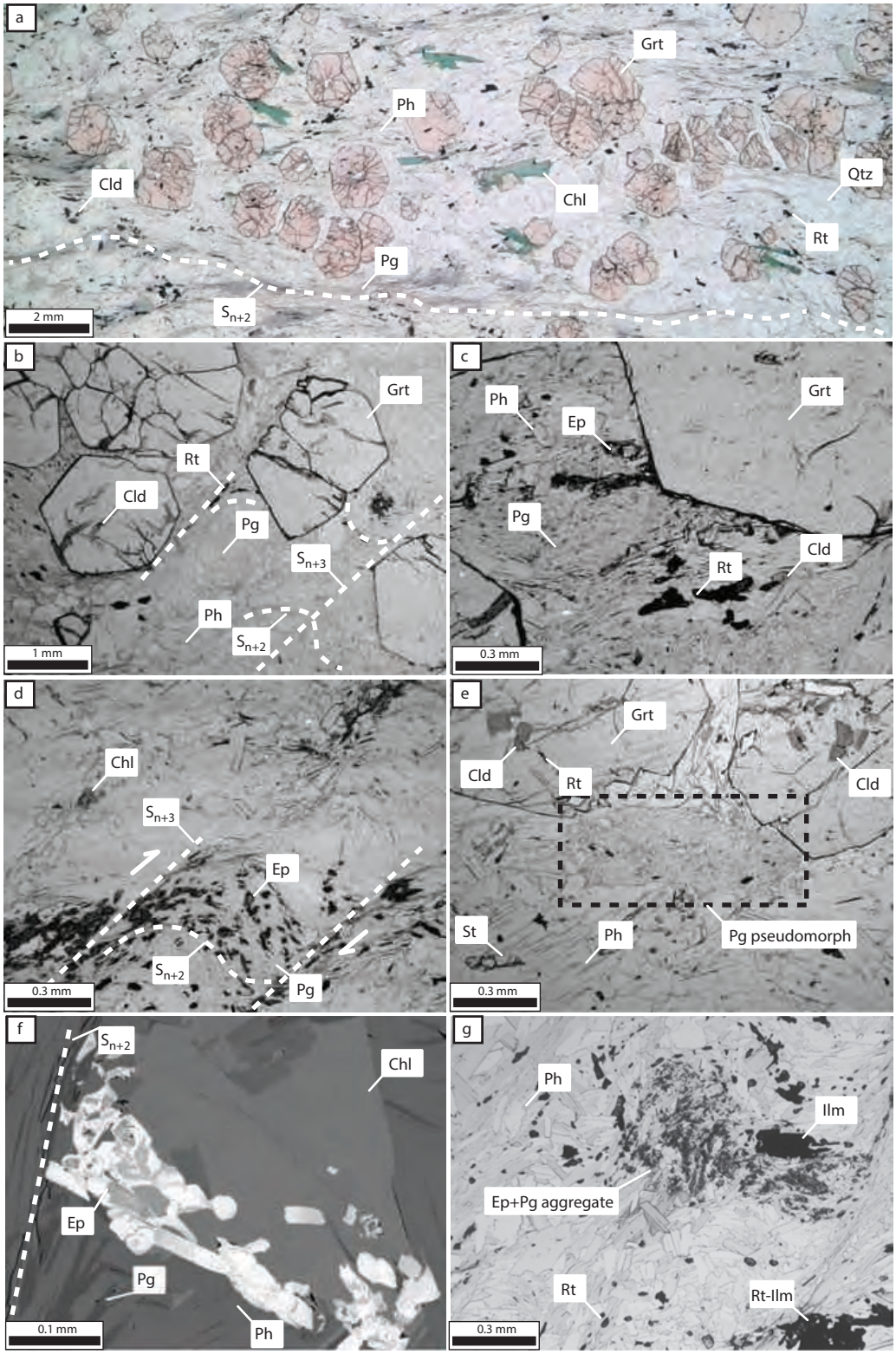

Fig. 4. Plane-polarized light photomicrographs of the studied samples showing typical microstructural features and assemblages. (a) General view of porphyro-lepidoblastic microstructure and S_{n+2} foliation; (b) garnet porphyroblasts with chloritoid inclusions in a mica-rich crenulated matrix; notice the contrast in grain-size between phengite and paragonite; (c) detail of mineral assemblage in the matrix; (d) C-S planes with truncated epidote + paragonite band; (e) paragonite-rich pseudomorph and garnet porphyroblasts with medium-grained chloritoid inclusions; (f) radial aggregate of epidote + chlorite (BSE image); note the discordance with respect to the S_{n+2} foliation; (g) tabular-shaped aggregate of epidote + paragonite.

Table 1. Representative microprobe analyses from garnet-paragonite-chloritoid schist. Oxide totals are presented unmodified. Cation totals were calculated with AX (Holland, 2009), which estimates the amount of ferric iron from stoichiometric criteria. $X_{Mg} = Mg/(Mg + Fe^{2+})$; $Al^{iv} = 4 - Si$; $Al^{vi} = Al - Al^{iv}$; $X_{Na} = Na/(Na + K)$; $Alm = 100[Fe^{2+}/(Fe^{2+} + Mn + Mg + Ca)]$; $Sps = 100[Mn/(Fe^{2+} + Mn + Mg + Ca)]$ $Prp = 100[Mg/(Fe^{2+} + Mn + Mg + Ca)]$; $Grs = 100[Ca/(Fe^{2+} + Mn + Mg + Ca)]$.

Mineral	Grt	Grt	Grt	Grt	Ph	Ph	Ph	Ph	Pg	Pg	Pg	Pg	Cld	Cld	Cld	Ep	Ep
Location	Rim	Rim	Core	Core	Rim	Rim	Core	Core	Matrix	Matrix	Matrix	Matrix	Matrix	Matrix	Matrix	Middle	Core
SiO_2	37.94	38.92	38.38	36.76	46.88	44.98	48.11	48.04	48.49	46.43	45.04	45.67	24.50	24.67	24.66	37.27	37.55
TiO_2	0.01	0.03	0.12	0.06	0.32	0.25	0.31	0.29	0.10	0.07	0.08	0.09	0.00	0.00	0.01	0.00	0.02
Al_2O_3	20.23	19.83	20.18	20.70	32.08	34.83	28.98	28.63	39.80	38.74	39.92	39.30	39.77	39.26	39.61	22.59	25.12
FeO	33.55	33.81	29.41	28.99	3.25	2.76	3.69	3.79	0.90	0.96	0.98	0.78	23.30	23.00	22.82	13.15	11.81
MnO	0.60	0.71	5.56	5.63	0.00	0.01	0.00	0.00	0.01	0.00	0.00	0.00	0.17	0.09	0.07	0.82	0.36
MgO	4.15	4.15	1.86	1.78	1.44	0.54	2.43	2.33	0.09	0.08	0.06	0.06	4.25	4.83	4.88	0.00	0.10
CaO	3.04	2.96	5.83	5.91	0.00	0.02	0.01	0.01	0.49	0.21	0.39	0.30	0.01	0.00	0.00	22.20	21.18
Na_2O	0.01	0.01	0.05	0.04	1.39	1.89	0.81	0.92	4.24	7.79	7.08	7.27	0.00	0.00	0.00	0.00	0.01
K_2O	0.01	0.01	0.00	0.00	9.49	9.09	10.02	9.86	1.01	0.65	0.86	0.82	0.00	0.01	0.00	0.00	0.00
Total	99.56	100.44	101.39	99.88	94.86	94.37	94.36	93.87	95.10	94.92	94.41	94.29	92.00	91.85	92.05	96.04	96.14
Si	3.04	3.09	3.05	2.96	3.16	3.04	3.26	3.28	3.07	2.99	2.92	2.96	1.01	1.01	1.01	3.00	3.02
Ti	0.00	0.00	0.01	0.00	0.02	0.01	0.02	0.02	0.01	0.00	0.00	0.00	0.00	0.00	0.00	0.00	0.00
Al	1.91	1.86	1.89	1.97	2.55	2.78	2.32	2.30	2.97	2.95	3.05	3.01	1.93	1.90	1.91	2.14	2.38
Fe^{3+}	0.01	0.00	0.00	0.11	0.01	0.00	0.05	0.03	0.03	0.00	0.00	0.00	0.06	0.08	0.07	0.86	0.62
Fe^{2+}	2.24	2.24	1.95	1.85	0.18	0.16	0.16	0.19	0.01	0.05	0.05	0.04	0.74	0.71	0.71	0.03	0.18
Mn	0.04	0.05	0.37	0.38	0.00	0.00	0.00	0.00	0.00	0.00	0.00	0.00	0.01	0.00	0.00	0.06	0.03
Mg	0.50	0.49	0.22	0.21	0.15	0.05	0.25	0.24	0.01	0.01	0.01	0.01	0.26	0.30	0.30	0.00	0.01
Ca	0.26	0.25	0.50	0.51	0.00	0.00	0.00	0.00	0.03	0.02	0.03	0.02	0.00	0.00	0.00	1.92	1.62
Na	0.00	0.00	0.01	0.01	0.18	0.25	0.11	0.12	0.52	0.97	0.89	0.91	0.00	0.00	0.00	0.00	0.00
K	0.00	0.00	0.00	0.00	0.82	0.78	0.87	0.86	0.08	0.05	0.07	0.07	0.00	0.00	0.00	0.00	0.24
Sum	8.00	7.98	8.00	8.00	7.05	7.08	7.03	7.03	6.73	7.04	7.03	7.02	4.00	4.00	4.00	8.00	8.10
Oxygens	12.00	12.00	12.00	12.00	11.00	11.00	11.00	11.00	11.00	11.00	11.00	11.00	6.00	6.00	6.00	12.50	12.50
X_{Mg}	0.18	0.18	0.10	0.10	0.45	0.26	0.61	0.56	0.36	0.13	0.10	0.13	0.26	0.29	0.30	0.00	0.06
Al^{iv}	–	–	–	–	0.84	0.96	0.74	0.72	0.93	1.01	1.08	1.04	–	–	–	–	–
Al^{vi}	–	–	–	–	1.71	1.82	1.58	1.58	2.03	1.94	1.98	1.97	–	–	–	–	–
X_{Na}	–	–	–	–	0.18	0.24	0.11	0.12	0.87	0.95	0.93	0.93	–	–	–	–	–
Alm	74	74	64	62	–	–	–	–	–	–	–	–	–	–	–	–	–
Sps	1	2	12	13	–	–	–	–	–	–	–	–	–	–	–	–	–
Prp	16	16	7	7	–	–	–	–	–	–	–	–	–	–	–	–	–
Grs	9	8	16	17	–	–	–	–	–	–	–	–	–	–	–	–	–

subhedral and exhibit optical distinct overgrowths. These epidotes are commonly related to replacement and late-crystallization microstructures, being distinguished from those occurring as inclusions within the garnet by their lower birefringence. Rutile often contains red lamellae (probably exsolved Ti-rich hematite) and is partially replaced by an intergrowth of ilmenite and magnetite.

A spaced S_{n+3} crenulation cleavage (Fig. 4b, d), consisting of reoriented medium- to coarse-grained mica domains, affects the S_{n+2} foliation and post-dates the paragonite-rich tabular aggregates. This crenulation cleavage is related to the local syn-kinematic growth of staurolite. Subsequent LT near-static retrogression is indicated by the occurrence of coarse-grained chlorite crosscutting the S_{n+3}–S_{n+2} foliation and filling garnet fractures.

3.3. Mineral chemistry

Garnet porphyroblasts are chemically zoned, with a bell-shaped distribution of Mn, suggestive of a single episode of growth (Fig. 5c; Woodsworth, 1977). Core to rim zonation is characterized by increasing pyrope (7–16 %) and almandine (62–74 %), and decreasing spessartine (13–1 %) and grossular content (17–8 %; Fig. 5b, c and Table 1). Both the concentric zonation and the euhedral shape of the garnet crystals indicate that neither diffusion nor resorption have significantly affected the original growth zonation, consequently the rim composition is interpreted as preserving the composition formed during peak metamorphism.

Phengitic muscovite occurs in various microstructural locations but only those associated with paragonite in the matrix and the coarse-grained flakes at the S-C planes (S_{n+3}) were analyzed. Phengite in the matrix is slightly zoned showing a decrease in the celadonite content from core to rim (Fig. 5b). Cores have Si = 3.28–3.30 pfu, $Al^{IV} = 0.72$–0.84 and $X_{Na} = 0.12$–0.15 ($X_{Na} = Na/(Na + K)$) whereas rims have Si = 3.04–3.16 pfu, $Al^{IV} = 0.84$–0.96 and $X_{Na} = 0.18$–0.24 (Table 1). Chemical differences between phengite/muscovite rims and the coarse-grained flakes related to the S_{n+3} foliation are indistinguishable. Paragonite occurring as fine- to medium-grained plates intergrown with phengite in the rock matrix has Si = 3.07

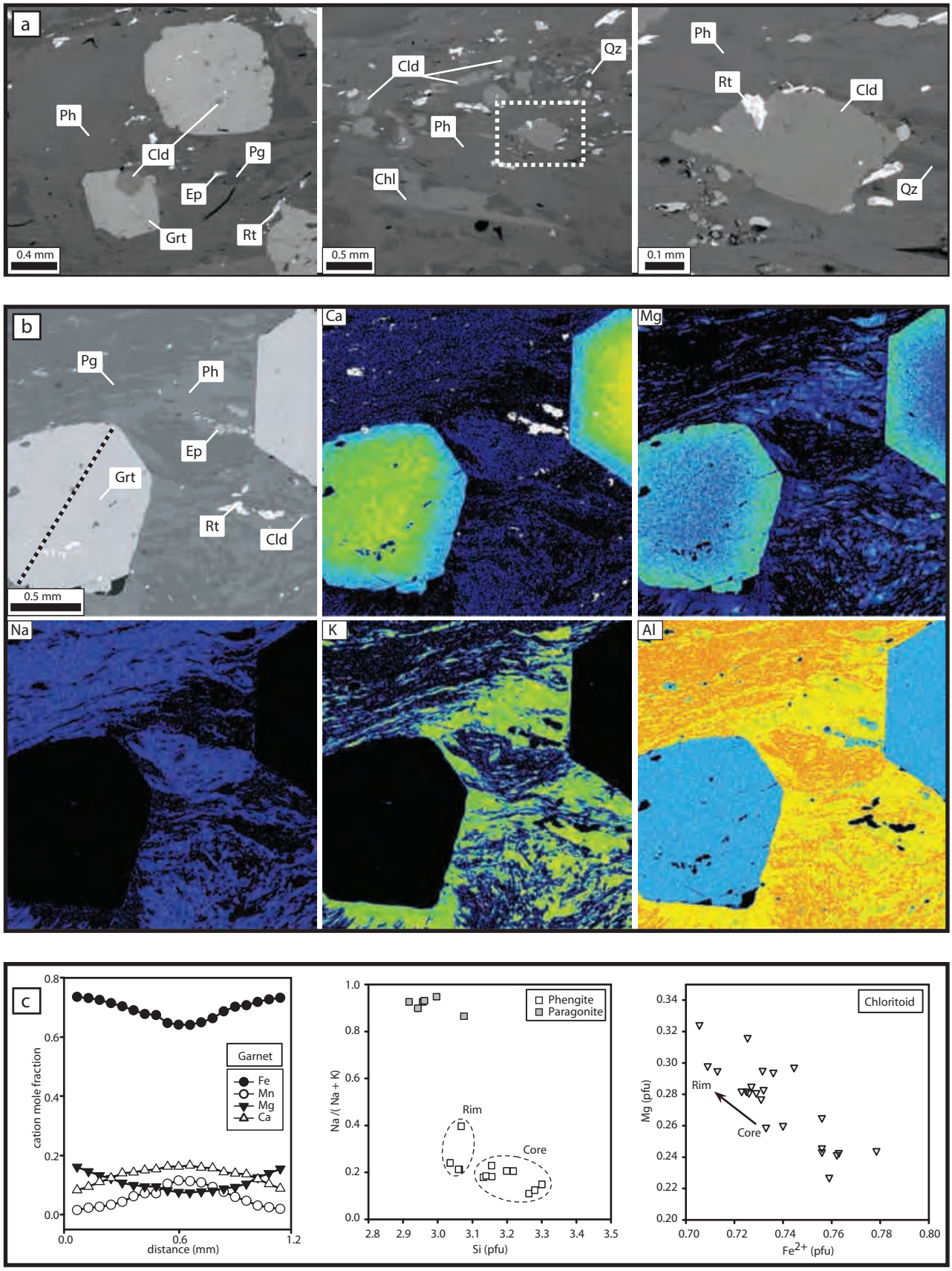

Fig. 5. (a) Backscattered-electron images of chloritoid showing its major associated minerals and microstructures; (b) X-ray compositional maps of garnet and mica-rich matrix; notice the slight compositional zoning of phengite, which is most evident in the Mg-map. The dotted black line indicates the core-rim profile of garnet shown in (c). Red to blue color scale indicates high to low concentrations respectively, but the intensities are not equivalent between images; (c) compositional variations of garnet, white mica and chloritoid in the studied metapelite. Cation totals were calculated using the program AX (Holland, 2009).

Table 2. Whole-rock compositions of the studied metapelite.

Sample	SiO_2	TiO_2	Al_2O_3	FeO(t)	MnO	MgO	CaO	Na_2O	K_2O	P_2O_5	Total	Rock type
XRF analyses (wt.%)												
CH24	49.92	0.97	26.27	9.54	0.25	1.74	1.01	1.74	4.84	0.22	96.51	grt + cld micaschist
CH35	52.88	1.25	24.15	10.24	0.15	1.84	1.02	1.31	4.42	0.21	97.47	grt + st micaschist

Sample	SiO_2	TiO_2	Al_2O_3	Fe_2O_3	FeO	MnO	MgO	CaO	Na_2O	K_2O	H_2O	Total	$X_{Fe_2O_3}$	Figure
Effective bulk compositions used to construct the phase diagrams (wt.%)														
CH24 reduction	52.67	1.03	27.72	–	9.04	–	1.83	0.75	1.84	5.11	Excess	100	0.00	7
CH24	52.49	1.02	27.63	0.60	8.49	0.26	1.83	0.75	1.83	5.09	Excess	100	0.06	8a, b, c, d
CH24 fractionated	53.47	1.08	28.04	0.51	7.19	0.10	1.80	0.46	1.94	5.41	Excess	100	0.06	9a, b, c
CH35 fractionated	56.17	1.37	25.41	0.55	7.78	0.00	1.90	0.50	1.45	4.88	Excess	100	0.06	9d

$X_{Fe_2O_3}$ calculated according to the modal mineral content using AX (Holland, 2009).
$X_{Fe_2O_3} = Fe_2O_3/Fe_2O_3(t)$; $Fe_2O_3(t) = Fe_2O_3 + (FeO \times 1.11)$.

–2.92 pfu, $Al^{IV} = 1.01–1.08$ and $X_{Na} = 0.90–0.95$. Fine-grained paragonite intimately associated with epidote forming tabular pseudomorphs has a more limited range of composition with Si = 2.95–2.96 pfu, $Al^{IV} = 1.04–1.06$ and $X_{Na} = 0.90–0.93$.

Chloritoid is relatively Fe-rich, with values of X_{Mg} (=Mg/(Mg + Fe^{2+})) ranging between 0.23 and 0.30. A representative porphyroblast revealed a slight zonation with $X_{Mg} = 0.28–0.30$ from core to rim. No compositional differences were detected between the chloritoids occurring as inclusions in garnet and those in the matrix. Epidote grains in the rock matrix exhibit optically distinguishable zonation with relative iron enrichment towards the margins, accompanied by the corresponding aluminum decrease. Cores contain $X_{Fe^{3+}} = 0.16 - 0.21$ ($X_{Fe^{3+}} = Fe^{3+}/(Fe^{3+} + Al)$), whereas rims contain $X_{Fe^{3+}} = 0.29$ (Table 1). The increase in the Fe content may indicate slightly more oxidizing conditions during epidote growth. Epidote inclusions in garnet were not analyzed, but these grains display higher birefringence colors than those in the matrix, which may reflect a compositional difference between both types of epidote.

4. Pressure–temperature constraints

4.1. Calculation parameters

Phase equilibria modeling was performed to provide a framework for understanding mineral growth and to constrain the conditions of metamorphism. Equilibrium phase diagrams were constructed over a range of *P*, *T*, bulk-rock ferric iron and bulk-rock H_2O conditions using the Gibbs free-energy minimization software Theriak-Domino (de Capitani & Brown, 1987; de Capitani & Petrakakis, 2010). Modeling was performed in the 10-component MnNCKFMASHTO (MnO–Na_2O–CaO–K_2O–FeO–MgO –Al_2O_3–SiO_2–H_2O–TiO_2–Fe_2O_3) system using the Holland & Powell (1998) thermodynamic database (updated to database 5.5 in 2003, and translated readable for Domino by D.K. Tinkham) with the following *a-X* models: white mica (Coggon & Holland, 2002); garnet and biotite (White *et al.*, 2005); chloritoid (Mahar *et al.*, 1997; White *et al.*, 2000); staurolite (Mahar *et al.*, 1997; Holland & Powell, 1998); epidote and chlorite (Holland & Powell, 1998); clinopyroxene (Green *et al.*, 2007), plagioclase (Holland & Powell, 2003) and an ideal ilmenite–geikielite–pyrophanite ternary model. Although amphibole appears to be common in HP pelitic rocks (*e.g.*, Chopin, 1981; El-Shazly & Liou, 1991; Bosse *et al.*, 2002; Wei & Song, 2008; López-Carmona *et al.*, 2013), this mineral was excluded from our calculations for two reasons: (i) amphibole was not identified in any of the studied samples and there is also no clear evidence of its former presence and (ii) to simplify the calculations. Kyanite, lawsonite, quartz, rutile, titanite and H_2O were considered as pure phases.

Compositions derived by X-ray fluorescence (XRF), X-ray elemental maps, and quantitative electron microprobe analyses were utilized to construct the equilibrium phase diagrams. The effective bulk-compositions were calculated by modification of whole-rock XRF analysis to account for minerals not included in the modeling (*e.g.*, apatite) and for chemical fractionation due to garnet growth (Table 2). Although several methods exist for estimating the effective bulk-composition (*e.g.*, Marmo *et al.*, 2002; Evans, 2004; Tinkham & Ghent, 2005), XRF data were considered suitable for our calculations because our samples show a large degree of equilibration over outcrop scales. Whole-rock XRF analyses were obtained using a Rigaku ZSX Primus II spectrometer at National Autonomous University of Mexico.

As the purpose of this approach is mainly to use phase diagrams as a framework to understand mineral growth trends, a complete assessment of the uncertainties involved in the calculations has not been applied. In addition to the uncertainties inherent to the thermodynamic data set, other sources of uncertainty, such as errors related to the effective bulk-composition chosen, *a-X* models and micro-chemical data, are difficult to assess.

4.2. Estimating metamorphic conditions

In order to get an overview of the *P–T* conditions, we carried out a preliminary assessment of the observed mineral assemblages (Fig. 6) by constructing a schematic

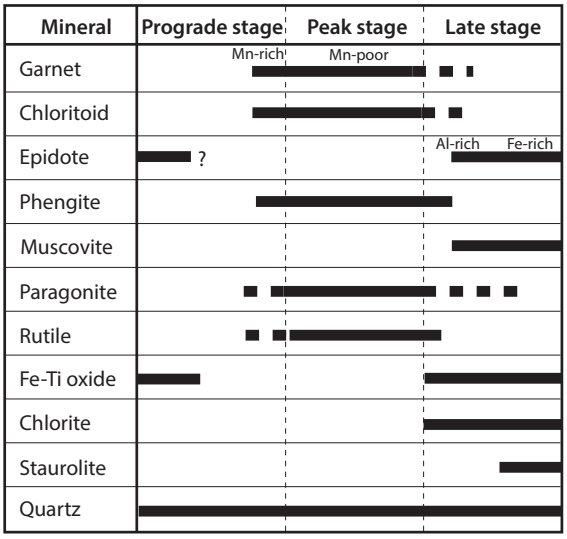

Fig. 6. Mineral parageneses for the different stages of metamorphism recorded in the studied samples.

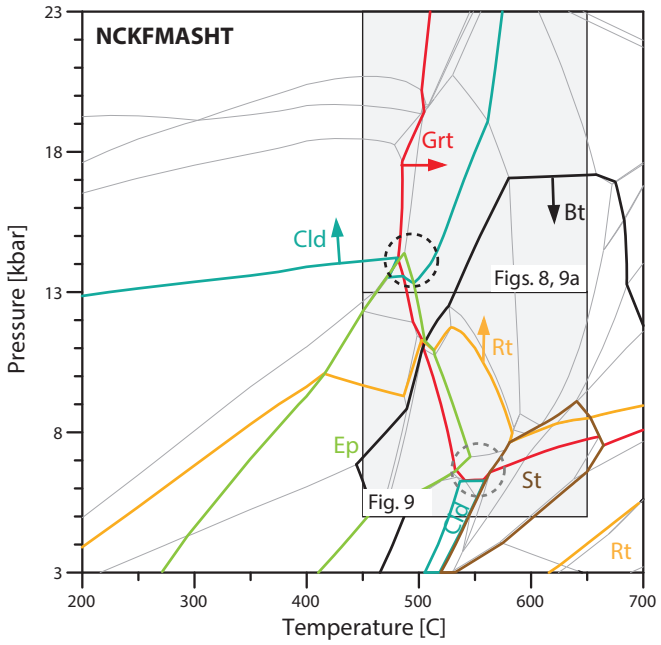

Fig. 7. Schematic *P–T* equilibrium phase diagram calculated for sample CH24 with the software Theriak-Domino (de Capitani & Petrakakis, 2010). The stability fields of major mineral phases are shown in color; notice the overlap of the stability fields of garnet and chloritoid at 500–550 and >13 kbar. Dashed circles indicate *P–T* conditions in which mineral assemblages containing Grt + Cld + Pg + Ms + Qtz are stable (see text). The bulk-composition used for the calculation is given in Table 2.

P–T equilibrium diagram in the system NCKFMASHT (Fig. 7), where Mn and Fe^{3+} were omitted for simplicity. The model system used in this calculation (Table 2) was a reduction of that used in further calculations (Figs. 8 and 9 ; see below), and the model parameters were those recommended for use with THERMOCALC for calculations on metapelites in the above system (http://www.metamorph.geo.uni-mainz.de/thermocalc/).

In principle, an assemblage containing garnet, chloritoid, phengite/muscovite, paragonite, epidote and quartz is predicted not only at *P* as high as >13 kbar, but also at *P* as low as 6 kbar (dashed circles in Fig. 7). The common occurrence of chloritoid-inclusions in garnet and the sporadic occurrence of staurolite in the studied schists (see petrography) are common features in barrovian-type metamorphic terranes. However, in the case of the studied metapelite additional constraints on the *P–T* conditions are provided by the absence of biotite and the ubiquitous occurrence of rutile. These observations are well outlined in Fig. 7 indicating minimal *P* of 13 kbar at 500–550 °C (the *P–T* limit of chloritoid). On the other hand, the local occurrence of staurolite related to S_{n+3} microstructures is interpreted as representing a late amphibolite-facies overprint (see petrography). The presence of epidote commonly related to reaction and late-crystallization microstructures provide a lower-*P* limit about of 14–15 kbar at 450–500 °C (Fig. 7). All these considerations will be explored in detail below.

4.3. High-pressure prograde stage

A set of *P–T* and *P–X* equilibrium phase diagrams (Fig. 8) were calculated to constrain the prograde metamorphic evolution taking into account the factors considered above. The effective bulk-composition used to model mineral equilibria during this stage (sample CH24; Table 2) was obtained from results of a whole-rock XRF analysis of a representative sample lacking significant retrogression. This assumes not only that this composition represents the effective chemical volume during the prograde stage, but also that there were no zoned phases at the time of the initial garnet growth. The XRF analysis was modified to subtract the apatite content by removing all P_2O_5 and the corresponding amount of CaO. A value of $X_{Fe_2O_3} = 0.06$ ($=Fe_2O_3/Fe_{total}$) was assumed, using the composition of the observed mineral assemblage as a guide to the oxidation state (Table 1). The fluid phase was initially considered to be in excess; the validity of this assumption is assessed below.

The *P–T* equilibrium phase diagram calculated for sample CH24 (Fig. 8a, b) constrains the prograde metamorphic evolution through chemical examination of chloritoid, phengite and garnet, considering the inferred peak mineral assemblage (Fig. 6). The red garnet-in line, and the blue chloritoid-out line on Fig. 8a limit the *P–T* range of interest to less than 600 °C. The steep-slope contours of X_{Mg} (dashed blue lines) reveal that chloritoid becomes more magnesian toward its high-temperature limit (~590 °C). The $X_{Mg} = 0.28$ isopleth, which corresponds to the measured composition of the core of chloritoid, defines a narrow band restricted to 540–550 °C, but lies within a considerably large *P* interval (at >16 kbar), which is characterized by a mineral assemblage consisting of garnet + phengite + paragonite + chloritoid + quartz + rutile + H_2O ± clinopyroxene ± chlorite ± magnetite (Fig. 8a). Despite the ubiquitous presence of chlorite in the sample, this mineral seems to have grown

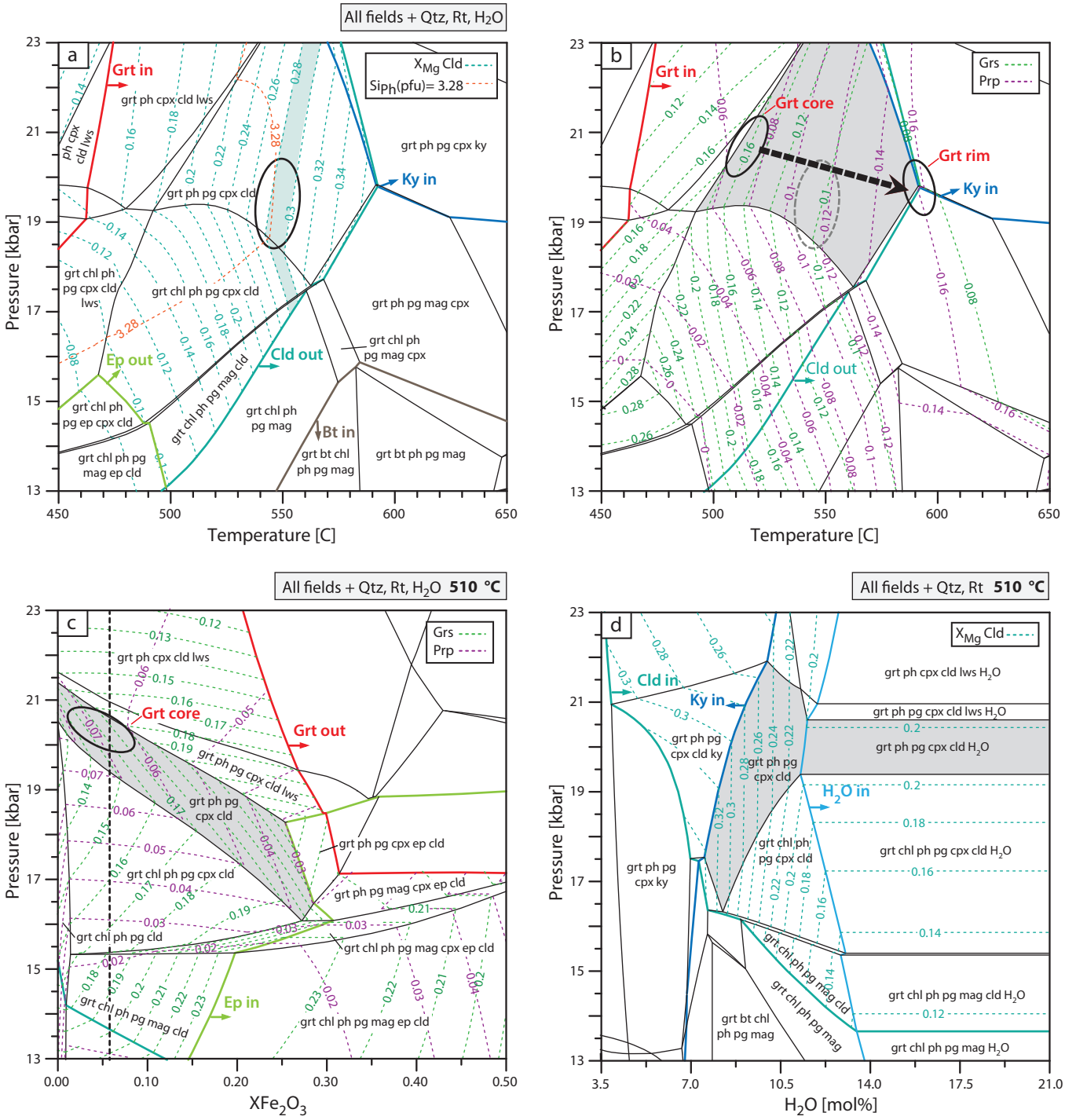

Fig. 8. CH24 equilibrium phase diagram analysis. The bulk-composition used is given in Table 2. Bold ellipses indicate where composition isopleths intersect, but do not represent a formal assessment of uncertainty. Gray shading highlights the fields that best satisfied both the isopleths intersection and the petrographic observations. (a) *P–T* equilibrium phase diagram with assemblages labeled. The chloritoid core-composition ($X_{Mg} = 0.28$) is indicated by the pale-blue band and the Si content in the core of phengite (3.28) by the orange line. (b) Topology as (a), contoured with pyrope and grossular isopleths. Dashed black arrow indicates the probable *P–T* trajectory immediately following the garnet-core growth. (c) Contoured $PX_{Fe_2O_3}$ equilibrium phase diagram calculated at 510 °C. The garnet-out and epidote-in lines delimit the maximum possible values of $X_{Fe_2O_3}$ for the modeling. The dashed black line indicates the $X_{Fe_2O_3}$ value used in (a) and (b). (d) Contoured *P*–H_2O equilibrium phase diagram calculated at 510 °C. Gray shaded fields as in (b) and (c) with extension to H_2O-undersatured conditions. "Cpx" refers to a jadeite–aegirine–omphacite solid solution with variable composition along the stability field.

during a late crystallization stage, so it is not contemporary with chloritoid. This suggests that chloritoid first nucleated at 530–550 °C and >18 kbar, namely above the stability field of chlorite (Fig. 8a). The subsequent growth of chloritoid must have been accompanied by an increase in *T*, as indicated by the chloritoid-rim composition (X_{Mg} = 0.30; Fig. 8a). The Si content measured in the core of phengite (3.28–3.30 pfu) allows a better constraint of *P*, since the isopleths of phengite and chloritoid intersect between 18.5 and 20 kbar (Fig. 8a). Further constraints on the prograde evolution of the sample are provided by consideration of the garnet's pyrope and grossular content. The concentric and bell-shaped distribution of Mn in garnet suggests that original growth zonation is preserved, so the core is interpreted to represent the composition of the initial garnet growth stage. The pyrope and grossular isopleths corresponding to the measured core-composition (*e.g.*, prp = 0.7 and grs = 0.16) join on a narrow zone (the ellipse in Fig. 8b), indicating conditions of ~20.5–21 kbar and 500–520 °C. Both, chloritoid–phengite and pyrope–grossular isopleth intersections overlap the field defined by the assemblage garnet + phengite + paragonite + jadeite + chloritoid (+quartz + rutile + H_2O), discarding chlorite as a phase in the primary paragenesis and suggesting the presence of a jadeitic clinopyroxene (*ca.* 4 vol.%), which was not observed during our petrographic analysis. The *T* conditions suggested by garnet isopleths are ~30 °C lower than those estimated from the chloritoid and phengite compositions. This discrepancy could be due either to uncertainties inherent in the calculations or to contrasts in the initial equilibration conditions of these minerals.

The effect of ferric iron content in the mineral stability was investigated by calculating a $PX_{Fe_2O_3}$ phase diagram at 510 °C (Fig. 8c). The most obvious result of considering ferric iron in the calculations is the stabilization of clinopyroxene at considerable lower *P* (>15.5 kbar) than in fully reduced conditions (>20.5 kbar). This diagram also reveals that the predicted jadeite-bearing assemblage extend towards lower *P* at higher oxidized conditions (gray shaded field in Fig. 8c). Pyrope and grossular isopleths (ellipse in Fig. 8c) join on a zone restricted to $X_{Fe_2O_3}$ values between 0.00 and 0.10, indicating ~20–21 kbar. Epidote shows a significant HP stabilization for $X_{Fe_2O_3}$ values higher than 0.15; even so, maximum *P* (~19 kbar) remains low compared with those indicated by garnet composition. Consequently, the chosen $X_{Fe_2O_3}$ value of 0.06 is considered to be adequate, and the $PX_{Fe_2O_3}$ assessment supports our interpretation that epidote crystallization has occurred during decompression.

Given the presence of hydrous minerals such as phengite, paragonite and chloritoid as inclusions within garnet and as matrix phases, the water content was considered to be in excess. The effect of this assumption was investigated by calculating a PX_{H_2O} phase diagram at the same *T* of 510 °C (Fig. 8d). This model indicates that values of >11.5 mol.% of H_2O are necessary to completely saturate the system; in H_2O-undersaturated conditions the interval of interest is limited by the kyanite-in curve. Below the H_2O-in curve, the field of interest (gray shaded area in Fig. 8d) extends to both lower and higher *P*. For instance, the assemblage garnet + phengite + paragonite + jadeite + chloritoid (+quartz + rutile) is predicted to be stable at pressures up to ~3 kbar lower and ~1.5 kbar higher than those considering H_2O in excess (Fig. 8d). As shown in Fig. 8d, the water content also has an influence on the position of the compositional isopleths. For instance, the X_{Mg} = 0.28 isopleth of chloritoid is predicted at 510 °C if the H_2O content is limited to ~8.5 mol.%. On the other hand, the lower pressure limit of chloritoid increases in inverse proportion to the amount of H_2O; so, the model with water in excess gives a minimum *P* estimate for the stability of chloritoid.

4.4. HP peak stage

Growth zoning profiles preserved towards garnet rims allow insight into the thermal evolution following equilibration of the core. The lack of a Mn-rich inflection at the rim of the analyzed garnet and the generally euhedral outline of the crystals (Fig. 5) suggest that the rim preserves the composition formed at the metamorphic peak. A first approach to estimating the peak conditions omits the effects of cation fractionation in the garnet, so pyrope and grossular isopleths can be evaluated in the same way as for the case of the core (Fig. 8b). The pyrope and grossular isopleths corresponding to the measured rim-composition (*e.g.*, prp = 0.16 and grs = 0.08) are nearly parallel, joining at 590–600 °C and 19.5–20 kbar (ellipse in Fig. 8b) where they overlap an assemblage consisting of garnet + phengite + paragonite + jadeite ± kyanite ± chloritoid (+quartz + rutile) to above the stability field of biotite. In contrast with the garnet core growth that is predicted to occur entirely within the stability field of chloritoid, the garnet rim is predicted to equilibrate very close to the chloritoid-out line, which coincide (and slightly overlaps) with the kyanite-in line at 19.5–20 kbar (Fig. 8b). Except for jadeite, this preliminary investigation coincides with the observed mineral assemblage, in particular with the very limited presence of anhedral kyanite grains. However, it has been demonstrated that the progressive elemental fractionation produced by the prograde garnet growth can determine the mineral assemblages and its modal proportions during the subsequent metamorphic evolution (*e.g.*, Marmo *et al.*, 2002; Tinkham & Ghent, 2005; St-Onge *et al.*, 2013). To account for the possible effects of garnet cation fractionation on mineral evolution, at the final stage of garnet growth, quantitative X-ray maps and chemical profiles in garnet were used to calculate a garnet-core composition, which was subtracted from the bulk composition used in Fig. 8 (sample CH24; Table 2). This approach is similar to the method described by Tinkham & Ghent (2005) and assumes (i) that garnet zoning in the studied samples is the main cause of chemical fractionation in the sample, because of its prominence and the high modal content of garnet, (ii) chemical zoning has a homogeneous concentric distribution, (iii) the volume of garnet core to remove can be

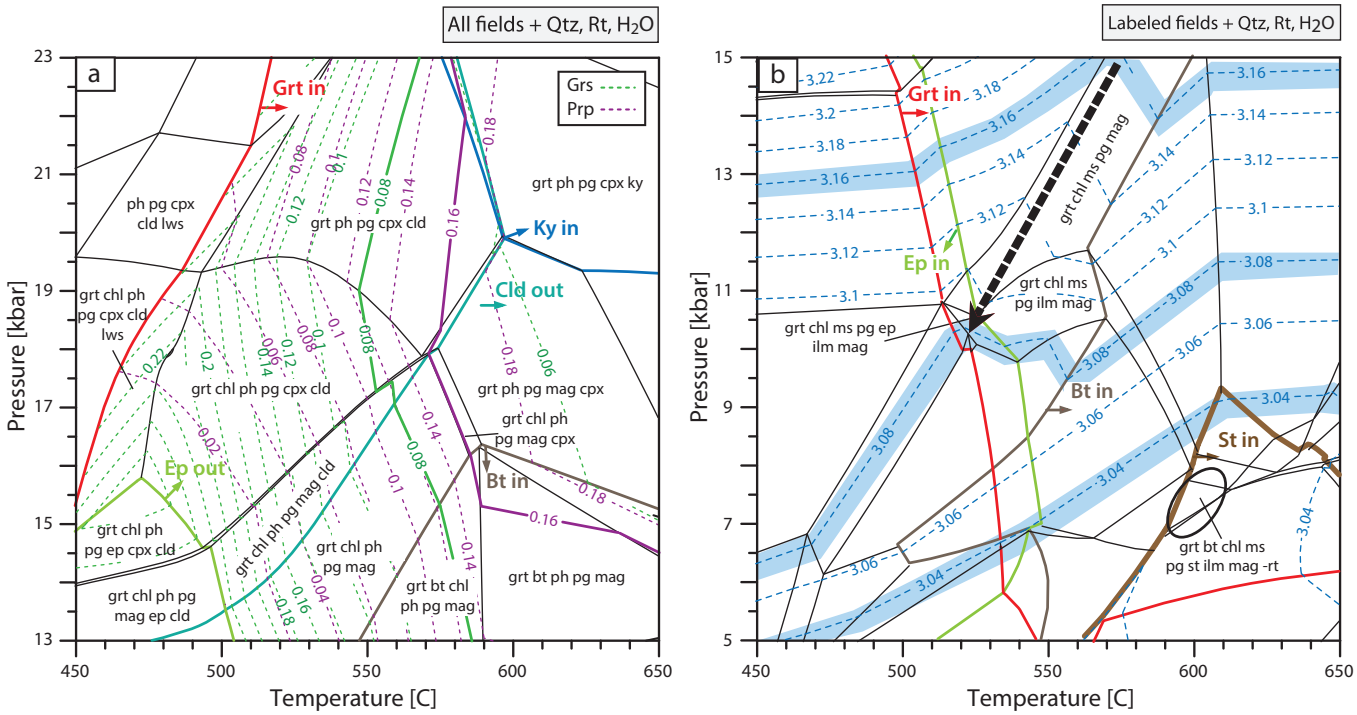

Fig. 9. CH24-fractionated (a) and CH35-fractionated (b) equilibrium phase diagram analysis. The used bulk-composition is given in Table 2. (a) Contoured *P–T* equilibrium phase diagram with assemblages labeled. Solid isopleths represent the measured composition of the garnet rims. (b) *P–T* equilibrium phase diagram at medium-pressure conditions, contoured with Si content (pfu) in phengite/muscovite. Blue bands highlight different rim composition of phengite. Dashed black arrow indicates the probable *P–T* trajectory following the metamorphic peak. "Cpx" refers to a jadeite–aegirine–omphacite solid solution with variable composition along the stability field.

approximated by spherical averaging techniques, and (iv) zoning patterns are proportional for all garnet sizes. The phase diagram calculated from the fractionated composition of sample CH24 is shown in Fig. 9a. The main difference between the non-fractionated and fractionated *P–T* phase diagrams is a slight shift of topology to higher *T* in the fractionated diagram, which is most evident in the garnet-in line. The application of this approximation to the calculation of an effective bulk composition after the equilibration of garnet core, does not give satisfactory results for the prediction of the topology of garnet isopleths (Fig. 9a), which remain parallel, but far from each other. For instance, the isopleths of grs = 0.08 and prp = 0.16 (rim composition) plot on ~550 and ~580 °C at 20 kbar, respectively. Additional attempts to assess the influence of H_2O content on the position of the compositional isopleths (not shown) did not return better results. We conclude that the chemical volume removed must not have been appropriate; particularly because of the omission of chloritoid in the fractionated volume and the amount of Ca removed (the garnet-core has grs = 0.17). Nevertheless we consider the calculated position of the pyrope isopleth to represent the best estimate of the peak *T*, because it does not change significantly in either of the investigated models. Further constraints on the *P–T* peak conditions of the sample are provided by the very limited occurrence of kyanite. The kyanite-in line marks a HP limit of ~20 kbar at 600 °C, if we consider the system to have been on an increasing-*T* trajectory, as is suggested by both the garnet and chloritoid zoning. Hence, a conservative interpretation indicates that the peak conditions of metamorphism for sample CH24 lie between 580 and 600 °C and 19.5–20 kbar.

4.5. Early decompression and amphibolite-facies overprint

A common feature of both the non-fractionated and fractionated equilibrium phase diagrams is the prediction of a steep narrow zone located between the chloritoid-out and the biotite-in lines which is characterized by chlorite-bearing assemblages below 18 kbar (Figs. 8a and 9a). The crystallization of chlorite overgrowing the peak assemblage, the replacement of rutile by Fe–Ti oxides and the absence of biotite indicate that the sample experienced partial reequilibration during a significant decompression from ~20 kbar to ~11 kbar without any notably change in *T* (Fig. 9a). Local reequilibration at ~11 kbar is also indicated by a decrease in the Si content towards the rim of phengite (Si = 3.8–3.16 pfu), and by the growth of epidote (Fig. 9b).

As described previously, the studied metapelite also comprises the local occurrence of staurolite overgrowing the S_{n+3} foliation, which is in apparent equilibrium with garnet, muscovite, paragonite, ilmenite and chlorite. This mineral assemblage and its associated microstructures are interpreted to represent a later amphibolite-facies over-

print related to further decompression (at ~9 kbar; Fig. 9). To constraint the *P–T* conditions of this late-stage overprint, a *P–T* equilibrium phase diagram was constructed for the staurolite-bearing sample CH35 (Fig. 9b) using the same modeling parameters as above. The effective bulk-composition used for this model (Table 2) was calculated in the same way as for the fractionated CH24 composition. The resulting *P–T* diagram predicts staurolite to be stable at <9.5 kbar and >560 °C, for the investigated *P* interval (5–15 kbar). On the other hand, biotite is predicted in all the staurolite-bearing fields, which is not present in the studied samples; consequently, it is not possible to reproduce fully the observed assemblage using this model. The model mineral assemblage that more approximates to the observed one is garnet + biotite + staurolite + chlorite + muscovite + paragonite + ilmenite + magnetite, which occurs in a small field (black ellipse in Fig. 9b) at ~590–620 °C and 7–8 kbar. The *P* conditions can be constrained by contouring the *P–T* phase diagram with the isopleths of Si content in muscovite (Fig. 9d). The composition of coarse-grained muscovite aligned to the S_{n+3} foliation (Si = 3.04 pfu) cross the staurolite-bearing field at 9–9.5 kbar (close to the upper pressure limit of staurolite). Thus, the best approach of the *P–T* conditions during the amphibolite-facies overprint obtained with this model is 7–9.5 kbar at 590–620 °C.

5. Discussion and conclusions

5.1. Metamorphic evolution of the HP metapelite

Integration of petrographic and mineral chemistry data, together with petrological modeling results enable the construction of a *P–T* path for the HP metapelite from northern Chuacús Complex. The resulting *P–T* trajectory is well constrained by the relatively narrow stability field of two contrasting parageneses, namely garnet + chloritoid + paragonite + phengite + rutile + quartz ± chlorite and staurolite + muscovite + chlorite + epidote + ilmenite + quartz ± paragonite ± garnet. An estimate of 20–21 kbar and 500–540 °C using the core compositions of garnet, chloritoid and phengite is interpreted to represent conditions of equilibration during an early stage of prograde HP metamorphism. Phase-equilibria modeling predicts that this early stage occurred in the stability field of jadeite (Fig. 8), but this phase was not observed during our petrographic analysis. In fact, paragonite is the only Na-rich phase in the studied samples. However, microstructural evidence of the probable former presence of jadeite is given by the occurrence of fine-grained paragonite pseudomorphs (Fig. 4e). Jadeite, partially or completely replaced by paragonite, appears to be a common feature in HP rocks that record blueschist- to eclogite-facies equilibration (*e.g.*, Guillot *et al.*, 1997; Ko *et al.*, 2005; Groppo *et al.*, 2006). Possible sodic pyroxene consuming reactions to form paragonite are as follows: (1) $3Jd + 2H = Pg + 3Qz + 2Na$ (Wohlers *et al.*, 2011), (2) $Jd + Ky + H_2O = Pg$ (Holland, 1979) and (3) Jd + Cld = Pg + Grt (Guillot *et al.*, 1997). On the other hand, fine aggregates of paragonite + epidote have been interpreted as indicators of former lawsonite (*e.g.*, Evans, 1990; Lapen *et al.*, 2003; Zack *et al.*, 2004; Song *et al.*, 2007; Li *et al.*, 2012; Tsujimori & Ernst, 2014). The progressive growth of garnet, chloritoid and phengite in these metapelites was accompanied by an increase in *T* until a peak-*T* condition of 580–600 °C and maximum *P* of ~19.5–20 kbar (Figs. 8a and 9b). Almost identical prograde *P–T* conditions were obtained by Ratschbacher *et al.* (2009) for a garnet-orthogneiss from north-central Chuacús. These prograde *P–T* conditions indicate that the metapelite we studied could be formed during a single progressive metamorphic process along a subduction geothermal gradient of 7–9 °C/km.

Similar mineral assemblages have been reported in metapelites from several other subducted continental-type terranes around the world (Table 3), as well as in metapelites associated with oceanic-type terranes (*e.g.*, Bosse *et al.*, 2002; Song *et al.*, 2007; Negulescu *et al.*, 2009). Peak *P–T* conditions recorded in the metapelite we have studied are comparable with those obtained in other continental suture zones with analogous lithologies (Fig. 10a), and range between the peak conditions obtained for garnet–chloritoid–glaucophane–lawsonite-bearing rocks and garnet–chloritoid–kyanite–bearing rocks, which provide a good match with our petrographic and modeling results. These mineral assemblages are good indicators of HP blueschist- to eclogite-facies metapelites (*e.g.*, Wei & Powell, 2004; Smye *et al.*, 2010; López-Carmona *et al.*, 2013).

The post-peak path is less well constrained, although decreasing *P* coupled with no significant change in *T* are indicated by the absence of biotite, and the presence of chlorite overgrowing the S_{n+2} foliation. Subsequent crystallization of staurolite related to the S_{n+3} foliation, indicates further decompression, until 9–9.5 kbar at 600–620 °C; however, these *P–T* conditions were not well constrained by our modeling at intermediate-*P* conditions, because the calculated phase diagram fails to reproduce adequately the observed mineral assemblage (garnet + staurolite + muscovite + paragonite + chlorite + quartz). Particularly problematic is biotite, which has not been observed in our samples although its presence was predicted in all staurolite-bearing fields. We concluded that this discrepancy is probably caused by problems with the used *a–X* models, inadequate definition of the effective bulk composition (*e.g.*, Fe/Mg ratio), inappropriate definition of oxidation conditions during the amphibolite-facies overprint, and kinetic factors that prevent the biotite crystallization during decompression. Despite all the above, the decompression trajectory during exhumation, suggested by both petrography and petrological modeling, indicates that late-stage heating is required to reach the stability field of staurolite, at ~600–620 °C, as has also suggested in other case studies (*e.g.*, Guillot *et al.*, 1997; Meyre *et al.*, 1999; Keller *et al.*, 2005; Le Bayon *et al.*, 2006; Groppo *et al.*, 2006).

Table 3. Localities of HP-metapelites with mineral assemblages and *P–T* peak conditions similar to those presented in this study. All cases refer to continental-type subducted crust, except those indicated with *, which are oceanic-type crust.

Locality	Author	Fig. 10a
Tauern Window, Austria	Holland, 1979; Hoschek *et al.*, 2010; Smye et al., 2010	5, 6
Bohemian Massif	Konopasek, 2001	8
Betic Cordillera, Spain	Smye *et al.*, 2010	7
Sesia zone, Italy	Compagnoni, 1977; Vuichard & Ballevre, 1988	
Rhodope, Greece	Mposkos & Liati, 1993	
Tso Morari, India	Guillot *et al.*, 1997	
Adula Nappe, Switzerland	Meyre *et al.*, 1999	
Ambin Massif, France	Ganne *et al.*, 2003	
Gran Paradiso, Italy	Chopin, 1981; Le Bayon *et al.*, 2006	3
Sardinia, Italy	Cruciani *et al.*, 2013	4
Iberian Massif, Spain	López-Carmona *et al.*, 2013	2
Turkey	Okay, 2002	1
Raspas Complex, Ecuador*	Gabriele *et al.*, 2003; Smye *et al.*, 2010	9
Bughea Complex, Carpathians*	Negulescu *et al.*, 2009; Smye *et al.*, 2010	10

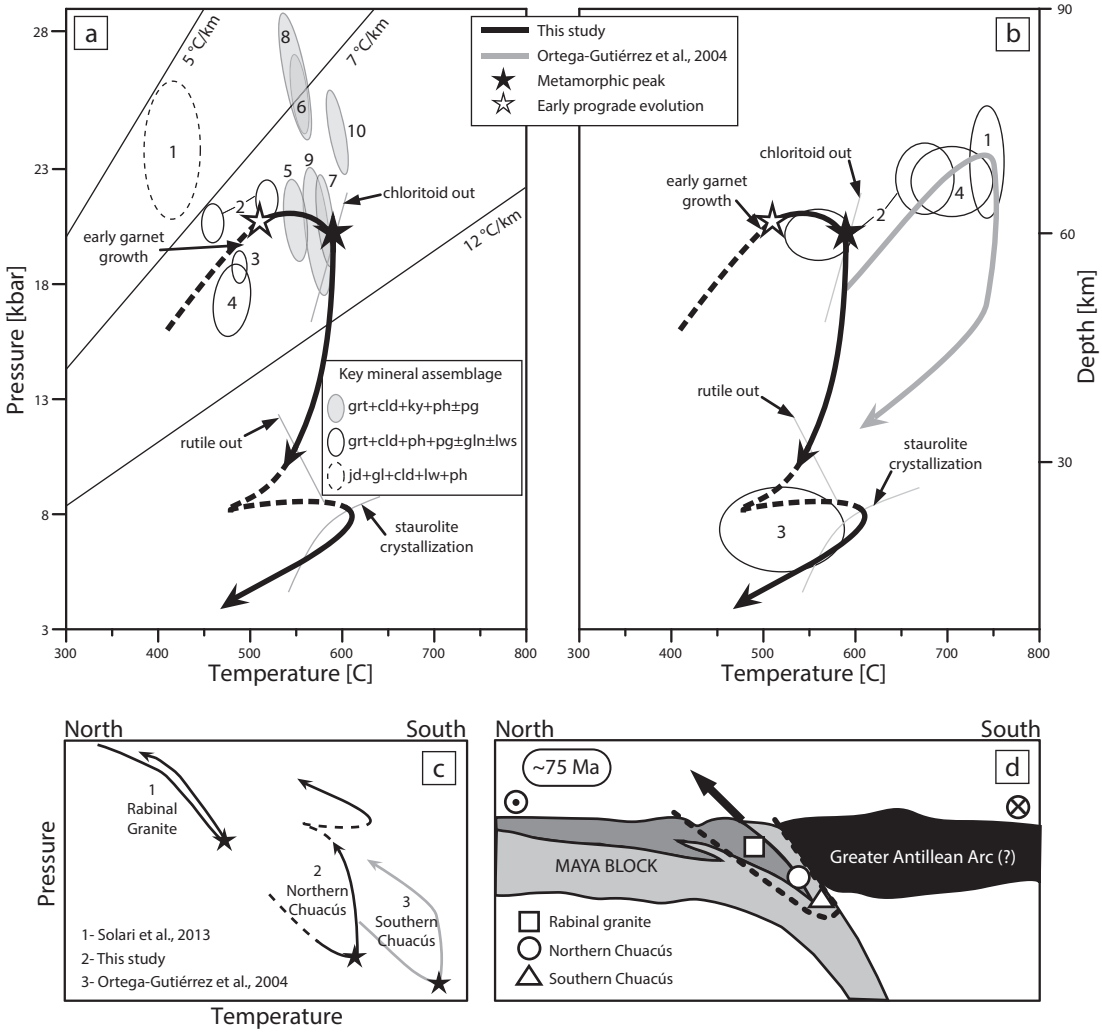

Fig. 10. Integrated results. (a) *P–T* path for the Grt-Cld-Pg metapelite and selected phase boundaries. The dashed portion is uncertain. Ellipses indicate *P–T* average conditions obtained for similar metapelites described elsewhere in the world (see Table 3 for references). (b) *P–T* path for the Grt-Cld-Pg metapelite compared with published *P–T* calculations for other localities in the Chuacús Complex. 1: Ortega-Gutiérrez *et al.* (2004); 2 and 3: Ratschbacher *et al.*, (2009); 4: Martens *et al.* (2012). (c) *P–T* paths obtained for the Chuacús Complex compared with that of the Rabinal Granite. (d) Schematic tectonic model modified from Brueckner *et al.* (2009) and Martens *et al.* (2012) showing the probable scenario for passive continental margin subduction along the southern edge of the North American–Caribbean plate boundary during the Late Cretaceous; notice the different position in depth among the Rabinal Granite, the northern and the southern Chuacús Complex.

5.2. Extension of HP metamorphism in the Guatemala Suture Zone

The Motagua serpentinite mélanges, which contain HP blocks recording an episode of Jurassic subduction, are discontinuously exposed along the Motagua fault zone (Brueckner *et al.*, 2009). In contrast, the Chuacús Complex records Late Cretaceous subduction (Martens *et al.*, 2012) and is a more coherent tectonic unit, about 20 km wide. Although eclogite-facies metamorphism has been described in the southern zone of the Chuacús Complex (*e.g.*, Ortega-Gutiérrez *et al.*, 2004; Martens *et al.*, 2012), adjacent to the Motagua fault zone, it is unknown how far it extends into other areas within the complex. For instance, the area studied (northern end of the complex; Figs. 1 and 2) had been considered to be part of a medium-pressure metamorphic zone, in part because of the widespread amphibolite-facies mineral assemblages (*e.g.*, hornblende + plagioclase ± garnet in metabasites, and muscovite + garnet ± staurolite in metapelites), but largely because of the scarcity of diagnostic eclogite-facies relics in the predominantly metasedimentary rocks. Thus, the new record of an occurrence of high-pressure metapelites implies that high-pressure metamorphism in the Chuacús Complex must extend at least 10 km further northwards than previously thought. Recent evidence of high-pressure metamorphism in the Rabinal area (Solari *et al.*, 2013), along with the results obtained in this study, extends the record of subduction-related metamorphism further north along the Guatemala Suture Zone and suggests that HP metamorphism in the southern edge of North America (Maya block) could extend more or less continuously along ~28 km, north to the Motagua fault zone.

5.3. Implications for the Late Cretaceous subduction

Although our estimates about prograde *P–T* conditions are in agreement with previous results obtained through conventional thermobarometric methods in one sample from north-central Chuacús (*e.g.*, Ratschbacher *et al.*, 2009), *P–T* peak conditions differ considerably from those estimated in metabasic rocks from south-central Chuacús. For instance, significantly higher temperatures (660–750 °C) at slightly higher *P* (21–24 kbar) have been obtained on retrogressed eclogites from the Agua Caliente-El Chol sector (Ortega-Gutiérrez *et al.*, 2004; Ratschbacher *et al.*, 2009; Martens *et al.*, 2012; Fig. 10b), at about 12 km south to the studied zone. On the other hand, Solari *et al.* (2013) obtained a *P–T* path for the deformed Rabinal Granite, 7 km north of the study zone (Fig. 2), indicating *P–T* peak conditions of 8.5 kbar and 300 °C, which suggest low blueschist-facies metamorphism related to subduction of the Rabinal Granite during latest Cretaceous. This indicates that both Chuacús Complex and Rabinal Granite experienced coeval processes of subduction and exhumation along the southern edge of the North America continental basement, and were then juxtaposed through the Baja Verapaz shear zone (Ortega-Obregón *et al.*, 2008), onto its current position. The above data together with the results presented in this study indicate that *P–T* peak conditions increase from north to south, *i.e.*, from the Rabinal area, to northern Chuacús Complex, then to the southern Chuacús Complex (Fig. 10c). Field and numerical-modeling studies of the exhumation of HP rocks have demonstrated that exhumation *P–T*-paths do not conform to one single uniform exhumation trajectory; instead assemblages of interrelated *P–T*-paths are characteristic (Willner *et al.*, 2002; Dale & Holland, 2003). Regional structures in the suture zones commonly delineate areas containing blocks with contrasting *P–T* trajectories, which indicates that the blocks have originated from different depths or even from different parts within a laterally continuous convergence zone (*e.g.*, oblique convergence). We suggest that this apparent succession of the *P–T* peak conditions recorded by the Chuacús Complex and the Rabinal Granite (Fig. 10d) has preserved part of the original thermal structure of the subduction zone in the southern margin of North America during the Cretaceous.

Acknowledgments: M.C. Macías Romo, Julie Chouinard and C. Linares López are thanked for their technical support during the analytical procedures. D. Tinkham is thanked for his help with THERIAK-DOMINO and for providing the database. Hans-Peter Schertl is gratefully acknowledged for his advice and constructive comments. The manuscript improved greatly from the suggestions by Philippa M. Black and the reviews by T. Tsujimori and an anonymous reviewer. This work was funded by the Mexican "Programa de Apoyo a Proyectos de Investigación e Innovación Tecnológica, DGAPA-UNAM" grant IN104914.

References

Bosse, V., Ballèvre, M., Vidal, O. (2002): Ductile thrusting recorded by the garnet isograd from blueschist-facies metapelites of the Ile de Groix, Armorican Massif, France. *J. Petrol.*, **43**, 485–510.

Brueckner, H.K., Avé Lallemant, H.G., Sisson, V.B., *et al.* (2009): Metamorphic reworking of a high pressure–low temperature mélange along the Motagua fault, Guatemala: a record of Neocomian and Maastrichtian transpressional tectonics. *Earth Planet. Sci. Lett.*, **284**, 228–235.

Chiari, M., Dumitrica, P., Marroni, M., Pandolfi, L., Principi, G. (2006): Radiolarian biostratigraphic evidence for a Late Jurassic age of the El Tambor Group ophiolites (Guatemala). *Ofioliti*, **31**, 141–150.

Chopin, C. (1981): Talc-phengite: a widespread assemblage in high-grade pelitic blueschists of the Western Alps. *J. Petrol.*, **22**, 628–650.

Coggon, R. & Holland, T.J.B. (2002): Mixing properties of phengitic micas and revised garnet–phengite thermobarometers. *J. Metamorphic Geol.*, **20**, 683–696.

Compagnoni, R. (1977): The Sesia-Lanzo Zone: high pressure–low temperature metamorphism in the Austroalpine continental margin. *Rend. Soc. Ital. Mineral. Petrol*, **33**, 335–374.

Compagnoni, R., Hirajima, T., Chopin, C. (1995): Ultra-high-pressure metamorphic rocks in the Western Alps. *in* "Ultrahigh pressure metamorphism", R.G. Coleman and X. Wang, eds. Cambridge University Press, New York, 206–243.

Cruciani, G., Franceschelli, M., Massonne, H.J., Carosi, R., Montomoli, C. (2013): Pressure–temperature and deformational evolution of high-pressure metapelites from Variscan NE Sardinia, Italy. *Lithos*, **175**, 272–284.

Dale, J. & Holland, T.J.B. (2003): Geothermobarometry, *P–T* paths and metamorphic field gradients of high-pressure rocks from the Adula Nappe, Central Alps. *J. Metamorphic Geol.*, **21**, 813–829.

de Capitani, C. & Brown, T.H. (1987): The computation of chemical equilibrium in complex systems containing non-ideal solutions. *Geochim. Cosmochim. Acta*, **51**, 2639–2652.

de Capitani, C. & Petrakakis, K. (2010): The computation of equilibrium assemblage diagrams with Theriak/Domino software. *Am. Mineral.*, **95**, 1006–1016.

Dengo, G. (1969): Problems of tectonic relations between Central America and the Caribbean. *Trans. Gulf Coast Assoc. Geol. Soc.*, **29**, 311–320.

El-Shazly, A.K. & Liou, J.G. (1991): Glaucophane chloritoid-bearing assemblages from NE Oman: petrologic significance and a petrogenetic grid for high P metapelites. *Contrib. Mineral. Petrol.*, **107**, 180–201.

Endo, S., Wallis, S.R., Tsuboi, M., Torres de Leon, R., Solari, L. (2012): Metamorphic evolution of lawsonite eclogites from Southern Motagua fault zone, Guatemala: insights from phase equilibria and Raman spectroscropy. *J. Metamorphic Geol.*, **30**, 143–164.

Evans, B.W. (1990): Phase relations of epidote-blueschists. *Lithos*, **25**, 3–23.

Evans, T.P. (2004): A method for calculating effective bulk composition modification due to crystal fractionation in garnet-bearing schist: implications for isopleth thermobarometry. *J. Metamorphic Geol.*, **22**, 547–557.

Gabriele, P., Ballèvre, M., Jaillard, E., Hernandez, J. (2003): Garnet-chloritoid-kyanite metapelites from the Raspas Complex (SW Ecuador). *Eur. J. Mineral.*, **15**, 977–989.

Ganne, J., Bussy, F., Vidal, O. (2003): Multi-stage garnet in the internal Briançonnais basement (Ambin Massif, Savoy): new petrological constraints on the blueschist-facies metamorphism in the Western Alps and tectonic implications. *J. Petrol.*, **44**, 1281–1308.

Green, E., Holland, T.J.B., Powell, R. (2007): An order–disorder model for omphacitic pyroxenes in the system jadeite–diopside hedenbergite–acmite, with applications to eclogitic rocks. *Am. Mineral.*, **92**, 1181–1189.

Groppo, C., Castelli, D., Compagnoni, R. (2006): Late chloritoid–staurolite assemblage in a garnet–kyanite-bearing metapelite from the ultrahigh-pressure Brossasco-Isasca unit (Dora-Maira Massif, Western Alps). New petrological constraints for a portion of the decompressional path. *Geol. Soc. Am. Spec. Papers*, **403**, 127–138.

Guillot, S., de Sigoyer, J., Lardeaux, J. M., Mascle, G. (1997): Eclogitic metasediments from the Tso Morari area (Ladakh, Himalaya): evidence for continental subduction during India-Asia convergence. *Contrib. Mineral. Petrol.*, **128**, 197–212.

Harlow, G.E., Hemming, S.R., Avé Lallemant, H.G., Sisson, V.B., Sorensen, S.S. (2004): Two high pressure–low-temperature serpentinite-matrix mélange belts, Motagua fault zone, Guatemala: a record of Aptian and Maastrichtian collisions. *Geology*, **32**, 17–20.

Holland, T.J.B. (1979): High water activities in the generation of high pressure kyanite eclogites of the Tauern Window, Austria. *J. Geol.*, **87**, 1–27.

— (2009): AX: a program to calculate activities of mineral end-members from chemical analyses. Available at: http://www.esc.cam.ac.uk/research/research-groups/holland/ax (accessed 01.12.14).

Holland, T.J.B. & Powell, R. (1998): An internally-consistent thermodynamic dataset for phases of petrological interest. *J. Metamorphic Geol.*, **16**, 309–344.

—, — (2003): Activity-composition relations for phases in petrological calculations: an asymmetric multicomponent formulation. *Contrib. Mineral. Petrol.*, **145**, 492–501.

Hoschek, G., Konzett, J., Tessadri, R. (2010): Phase equilibria in quartzitic garnet-kyanite-chloritoid micaschist from the Eclogite Zone, Tauern Window, Eastern Alps. *Eur. J. Mineral.*, **22**, 721–732.

Keller, L.M., Abart, R., Schmid, S.M., De Capitani, C. (2005): Phase relations and chemical composition of phengite and paragonite in pelitic schists during decompression: a case study from the Monte Rosa nappe and Camughera-Moncucco unit, Western Alps. *J. Petrol.*, **46**, 2145–2166.

Ko, Z.W., Enami, M., Aoya, M. (2005): Chloritoid and barroisite-bearing pelitic schists from the eclogite unit in the Besshi district, Sanbagawa metamorphic belt. *Lithos*, **81**, 79–100.

Konopasek, J. (2001): Eclogitic micaschists in the central part of the Krušné hory Mountains (Bohemian Massif). *Eur. J. Mineral.*, **13**, 87–100.

Lapen, T.J., Johnson, C.M., Baumgartner, L.P., Mahlen, N.J., Beard, B.L., Amato, J.M. (2003): Burial rates during prograde metamorphism of an ultra-high-pressure terrane: an example from Lago di Cignana, western Alps, Italy. *Earth Planet. Sci. Lett.*, **215**, 57–72.

Le Bayon, B., Pitra, P., Ballevre, M., Bohn, M. (2006): Reconstructing *P–T* paths during continental collision using multi-stage garnet (Gran Paradiso nappe, Western Alps). *J. Metamorphic Geol.*, **24**, 477–496.

Li, J.L., Klemd, R., Gao, J., Meyer, M. (2012): Coexisting carbonate-bearing eclogite and blueschist in SW Tianshan, China: petrology and phase equilibria. *J. Asian Earth Sci.*, **60**, 174–187.

Liou, J.G., Zhang, R.Y., Jahn, B.M. (1997): Petrology, geochemistry and isotope data on a ultrahigh-pressure jadeite quartzite from Shuanghe, Dabie Mountains, East-central China. *Lithos*, **41**, 59–78.

López-Carmona, A., Pitra, P., Abati, J. (2013): Blueschist-facies metapelites from the Malpica-Tui Unit (NW Iberian Massif): phase equilibria modelling and H_2O and Fe_2O_3 influence in high-pressure assemblages. *J. Metamorphic Geol.*, **31**, 263–280.

Mahar, E.M., Baker, J.M., Powell, R., Holland, T.J.B., Howell, N. (1997): The effect of Mn on mineral stability in metapelites. *J. Metamorphic Geol.*, **15**, 223–238.

Mann, P. (2007): Overview of the tectonic history of northern Central America. *Geol. Soc. Am. Spec. Papers*, **428**, 1–19.

Marmo, B.A., Clarke, G.L., Powell, R. (2002): Fractionation of bulk rock composition due to porphyroblast growth: effects on eclogite facies mineral equilibria, Pam Peninsula, New Caledonia. *J. Metamorphic Geol.*, **20**, 151–165.

Martens, U.C., Brueckner, H.K., Mattinson, C.G., Liou, J.G., Wooden, J.L. (2012): Timing of eclogite-facies metamorphism of the Chuacús Complex, Central Guatemala: record of Late Cretaceous continental subduction of North America's sialic basement. *Lithos*, **146**, 1–10.

McBirney, A.R. (1963): Geology of a part of the central Guatemalan cordillera. *Calif. Univ. Publ. Geol. Sci.*, **38**, 177–242.

Meyre, C., De Capitani, C., Zack, T., Frey, M. (1999): Petrology of high-pressure metapelites from the Adula nappe (Central Alps, Switzerland). *J. Petrol.*, **40**, 199–213.

Mposkos, E. & Liati, A. (1993): Metamorphic evolution of metapelites in the high-pressure terrane of the Rhodope zone, Northern Greece. *Can. Mineral.*, **31**, 401–401.

Negulescu, E., Săbău, G., Massonne, H.J. (2009): Chloritoid-bearing mineral assemblages in high-pressure metapelites from the Bughea Complex, Leaota Massif (South Carpathians). *J. Petrol.*, **50**, 103–125.

Okay, A. I. (2002): Jadeite-chloritoid-glaucophane-lawsonite blueschists in north-west Turkey: unusually high P/T ratios in continental crust. *J. Metamorphic Geol.*, **20**, 757–768.

Ortega-Gutiérrez, F., Solari, L.A., Sole, J., *et al.* (2004): Polyphase, high-temperature eclogite facies metamorphism in the Chuacus Complex, central Guatemala; petrology, geochronology, and tectonic implications. *Int. Geol. Rev.*, **46**, 445–470.

Ortega-Obregón, C., Solari, L.A., Keppie, J.D., Ortega-Gutiérrez, F., Solé, J., Morán-Ical, S. (2008): Middle-Late Ordovician magmatism and Late Cretaceous collision in the southern Maya block, Rabinal-Salamá area, central Guatemala: implications for North America-Caribbean plate tectonics. *Geol. Soc. Am. Bull.*, **120**, 556–570.

Pindell, J.L. & Barrett, S.F. (1990): Geological evolution of the Caribbean region: a plate tectonic perspective. *Caribb. Reg.*, 405–432.

Ratschbacher, L., Franz, L., Min, M., *et al.* (2009): The North American-Caribbean Plate boundary in Mexico-Guatemala-Honduras. *Geol. Soc. Lond. Spec. Publ.*, **328**, 219–293.

Rosencrantz, E. & Mann, P. (1991): SeaMARC II mapping of transform faults in the Cayman Trough. *Caribb. Sea Geol.*, **19**, 690–693.

Rosenfeld, J.H. (1981): Geology of the Western Sierra de Santa Cruz, Guatemala, Central America: an Ophiolite Sequence. *In*: Ph.D. Thesis, State University of New York at Binghamton, 313 p.

Smye, A.J., Greenwood, L.V., Holland, T.J.B. (2010): Garnet-chloritoid-kyanite assemblages: eclogite facies indicators of subduction constraints in orogenic belts. *J. Metamorphic Geol.*, **28**, 753–768.

Solari, L., Gómez-Tuena, A., Ortega-Gutiérrez, F., Ortega-Obregón, C. (2011): The Chuacús Metamorphic Complex, central Guatemala: geochronological and geochemical constraints on its Paleozoic-Mesozoic evolution. *Geol. Acta*, **9**, 329–350.

Solari, L., Garcia-Casco, A., Martens, U., Lee, J.K.W., Ortega-Rivera, A. (2013): Late cretaceous subduction of the continental basement of the Maya Block (Rabinal granite, Central Guatemala): tectonic implications for the geodynamic evolution of Central America. *Geol. Soc. Am. Bull.*, **125**, 625–639.

Song, S.G., Zhang, L.F., Niu, Y., *et al.* (2007): Eclogite and carpholite-bearing metasedimentary rocks in the North Qilian suture zone, NW China: implications for Early Palaeozoic cold oceanic subduction and water transport into mantle. *J. Metamorphic Geol.*, **25**, 547–563.

St-Onge, M.R., Rayner, N., Palin, R.M., Searle, M.P., Waters, D.J. (2013): Integrated pressure-temperature-time constraints for the Tso Morari dome (Northwest India): implications for the burial and exhumation path of UHP units in the western Himalaya. *J. Metamorphic Geol.*, **31**, 469–504.

Tinkham, D.K. & Ghent, E.D. (2005): Estimating PT conditions of garnet growth with isochemical phase-diagram sections and the problem of effective bulk-composition. *Can. Mineral.*, **43**, 35–50.

Tsujimori, T., Liou, J.G., Coleman, R.G. (2004): Comparison of two contrasting eclogites from the Motagua fault zone, Guatemala: southern lawsonite eclogite versus northern zoisite eclogite. *Geol. Soc. Am. Abst. Prog.* **36**, 136.

—, —, — (2005): Coexisting retrograde jadeite and omphacite in a jadeite-bearing lawsonite eclogite from the Motagua Fault Zone, Guatemala. *Am. Mineral.*, **90**, 836–842.

Tsujimori, T., Sisson, V.B., Liou, J.G., Harlow, G.E., Sorensen, S.S. (2006): Petrologic characterization of Guatemalan lawsonite eclogite; eclogitization of subducted oceanic crust in a cold subduction zone. *Geol. Soc. Am. Spec. Paper*, **403**, 147–168.

Tsujimori, T. & Ernst, W. G. (2014): Lawsonite blueschists and lawsonite eclogites as proxies for palaeo-subduction zone processes: a review. *J. Metamorphic Geol.*, **32**, 437–454.

Van den Boom, G. (1972): Petrofazielle Gliederung des metamorphen Grundgebirges in der Sierra de Chuacús, Guatemala. *Beih. Geol. Jahrb.*, **122**, 5–49.

Vuichard, J.P. & Ballevre, M. (1988): Garnet–chloritoid equilibria in eclogitic pelitic rocks from the Sesia zone (Western Alps): their bearing on phase relations in high pressure metapelites. *J. Metamorph. Geol.*, **6**, 135–157.

Wei, C. & Powell, R. (2004): Calculated phase relations in high-pressure metapelites in the system NKFMASH (Na_2O-K_2O-FeO-MgO-Al_2O_3-SiO_2-H_2O). *J. Petrol.*, **45**, 183–202.

Wei, C.J. & Song, S.G. (2008): Chloritoid-glaucophane schist in the north Qilian orogen, NW China: phase equilibria and *P–T* path from garnet zonation. *J. Metamorphic Geol.*, **26**, 301–316.

White, R.W., Pomroy, N.E., Powell, R. (2005): An in situ metatexite-diatexite transition in upper amphibolite facies rocks from Broken Hill, Australia. *J. Metamorphic Geol.*, **23**, 579–602.

White, R.W., Powell, R., Holland, T.J.B., Worley, B.A. (2000): The effect of TiO_2 and Fe_2O_3 on metapelitic assemblages at greenschist and amphibolite facies conditions: mineral equilibria calculations in the system K_2O-FeO-MgO-Al_2O_3-SiO_2-H_2O-TiO_2-Fe_2O_3. *J. Metamorphic Geol.*, **18**, 497-512.

Whitney, D.L. & Evans, B.W. (2010): Abbreviations for names of rock-forming minerals. *Am. Mineral.*, **95**, 185.

Willner, A.P., Sebazungu, E., Gerya, T.V., Maresch, W.V., Krohe, A. (2002): Numerical modelling of PT-paths related to rapid exhumation of high-pressure rocks from the crustal root in the Variscan Erzgebirge Dome (Saxony/Germany). *J. Geodyn.*, **33**, 281–314.

Woodsworth, G.J. (1977): Homogenization of zoned garnets from pelitic schists. *Can. Mineral.*, **15**, 230–242.

Wohlers, A., Manning, C. E., Thompson, A.B. (2011): Experimental investigation of the solubility of albite and jadeite in H_2O, with paragonite+quartz at 500 and 600 °C, and 1–2.25 GPa. *Geochim. Cosmochim. Acta*, **75**, 2924–2939.

Zack, T., Rivers, T., Brumm, R., Kronz, A. (2004): Cold subduction of oceanic crust. Implications from a lawsonite eclogite from the Dominican Republic. *Eur. J. Mineral.*, **16**, 909–916.

Received 30 September 2015
Modified version received 30 May 2016
Accepted 13 July 2016

3

Origen y evolución metamórfica de las eclogitas y metapelitas de alta presión asociadas del Complejo Chuacús

---

Maldonado, R., Weber, B., Ortega-Gutiérrez, F., & Solari, L. A. (2018). High-pressure metamorphic evolution of eclogite and associated metapelite from the Chuacús complex (Guatemala Suture Zone): Constraints from phase equilibria modelling coupled with Lu-Hf and U-Pb geochronology. *Journal of Metamorphic Geology*, 36(1), 95-124.

CONTRIBUCIÓN DE LOS COAUTORES

Roberto Maldonado: planeación del proyecto, trabajo de campo, obtención, procesamiento e interpretación de los datos, redacción del artículo.

Bodo Weber: supervisión y asistencia en la metodología analítica, procesamiento e interpretación de los datos geocronológicos, revisión del borrador del artículo.

Fernando Ortega Gutiérrez: supervisión del trabajo, revisión del borrador del artículo.

Luigi A. Solari: supervisión y asistencia en la metodología analítica, revisión del borrador del artículo.

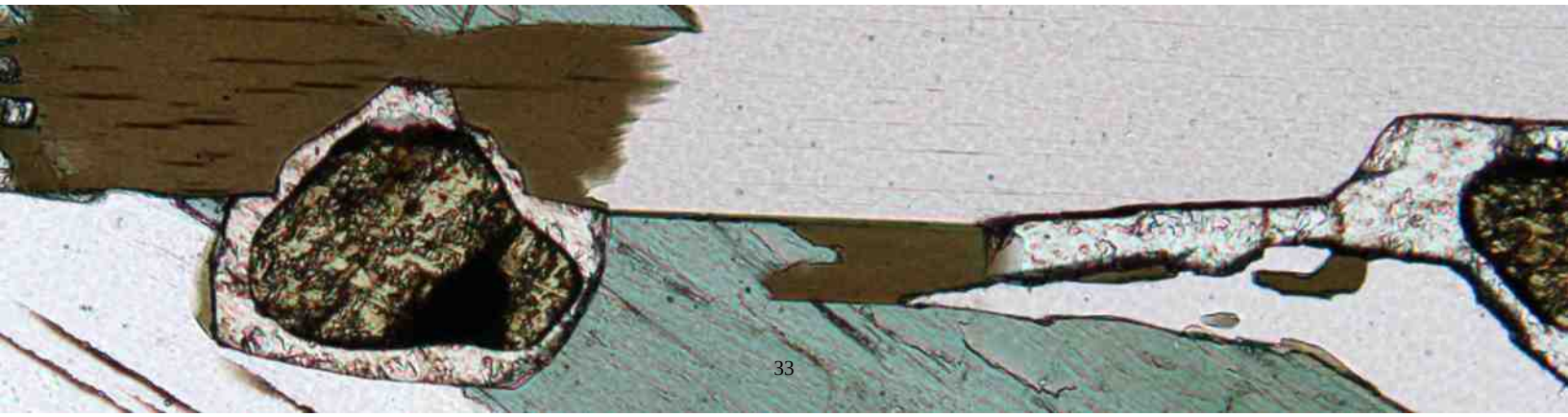

Received: 21 April 2017 | Accepted: 3 October 2017

DOI: 10.1111/jmg.12285

ORIGINAL ARTICLE

WILEY Journal of METAMORPHIC GEOLOGY

High-pressure metamorphic evolution of eclogite and associated metapelite from the Chuacús complex (Guatemala Suture Zone): Constraints from phase equilibria modelling coupled with Lu-Hf and U-Pb geochronology

Roberto Maldonado[1] | **Bodo Weber**[2] | **Fernando Ortega-Gutiérrez**[1] | **Luigi A. Solari**[3]

[1]Instituto de Geología, Universidad Nacional Autónoma de México, Ciudad Universitaria, México D.F., Mexico

[2]Departamento de Geología, Centro de Investigación Científica y de Educación Superior de Ensenada, Ensenada B.C., Mexico

[3]Centro de Geociencias, Universidad Nacional Autónoma de México, Campus Juriquilla, Querétaro, Mexico

Correspondence
Roberto Maldonado, Instituto de Geología, Universidad Nacional Autónoma de México, Ciudad Universitaria, 04510 México D.F., Mexico.
Email: maldonadovr@gmail.com

Funding information
Programa de Apoyo a Proyectos de Investigación e Innovación Tecnológica, DGAPA-UNAM, Grant/Award Number: IN104914

Handling editor: Donna Whitney

Abstract

As is common in suture zones, widespread high-pressure rocks in the Caribbean region reached eclogite facies conditions close to ultrahigh-pressure metamorphism. Besides eclogite lenses, abundant metapelitic rocks in the Chuacús complex (Guatemala Suture Zone) also preserve evidence for high-pressure metamorphism. A comprehensive petrological and geochronological study was undertaken to constrain the tectonometamorphic evolution of eclogite and associated metapelite from this area in central Guatemala. The integration of field and petrological data allows the reconstruction of a previously unknown segment of the prograde *P–T* path and shows that these contrasting rock types share a common high-pressure evolution. An early stage of high-pressure/low-temperature metamorphism at 18–20 kbar and 530–580°C is indicated by garnet core compositions as well as the nature and composition of mineral inclusions in garnet, including kyanite–jadeite–paragonite in an eclogite, and chloritoid–paragonite–rutile in a pelitic schist. Peak high-pressure conditions are constrained at 23–25 kbar and 620–690°C by combining mineral assemblages, isopleth thermobarometry and Zr-in-rutile thermometry. A garnet/whole-rock Lu-Hf date of 101.8 ± 3.1 Ma in the kyanite-bearing eclogite indicates the timing of final garnet growth at eclogite facies conditions, while a Lu-Hf date of 95.5 ± 2.1 Ma in the pelitic schist reflects the average age of garnet growth spanning from an early eclogite facies evolution to a final amphibolite facies stage. Concordant U-Pb LA-ICP-MS zircon data from the pelitic schist, in contrast, yield a mean age of 74.0 ± 0.5 Ma, which is equivalent to a U-Pb monazite lower-intercept age of 73.6 ± 2.0 Ma in the same sample, and comparable within errors with a less precise U-Pb lower-intercept age of 80 ± 13 Ma obtained in post-eclogitic titanite from the kyanite-bearing eclogite. These U-Pb metamorphic ages are interpreted as dating an amphibolite facies overprint. Protolith U-Pb zircon ages of 167.1 ± 4.2 Ma and 424.6 ± 5.0 Ma from two eclogite samples reveal that mafic precursors in the Chuacús complex originated in multiple tectonotemporal settings from the Silurian to Jurassic. The integration of petrological and geochronological data suggests that subduction of the continental margin of the North American plate (Chuacús complex) beneath the Greater Antilles arc occurred during an Albian-Cenomanian pre-collisional stage, and that a subsequent Campanian collisional stage is

probably responsible of the amphibolite facies overprint and late syncollisional exhumation.

KEYWORDS
Chuacús complex, Guatemala Suture Zone, high-pressure metamorphism, Lu-Hf and U-Pb geochronology, phase equilibria modelling

1 | INTRODUCTION

Petrological and geochronological studies of subduction-zone metamorphism have provided valuable insights into the subduction/collision zone geodynamics and orogenic processes (e.g. Beltrando, Compagnoni, & Lombardo, 2010; Chopin, 2003; Ernst & Liou, 2008; Liou, Tsujimori, Zhang, Katayama, & Maruyama, 2004; Zheng, 2012). In particular, several comprehensive studies of eclogite-hosting metamorphic sequences have revealed that host-rocks may share a common metamorphic evolution with the enclosed eclogite (Carswell, Wilson, & Zhai, 2000; Janák et al., 2009; Li, Klemd, Gao, Jiang, & Song, 2015; Meyre, de Capitani, Zack, & Frey, 1999; Song et al., 2007; Zhang, Meng, & Yang, 2004). This has two relevant implications: (1) it allows recognition of the nature of the lithospheric sequence involved in the subduction, and (2) it suggests that the sequence was subducted and exhumed as a relatively coherent unit. Both aspects are crucial in regional correlations and tectonic interpretations. Depending on the origin of the subducted lithosphere, two contrasting types of convergent zones have been recognized in nature: the Pacific (oceanic) and Alpine (continental) (e.g. Ernst, 2005; Guillot, Hattori, Agard, Schwartz, & Vidal, 2009; Zheng, Ye, & Zhang, 2009). Transitional settings between these subduction/collision types are common. Indeed, a particular subduction zone may evolve from one type to another, or two different types may coexist along one subduction zone (Guillot et al., 2009). The particular case of continental subduction during arc-continent convergence (e.g. underflow of a continental margin beneath an island arc) is not explicitly distinguished in this categorization, where the hangingwall plate is assumed to be of continental nature. Nevertheless, several studies have shown that continental subduction in an arc-continent setting plays an important role in building high-pressure (HP) to ultrahigh-pressure (UHP) terranes (e.g. Baldwin, Webb, & Monteleone, 2008; Beane & Leech, 2007; Beyssac, Negro, Simoes, Chan, & Chen, 2008; Brown, Wu, Feng, Chao, & Huang, 2015; Brown et al., 2006; Kadarusman et al., 2010; Majka et al., 2014; Matte, 2006; Monteleone et al., 2007; Tsai, Iizuka, & Ernst, 2013).

The HP Chuacús complex in the Guatemala Suture Zone records continental subduction of the North American plate beneath the Greater Antilles arc during the Cretaceous (Martens, Brueckner, Mattinson, Liou, & Wooden, 2012; Pindell, Maresch, Martens, & Stanek, 2012). In spite of the available petrographic, thermobarometric and geochronological data, knowledge about its *P–T–t* evolution is very limited, in particular, its early HP metamorphic stage (Maldonado, Ortega-Gutiérrez, & Hernández-Uribe, 2016). Furthermore, although a Late Cretaceous age for subduction-zone metamorphism is widely recognized along the Caribbean plate boundary, recent geochronological work in other localities reveals that the tectonometamorphic evolution of circum-Caribbean subduction is more complex and prolonged than previously thought (e.g. Blanco-Quintero et al., 2011; Cárdenas-Párraga et al., 2012; Escuder-Viruete et al., 2013; Flores, Martens, Harlow, Brueckner, & Pearson, 2013; Flores et al., 2015; García-Casco, Torres-Roldán, Millán, Monié, & Schneider, 2002; Krebs et al., 2008; Lázaro et al., 2009; Schertl et al., 2012; Yui et al., 2012).

This work focuses on eclogite and related HP metapelite from the Chuacús complex. It seeks to elucidate the metamorphic-temporal relationships and to quantify the *P–T–t* path by linking the petrological and geochronological aspects. Therefore, detailed petrological data and phase equilibria calculations are presented that constrain a previously unknown segment of the prograde *P–T* evolution and provide a framework for the geochronological analyses presented here. The geochronological analyses combine multimineral U-Pb and Lu-Hf garnet/whole-rock data that allows determination of: (1) the age of the HP subduction-related event and a subsequent medium-pressure (MP) overprint, and (2) the age of the igneous protoliths of the eclogite bodies. The results are discussed and evaluated by considering the implications of the integrated *P–T–t* path of the Chuacús complex with respect to the tectonic evolution of the Guatemala Suture Zone and the Caribbean during the Cretaceous.

2 | THE GUATEMALA SUTURE ZONE AND THE CHUACÚS COMPLEX

The Guatemala Suture Zone (GSZ; Brueckner et al., 2009; Flores et al., 2013) is a complex assemblage of fault-bounded continental blocks and oceanic thrust slices

located along the current North American-Caribbean plate boundary in Central America (Figure 1). The amalgamation of the GSZ records subduction, oceanic closure, collision, exhumation and lateral tectonic transport resulting from the North American–Farallon–South American plate interactions responsible for the Caribbean plate evolution from the Jurassic to the present (e.g. Brueckner et al., 2009; Harlow, Hemming, Lallemant, Sisson, & Sorensen, 2004; Martens et al., 2012; Ortega-Gutiérrez et al., 2004; Pindell, 1990; Pindell et al., 2012; Solari, García-Casco, Martens, Lee, & Ortega-Rivera, 2013; Sutter, 1979; Tsujimori, Sisson, Liou, Harlow, & Sorensen, 2006). A synthesis of the regional geology of the GSZ, including description of their HP belts, has been recently presented in Flores et al. (2013) and Maldonado et al. (2016), thus only a brief summary of most relevant petrological and geochronological features are presented below.

Four HP localities have been recognized in the GSZ: (1) the South and (2) North Motagua serpentinite mélanges, (3) the Rabinal granite and (4) the Chuacús complex (Figure 1b). The South and North Motagua serpentinite mélanges (subducted oceanic lithosphere) include blocks of lawsonite-bearing eclogite and garnet blueschist that underwent high-pressure/low-temperature (HP/LT) conditions of 25–26 kbar and 480–520°C (Endo, Wallis, Tsuboi, Torres de León, & Solari, 2012; Harlow et al., 2004; Tsujimori, Liou, & Coleman, 2005; Tsujimori et al., 2006), and strongly retrogressed clinozoisite eclogite bodies that reached higher temperatures of 500–650°C at lower pressures of 20–22 kbar (Brueckner et al., 2009; Harlow et al.,

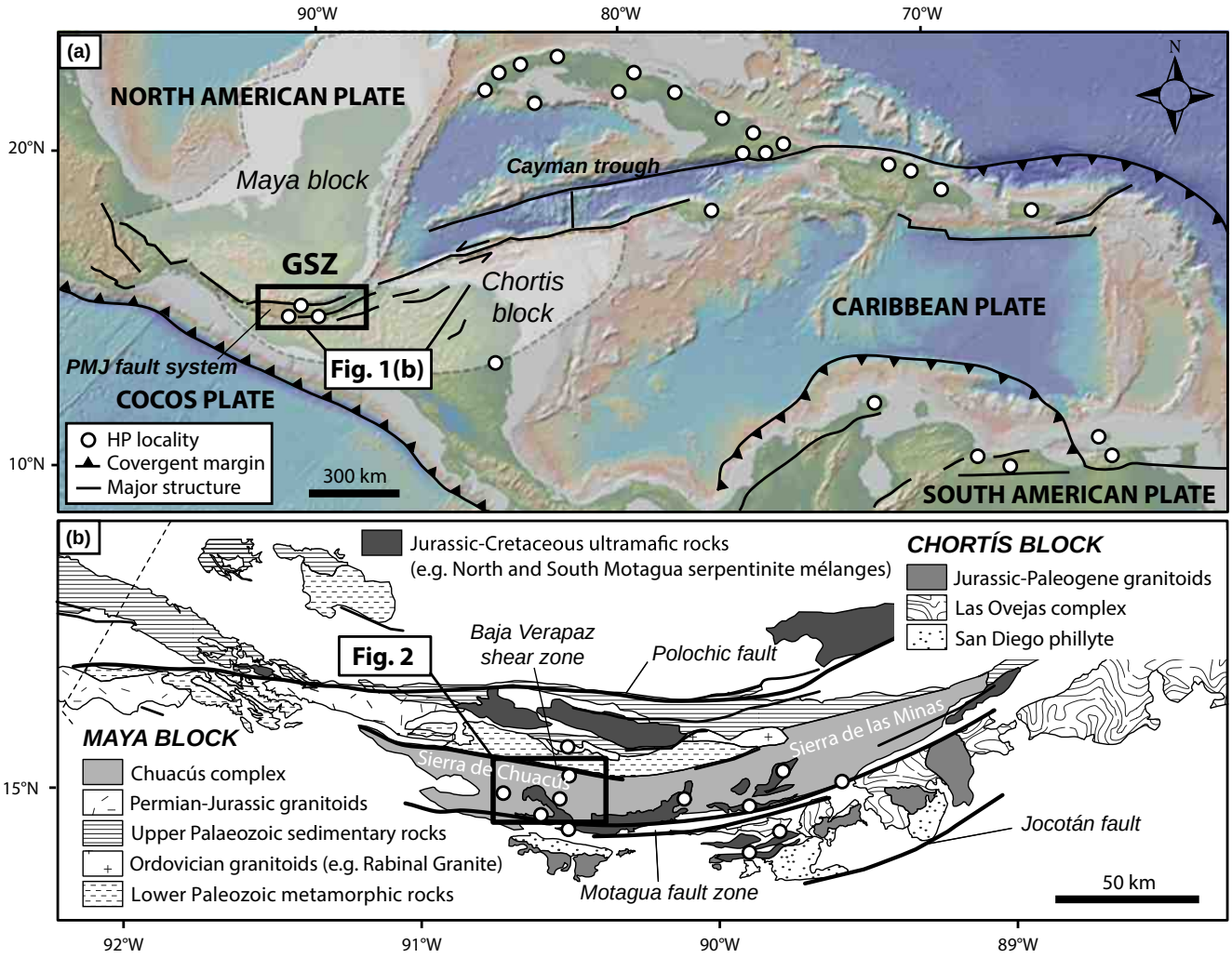

FIGURE 1 (a) Tectonic setting of the Caribbean suture system modified from Martens et al. (2012) and Flores et al. (2015). Circles and bold lines denote high-pressure localities and major fault zones, respectively; note the location of the Guatemala Suture Zone (GSZ; rectangle); (b) simplified geological map of the GSZ (after Anderson, Burkart, Clemons, Bohnenberger, & Blount, 1973; Kesler, Josey, & Collins, 1970; Ratschbacher et al., 2009) showing the main HP localities (after Harlow et al., 2004; Ortega-Gutiérrez et al., 2004; Tsujimori et al., 2006; Martens et al., 2012; Solari et al., 2013). Base relief map was obtained from GeoMapApp version 3.5.2 (http://www.geomapapp.org)

2004; Tsujimori, Liou, & Coleman, 2004), respectively. Reported metamorphic ages of eclogite from both mélanges are similar, ranging from 144 to 125 Ma (mineral/whole-rock Sm-Nd isochrons; Brueckner et al., 2009). Phengite jadeitite blocks from the southern serpentinite mélange yielded U-Pb zircon ages that are consistent (equal within errors or slightly older) with the above-mentioned Sm-Nd ages (Flores et al., 2013; Fu et al., 2010); however, jadeitite from the northern serpentinite mélange yielded significantly younger U-Pb zircon ages ranging between 98 and 72 Ma (Flores et al., 2013; Yui et al., 2010). Similarly, cooling ages are different between the two units. The $^{40}Ar/^{39}Ar$ phengite ages from HP blocks yielded 125–113 Ma for the southern mélange and 77–65 Ma for the northern mélange (Harlow et al., 2004). The tectonic significance of this temporal discrepancy remains unclear, but some authors considered it as evidence for a later HP event recorded in the northern mélange (Flores et al., 2013). Whatever the explanation of this difference, the available petrological and geochronological data suggest that these units may constitute two separate belts that underwent coeval HP metamorphism during the Early Cretaceous and then followed separate tectonothermal evolution, until they were juxtaposed by strike slip movement along the Motagua fault zone (e.g. Brueckner et al., 2009; Harlow et al., 2004).

The Rabinal Granite (S-type pluton) represents the northernmost occurrence of HP metamorphic rocks in the GSZ (Figure 1b), as has been recently documented by Solari et al. (2013). Phengite barometry combined with two-feldspar thermometry from this variably deformed pluton suggests minimal *P–T* conditions of ~8 kbar at 280–330°C, indicating low blueschist facies metamorphism related to continental subduction. Moreover, $^{40}Ar/^{39}Ar$ dating of phengite yielded a mean age of 70.1 ± 0.55 Ma, interpreted as the time of recrystallization at HP conditions (Solari et al., 2013).

The Chuacús complex (Ortega-Gutiérrez et al., 2004) is a medium- to high-grade metamorphic belt ~220 km long and <30 km wide that extends between the Cabañas fault and the Baja Verapaz shear zone (Ortega-Obregón et al., 2008) in the core of the GSZ (Figure 1b). It mostly consists of a thick, polydeformed sequence of interlayered quartzofeldspathic gneiss, amphibolite, pelitic schist and marble, which preserves evidence of eclogite facies metamorphic equilibration (Maldonado et al., 2016; Martens et al., 2012; Ortega-Gutiérrez et al., 2004; Ratschbacher et al., 2009). The deepest portion of the belt is exposed in the Sierra de Chuacús region (Figure 1b), where Ortega-Gutiérrez et al. (2004) documented HP (probably UHP) conditions for the first time. The presence of eclogitic relicts in other sectors (e.g. Sierra de las Minas) has not been verified, and the scale of the HP metamorphism in what is currently considered the Chuacús complex is mostly unknown (Figure 1b).

Eclogite bodies in the Sierra de Chuacús occur as discontinuous bands and lenses mainly within the gneissic component of the sequence. The primary eclogitic mineral assemblage, consisting of omphacite+garnet+rutile+quartz±phengite±epidote/clinozoisite±Ca-Na amphibole, yielded *P–T* peak conditions of 660–750°C and 21–24 kbar (Martens et al., 2012; Ortega-Gutiérrez et al., 2004; Ratschbacher et al., 2009). This stage was followed by isothermal decompression at 660°C to 13 kbar (Ratschbacher et al., 2009), producing widespread partial melting and subsequent emplacement of late- to post-tectonic pegmatite dikes (Martens et al., 2012; Ortega-Gutiérrez et al., 2004; van den Boom, 1972). A regional amphibolite facies overprint of albite+Ca-Na to Ca amphibole±biotite±garnet±titanite partially replaced the eclogitic mineralogy at 450–550°C and 7–8 kbar (Ratschbacher et al., 2009).

U-Pb zircon dating of one eclogite sample from the Palibatz area (Figure 2) yielded a *c*. 227 Ma age for the protolith crystallization (Martens et al., 2012). Moreover, two younger ages of *c*. 77 Ma (Sm-Nd isochron) and *c*. 75 Ma (U-Pb on zircon) have been interpreted to date the eclogite facies metamorphism (Martens et al., 2012), whereas a K-Ar age of retrograde hornblende yielded a *c*. 73 Ma age (Ortega-Gutiérrez et al., 2004) for a subsequent amphibolite facies overprint. In addition, two U-Pb zircon ages of *c*. 74 Ma, obtained from related gneissic rocks, have been interpreted to date the amphibolite facies overprint (Martens et al., 2012), whereas other cooling ages in the range of 76–56 Ma were obtained by Rb-Sr, K-Ar and $^{40}Ar/^{39}Ar$ dating of amphibole and white mica from different rock types (Ortega-Gutiérrez et al., 2004; Ortega-Obregón et al., 2008; Ratschbacher et al., 2009; Solari, Gómez-Tuena, Ortega-Gutiérrez, & Ortega-Obregón, 2011; Sutter, 1979).

Metasedimentary rocks from the Sierra de Chuacús cover a wide range of compositions, being predominantly psammitic and pelitic. Three distinctive mineral assemblages have been previously described in metapelite: (1) garnet+staurolite+muscovite±chloritoid±kyanite (McBirney, 1961), (2) garnet+kyanite+phengite+rutile (Ortega-Gutiérrez et al., 2004) and (3) garnet+chloritoid+paragonite+phengite+rutile (Maldonado et al., 2016). Phase equilibria modelling of the latter assemblage constrained an early stage of prograde HP/LT metamorphism at 20–21 kbar and 500–540°C, as well as *P–T* peak conditions of ~20 kbar and 580–600°C (Maldonado et al., 2016). U-Pb zircon dating of one garnet–kyanite–rutile bearing metapelite from the Pachalum area (Figure 2) yielded a lower-intercept age of *c*. 220 Ma, interpreted as the timing of metamorphism (Solari et al., 2011). Cooling ages obtained by K-Ar and $^{40}Ar/^{39}Ar$ dating of white mica and biotite from non-pelitic metasedimentary rocks range from 74 to

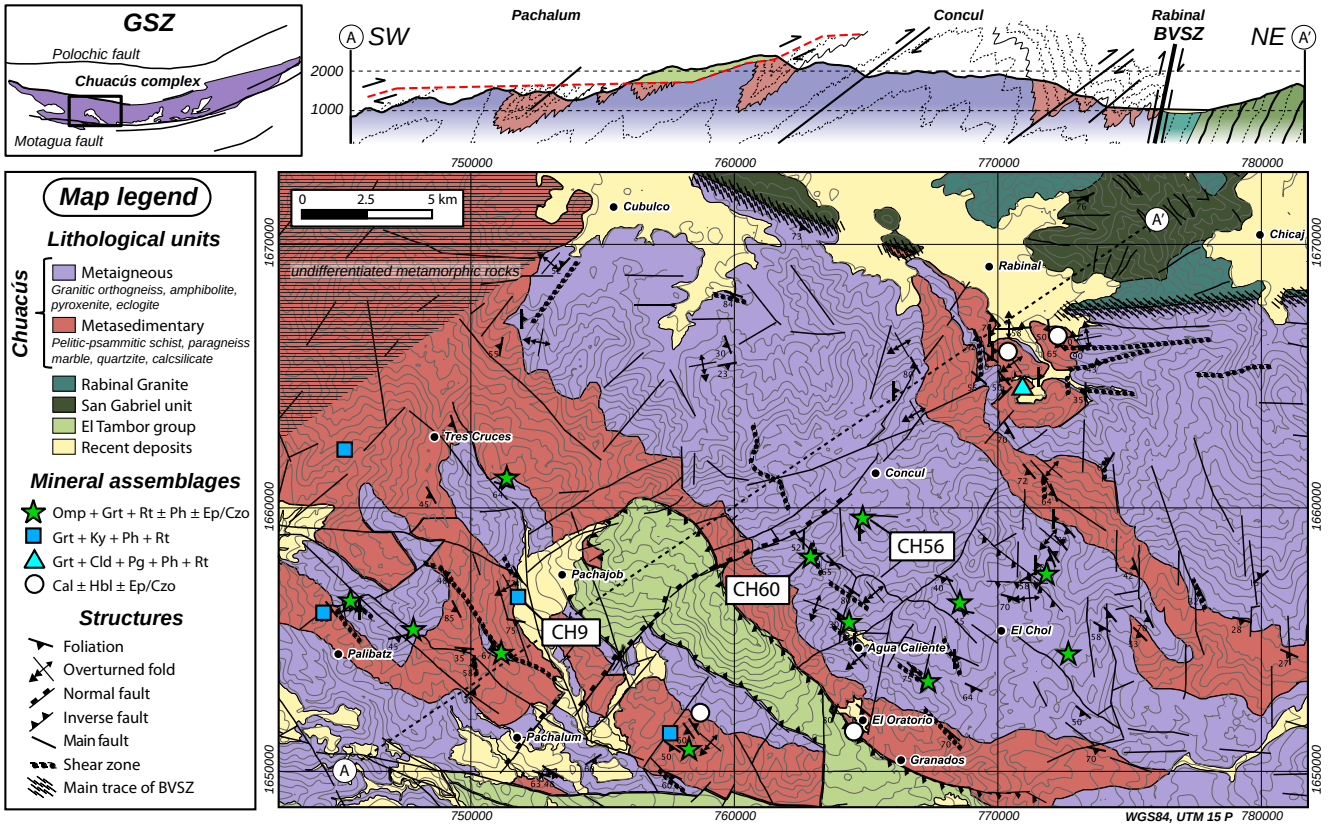

FIGURE 2 Simplified geological map and structural cross-section of the study area (modified from Morán-Ical, Chiquín, & Requena, 2001; and Ortega-Obregón et al., 2008). Colour symbols highlight localities with key mineral assemblages. Locations of samples CH9, CH56 and CH60 are also shown. BVSZ, Baja Verapaz shear zone

65 Ma (Ortega-Obregón et al., 2008; Ratschbacher et al., 2009).

3 | ANALYTICAL PROCEDURES

Major mineral compositions were analysed with a CAMECA SX-100 electron microprobe at the CAMCOR facility, University of Oregon, while measurements of rutile compositions were carried out on a JEOL JXA-8500F field-emission electron microprobe at the GeoAnalytical Lab, Washington State University, applying the method of Neill, Mattinson, Donovan, Hernández-Uribe, and Sains (2016). Backscattered electron (BSE) and cathodoluminescence (CL) images were acquired on a Zeiss EVO MA10 scanning electron microscope at the Instituto de Geología, Universidad Nacional Autónoma de México (IG UNAM). X-ray compositional maps of garnet were obtained with a JEOL JXA-8900R Superprobe at the Laboratorio Universitario de Petrología, UNAM. Mineral abbreviations in figures and tables follow Whitney and Evans (2010). Major-element whole-rock compositions were acquired by XRF using a Rigaku ZSX Primus II spectrometer at the IG UNAM. The U-Pb data of zircon, titanite and monazite, as well as the trace element concentrations in zircon and garnet, were acquired by LA-ICP-MS at the Laboratorio de Estudios Isotópicos (LEI), Centro de Geociencias, UNAM, using a Resonetics M-50 excimer laser ablation system coupled to a Thermo ICap Qc ICP-MS. Sample processing for Lu-Hf geochronology was performed in PicoTrace clean lab facilities at Centro de Investigación Científica y de Educación Superior de Ensenada (CICESE), following procedures of Smit, Scherer, Bröcker, and van Roermund (2010) and Estrada-Carmona, Weber, Scherer, Martens, and Elías-Herrera (2016), as well as methods modified from Münker, Weyer, Scherer, and Mezger (2001) and Sprung, Scherer, Upadhyay, Leya, and Mezger (2010) by González-Guzmán, Weber, Tazzo-Rangel, and Solari (2016). Measurements of Lu and Hf isotope ratios were carried out on a Thermo Neptune Plus MC-ICP-MS installed at the LEI, Centro de Geociencias, UNAM, following methods described in González-Guzmán et al. (2016). Further detailed description of analytical procedures, including mineral separation methods, chemical procedures, acquisition of isotopic and trace element data, as well as reproducibilities, is given in Appendix S1.

4 | PETROGRAPHY AND MINERAL CHEMISTRY

4.1 | Field relations and petrography

The fieldwork and sampling was focused in the Sierra de Chuacús region (Figures 1b and 2). The metamorphic sequence can be divided into: (1) a metasedimentary unit, consisting of intercalated pelitic-psammitic schist, paragneiss, marble, quartzite and calcsilicate rock; and (2) a metaigneous unit, which comprises granitic orthogneiss and amphibolite, with minor eclogite and pyroxenite bodies. The predominant structural trend is defined by a NW-SE-striking, SW-dipping axial-plane foliation (S_{n+2}), which resulted from the tight-isoclinal folding of an earlier high-*T* foliation (S_{n+1}). Locally developed high-strain shear zones (S_{n+3}) subparallel overprint S_{n+2} on the scale of metres to kilometres, indicating later NE-vergent folding and thrusting (Figure 2). For more details about ductile-brittle deformation, see Ratschbacher et al. (2009).

Eclogite bodies occur as centimetre- to metre-scale bands and lenses chiefly within granitic orthogneiss (Figure 3a), but also are hosted by pelitic schist (Figure 3b). Macroscopically, they are fine- to coarse-grained, and granoblastic to foliated rocks that exhibit a variable degree of amphibolite facies retrogression (Figure 3c,d). They are composed of a light greenish matrix of clinopyroxene with ~40–50 vol.% of garnet porphyroblasts, usually <2 mm in diameter, and common dark green to dark patches of amphibole. Some eclogite contain macroscopically visible rutile and white mica (Figure 3d). Fifty rock samples were collected in a ~30 × 10 km area, at the southern part of the studied zone (Figure 2); however, some of the rocks sampled are garnet–rutile amphibolite (no pyroxene preserved) and garnet pyroxenite (low-Na clinopyroxene). Two samples of representative eclogite textural varieties were chosen for detailed study: a coarse-grained kyanite-bearing eclogite (sample CH60) and a fine-grained foliated eclogite (sample CH56).

Metapelite is widely distributed in the studied zone, but the southwestern and northeastern areas preserve the most prominent outcrops (Figure 2). These rocks are mostly medium- to coarse-grained garnet-mica schist, which commonly alternate at metre- to kilometre-scale with quartzofeldspathic gneiss, marble and quartzite. Garnet–kyanite pelitic schist exposed in the southwestern part of the studied zone (Figure 2), analogous to those described by Ortega-Gutiérrez et al. (2004), is spatially associated with eclogite bodies. Macroscopically, they are coarse-grained schistose rocks composed of large garnet (up to 3 cm) and

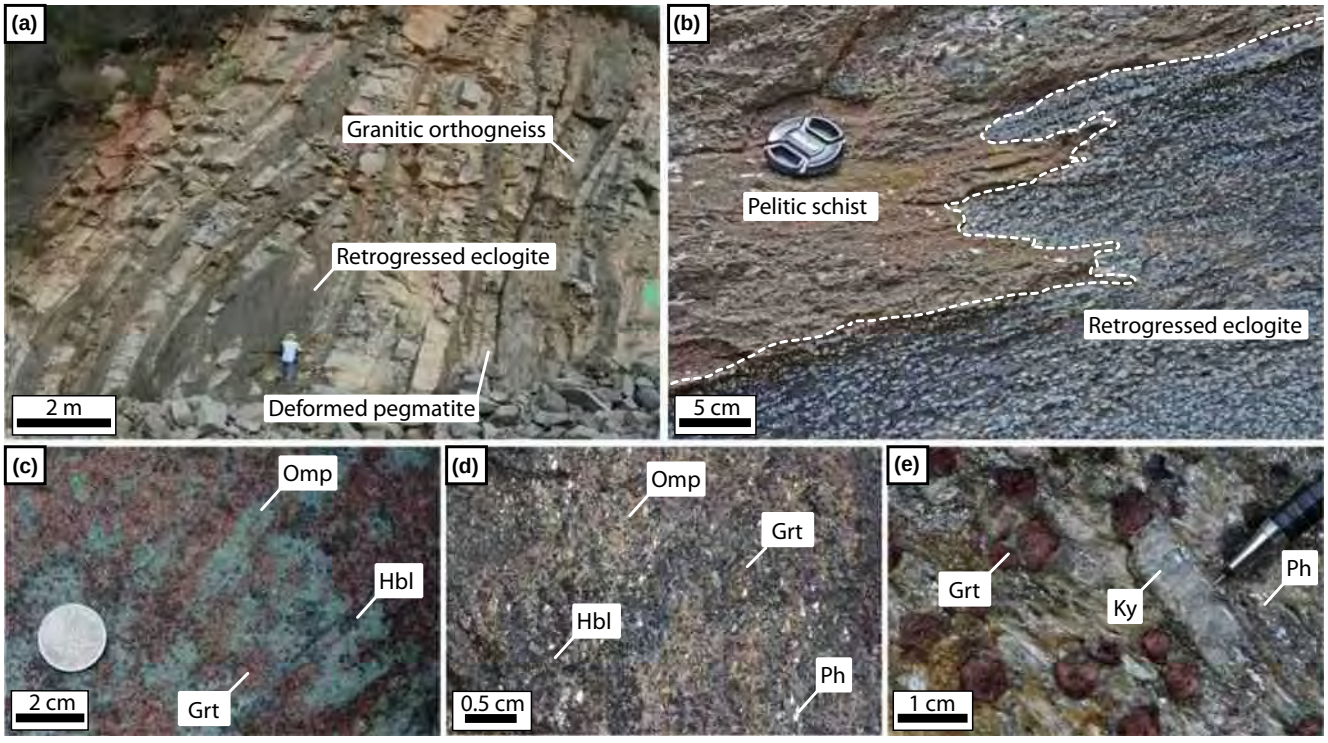

FIGURE 3 Outcrop photographs of eclogites and metapelites from the study area. (a) Metre-sized boudin of retrogressed eclogite hosted by granitic orthogneiss; (b) contact relationship between retrogressed eclogite and pelitic schist; (c) medium-grained eclogite lens showing a moderate degree of amphibolite facies retrogression; (d) phengite-bearing eclogite with strong amphibolite facies retrogression; (e) detail of a coarse-grained garnet–kyanite pelitic schist

kyanite (up to 15 cm) porphyroblasts set in a silvery matrix of white mica and quartz (Figure 3e). Four outcrops of this sequence were sampled in the Palibatz-Pachalúm area (Figure 2), and one representative sample (CH9) was chosen for detailed study.

4.1.1 | Kyanite-bearing eclogite (CH60)

Sample CH60 is a coarse-grained eclogite (Figure 4a–c) composed of garnet, clinopyroxene, amphibole, plagioclase, epidote–clinozoisite, rutile, quartz, phengite, apatite, titanite, paragonite, kyanite (exclusively present as inclusion in garnet), Fe-Ti oxides and zircon. Relict prograde phases in this sample are mostly recognized as inclusions in idiomorphic garnet porphyroblasts (Grt_1<3 mm, exceptionally ~1 cm; Figure 4b) and include plagioclase (Pl_1), epidote–clinozoisite (Ep_1), clinopyroxene (Cpx_1), kyanite, paragonite, rutile and quartz (Figure 5a–d). Kyanite inclusions (<20 μm) are associated with Pl_1, quartz and paragonite (Figure 5b), which are relatively abundant in the garnet cores (Figure 5c); meanwhile, Cpx_1 inclusions tend to be concentrated towards garnet rims (Figure 5d). The peak eclogite assemblage consists of Grt_1 in textural equilibrium with matrix clinopyroxene (Cpx_2), phengite, rutile, quartz and apatite. Cpx_2 shows lamellae of green amphibole and forms granoblastic aggregates partially replaced by plagioclase (Pl_2)+amphibole±clinopyroxene (Cpx_3) ±epidote–clinozoisite (Ep_2) intergrowths, typically occurring as medium- to coarse-grained symplectites. Phengite represents ~1–2 vol.% of the sample and occurs either as corroded grains rimmed by Pl_2±biotite symplectites or rounded sheets enclosed by post-eclogitic amphibole. In

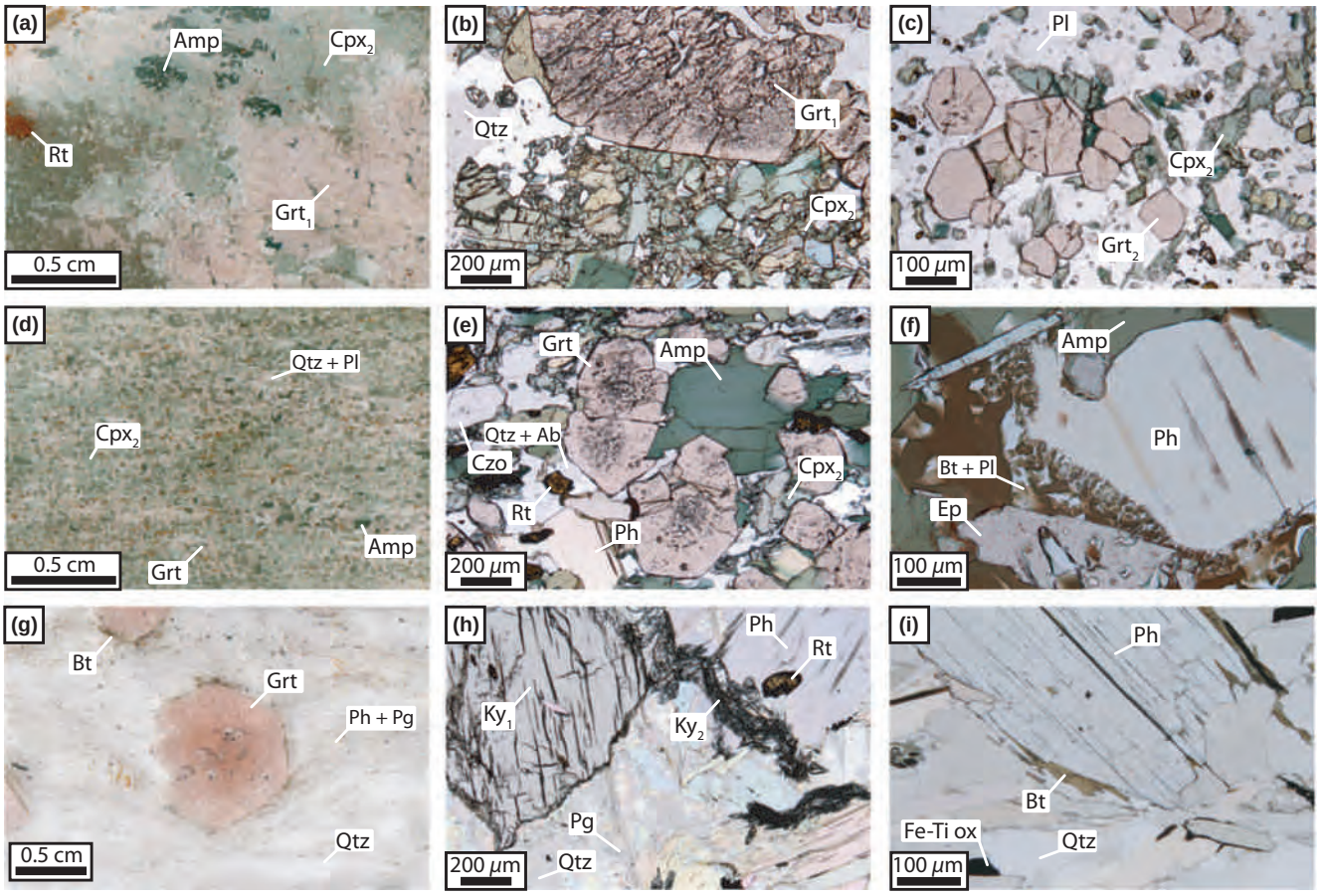

FIGURE 4 Petrographic features of the samples. (a–c) Kyanite-bearing eclogite (sample CH60), (d–f) eclogite (sample CH56), and (g–i) garnet–kyanite pelitic schist (sample CH9). (a) Thin-section showing typical microstructures and assemblages. (b) Detail of (a) showing an equilibrated texture of poikiloblastic garnet (Grt_2)+clinopyroxene (Cpx_2). (c) Inclusion-poor idioblastic garnet (Grt_2) and corroded clinopyroxene (Cpx_2) within a plagioclase pseudomorph after garnet (Grt_1). (d) Thin-section view showing typical microstructures and assemblages. (e) Detail of (d) showing a garnet+clinopyroxene (Cpx_2)+phengite+epidote–clinozoisite+quartz intergrowth partially replaced by plagioclase+amphibole (note the inclusion-rich cores of garnet). (f) Biotite+plagioclase symplectite around phengite. (g) Thin-section view showing typical microstructures and assemblages. (h) Detail of kyanite (Ky_1) and phengite showing a fine-grained overgrowth of kyanite (Ky_2). (i) Detail of phengite with an incipient corona of biotite. All images are plane-polarized light views, except (a, d, g) that are scanned thin sections

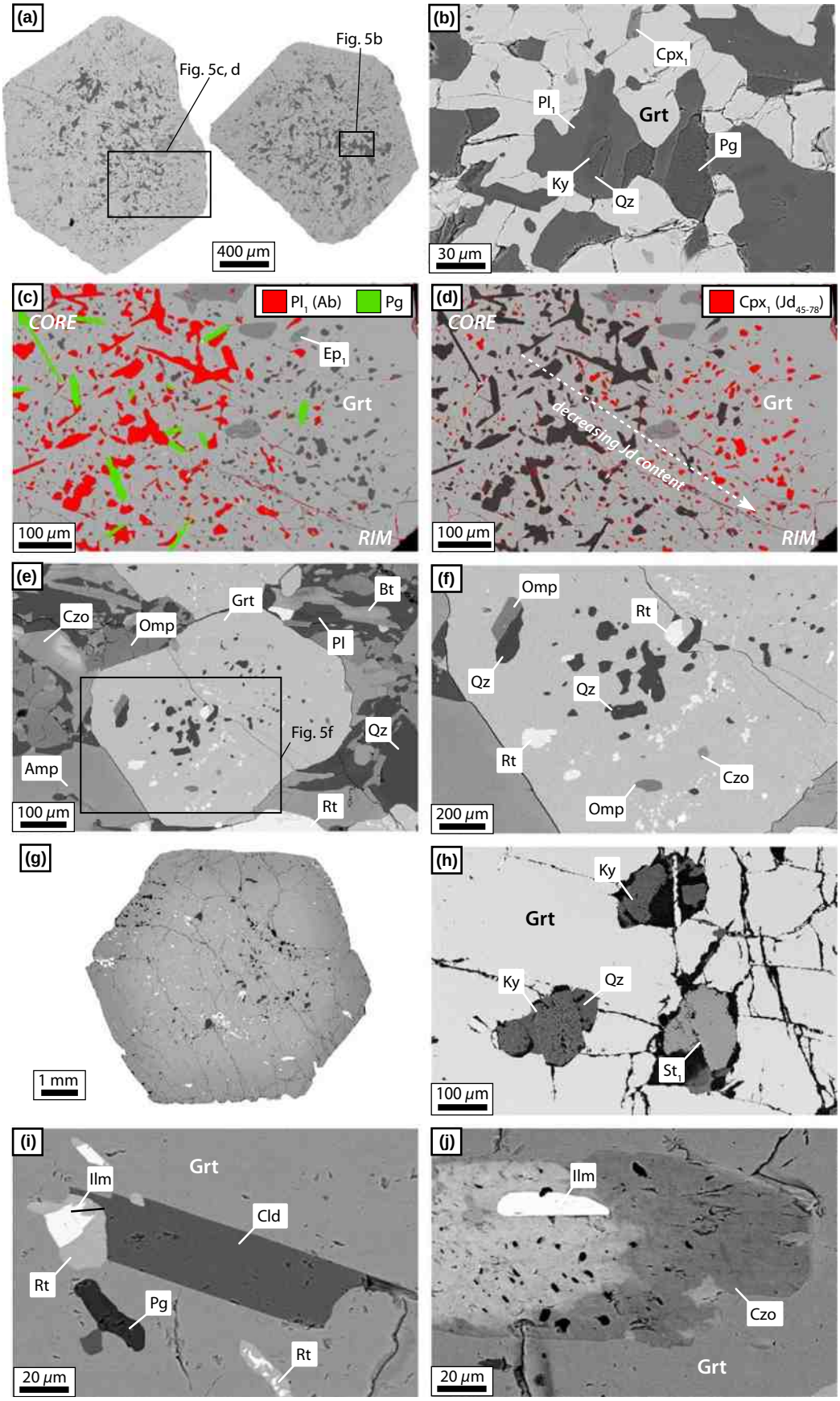

FIGURE 5 BSE images of the inclusions in garnet from the studied samples. (a–d) Kyanite-bearing eclogite (sample CH60), (e, f) eclogite (sample CH56) and (g–j) garnet–kyanite pelitic schist (sample CH9)

some cases, this mineral has completely reacted and only the characteristic flake-like plagioclase±biotite pseudomorphs after phengite are preserved. Rutile is partially replaced by titanite and occurs either as needle-shaped grains or polygonal aggregates associated with apatite and zircon. Some strongly retrogressed lenses are characterized by the presence of coarse rounded plagioclase pseudomorphs after garnet, which host relatively small (<1 mm), inclusion-poor garnet idioblasts (Grt_2) and fine-grained amoeboid relicts of clinopyroxene (Figure 4c).

4.1.2 | Eclogite (CH56)

Sample CH56 is a fine-grained foliated eclogite with moderate retrogression. This rock is composed of garnet, clinopyroxene, amphibole, quartz, phengite, plagioclase, clinozoisite and epidote, with minor rutile, apatite, Fe-Ti oxides, biotite, titanite and zircon (Figure 4d–f). Relict prograde phases are quartz, rutile, clinopyroxene (Cpx_1), clinozoisite (Czo_1), plagioclase (Pl_1), apatite, Fe-Ti oxides and titanite (Ttn_1), which mostly occur as inclusions in garnet porphyroblasts (Figures 4e and 5e,f). Garnet, clinopyroxene (Cpx_2), phengite, clinozoisite (Czo_2), quartz and rutile in the rock matrix are in textural equilibrium and constitute the peak eclogite assemblage. Garnet occurs as idioblastic to rounded porphyroblasts (<2 mm) with inclusion-rich cores, locally showing planar inclusion trails that are discontinuous with the matrix foliation. In some eclogite bodies similar to this sample, garnet displays atoll microstructures or is replaced by epidote-rich symplectites. Cpx_2 (<1 mm) is present as elongated to equant grains with embayed boundaries, being replaced by plagioclase (Pl_2) and, locally, by fine-grained Pl_2+clinopyroxene (Cpx_3)±amphibole symplectites. Coarse-grained phengite (up to 1 mm) occurs as aligned flakes and is partially replaced along its boundaries by fine-grained biotite+Pl_2±quartz symplectites (Figure 4f). Czo_2 (<2 vol.%), which commonly displays optically visible zoning and inclusion-rich cores, is present as aligned tabular crystals in mutual contact with garnet, Cpx_2 and phengite. Rutile occur as irregular grains rimmed by titanite (Ttn_2).

4.1.3 | Garnet–kyanite pelitic schist (CH9)

Sample CH9 is a coarse-grained pelitic schist composed of centimetric garnet and kyanite porphyroblasts set in a finer-grained matrix of phengite, quartz, paragonite, rutile and apatite, with minor epidote–clinozoisite, biotite, chlorite, chloritoid, staurolite, tourmaline, Fe-Ti oxides, zircon and monazite (Figure 4g–i). The dominant foliation fabric is defined by alternating white mica-rich and quartz-rich domains (Figure 4g). Garnet porphyroblasts (10–15 vol.%) are mostly idioblastic and display concentric colour zoning, with dark red cores and pinkish rims (Figure 4g). Most crystals are inclusion-rich and some cores show helicitic inclusion trails discontinuous towards the rims. Mineral inclusions of quartz, phengite, kyanite, paragonite, chlorite, epidote–clinozoisite, chloritoid, staurolite, rutile and Fe-Ti oxides are common in garnet (Figure 5g–j). Two generations of kyanite are recognized: one is present as idioblastic poikiloblasts (Ky_1, 5–10 vol.%) with inclusions mainly of quartz, rutile, Fe-Ti oxides, phengite, garnet and monazite; a second generation (Ky_2) occurs as fine-grained intergrowths of kyanite and quartz replacing white mica. Some Ky_1 crystals show embayments of paragonite–phengite and Ky_2 along grain boundaries (Figure 4h). Coarse-grained phengite (up to 1 cm) occurs as aligned flakes that are locally crenulated and shows incipient replacement by biotite on the rims (Figure 4i). Matrix paragonite is present as fine-grained aggregates in apparent textural equilibrium with phengite. Rutile (<2 vol.%) commonly occurs as both micrometre-scale-oriented needles and twinned bicrystals within garnet and kyanite, but most is present as irregular grains in the matrix, where locally it is rimmed by Fe-Ti oxides. Chloritoid and staurolite (St_1) mainly occur as inclusions in garnet (Figure 5h,i), but they are also present as irregular, pre-kinematic grains in the rock matrix. Additionally, some staurolite crystals (St_2) are subidioblastic and display a syn- to post-kinematic character.

4.2 | Mineral chemistry

4.2.1 | Kyanite-bearing eclogite (CH60)

Representative chemical compositions of major phases are presented in Table 1; end-member concentrations are given in mole fractions. Garnet poikiloblasts (Grt_1) in sample CH60 have compositionally flat profiles (alm = 0.56–0.60, grs = 0.24–0.27; prp = 0.15–0.16, sps = 0.01; Figures 6a and 7a,d). Fine-grained garnet idioblasts (Grt_2) within plagioclase pseudomorphs are chemically zoned with an inner domain displaying a bell-shaped profile of grossular (grs = 0.19–0.28) and spessartine (sps = 0.02–0.03), and an increase in almandine (from alm = 0.57 to alm = 0.63) and pyrope (from prp = 0.12 to prp = 0.16); an outer domain is characterized by increasing grossular (grs = 0.19 to grs = 0.22) and spessartine (sps = 0.02 to sps = 0.03), and decreasing almandine (alm = 0.63 to alm = 0.61) and pyrope (prp = 0.16 to prp = 0.14) towards the rim.

Three generations of clinopyroxene are distinguished on the basis of microstructure and chemical composition (Figure 6b). Clinopyroxene included in garnet (Cpx_1) ranges

TABLE 1 Representative microprobe analyses of the studied samples. Cation totals were calculated with the programme AX (Holland, 2014), which estimates the amount of ferric iron from stoichiometric criteria X_{Mg} = Mg/(Mg + Fe^{2+}); alm = Fe^{2+}/(Fe^{2+} + Mn + Mg + Ca); sps = Mn/(Fe^{2+} + Mn + Mg + Ca); prp = Mg/(Fe^{2+} + Mn + Mg + Ca); grs = Ca/(Fe^{2+} + Mn + Mg + Ca); jd, ae and q end-members according to Morimoto (1988); X_{Na} = Na/Na + K; $X_{Fe^{3+}}$ = Fe^{3+}/(Fe^{3+} + (Al − 2))

Sample	CH60	CH60	CH60	CH60	CH60	CH60	CH60	CH60	CH56	CH56	CH56	CH56	CH56	CH56	CH56	CH56	CH9	CH9	CH9	CH9	CH9	CH9	CH9	CH9	CH9
Mineral	Grt	Grt	Cpx	Cpx	Cpx	Ph	Pg	Ep/Czo	Grt	Grt	Cpx	Cpx	Ph	Ph	Ep/Czo	Ep/Czo	Grt	Grt	Grt	Ph	Ph	Pg	Ep/Czo	Cld	St
Location	core	rim	core	rim	inclus	matrix	inclus	inclus	core	rim	core	rim	matrix	matrix	matrix	matrix	core	mid	rim	matrix	matrix	matrix	inclus	inclus	inclus
SiO_2	38.49	38.85	54.49	53.57	57.87	48.59	47.32	37.90	38.02	37.66	55.10	53.80	49.95	50.31	38.64	39.02	37.74	38.07	38.05	48.27	48.16	46.41	37.09	24.39	28.36
TiO_2	0.07	0.05	0.15	0.07	0.02	0.66	0.10	0.06	0.12	0.02	0.08	0.15	0.67	0.63	0.17	0.13	0.10	0.05	0.04	0.55	0.50	0.05	0.01	0.02	0.56
Al_2O_3	21.09	20.89	9.53	6.87	18.78	26.58	39.79	28.14	19.49	19.67	8.04	6.53	27.00	27.22	22.91	24.71	20.61	21.13	21.80	30.68	30.57	38.44	22.64	40.60	51.74
FeO	27.18	26.96	9.29	9.75	5.99	4.60	0.63	7.72	26.67	27.65	8.49	9.81	3.23	3.45	12.35	8.40	31.35	33.18	31.34	3.23	3.20	0.83	12.60	22.17	12.41
MnO	0.39	0.41	0.02	0.01	0.12	0.03	0.00	0.02	0.59	0.91	0.02	0.04	0.00	0.00	0.04	0.00	2.41	0.67	0.08	0.01	0.02	0.00	0.35	0.08	0.09
MgO	3.97	3.87	6.48	8.28	1.80	2.85	0.06	0.14	3.32	3.81	7.75	8.79	3.41	3.47	0.10	0.10	2.65	4.50	6.45	1.81	1.65	0.17	0.04	4.53	2.16
CaO	9.21	9.43	12.52	15.80	3.24	0.11	0.35	23.10	11.15	8.70	13.51	16.62	0.02	0.04	22.44	22.71	5.39	2.87	2.29	0.00	0.07	0.76	22.37	0.00	0.00
Na_2O	0.02	0.02	6.70	5.34	12.42	0.43	7.29	0.00	0.01	0.02	6.17	4.60	0.28	0.30	0.00	0.00	0.02	0.03	0.03	1.85	1.98	6.78	0.01	0.00	0.07
K_2O	0.00	0.00	0.00	0.00	0.02	10.78	0.49	0.00	0.00	0.00	0.00	0.00	10.39	10.29	0.00	0.00	0.00	0.01	0.01	8.31	8.15	0.66	0.01	0.00	0.00
Total	100.41	100.47	99.17	99.69	100.25	94.62	96.03	97.07	99.36	98.43	99.15	100.34	94.96	95.71	96.65	95.06	100.28	100.51	100.08	94.70	94.30	94.13	95.11	91.78	95.40
Si	3.01	3.04	1.99	1.96	2.01	3.32	3.00	2.97	3.02	3.02	2.01	1.96	3.36	3.35	3.06	3.11	3.02	3.01	2.98	3.24	3.24	3.01	3.01	1.00	4.01
Ti	0.00	0.00	0.00	0.00	0.00	0.03	0.01	0.00	0.01	0.00	0.00	0.00	0.03	0.03	0.01	0.01	0.01	0.00	0.00	0.03	0.03	0.00	0.00	0.00	0.06
Al	1.95	1.93	0.41	0.30	0.77	2.14	2.97	2.60	1.82	1.86	0.35	0.28	2.14	2.14	2.14	2.32	1.94	1.97	2.01	2.42	2.43	2.94	2.16	1.96	8.62
Fe^{3+}	0.03	0.00	0.08	0.17	0.06	0.04	0.00	0.40	0.13	0.10	0.07	0.11	0.05	0.09	0.81	0.55	0.02	0.01	0.03	0.00	0.00	0.00	0.84	0.04	0.00
Fe^{2+}	1.75	1.76	0.20	0.13	0.12	0.23	0.03	0.11	1.64	1.75	0.19	0.19	0.13	0.10	0.01	0.01	2.08	2.18	2.02	0.18	0.18	0.05	0.02	0.72	1.47
Mn	0.03	0.03	0.00	0.00	0.00	0.00	0.00	0.00	0.04	0.06	0.00	0.00	0.00	0.00	0.00	0.00	0.16	0.05	0.01	0.00	0.00	0.00	0.02	0.00	0.01
Mg	0.46	0.45	0.35	0.45	0.09	0.29	0.01	0.02	0.39	0.46	0.42	0.48	0.34	0.34	0.01	0.01	0.32	0.53	0.75	0.18	0.17	0.02	0.01	0.28	0.46
Ca	0.77	0.79	0.49	0.62	0.12	0.01	0.02	1.94	0.95	0.75	0.53	0.65	0.00	0.00	1.91	1.94	0.46	0.24	0.19	0.00	0.01	0.05	1.94	0.00	0.00
Na	0.00	0.00	0.47	0.38	0.84	0.06	0.90	0.00	0.00	0.00	0.44	0.33	0.04	0.04	0.00	0.00	0.00	0.01	0.01	0.24	0.26	0.85	0.00	0.00	0.02
K	0.00	0.00	0.00	0.00	0.00	0.94	0.04	0.00	0.00	0.00	0.00	0.00	0.89	0.87	0.00	0.00	0.00	0.00	0.00	0.71	0.70	0.06	0.00	0.00	0.00
Sum	8.00	8.00	4.00	4.00	4.00	7.06	6.98	8.03	8.00	8.00	4.00	4.00	6.98	6.97	7.95	7.95	8.00	8.00	8.00	7.00	7.00	6.97	8.00	4.00	14.64
Oxygen	12.00	12.00	6.00	6.00	6.00	11.00	11.00	12.50	12.00	12.00	6.00	6.00	11.00	11.00	12.50	12.50	12.00	12.00	12.00	11.00	11.00	11.00	12.50	6.00	23.00
X_{Mg}	0.21	0.20	–	–	–	–	–	–	0.19	0.21	–	–	–	–	–	–	0.13	0.20	0.27	–	–	–	–	0.28	0.24
alm	0.58	0.58	–	–	–	–	–	–	0.54	0.58	–	–	–	–	–	–	0.69	0.73	0.68	–	–	–	–	–	–
sps	0.01	0.01	–	–	–	–	–	–	0.01	0.02	–	–	–	–	–	–	0.05	0.01	0.00	–	–	–	–	–	–
prp	0.15	0.15	–	–	–	–	–	–	0.13	0.15	–	–	–	–	–	–	0.10	0.18	0.25	–	–	–	–	–	–
grs	0.26	0.26	–	–	–	–	–	–	0.31	0.25	–	–	–	–	–	–	0.15	0.08	0.06	–	–	–	–	–	–
jd	–	–	0.40	0.25	0.78	–	–	–	–	–	0.36	0.24	–	–	–	–	–	–	–	–	–	–	–	–	–
ae	–	–	0.08	0.14	0.06	–	–	–	–	–	0.07	0.09	–	–	–	–	–	–	–	–	–	–	–	–	–
q	–	–	0.52	0.61	0.17	–	–	–	–	–	0.57	0.67	–	–	–	–	–	–	–	–	–	–	–	–	–
X_{Na}	–	–	–	–	–	0.94	0.04	–	–	–	–	–	0.96	0.96	–	–	–	–	–	0.75	0.73	0.06	–	–	–
$X_{Fe^{3+}}$	–	–	–	–	–	–	–	0.13	–	–	–	–	–	–	0.27	0.19	–	–	–	–	–	–	0.28	–	–

from jadeite (jd = 0.75–0.78, aeg = 0.06, q = 0.17–0.20) to omphacite (jd = 0.45–0.70, aeg = 0.01–0.12, q = 0.25–0.48), in contrast to the matrix clinopyroxene (Cpx_2) that is exclusively omphacitic (jd ≤ 0.4) and displays irregular to concentric zoning with relatively jadeite-rich cores (jd = 0.30–0.40, aeg = 0.07–0.14, q = 0.49–0.59) and jadeite-poorer rims (jd = 0.25–0.30, aeg = 0.12–0.16, q = 0.54–0.61). Fine-grained clinopyroxene within symplectites (Cpx_3) shows a decrease in jadeite and an increase in Ca, ranging from omphacite to Al-Na diopside (jd = 0.05–0.17, aeg = 0.05–0.12, q = 0.73–0.89).

Phengite flakes in the matrix are zoned with maximum Si at the core (Si = 3.32 pfu, Fe^{2+} + Mg = 0.52, K/K + Na = 0.94) and a decline in Si and Fe^{2+} + Mg towards the rim (Si = 3.21 pfu, Fe^{2+} + Mg = 0.37–0.38, K/K + Na = 0.84–0.85; Figure 6c). Amphibole is pargasite to ferro-pargasite, with cores characterized by B-site occupancy of Na_B = 0.26 pfu, A-site occupancy of $(Na + K)_A$ = 0.85–0.86 pfu, Si = 6.32–6.33 pfu and X_{Mg} (Mg/Mg + Fe^{2+}) = 0.52, and rims with Na_B = 0.39 pfu, $(Na + K)_A$ = 0.83–84 pfu, Si = 6.38–6.42 pfu and X_{Mg} = 0.53–0.54 (Figure 6e). Matrix plagioclase (Pl_2) is albite with anorthite content between 0.07 and 0.09. Epidote–clinozoisite inclusions (Ep_1) in garnet are zoned and contain X_{Fe} = Fe^{3+}/Fe^{3+} + Al = 0.10–0.19 (Figure 6d), whereas paragonite inclusions have Si = 2.97–3.04 pfu, K/(K + Na) = 0.04–0.08 and Fe^{2+} + Mg = 0.04–0.07 (Figure 6c).

4.2.2 | Eclogite (CH56)

Garnet porphyroblasts are chemically zoned (Figures 6a and 7b) with oscillations in almandine (alm = 0.52–0.60), pyrope (prp = 0.12–0.18) and grossular (grs = 0.29–0.22), as well as a bell-shaped distribution of spessartine (sps = 0.01–0.05; Figure 7d). Clinopyroxene composition varies widely according to its microstructural position (Figure 6b). Large grains in the matrix are omphacite (Cpx_2) concentrically to irregularly zoned, with jd = 0.31–39, aeg = 0.05–0.14, q = 0.54–0.56 at the core and jd = 0.20–0.24, aeg = 0.09–0.10, q = 0.67–0.68 at the rim. Fine-grained clinopyroxene within symplectites (Cpx_3) is marked by a substantial decrease in jadeite and a rise in Ca (jd = 0.06–0.17, aeg = 0.0–0.07, q = 0.82–0.92) with respect to Cpx_2. Coarse-grained phengite in the matrix is zoned with maximum Si at the core (Si = 3.36 pfu, Fe^{2+} + Mg = 0.47, K/K + Na = 0.97) and a decline in Si, Fe^{2+} + Mg and K/K + Na towards the rim (Si = 3.26 pfu, Fe^{2+} + Mg = 0.35, K/K + Na = 0.89; Figure 6c). Matrix clinozoisite Czo_2 has X_{Fe} = Fe^{3+}/Fe^{3+} + Al = 0.03–0.27 (Figure 6d). Amphibole is katophorite to pargasite with Na_B = 0.43–0.52 pfu, $(Na + K)_A$ = 0.72–75 pfu, Si = 6.63–6.70 pfu and X_{Mg} = 0.51–0.53 (Figure 6e). Biotite replacing phengite has X_{Mg} = 0.59–0.60 and Ti = 0.10–0.11 pfu. Matrix plagioclase Pl_2 is albite, with anorthite content between 0.07 and 0.08.

4.2.3 | Garnet–kyanite pelitic schist (CH9)

Garnet porphyroblasts from sample CH9 are strongly zoned, with decreasing spessartine (from sps = 0.09 to sps = 0.01) and grossular (from grs = 0.18 to grs = 0.08), and increasing almandine (from alm = 0.66 to alm = 0.73) and pyrope (from prp = 0.10 to prp = 0.18) from core towards the rim (Figures 6a and 7c,d). This zoning trend is maintained at the rim, except for almandine, which decreases (alm = 0.67, prp = 0.26, grs = 0.06, sps = 0). Zn concentration in garnet (measured by LA-ICP-MS) follows an identical pattern to that of almandine, showing maximum concentration (150 ppm) at an intermediate position between core and rim, and a sudden decrease (25 ppm) at the rim (Figure 7d). These abrupt compositional changes in garnet reveal two clearly distinct growth zones (Grt_1 and Grt_2 in Figure 7c). Coarse-grained phengite in the matrix is zoned with maximum celadonite content at the core (Si = 3.24 pfu, Fe^{2+} + Mg = 0.36) and a decrease in Si and Fe^{2+} + Mg towards the rim (Si = 3.12 pfu, Fe^{2+} + Mg = 0.20; Figure 6c). Fine-grained paragonite in the matrix has Si = 2.97–3.07 pfu, K/(K + Na) = 0.06–0.20 and Fe^{2+} + Mg = 0.02–0.06 (Figure 6c). Chloritoid and staurolite inclusions in garnet are relatively Fe-rich, with X_{Mg} (Mg/(Mg + Fe^{2+}) ranging between 0.24–0.31 and 0.24–0.25, respectively. Inclusions of epidote–clinozoisite in garnet are relatively Fe^{3+}-rich with X_{Fe} = Fe^{3+}/Fe^{3+} + Al = 0.25–0.27 (Figure 6d).

5 | THERMOBAROMETRIC CALCULATIONS

5.1 | Zr-in-rutile thermometry

The Zr content in rutile was used to calculate the temperature according to Tomkins, Powell, and Ellis (2007). It has been shown that the partitioning of Zr into rutile is strongly temperature dependent in assemblages containing rutile+zircon+quartz (e.g. Watson, Wark, & Thomas, 2006; Zack, Moraes, & Kronz, 2004). This thermometer has proven to be a valuable thermometric alternative in eclogite (e.g. Zhang, Ellis, Christy, Zhang, & Song, 2010) in which the traditional approach to constrain temperature has been the problematic Fe-Mg exchange between garnet and omphacite (e.g. Krogh Ravna & Terry, 2004). Measurements were performed in matrix rutile grains (>100 μm) lacking reaction microstructures and displaying variable morphologies, including irregular, polygonal and needle-shaped grains, as well as twinned bicrystals. Rutile was also analysed for Si

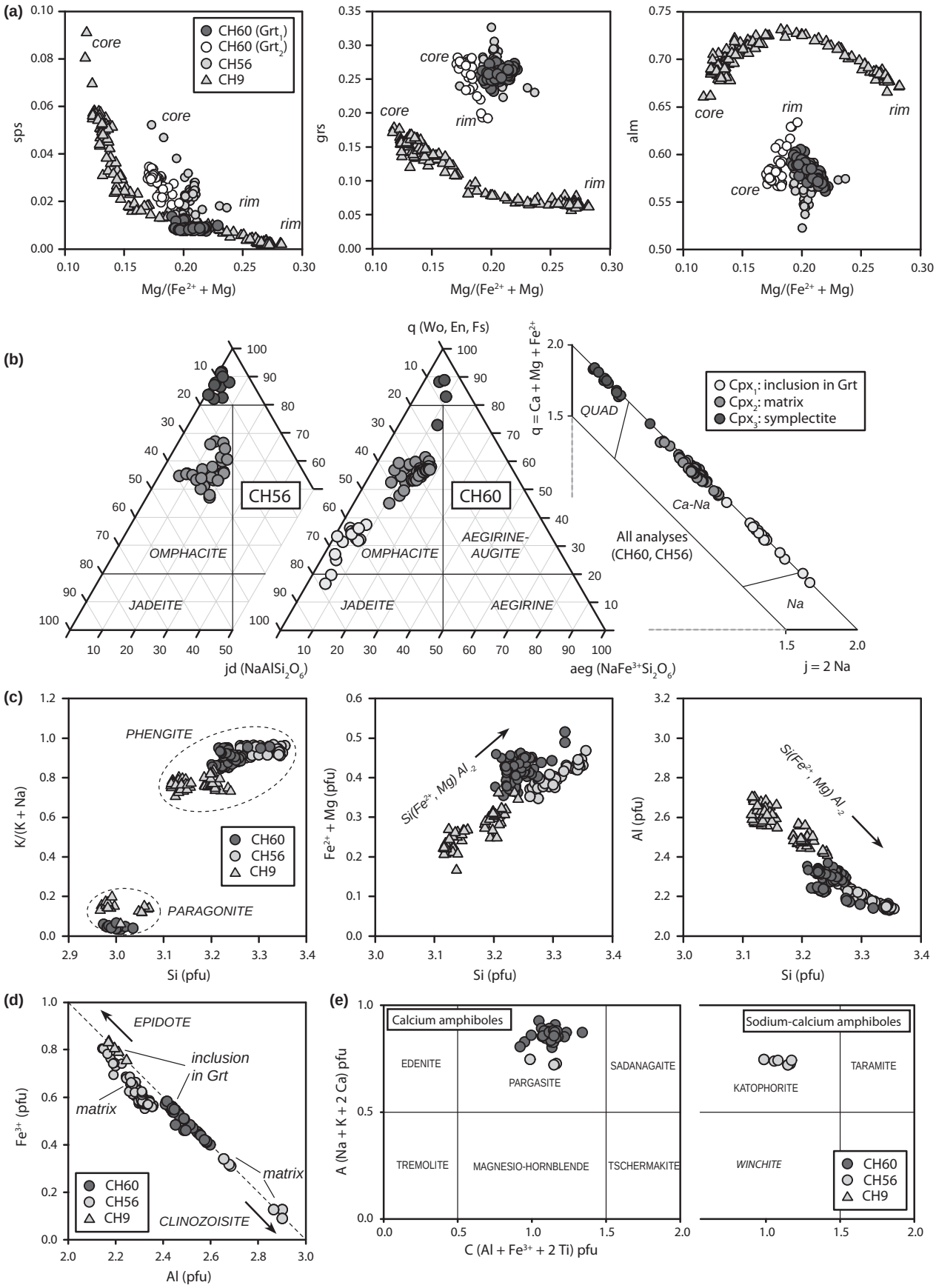

FIGURE 6 Mineral composition of (a) garnet, (b) pyroxene according to Morimoto (1988), (c) white mica, (d) epidote–clinozoisite and (e) amphibole according to Hawthorne et al. (2012). CH60: kyanite-bearing eclogite, CH56: eclogite, and CH9: garnet–kyanite pelitic schist

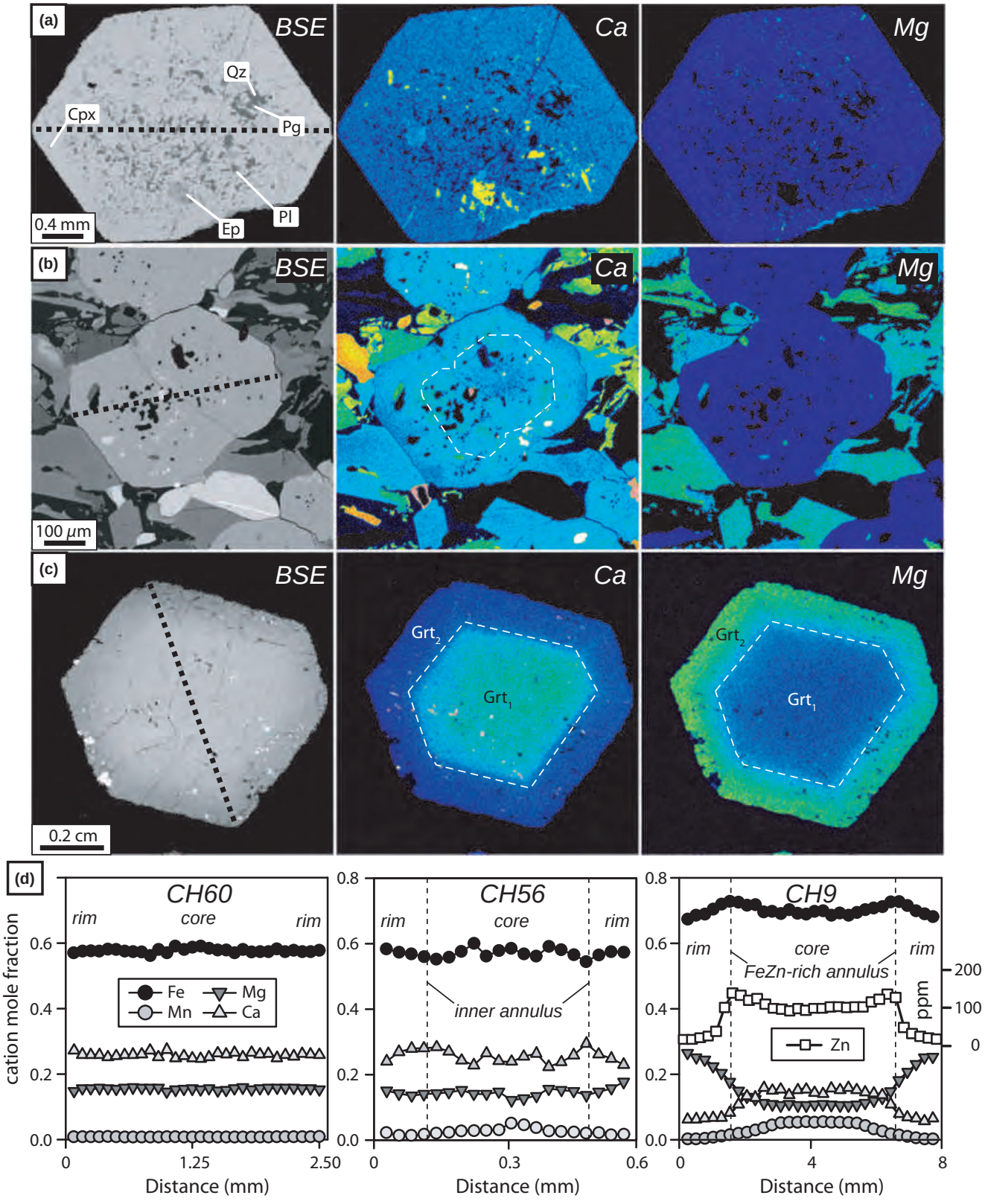

FIGURE 7 (a–c) BSE images and X-ray compositional maps of garnet from samples CH60 (Grt_1; a), CH56 (b) and CH9 (c). (d) Rim-to-rim zoning profiles of major elements in garnet; a Zn concentration (ppm) profile in sample CH9 is also included. Dotted black lines in the BSE images indicate the location of measured zoning profiles shown in (d). Dashed white lines in (b) and (c) refer to labels in (d)

and Nb to account the possible interference of zircon micro-inclusions. Zr concentrations among all analysed rutile grains range between 125–232 (sample CH60), 118–203 (sample CH56) and 215–295 (sample CH9) ppm. Since the Tomkins et al. (2007) thermometer includes a pressure dependence for the substitution of Zr in rutile coexisting with quartz and zircon, a pressure value of 20 kbar was used (Maldonado et al., 2016), resulting in average temperatures ($\pm\sigma$) of 657 ± 13 (n = 12), 647 ± 13 (n = 12) and 681 ± 8°C (n = 12), respectively (Figure 8). Such temperatures are ~20°C higher if a pressure of 24 kbar is assumed (e.g. Martens et al., 2012). Considering that rutile may not have been always equilibrated with quartz or zircon during growth, some temperatures may be either too high or too low. Following the suggestion of Tomkins et al. (2007), the upper ends of the boxes in Figure 8 represent a conservative estimation of peak temperatures.

5.2 | Phase equilibria modelling

5.2.1 | Calculation method

The studied samples preserve both microstructural and mineralogical features that reveal a HP metamorphic evolution. Thus, we used a thermodynamic modelling approach to investigate prograde mineral growth and provide an estimate of peak metamorphic conditions. Equilibrium phase diagrams were constructed over a range of pressure, temperature, bulk-rock ferric iron and bulk-rock H_2O conditions with the Gibbs free-energy minimization software Theriak-Domino (de Capitani & Brown, 1987; de Capitani & Petrakakis, 2010), implementing the Holland and Powell (1998) thermodynamic database (updated to database 5.5 in 2003, and translated readable for Theriak-Domino by D. K. Tinkham). For eclogite samples (CH60 and CH56), the calculations were performed in the NCKFMASHTO system using the following a–x models: garnet and biotite (White, Powell, & Holland, 2007), amphibole and clinopyroxene (Diener & Powell, 2012), white mica (Coggon & Holland, 2002), epidote and chlorite (Holland & Powell, 1998), ilmenite-hematite (White, Powell, Holland, & Worley, 2000), plagioclase-K-feldspar (Holland & Powell, 2003) and spinel-magnetite (White, Powell, & Clarke, 2002). For the Grt-Ky metapelite sample (CH9), Mn was additionally considered in the system, and the following a-x models were used: garnet and biotite (White, Pomroy, & Powell, 2005), white mica (Coggon & Holland, 2002), chloritoid (Mahar, Baker, Powell, Holland, & Howell, 1997; White et al., 2000), staurolite (Holland & Powell, 1998; Mahar et al., 1997), epidote, chlorite and talc (Holland & Powell, 1998), plagioclase (Holland & Powell, 2003) and spinel-magnetite (White et al., 2002). Ilmenite and carpholite were considered to be ideal solutions of Fe-Mg-Mn and Fe-Mg end-members, respectively. Albite, lawsonite, rutile, titanite, quartz, coesite, kyanite, zoisite and H_2O were considered as pure phases.

The effective bulk compositions were calculated by modification of the whole-rock X-ray fluorescence analyses (Table 2). All P_2O_5 was removed and the total CaO was proportionally adjusted to account for the chemical contribution of apatite. The values of $X_{Fe^{3+}} = Fe_2O_3/Fe_2O_3(t)$ were set on the basis of P–$X_{Fe^{3+}}$ space analysis (eclogite samples) and according to the value of the QFM buffer in

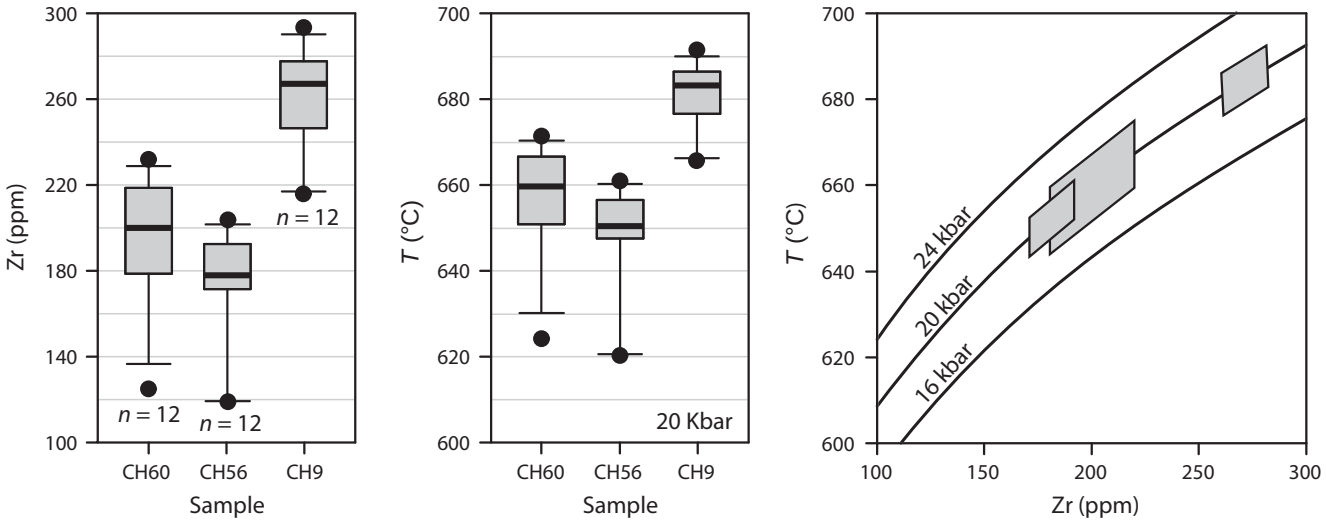

FIGURE 8 Box-plots of Zr content in rutile and temperatures from the Zr-in-rutile thermometer of Tomkins et al. (2007). The length of the box is given by the interquartile range of the data, the line across the box represents the median of the data, the whiskers extend to the furthest datapoint that is within 1.5 times the interquartile range from the box, and the dots are outliers

TABLE 2 Whole-rock compositions of the studied samples

Sample	SiO_2	TiO_2	Al_2O_3	Fe_2O_3 (*t*)	MnO	MgO	CaO	Na_2O	K_2O	P_2O_5	Total	Rock type
XRF analyses (wt%)												
CH60	45.99	2.78	15.88	17.00	0.26	5.20	8.75	3.44	0.19	0.13	99.62	Ky-bearing eclogite
CH56	45.93	3.52	14.20	16.39	0.25	5.76	9.21	2.78	0.81	0.55	99.40	Eclogite
CH9	51.68	1.34	25.62	9.89	0.18	1.97	0.96	1.12	4.53	0.18	97.45	Grt-Ky pelitic schist

Sample	SiO_2	TiO_2	Al_2O_3	Fe_2O_3	FeO	MnO	MgO	CaO	Na_2O	K_2O	H_2O	Total	$^aXFe_2O_3$	Figure
Effective bulk compositions used to construct the phase diagrams (wt%)														
CH60	47.16	2.85	16.29	1.39	14.45	–	5.33	8.80	3.53	0.19	Excess	100.00	0.08	9b,c
CH56	47.56	3.65	14.71	3.39	12.23	–	5.96	8.79	2.87	0.84	Excess	100.00	0.20	9e,f
CH9	53.79	1.39	26.67	0.21	9.09	0.18	2.05	0.75	1.16	4.71	Excess	100.00	0.02	9g,i

$^aXFe_2O_3 = Fe_2O_3/Fe(t)$; $Fe(t) = Fe_2O_3 + (FeO*1.11)$.

typical pelitic compositions (e.g. Diener & Powell, 2010, metapelite sample). Fluid phase was considered to be pure water and in excess. The effect of chemical fractionation due to mineral zonation does not affect significantly the results, so bulk composition fractionation calculations are not presented. Suprasolidus equilibria were not considered here, thus phase relations at the HT portion of the calculated phase diagrams may be metastable with respect to melt stability.

As the purpose of this approach is mainly to use phase diagrams as a framework to understand mineral growth trends, a complete assessment of the uncertainties involved in the calculations has not been applied. In addition to the uncertainties inherent to the thermodynamic data, other sources of uncertainty, such as errors related to the effective bulk-composition chosen, *a–x* models and micro-chemical data, are difficult to assess as a whole.

5.2.2 | Kyanite-bearing eclogite (CH60)

The metamorphic evolution of the CH60 eclogite was initially investigated using a $P–X_{Fe^{3+}}$ phase diagram constructed over a pressure range of 18–30 kbar at 660°C (Zr-in-rutile temperature; Figure 9a). This allows evaluation of the effect of varying the oxidation state on the predicted mineral assemblages along a pressure range that encompasses previous barometric calculations in the studied zone (e.g. Maldonado et al., 2016; Martens et al., 2012; Ortega-Gutiérrez et al., 2004; Ratschbacher et al., 2009). The observed matrix assemblage (bold text in Figure 9a) is predicted to be stable in a 6-variant field at relatively low $X_{Fe^{3+}}$ values (<0.12); at higher $X_{Fe^{3+}}$ values, kyanite is stable over the entire $P–X_{Fe^{3+}}$ interval. Garnet porphyroblasts (Grt_1) lack compositional zoning, but are rich in prograde mineral inclusions that are not preserved in the rock matrix (Figure 5a–d). The calculated isopleth of grs = 0.24 (calculated in terms of the alm, prp, grs and adr end-members), representing the average grossular content in garnet, is in the upper pressure part of the observed mineral assemblage field, close to the quartz/coesite boundary. Furthermore, the isopleth of Si = 3.32 (pfu), corresponding to the phengite with the highest celadonite content, is predicted to be close to the grs = 0.24 isopleth at $X_{Fe^{3+}}$~0.1 (dashed ellipse in Figure 9a).

A *P–T* phase diagram constructed at $X_{Fe^{3+}}$ = 0.08 and 550–750°C (Figure 9b) shows that the observed high-variance assemblage is stable over a relatively large field at >610°C, beyond the Ky-out and Pg-out lines. In this field, contours of Si in phengite are subhorizontal, increasing directly as pressure rises, which contrasts with their steep slope at lower temperature (Figure 9c). The phengite with Si = 3.32 (pfu) indicates minimal pressure conditions of ~24 kbar. However, grossular in garnet is slightly underestimated and the composition of garnet with grs = 0.24 is outside the field of interest. Grossular tends to decrease with increasing temperature until 600–620°C and then to increase again at higher *P–T* conditions (Figure 9c). Contours of grossular at >620°C (grs = 0.21–0.22) are widely spaced and are almost insensitive to pressure variations; hence, the model is not able to properly reproduce the subtle variations in the composition of garnet and these isopleths cannot be used to further constrain the peak metamorphic conditions. We, therefore, suggest that Si-isopleth barometry of phengite (≥24 kbar), combined with Zr-in-rutile thermometry (680°C) provide the best estimate of the peak HP metamorphic conditions (dashed ellipse in Figure 9c).

However, despite the impossibility of using garnet composition to constrain the *P–T* conditions, part of the prograde mineral evolution can be traced qualitatively by analysing the mineral inclusions in garnet on the basis of the predicted mineral assemblages below 24 kbar (ellipse in Figure 9b). Epidote–clinozoisite (Ep_1), paragonite, kyanite and jadeite-rich clinopyroxene (jd > 0.45) are only preserved as inclusions in garnet. Eclogitic assemblages containing these phases are successfully predicted above

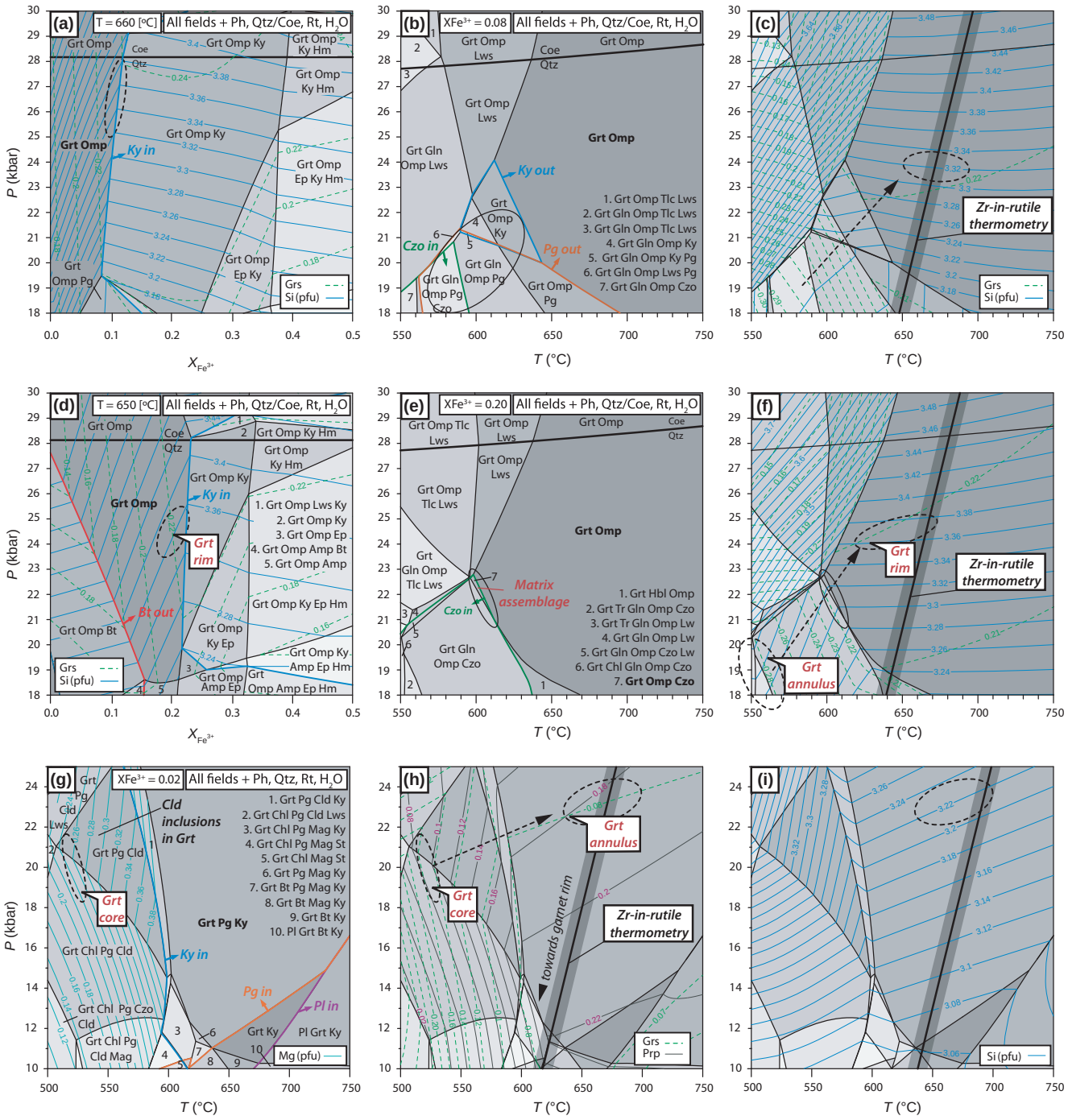

FIGURE 9 Equilibrium phase diagrams for the effective bulk compositions given in Table 2. Bold-labelled fields represent the observed peak assemblages. Dashed ellipses indicate areas of *P*–*T*–*X* equilibration constrained by comparing modelled with analysed assemblages and mineral compositions, but does not represent a formal assessment of uncertainty. Solid ellipses indicate probable prograde stages inferred on the basis of mineral inclusions, and dashed arrows denote the resulting prograde *P*–*T* paths. (a–c) Calculations for the kyanite-bearing eclogite (sample CH60), (d–f) calculations for the eclogite (sample CH56) and (g–i) calculations for the garnet–kyanite pelitic schist (sample CH9). Results of Zr-in-rutile thermometry are also presented

560°C (Figure 9b). This suggests that initial garnet crystallization probably occurred at <21 kbar and ~560°C. Moreover, the presence of jadeite sensu stricto together with albite, paragonite, quartz and kyanite, as well as the absence of glaucophane as inclusions in garnet, suggest that garnet may have initially grown within a chemically differentiated Al- and Na-rich medium (e.g. Endo & Tsuboi, 2013).

5.2.3 | Eclogite (CH56)

The CH56 eclogite was evaluated in the same way as sample CH60 by calculating a P–$X_{Fe^{3+}}$ phase diagram over a pressure range of 18–30 kbar at 650° (Figure 9d). Clinozoisite, present either as an inclusion in garnet or as a matrix phase (Figure 5e,f), is not predicted to be stable over the analysed interval. The observed peak assemblage (-Czo) corresponds to a relatively narrow field between the biotite-out and kyanite-in lines at $X_{Fe^{3+}}$ <0.23 (Figure 9d). Garnet zoning in sample CH56 is interpreted as a result of prograde growth; meanwhile phengite with the maximum celadonite is considered to be part of the peak HP assemblage. The composition of garnet with grs = 0.22 (garnet rim) and phengite with Si = 3.36 (maximum celadonite content) is best modelled at $X_{Fe^{3+}}$ = 0.20, indicating pressures of 24–25 kbar (dashed ellipse in Figure 9d).

A P–T phase diagram constructed over a range of 18–30 kbar and 550–750°C at $X_{Fe^{3+}}$ = 0.20 (Figure 9e) shows that the peak assemblage (-Czo) is stable over a relatively large field at >600°C, whereas this assemblage plus clinozoisite corresponds to a narrow field situated at ~22 kbar and ~600°C (ellipse in Figure 9e). The calculated garnet isopleths of grs = 0.28–0.29, corresponding to the measured composition of an inner annulus with the maximum grossular content (Figure 7b,d), suggest prograde garnet growth at 18–20 kbar and ~550°C (dashed ellipse in Figure 9f), within the stability field of garnet+glaucophane +omphacite+clinozoisite+phengite+quartz+rutile, consistent with the observed inclusions in garnet, except for glaucophane that has not been detected (Figure 5f). In addition, modelled garnet rim and phengite compositions are in agreement with the Zr-in rutile temperature, indicating peak HP conditions of 24–25 kbar and 620–670°C just above the clinozoisite stability field (dashed ellipse in Figure 9f).

5.2.4 | Garnet–kyanite pelitic schist (CH9)

The metamorphic evolution of the CH9 metapelite was evaluated using a series of P–T phase diagrams calculated over a range of 10–25 kbar and 500–750°C (Figure 9g–i). A value of $X_{Fe^{3+}}$ = 0.02 was chosen, similar to the value of the QFM buffer in typical pelitic compositions (e.g. Diener & Powell, 2010). Garnet, phengite and rutile are predicted to be stable over the whole P–T space; meanwhile, paragonite is predicted towards relative HP/LT conditions, kyanite above 560°C and chloritoid at a maximum temperature of 600°C (Figure 9g). In particular, the observed well-equilibrated peak assemblage corresponds to a 6-variant field between the kyanite-in and paragonite-in lines (Figure 9g).

The calculated garnet isopleths of grs = 0.15–0.16 and prp = 0.10–0.11, corresponding to the measured core composition, are subparallel and roughly join at ~19 kbar and ~530°C, inside the stability field of chloritoid and outside the stability field of kyanite (Figure 9h). Furthermore, the calculated chloritoid isopleths of X_{Mg} = 0.24–0.31 (Figure 9g), corresponding to the compositional range of chloritoid inclusions in garnet (Figure 5i), overlap the modelled garnet core composition. Therefore, we interpret that garnet may have initially grown within the stability field of garnet+chlorite+paragonite+chloritoid+phengite+quartz+rutile, and that temperature tentatively increased as garnet grew until reaching the stability field of kyanite. This interpretation is in agreement with the rise of pyrope towards the garnet rim and with the presence of kyanite as either an inclusion in garnet or peak-stage phase. The local occurrence of staurolite included in garnet (Figure 5h) could be related to a previous, partially preserved prograde stage.

Peak HP metamorphic conditions can be constrained considering the composition of the relatively FeZn-rich annulus in garnet (Figure 7d), characterized by grossular and pyrope contents of 0.8 and 0.18, respectively. The corresponding calculated isopleths intersect at ~23 kbar and ~640°C, within the stability field of garnet+paragonite+kyanite+phengite+quartz+rutile (Figure 9g,h), which is in agreement with the observed peak assemblage. Further constraints on the peak metamorphic conditions are provided by the composition of phengite with Si = 3.24, whose calculated isopleth largely coincides with the position of the garnet isopleths (Figure 9i). These considerations together with the obtained Zr-in-rutile temperature allow definition of a P–T range of 23–25 kbar and 640–690°C that we interpret as representing the peak HP metamorphic conditions attained by the CH9 metapelite (dashed ellipse in Figure 9h,i). Finally, taking into account the observed compositional change towards garnet rims (Figure 6a), together with the predicted trend for grossular and pyrope isopleths (Figure 9h), this unfractionated model shows that garnet rims (Grt_2) probably crystallized at intermediate P–T conditions. This is also supported by the abrupt decrease in Zn at the garnet rim (Figure 7d) that suggests final garnet growth coeval with staurolite crystallization. However, modelling this metamorphic stage would require a model that considers the effect of garnet fractionation on the effective bulk composition, which is beyond the scope of this study.

6 | GEOCHRONOLOGY AND TRACE ELEMENT DATA

The kyanite-bearing eclogite (CH60), eclogite (CH56) and garnet–kyanite pelitic schist (CH9) samples were used in order to investigate: (1) protolith ages and possible regional correlations and (2) the timing of HP metamorphism in the studied zone. These samples contain key minerals

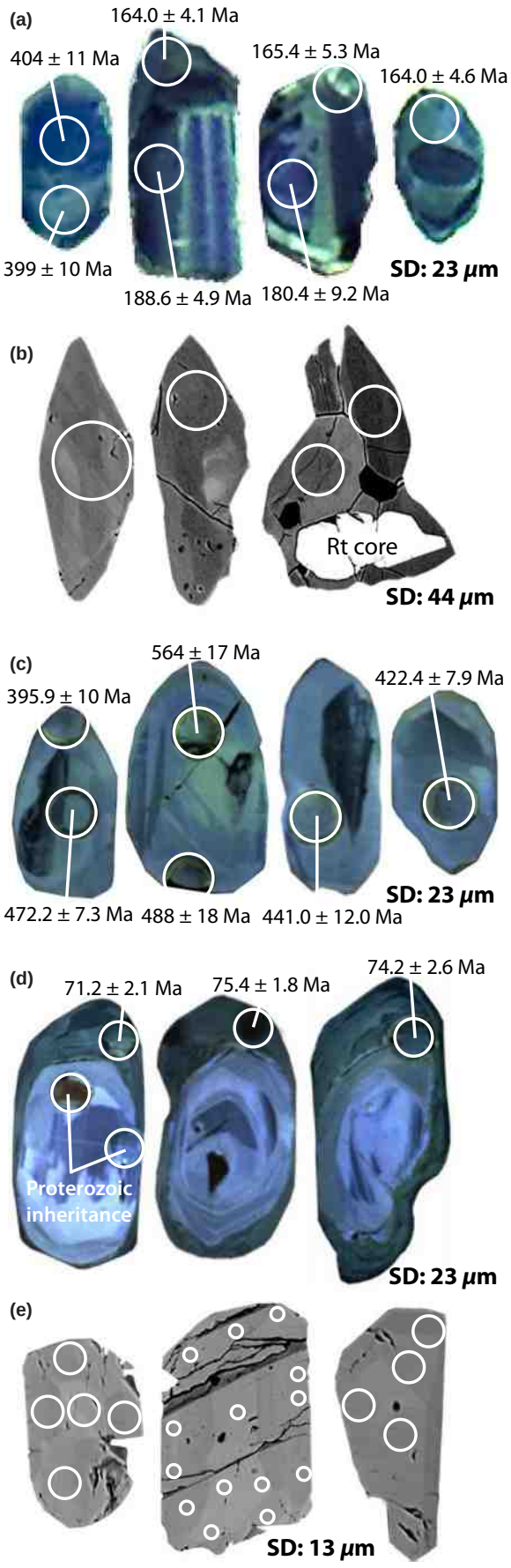

FIGURE 10 Representative CL/BSE images of minerals used for U-Pb dating. (a) Zircon and (b) titanite from sample CH60, (c) zircon from sample CH56, and (d) zircon and (e) monazite sample CH9. SD: spot diameter

suitable to apply the U-Pb and Lu-Hf isotopic systems. For this purpose, zircon from the three samples was used for U-Pb geochronology, whereas garnet from samples CH9 ($Grt_{1–2}$) and CH60 (Grt_1) together with whole-rock aliquots was used for Lu-Hf dating. See Appendix S1 for a detailed explanation of the criteria used for garnet separation. In addition, monazite from sample CH9 and titanite from sample CH60 were also employed for U-Pb geochronology. Trace element geochemistry of metamorphic zircon and garnet was also analysed to further correlate and constrain the time of their growth. Uranium-Pb and trace element data are available in Tables S1 and S2, respectively.

6.1 | U-Pb geochronology

Kyanite-bearing eclogite (CH60): this sample contains scarce prismatic to rounded zircon crystals. The CL images reveal inherited, corroded cores with variable zoning and some high-luminescent euhedral rims (Figure 10a). Five core analyses yielded concordant ages at *c*. 294 Ma (Th/U = 0.05) and *c*. 400 Ma (Th/U = 0.25–0.39; grey ellipses in Figure 11a). Nine rim analyses yielded concordant to slightly discordant results in the range of 184–164 Ma, which define a mean $^{206}Pb/^{238}U$ age of 167.1 ± 4.2 Ma (MSWD = 1.3; Th/U = 0.01–0.36; Figure 11b). Zircon rims with such a U-Pb mean age show positive Ce anomalies and no Eu anomalies (Figure 12a), as well as steep MREE-HREE profiles with $(Lu/Gd)_N$ ratios of 37–104, typical of magmatic crystallization. No younger ages were found in the analysed zircon grains. Figure 10b shows BSE images of representative titanite crystals from sample CH60 displaying complex zoning with apparent low-luminescence cores. Thirty-seven titanite analyses yielded discordant results that define in the Tera-Wasserburg diagram a relatively imprecise discordia line with a lower-intercept age of 80 ± 13 Ma (MSWD = 1.4; Figure 11g), which reflects the time of titanite crystallization.

Eclogite (CH56): this sample contains abundant prismatic to rounded zircon crystals that display inherited cores with oscillatory zoning and high-luminescent rims (Figure 10c). Thirty-six analyses from zircon cores yielded concordant ages in the 653–472 Ma interval (Th/U = 0.25–1.41; Figure 11c), which display REE patterns with pronounced positive Ce anomalies, subtle negative Eu anomalies, and steep MREE-HREE trends with high $(Lu/Gd)_N$ ratios of 19–73 (Figure 12b). The isotope data from 18 measurements on rims resulted in concordant ages between

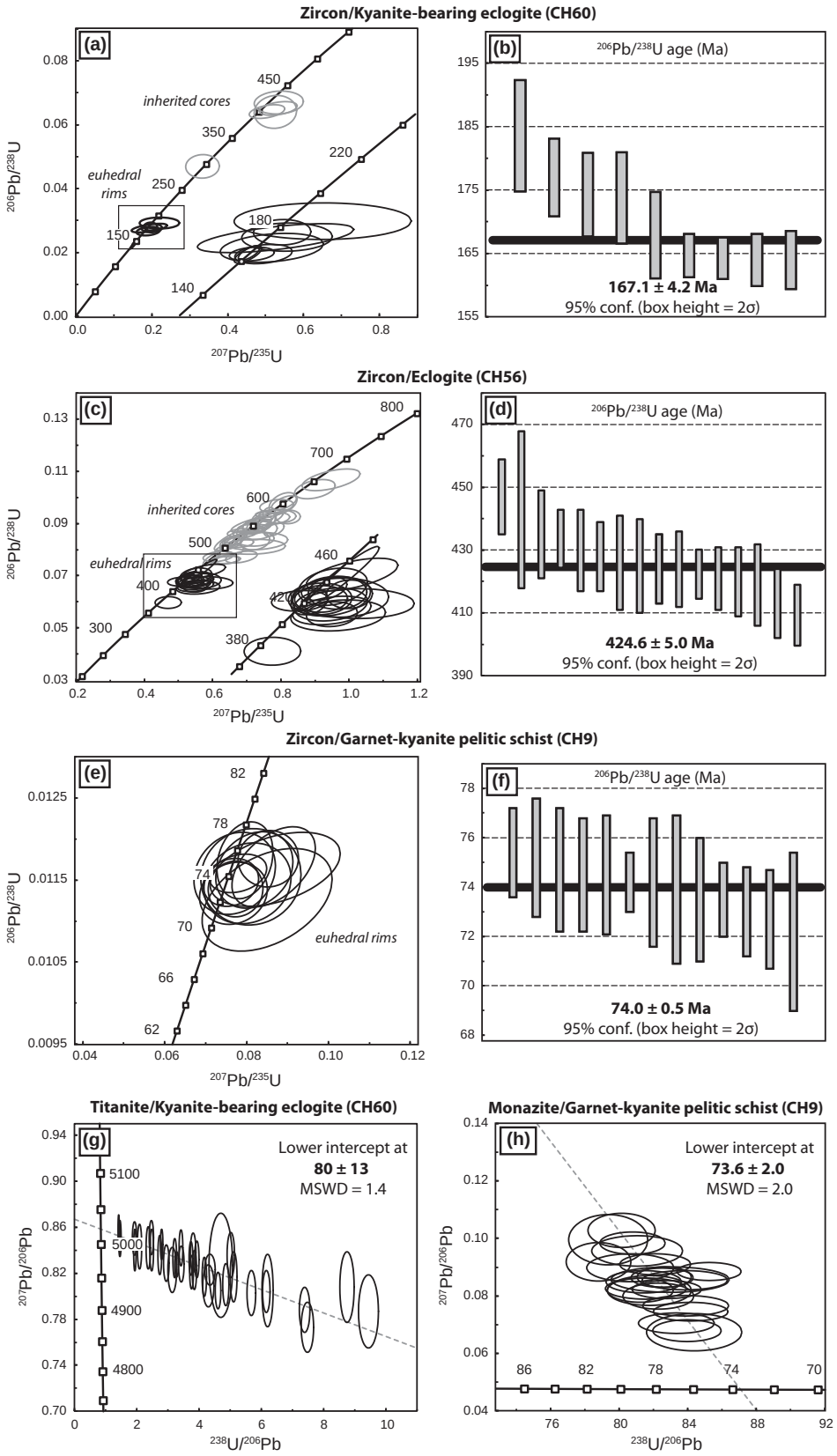

FIGURE 11 Concordia diagrams and $^{206}Pb/^{238}U$ mean ages. (a, b) Zircon data for the kyanite-bearing eclogite (sample CH60), (c, d) zircon data for the eclogite (sample CH56), (e, f) zircon data for the garnet–kyanite pelitic schist (sample CH9), (g) titanite data for the kyanite-bearing eclogite (sample CH60), and (h) monazite data for the garnet–kyanite pelitic schist (sample CH9). All uncertainties are shown at the 2σ level calculated with Isoplot 3.75 (Ludwig, 2012)

447 and 375 Ma (Th/U = 0.34–0.87), of which a cluster of 16 yielded a mean $^{206}Pb/^{238}U$ age of 424.6 ± 5.0 Ma (MSWD = 2.7; Th/U = 0.36–0.87; Figure 11c,d). Although this group displays variable Eu anomalies (mostly negative) and considerably lower REE contents in comparison with core compositions (Figure 12b), overall textural and chemical features suggest a magmatic origin for the zircon rims with *c*. 424 Ma U-Pb ages. The youngest point, with a $^{206}Pb/^{238}U$ age of 375.0 ± 11.0 Ma and a relatively high Th-U ratio (0.45), probably is related to an episode of Pb loss in response of later metamorphism. Some low-luminescent, probably metamorphic overgrowths, were not thick enough to be measured with the used 23 μm spot, and consequently, no younger metamorphic ages can be reported from this sample.

Garnet–kyanite pelitic schist (CH9): Figure 10d shows CL images of some typical zircon grains from the metapelite sample CH9 displaying high-luminescence inherited cores and darker overgrowths. The inherited cores yielded mostly Meso- to Neoproterozoic ages and will not be addressed in this work. A group of 13 concordant analyses of overgrowths (Figure 11e) yielded Th/U values below 0.01 (see below), and a mean $^{206}Pb/^{238}U$ age of 74.0 ± 0.5 Ma (MSWD = 0.75; Figure 11f). In these overgrowths, the MREE and HREE contents are about one order of magnitude lower compared to the inherited cores (Figure 12c). The corresponding chondrite-normalized REE patterns show positive Ce anomalies and slightly negative or no Eu anomalies, as well as steep MREE-HREE profiles with $(Lu/Gd)_N$ ratios of 14–22. Only one spot analysis displays a REE pattern with flat HREE profile ($(Lu/Gd)_N$ = 3). These overgrowths have extremely low Th/U values of 0.004–0.007, while their Ti contents (6–8 ppm) yield Ti-in-zircon temperatures (Ferry & Watson, 2007) between 694 and 721°C, with a mean of 711°C (*n* = 13). In addition, three monazite matrix grains displaying sector zoning were analysed (Figure 10e). Twenty-three analyses yielded discordant results, with a lower intercept of 73.6 ± 2.0 Ma (MSWD = 2.0; Figure 11h), which is equivalent to the U-Pb age of the zircon overgrowths.

6.2 | Lu-Hf geochronology

The Lu-Hf isotopic results are summarized in Table 3, and the calculated isochron diagrams are shown in Figure 13. Two entire-garnet fractions (Grt_1; 2–3 mm diameter) and one whole-rock aliquot were analysed from the kyanite-bearing eclogite sample (CH60). In the Lu-Hf isochron plot (Figure 13a), these data define a regression line whose slope corresponds to an age of 101.8 ± 3.1 Ma (2σ, MSWD = 2.2), which bears on the time interval of garnet growth under HP conditions.

TABLE 3 Lu-Hf data

Fraction	Lu (ppm)	Hf (ppm)	$^{176}Lu/^{177}Hf$	$^{176}Hf/^{177}Hf$	Err %[a]
CH9-WR	0.84	8.70	0.0138	0.282464	0.0011
CH9-Grt-1	3.26	0.75	0.6199	0.283541	0.0044
CH9-Grt-2	5.78	1.35	0.6106	0.283528	0.0011
CH9-Grt-3	2.92	0.69	0.6035	0.283531	0.0026
CH9-Grt-r	2.53	0.35	1.0309	0.284100	0.0063
CH60-WR	0.40	2.28	0.0250	0.282440	0.0011
CH60-Grt-1	1.21	0.20	0.8628	0.284096	0.0101
CH60-Grt-2	1.30	0.14	1.3243	0.284900	0.0162

[a]Errors include standard error on $^{176}H/^{177}Hf$ and error on blank correction (0.6 ± 0.4 ng Hf blank; propagated errors). Minimum error used for calculations is the typical external reproducibility of 0.003%; if propagated error is bigger, this is used for $^{176}Hf/^{177}Hf$ and 1% external reproducibility is used for $^{176}Lu/^{177}Hf$.

Four garnet fractions and one whole-rock aliquot were analysed from the metapelite sample CH9. Three single-garnet fractions (Grt_{1-2}; 8–10 mm diameter) together with the whole-rock aliquot yielded a Lu-Hf isochron age of 95.5 ± 2.1 Ma (2σ; MSWD = 0.30; Figure 13b), which refers to the entire-garnet growth period that involves both core growth under eclogite facies conditions and post-eclogitic rim crystallization. A significantly younger, two-point isochron age of 85.2 ± 2.7 Ma was obtained by pairing a garnet rim (Grt_2) fraction (see Appendix S1; Grt-r in Figure 13b) with the whole-rock aliquot. Since this garnet rim fraction corresponds to the relatively Ca-poor, post-eclogitic garnet (Figure 7c), this date is related to the time of garnet rim growth under MP conditions.

6.3 | Trace elements in garnet

Two garnet crystals from each sample were analysed. Bulk REE content in garnet (Grt_1) from sample CH60 is relatively low in comparison with garnet from sample CH9 (Figure 12a,c). Core analyses display chondrite-normalized REE patterns with slightly positive Eu anomalies and relatively low HREE contents, while rim measurements lack Eu anomalies and display a considerably enrichment in HREE. Despite the lack of major-element zoning in garnet from sample CH60, the REE+Y distribution displays strong zoning profiles (Figure 14a). Overall, Nd to Gd profiles are characterized by central peaks and concentrations increasing rimward, in contrast with Tb to Lu and Y profiles that display a progressive increase from core to rim, with some apparent near-to-rim annular maxima.

In garnet from sample CH9, the chondrite-normalized REE patterns (Figure 12c) show flat HREE profiles with almost imperceptible negative Eu anomalies in core analyses, which are further attenuated towards inner and rim

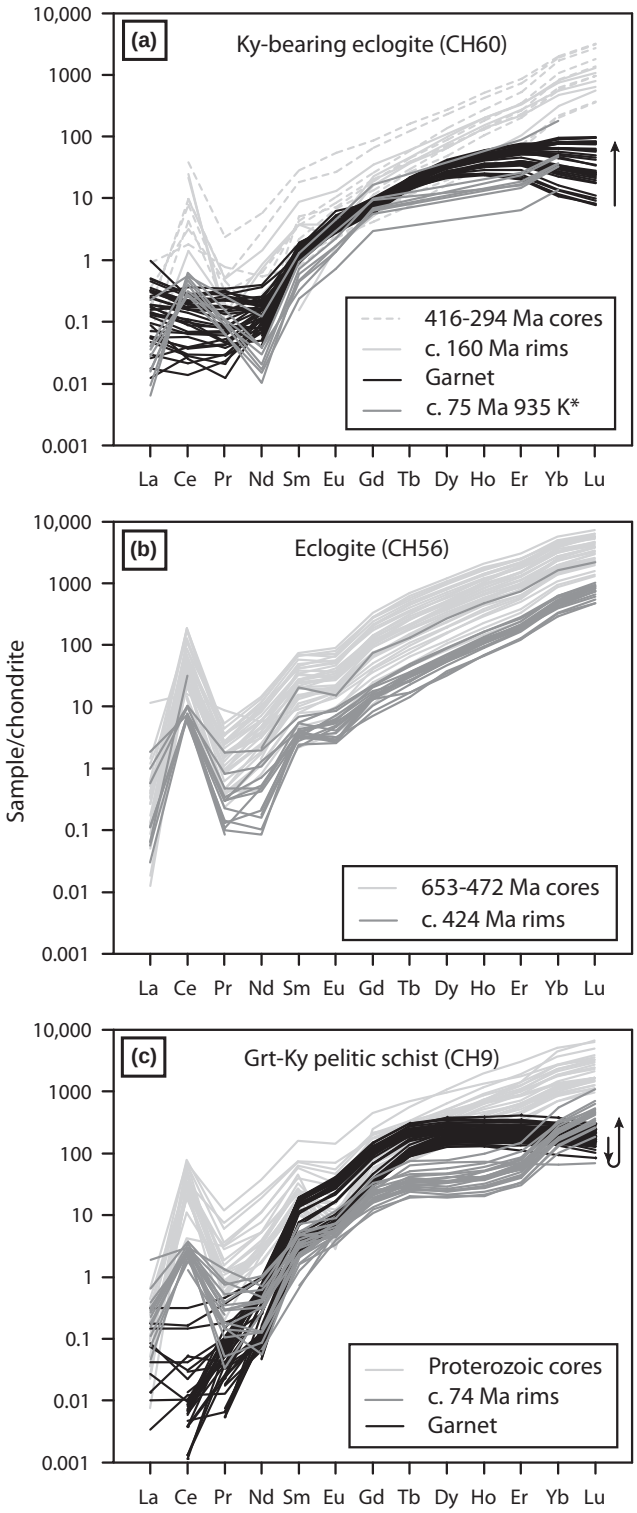

FIGURE 12 Chondrite-normalized REE patterns of zircon from samples CH60 (a), CH56 (b) and CH9 (c). Garnet REE patterns from samples CH60 (Grt_1) and CH9 are also included. Arrows in (a) and (c) denote the core-to-rim fractionation trend of HREE in garnet. Chondrite values are after McDonough and Sun (1995). *Zircon data from Martens et al. (2012)

zones. Analysed crystals, displaying major-element growth zoning, are also strongly zoned in REE+Y, with concentration profiles that vary with atomic number as well (Figure 14b). Zoning patterns of Nd to Tb show flat inner profiles, which correspond to the relatively Ca-rich garnet formed at HP conditions; meanwhile, an abrupt concentration increase with annular maxima is observed rimward. The profiles of Dy to Lu and Y display a bell-shaped distribution in the core (Grt_1), but lacking of the typical central peaks, which may have been missed if garnet was not sectioned precisely through its centre. A sharp increase in the concentration of these elements, together with low-intensity spikes, is observed rimward. Particularly, a drop in Lu concentration (lowest Lu values), located close to the rim, correspond to the annular maximum of Sm. The abrupt pattern change observed in all REE towards garnet rim (Grt_2) is clearly analogous to the major-element (+Zn) zoning, suggesting that REE distribution was, in part, controlled by changes in the garnet-forming reactions after HP peak.

7 | DISCUSSION AND CONCLUSIONS

7.1 | *P–T* evolution

The integration of field data, petrography, mineral chemistry and phase equilibria modelling allows reconstruction of a previously unknown segment of the prograde trajectory of eclogite and metapelite from the Chuacús complex, which underwent a common HP evolution. The earliest discernible stage of the prograde path is recorded, first, by garnet core compositions at ~18–20 kbar and 530–580°C, just beyond the stability field of lawsonite (Figure 9). In addition, the nature and composition of inclusions in garnet (Figure 5), including jadeite–kyanite–paragonite (eclogite) and chloritoid–paragonite–rutile (metapelite), further confirm the record of these early HP/LT metamorphic conditions. In particular, the presence of jadeite (jd = 0.75–0.78), kyanite and paragonite inclusions in the eclogite CH60 is diagnostic and constrains the initial garnet growth close to the reaction paragonite = jadeite+kyanite+H_2O (Holland, 1979) at <21 kbar and 600°C (Figure 9c). Comparable *P–T* conditions have been reported from several jadeite-bearing eclogite localities, such as the southern Motagua fault zone, Guatemala (Tsujimori et al., 2006), the Zermatt-Saas ophiolite, western Alps (Bucher & Grapes, 2009), the Monviso ophiolite, western Alps (Groppo & Castelli, 2010) and the Sanbagawa belt, Japan (Endo & Tsuboi, 2013). Minimum peak HP conditions of 23–25 kbar and 620–690°C determined here by combining mineral assemblages, isopleth thermobarometry and Zr-in-rutile thermometry are consistent among the studied samples, and in accordance with previous thermobarometric estimations (Maldonado et al., 2016; Martens et al., 2012; Ortega-Gutiérrez et al., 2004; Ratschbacher et al., 2009).

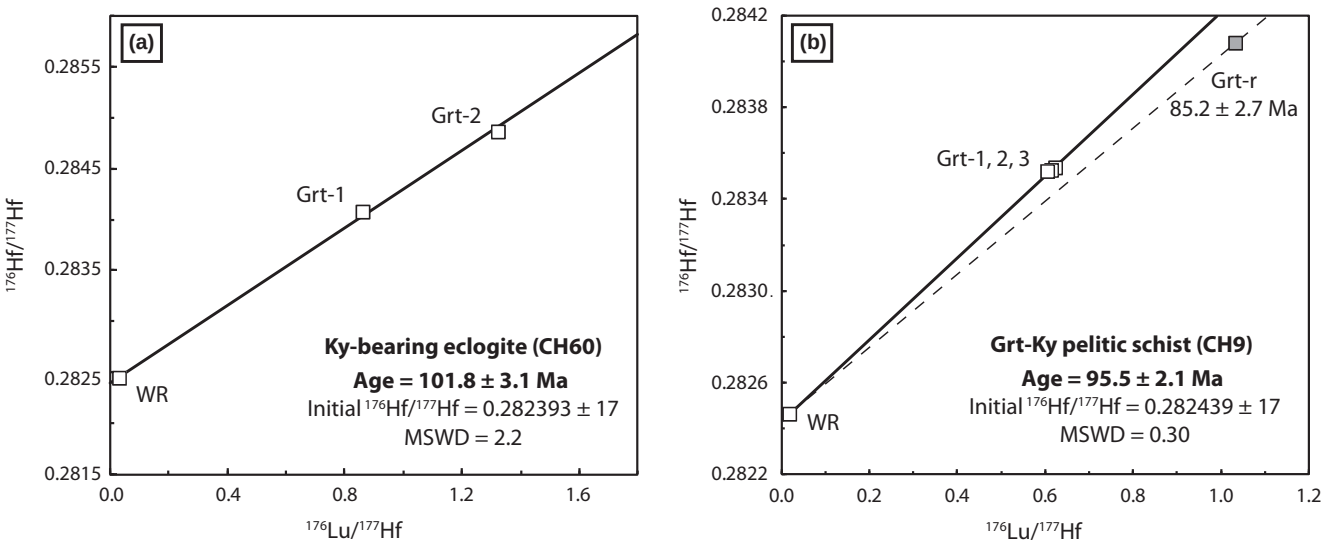

FIGURE 13 Lu-Hf isochron plots for the kyanite-bearing eclogite CH60 (a) and the garnet–kyanite pelitic schist CH9 (b). Error bars are smaller than squares

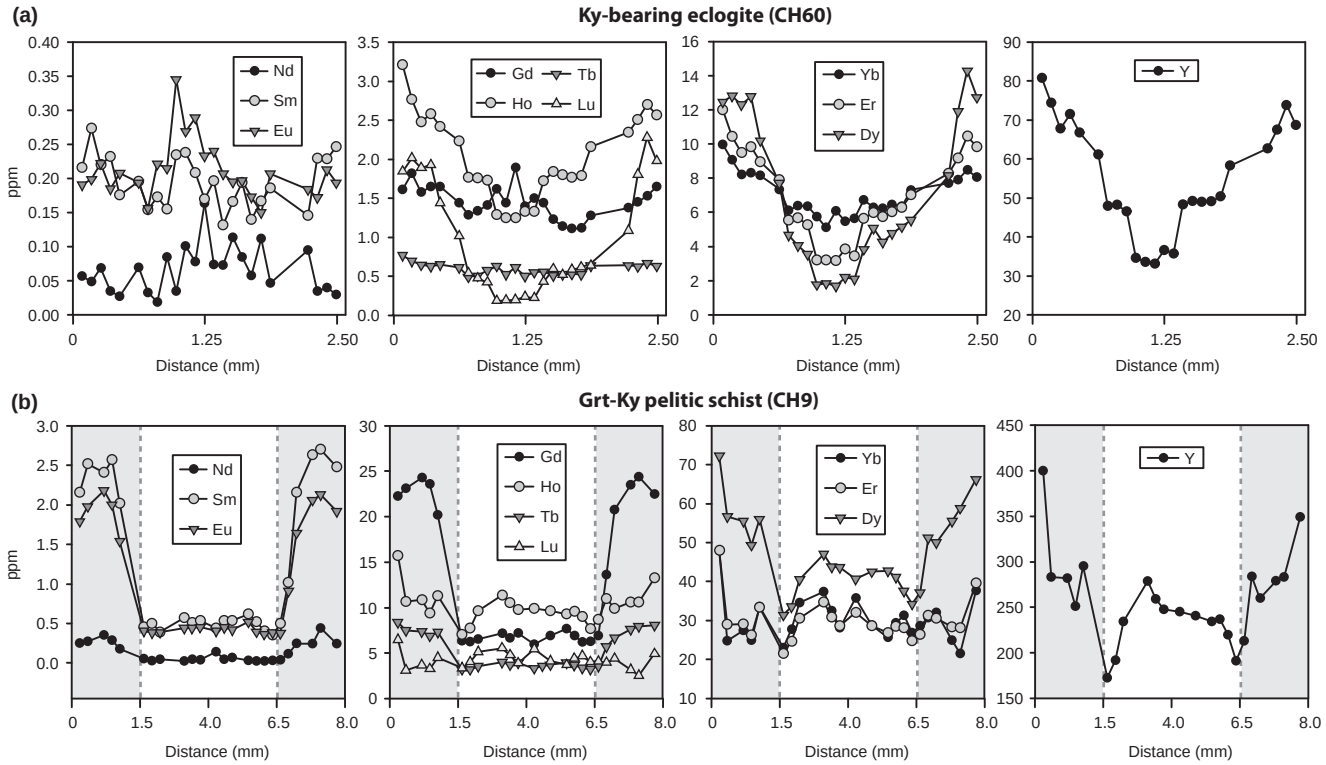

FIGURE 14 Trace-element zoning profiles in garnet from the kyanite-bearing eclogite CH60 (Grt_1; a) and the garnet–kyanite pelitic schist CH9 (b). Shaded grey bars in (b) indicate the post-eclogitic garnet rim (Grt_2), while the FeZn-rich annulus (Figure 7a) is marked by dashed line. Note the scale exaggeration for garnet rims in (b)

The post-eclogitic metamorphic evolution was not addressed in depth in this work, but a stage of isothermal decompression is revealed by post-peak formation of diopsidic clinopyroxene+plagioclase symplectites replacing omphacite, while an amphibolite facies overprint under fluid-present conditions is indicated by the successive crystallization of H_2O-bearing phases. All these petrographic features have been previously recognized in the Chuacús complex (e.g. Ortega-Gutiérrez et al., 2004) and explained in terms of immediate post-eclogitic retrogression (Martens et al., 2012). Nevertheless, occurrence of chemically distinct garnet regrowth (Grt_2) in the eclogite CH60

(Figures 4c and 6a) and fine-grained kyanite (Ky_2) in the metapelite CH9 (Figure 4h) strongly suggest that the Chuacús complex experienced a more complicated, previously unrecognized, post-eclogitic evolution. Since an increase in *P–T* would be expected to be necessary to promote nucleation and regrowth of both Grt_2 and Ky_2, we suggest that this process was the result of a new stage of prograde equilibration.

7.2 | Protolith ages of eclogite from the Chuacús complex

The protolith age of eclogite from the Chuacús complex has been poorly documented. Here, we present two contrasting U-Pb zircon protolith ages of *c*. 167 and 425 Ma for the eclogite samples CH60 and CH56, respectively (Figure 11a–d). These data together with previously reported U-Pb zircon ages of *c*. 226 Ma (Martens et al., 2012; Solari et al., 2011) indicate that mafic protoliths of eclogite originated in multiple tectonotemporal settings during the Silurian, Triassic and Jurassic. The *c*. 425 and 226 Ma ages are only comparable with the magmatic ages reported for granitic and gabbroic rocks from the Maya Block (North American plate; Schaaf et al., 2002; Weber, Cameron, Osorio, & Schaaf, 2005; Weber, Scherer, Martens, & Mezger, 2012), whereas the protolith age of *c*. 167 Ma is slightly younger than andesitic volcanic rocks in Chiapas but within the range of Nazas arc magmatism (Godínez-Urban et al., 2011), and older but similar to eclogite protolith and gabbro ages reported in the Greater Antilles (Escuder-Viruete, Friedman, Castillo-Carrión, Jabites, & Pérez-Estaún, 2011; Krebs et al., 2008; Rojas-Agramonte et al., 2012).

7.3 | Timing of HP subduction metamorphism

The U-Pb (zircon, monazite and titanite) and Lu-Hf (garnet/whole-rock) metamorphic ages were obtained for two contrasting rock types, the eclogite CH60 and the metapelite CH9. Concordant U-Pb zircon data from the metapelite CH9 yielded a mean age of 74.0 ± 0.5 Ma (Figure 11e,f), which is equivalent to the U-Pb monazite lower-intercept age of 73.6 ± 2.0 Ma (same sample), and comparable within errors with the U-Pb lower-intercept age of 80 ± 13 Ma obtained for post-eclogitic titanite from the eclogite CH60. In marked contrast to U-Pb ages, the Lu-Hf garnet/whole-rock analyses yielded considerably older ages of 101.8 ± 3.1 Ma and 95.5 ± 2.1 Ma for the eclogite and the metapelite, respectively (Figure 13).

Morphological/textural features, REE patterns and very low Th/U values (0.004–0.007) in zircon rims from sample CH9 are characteristic of metamorphic growth (e.g. Chen, Zheng, & Xie, 2010). However, the chondrite-normalized REE patterns do not show the typical flat MREE-HREE profiles (Figure 12c) commonly interpreted as indicative of zircon crystallization coeval with garnet growth (e.g. Harley, Kelly, & Möller, 2007; Rubatto & Hermann, 2003). Two interpretations potentially explain this feature: (1) zircon was formed by dissolution and recrystallization of inherited domains instead of metamorphic growth, so that metamorphic rims recycled/inherited the REE signatures of the cores; or (2) zircon and garnet are not contemporaneous; hence, zircon could have grown, in part, at the expense of HP phases (e.g. garnet, rutile). Interpretation (1) is likely not viable due to marked differences between core and rim REE patterns (Figure 12c), and thus interpretation (2) is favoured. In such a scenario, zircon growth could be promoted by the relatively HT transition from rutile to titanite (eclogite) and rutile to Fe-Ti oxides (metapelite) during the amphibolite facies overprint. Models of Zr mass balance in MORB and pelitic compositions along representative HP *P–T* paths (e.g. Alpine-type) indicate that assemblages containing garnet and rutile incorporate progressively more Zr during prograde evolution and initial exhumation, which consequently prevents zircon growth (Kohn, Corrie, & Markley, 2015). Thus, from a mass-balance perspective, zircon should preferentially grow during exhumation and cooling, as documented in a number of studies (e.g. Leech, Singh, & Jain, 2007; Sartini-Rideout, Gilotti, & McClelland, 2009). Moreover, very low Th/U (<0.02) zircon domains also may be associated with late-stage mineral-fluid interactions at temperatures below those of the metamorphic peak (e.g. Harley et al., 2007).

Garnet from sample CH9 displays major-element zoning profiles indicative of prograde growth, whereas garnet from sample CH60 is unzoned (Figure 7a,d). An original lack of major-element zoning is feasible not only by the fact that calculated temperatures (~660°C) seem to be not high enough for diffusional resetting, as reflected by zoning retention in garnet from sample CH9 that experienced analogous *P–T* metamorphic conditions, but also by the restricted garnet compositions predicted along the derived *P–T* path (Figure 9d). Therefore, as diffusion rates of REE+Y are slower than those of divalent cations in garnet (Bloch, Ganguly, Hervig, & Cheng, 2015; Carlson, 2012), the distribution of Lu in both garnet types is interpreted to reflect unmodified growth patterns established well below the estimated effective closure temperatures of the Lu-Hf system in garnet (e.g. Smit, Scherer, & Mezger, 2013).

Numerous studies have shown that Lu is primarily concentrated in garnet cores (e.g. Lapen et al., 2003; Skora et al., 2006; Smit et al., 2010); hence, as age information depends on the concentration of the parent element, Lu-Hf ages tend to be biassed towards the age of core growth. However, atypical Lu distribution in garnet from the

eclogite CH60, with Lu concentrated rimward (Figure 14a), suggests that the Lu-Hf age of *c*. 101 Ma is skewed towards the final stage of garnet growth (i.e. HP peak). Interpretation of the Lu-Hf age of *c*. 95 Ma, for the metapelite CH9, is not so straightforward due to three facts: (1) the bell-shaped distribution of HREE in the garnet core (HP Grt_1) suggests that a central peak of Lu may have been missed if garnet was not sectioned precisely through its centre, (2) an appreciable rise in Lu is observed on the edge of garnet (Figure 14b), and (3) the garnet rim (Grt_2; 40–45 vol.%) grew during a post-eclogitic, MP stage (see above). Therefore, this age must represent an average age of the timespan of garnet growth, including both HP and MP stages. The two-point isochron age of *c*. 85 Ma (Figure 13b), pairing whole rock with the garnet rim fraction, is interpreted as the age of post-eclogitic garnet growth at MP conditions, but the possibility of reflecting mixed ages cannot be ruled out because garnet rim separation did not follow strict micro-chemical criteria.

Previous geochronological works in the study area have been mainly focused on reconstructing the Late Cretaceous metamorphic evolution of the Chuacús complex. Most of the ages are in the range of 76–56 Ma, and correspond to the late-stage evolution below ~500°C (Martens et al., 2012; Ortega-Gutiérrez et al., 2004; Ortega-Obregón et al., 2008; Ratschbacher et al., 2009; Solari et al., 2011; Sutter, 1979). Metamorphic ages from HT geochronometers are scarce, most of them consisting of U-Pb zircon ages of *c*. 74 Ma that have been interpreted as the timing of an amphibolite facies overprint, coincident with widespread pegmatite emplacement (Martens et al., 2012; Ratschbacher et al., 2009; Solari et al., 2011). Our U-Pb zircon, monazite and titanite ages further corroborate these previous interpretations. Conversely, on the basis of zircon REE patterns lacking Eu anomalies and displaying depletion in HREE (Figure 12a), suggestive of zircon growth in a plagioclase-free, garnet-rich assemblage, a previous U-Pb zircon age of *c*. 75 Ma from an eclogite sample was interpreted as dating the eclogite facies metamorphic event (Martens et al., 2012). Several studies, however, have demonstrated that this criterion does not necessarily discriminate among a large range of *P–T* conditions (Kohn et al., 2015), as well as diverse zircon-forming processes (e.g. Chen et al., 2010). For instance, REE patterns of zircon core analyses from the above-referred sample also lack Eu anomalies (see figure 5a in Martens et al., 2012), and therefore, the absence of such anomalies in metamorphic rims could also be due to chemical recycling from older zircon. Furthermore, since the sample REE budget may remain sequestrated in eclogitic garnet even during subsequent *P–T* evolution and, besides, there is evidence for post-eclogitic garnet growth in similar eclogite (this work), the relative HREE depletion in zircon could also be explained in this way. Thus, this REE-based evidence is not ultimately conclusive. Martens et al. (2012) also presented a clinopyroxene/garnet/whole-rock Sm-Nd isochron age of 77 ± 13 Ma for an eclogite sample located close to our sample CH60, which was interpreted as the timing of eclogite facies metamorphism. Even within error, this age is considerably younger than the Lu-Hf ages presented here, and unfortunately, no petrographic or geochemical data (e.g. REE) are available for a complete evaluation of ages obtained from both isotopic systems. We presume that this Sm-Nd age could be influenced by the occurrence of late-stage garnet.

In summary, the integration of previous geochronological data together with those presented in this work leads us to suggest that continental subduction and HP metamorphism in the Chuacús complex were active during the Albian-Cenomanian, and an amphibolite facies overprint, likely at increasing *P–T*, took place during the Campanian.

7.4 | Tectonic implications and correlations in the Caribbean zone

Petrological and geochronological data obtained in this work suggest that the Chuacús complex experienced prograde, subduction-related metamorphism under a low thermal regime of ~9°C/km (Figure 15a) *c*. 25 Ma earlier than previously documented. Hence, previous tectonometamorphic models do not explicitly distinguish between subduction- and collision-related metamorphism during the Cretaceous evolution of the Chuacús complex. Here, we differentiate, on the basis of previous tectonic models (García-Casco, Iturralde-Vinent, & Pindell, 2008; Martens et al., 2012; Pindell & Kennan, 2009; Pindell et al., 2012; Ratschbacher et al., 2009), between: (1) an early pre-collisional prograde stage, dominated by subduction-related metamorphism of both oceanic and continental crust, and (2) a subsequent collisional stage marked by an amphibolite facies overprint and syncollisional exhumation (Figure 15b). This interpretation is in accordance with a number of thermomechanical models for continental subduction (e.g. Boutelier & Chemenda, 2011).

The pre-collisional stage initiated with the onset of southwest-dipping subduction of the Proto-Caribbean oceanic crust under the Greater Antilles Arc during the Early Cretaceous (*c*. 140 Ma; Pindell et al., 2012), which eventually led to the successive pre-Albian subduction of the thinned passive margin of the North American plate (e.g. Caribeana-type; García-Casco et al., 2008) and the consequent Albian-Cenomanian HP metamorphism of its continental basement (this work). The beginning of the arc-continent collisional stage occurred during the Campanian (Martens et al., 2012), and was, hypothetically, promoted by the arrival of thicker North American continental crust

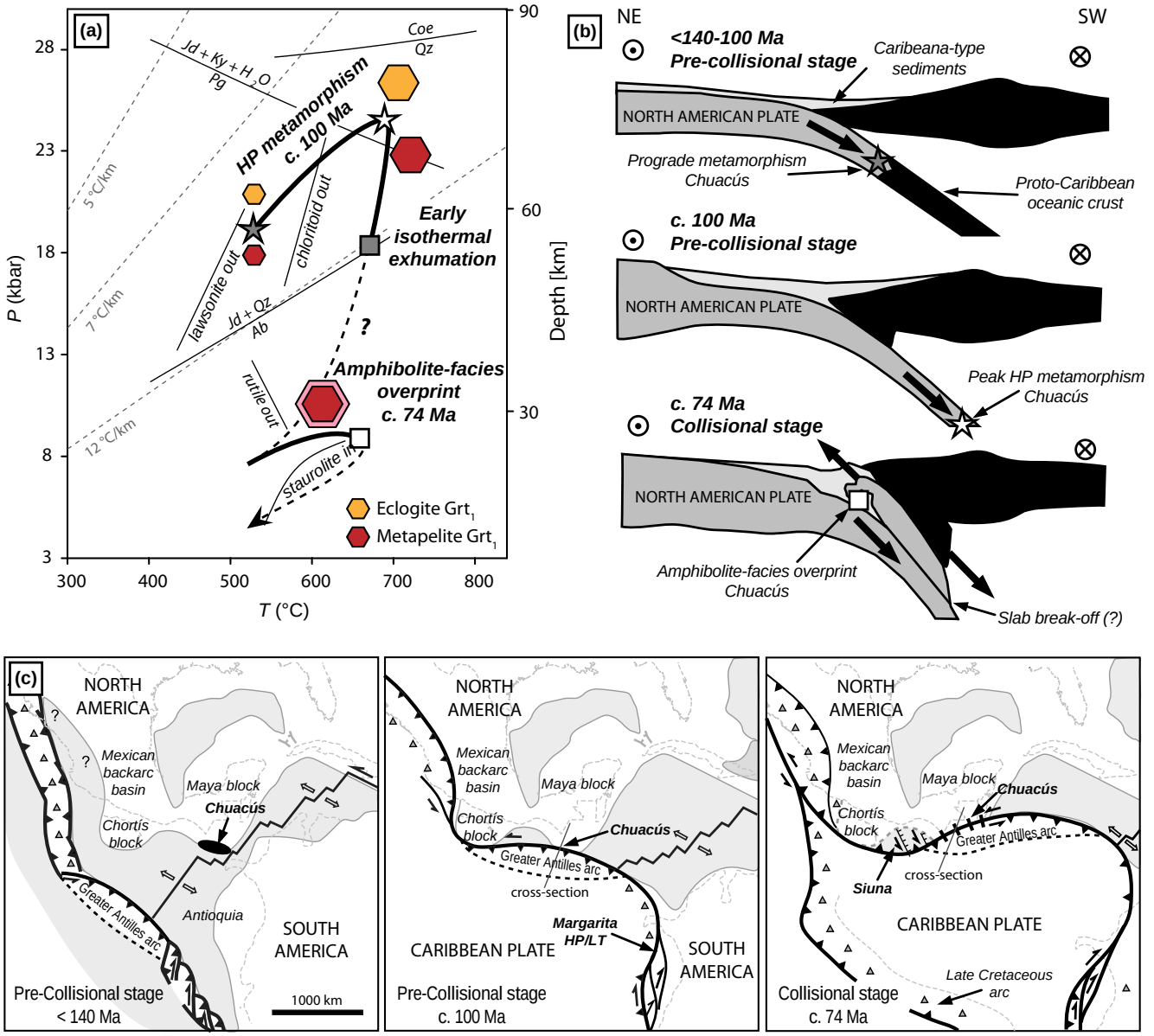

FIGURE 15 (a) Synthesis of the *P–T–t* constraints showing some relevant stability limits as reference. Dashed segments of the *P–T* path are inferred. (b) Schematic cross-section of the Cretaceous North American-Caribbean subduction zone showing the proposed evolution of the southern margin of the North American plate (Maya block). (c) Palaeogeographic reconstructions of the Caribbean region for early to latest-Cretaceous times (Pindell & Kennan, 2009; Pindell et al., 2012), showing the inferred position of the Chuacús complex during major tectonometamorphic stages

at the subduction zone and, perhaps, by slab break-off (e.g. Chemenda, Mattauer, & Bokun, 1996; Sizova, Gerya, & Brown, 2014). The cool subduction-related regime must have been replaced by higher thermal conditions (~20°C/km) coeval with partial exhumation, renewed tectonic burial with an amphibolite facies overprint, partial melting, pegmatite emplacement and shortening deformation, all of which marked the transition from a Pacific-type (accretionary) to an Alpine-type (collisional) subduction. Late syncollisional exhumation was characterized by sinistral-transpressive deformation resulting in N-S shortening by folding and reverse shear zones (e.g. Ratschbacher et al., 2009).

Several geochronological results throughout the Caribbean suture system indicate that pre-Campanian, particularly Albian-Cenomanian, HP metamorphism is not exclusive of the Chuacús complex. In fact, recent geochronological studies on HP rocks from other localities in Guatemala (Flores et al., 2013; Yui et al., 2012), Cuba (Blanco-Quintero et al., 2011; Cárdenas-Párraga et al., 2012; García-Casco et al., 2002; Lázaro et al., 2009), Dominican Republic (Escuder-Viruete et al., 2013; Krebs

et al., 2008; Schertl et al., 2012), and northern South America (Maresch et al., 2009; Weber et al., 2011) reported ages that span 118 to 80 Ma. Interesting, all the above-referred ages were obtained from HP rocks with oceanic-crust affinities (e.g. Pacific-type subduction), except for the Chuacús complex (this work) and Isla Margarita (Maresch et al., 2009) that involve continental basement. This could be explained by considering the inferred extreme palaeogeographic position of these zones with regard to the NE migration of the Greater Antilles Arc during the Cretaceous (Pindell et al., 2012; Figure 15c), which probably promoted an early subduction of the continental margins of the North American and the South American plates.

Finally, our data indicate that the exhumation of the Chuacús complex probably occurred under an initial relatively slow rate, which could have significantly accelerated from the Campanian, as a result of the local reduction of the interplate pressure promoted by the NE propagation of deformation (e.g. Escuder-Viruete et al., 2013). The time elapsed since the subduction-related metamorphism to the final stage of exhumation (*c*. 25 Ma) manifests a long-lasting tectonic process that occurred during the Cretaceous along the North American-Caribbean plate boundary.

ACKNOWLEDGEMENTS

This work was funded by the Mexican "Programa de Apoyo a Proyectos de Investigación e Innovación Tecnológica, DGAPA-UNAM" grant IN104914. M. C. Macías-Romo, C. Ortega-Obregón, S. Padilla-Ramírez and C. Linares-López are thanked for their technical support during the analytical procedures. We appreciate constructive reviews by K. E. Flores and an anonymous reviewer. D. L. Whitney is thanked for editorial handling and for several comments that also aided in the manuscript clarity.

REFERENCES

Anderson, T. H., Burkart, B., Clemons, R. E., Bohnenberger, O. H., & Blount, D. N. (1973). Geology of the western Altos Cuchumatanes, northwestern Guatemala. *Geological Society of America Bulletin*, *84*(3), 805–826.

Baldwin, S. L., Webb, L. E., & Monteleone, B. D. (2008). Late Miocene coesite-eclogite exhumed in the Woodlark Rift. *Geology*, *36* (9), 735–738.

Beane, R., & Leech, M. (2007). The Maksyutov Complex: The first UHP terrane 40 years later. *Geological Society of America Special Papers*, *419*, 153–169.

Beltrando, M., Compagnoni, R., & Lombardo, B. (2010). (Ultra-) High-pressure metamorphism and orogenesis: An Alpine perspective. *Gondwana Research*, *18*(1), 147–166.

Beyssac, O., Negro, F., Simoes, M., Chan, Y. C., & Chen, Y. G. (2008). High-pressure metamorphism in Taiwan: From oceanic subduction to arc-continent collision? *Terra Nova*, *20*(2), 118–125.

Blanco-Quintero, I. F., Rojas-Agramonte, Y., García-Casco, A., Kröner, A., Mertz, D. F., Lázaro, C., … Renne, P. R. (2011). Timing of subduction and exhumation in a subduction channel: Evidence from slab melts from La Corea Mélange (eastern Cuba). *Lithos*, *127*(1), 86–100.

Bloch, E., Ganguly, J., Hervig, R., & Cheng, W. (2015). ^{176}Lu–^{176}Hf geochronology of garnet I: Experimental determination of the diffusion kinetics of Lu^{3+} and Hf^{4+} in garnet, closure temperatures and geochronological implications. *Contributions to Mineralogy and Petrology*, *169*(2), 12.

Boutelier, D., & Chemenda, A. (2011). Physical modeling of arc–continent collision: A review of 2D, 3D, purely mechanical and thermo-mechanical experimental models. In D. Brown & P. D. Ryan (Eds.), *Arc-continent collision* (pp. 445–473). Berlin, Heidelberg: Springer.

Brown, D., Spadea, P., Puchkov, V., Alvarez-Marron, J., Herrington, R., Willner, A. P., … Juhlin, C. (2006). Arc–continent collision in the Southern Urals. *Earth-Science Reviews*, *79*(3), 261–287.

Brown, D., Wu, Y. M., Feng, K. F., Chao, W. A., & Huang, H. H. (2015). Imaging high-pressure rock exhumation in eastern Taiwan. *Geology*, *43*(7), 651–654.

Brueckner, H. K., Lallemant, H. G. A., Sisson, V. B., Harlow, G. E., Hemming, S. R., Martens, U., … Sorensen, S. S. (2009). Metamorphic reworking of a high pressure–low temperature mélange along the Motagua fault, Guatemala: A record of Neocomian and Maastrichtian transpressional tectonics. *Earth and Planetary Science Letters*, *284*(1), 228–235.

Bucher, K., & Grapes, R. (2009). The eclogite-facies Allalin Gabbro of the Zermatt-Saas ophiolite, Western Alps: A record of subduction zone hydration. *Journal of Petrology*, *50*(8), 1405–1442.

Cárdenas-Párraga, J., García-Casco, A., Harlow, G. E., Blanco-Quintero, I. F., Rojas Agramonte, Y., & Kröner, A. (2012). Hydrothermal origin and age of jadeitites from Sierra del Convento Mélange (Eastern Cuba). *European Journal of Mineralogy*, *24*(2), 313–331.

Carlson, W. D. (2012). Rates and mechanism of Y, REE, and Cr diffusion in garnet. *American Mineralogist*, *97*(10), 1598–1618.

Carswell, D. A., Wilson, R. N., & Zhai, M. G. (2000). Metamorphic evolution, mineral chemistry and thermobarometry of schists and orthogneisses hosting ultra-high pressure eclogites in the Dabieshan of central China. *Lithos*, *52*(1), 121–155.

Chemenda, A. I., Mattauer, M., & Bokun, A. N. (1996). Continental subduction and a mechanism for exhumation of high-pressure metamorphic rocks: New modelling and field data from Oman. *Earth and Planetary Science Letters*, *143*(1–4), 173–182.

Chen, R. X., Zheng, Y. F., & Xie, L. (2010). Metamorphic growth and recrystallization of zircon: Distinction by simultaneous in-situ analyses of trace elements, U-Th–Pb and Lu–Hf isotopes in zircons from eclogite-facies rocks in the Sulu orogen. *Lithos*, *114*(1), 132–154.

Chopin, C. (2003). Ultrahigh-pressure metamorphism: Tracing continental crust into the mantle. *Earth and Planetary Science Letters*, *212*(1), 1–14.

Coggon, R., & Holland, T. J. B. (2002). Mixing properties of phengitic micas and revised garnet-phengite thermobarometers. *Journal of Metamorphic Geology*, *20*(7), 683–696.

de Capitani, C., & Brown, T. H. (1987). The computation of chemical equilibrium in complex systems containing non-ideal solutions. *Geochimica et Cosmochimica Acta*, *51*(10), 2639–2652.

de Capitani, C. D., & Petrakakis, K. (2010). The computation of equilibrium assemblage diagrams with Theriak/Domino software. *American Mineralogist*, *95*(7), 1006–1016.

Diener, J. F. A., & Powell, R. (2010). Influence of ferric iron on the stability of mineral assemblages. *Journal of Metamorphic Geology*, *28*(6), 599–613.

Diener, J. F. A., & Powell, R. (2012). Revised activity–composition models for clinopyroxene and amphibole. *Journal of Metamorphic Geology*, *30*(2), 131–142.

Endo, S., & Tsuboi, M. (2013). Petrogenesis and implications of jadeite-bearing kyanite eclogite from the Sanbagawa belt (SW Japan). *Journal of Metamorphic Geology*, *31*(6), 647–661.

Endo, S., Wallis, S. R., Tsuboi, M., Torres de León, R., & Solari, L. A. (2012). Metamorphic evolution of lawsonite eclogites from the southern Motagua fault zone, Guatemala: Insights from phase equilibria and Raman spectroscopy. *Journal of Metamorphic Geology*, *30*(2), 143–164.

Ernst, W. G. (2005). Alpine and Pacific styles of Phanerozoic mountain building: Subduction-zone petrogenesis of continental crust. *Terra Nova*, *17*(2), 165–188.

Ernst, W. G., & Liou, J. G. (2008). High-and ultrahigh-pressure metamorphism: Past results and future prospects. *American Mineralogist*, *93*(11–12), 1771–1786.

Escuder-Viruete, J., Friedman, R., Castillo-Carrión, M., Jabites, J., & Pérez-Estaún, A. (2011). Origin and significance of the ophiolitic high-P mélanges in the northern Caribbean convergent margin: Insights from the geochemistry and large-scale structure of the Río San Juan metamorphic complex. *Lithos*, *127*(3), 483–504.

Escuder-Viruete, J., Valverde-Vaquero, P., Rojas-Agramonte, Y., Gabites, J., Castillo-Carrión, M., & Pérez-Estaún, A. (2013). Timing of deformational events in the Río San Juan complex: Implications for the tectonic controls on the exhumation of high-P rocks in the northern Caribbean subduction–accretionary prism. *Lithos*, *177*, 416–435.

Estrada-Carmona, J., Weber, B., Scherer, E. E., Martens, U., & Elías-Herrera, M. (2016). Lu-Hf geochronology of Mississippian high-pressure metamorphism in the Acatlán Complex, southern México. *Gondwana Research*, *34*, 174–186.

Ferry, J. M., & Watson, E. B. (2007). New thermodynamic models and revised calibrations for the Ti-in-zircon and Zr-in-rutile thermometers. *Contributions to Mineralogy and Petrology*, *154*(4), 429–437.

Flores, K. E., Martens, U. C., Harlow, G. E., Brueckner, H. K., & Pearson, N. J. (2013). Jadeitite formed during subduction: In situ zircon geochronology constraints from two different tectonic events within the Guatemala Suture Zone. *Earth and Planetary Science Letters*, *371*, 67–81.

Flores, K. E., Skora, S., Martin, C., Harlow, G. E., Rodríguez, D., & Baumgartner, P. O. (2015). Metamorphic history of riebeckite-and aegirine-augite-bearing high-pressure–low-temperature blocks within the Siuna Serpentinite Mélange, northeastern Nicaragua. *International Geology Review*, *57*(5–8), 943–977.

Fu, B., Valley, J. W., Kita, N. T., Spicuzza, M. J., Paton, C., Tsujimori, T., … Harlow, G. E. (2010). Multiple origins of zircons in jadeitite. *Contributions to Mineralogy and Petrology*, *159*(6), 769–780.

García-Casco, A., Iturralde-Vinent, M. A., & Pindell, J. (2008). Latest Cretaceous collision/accretion between the Caribbean Plate and Caribeana: Origin of metamorphic terranes in the Greater Antilles. *International Geology Review*, *50*(9), 781–809.

García-Casco, A., Torres-Roldán, R. L., Millán, G., Monié, P., & Schneider, J. (2002). Oscillatory zoning in eclogitic garnet and amphibole, Northern Serpentinite Melange, Cuba: A record of tectonic instability during subduction? *Journal of Metamorphic Geology*, *20*(6), 581–598.

Godínez-Urban, A., Lawton, T. F., Garza, R. S. M., Iriondo, A., Weber, B., & López-Martínez, M. (2011). Jurassic volcanic and sedimentary rocks of the La Silla and Todos Santos Formations, Chiapas: Record of Nazas arc magmatism and rift-basin formation prior to opening of the Gulf of Mexico. *Geosphere*, *7*(1), 121–144.

González-Guzmán, R., Weber, B., Tazzo-Rangel, M. D., & Solari, L. (2016). Validation of digestion and element separation methods and a new data reduction program (IsotopeHf®) for Lu-Hf isotope dilution analysis by MC-ICP-MS. *Revista Mexicana de Ciencias Geológicas*, *33*(2).

Groppo, C., & Castelli, D. (2010). Prograde *P–T* evolution of a lawsonite eclogite from the Monviso meta-ophiolite (Western Alps): Dehydration and redox reactions during subduction of oceanic FeTi-oxide gabbro. *Journal of Petrology*, *51*(12), 2489–2514.

Guillot, S., Hattori, K., Agard, P., Schwartz, S., & Vidal, O. (2009). Exhumation processes in oceanic and continental subduction contexts: A review. In S. Lallemand & F. Funiciello (Eds.), *Subduction zone geodynamics* (pp. 175–205). Berlin, Heidelberg: Springer.

Harley, S. L., Kelly, N. M., & Möller, A. (2007). Zircon behaviour and the thermal histories of mountain chains. *Elements*, *3*(1), 25–30.

Harlow, G. E., Hemming, S. R., Lallemant, H. G. A., Sisson, V. B., & Sorensen, S. S. (2004). Two high-pressure–low-temperature serpentinite-matrix mélange belts, Motagua fault zone, Guatemala: A record of Aptian and Maastrichtian collisions. *Geology*, *32*(1), 17–20.

Hawthorne, F. C., Oberti, R., Harlow, G. E., Maresch, W. V., Martin, R. F., Schumacher, J. C., … Welch, M. D. (2012). Nomenclature of the amphibole supergroup. *American Mineralogist*, *97*(11–12), 2031–2048.

Holland, T. J. B. (1979). High water activities in the generation of high pressure kyanite eclogites of the Tauern Window, Austria. *The Journal of Geology*, *87*(1), 1–27.

Holland, T. (2014). *AX: A program to calculate activities of mineral endmembers from chemical analyses (usually determined by electron microprobe)*. Retrieved from http://www.esc.cam.ac.uk/research/research-groups/research-projects/tim-hollands-software-pages/ax.

Holland, T. J. B., & Powell, R. (1998). An internally consistent thermodynamic data set for phases of petrological interest. *Journal of Metamorphic Geology*, *16*(3), 309–343.

Holland, T., & Powell, R. (2003). Activity–composition relations for phases in petrological calculations: An asymmetric multicomponent formulation. *Contributions to Mineralogy and Petrology*, *145*(4), 492–501.

Janák, M., Cornell, D., Froitzheim, N., De Hoog, J. C., Broska, I., Vrabec, M., … Hurai, V. (2009). Eclogite-hosting metapelites from the Pohorje Mountains (Eastern Alps): PT evolution, zircon geochronology and tectonic implications. *European Journal of Mineralogy*, *21*(6), 1191–1212.

Kadarusman, A., Maruyama, S., Kaneko, Y., Ota, T., Ishikawa, A., Sopaheluwakan, J., … Omori, S. (2010). World's youngest blueschist belt from Leti Island in the non-volcanic Banda outer arc of Eastern Indonesia. *Gondwana Research*, *18*(1), 189–204.

Kesler, S. E., Josey, W. L., & Collins, E. M. (1970). Basement rocks of western nuclear Central America: The western Chuacús Group, Guatemala. *Geological Society of America Bulletin*, *81*(11), 3307–3322.

Kohn, M. J., Corrie, S. L., & Markley, C. (2015). The fall and rise of metamorphic zircon. *American Mineralogist*, *100*(4), 897–908.

Krebs, M., Maresch, W. V., Schertl, H. P., Münker, C., Baumann, A., Draper, G., … Trapp, E. (2008). The dynamics of intra-oceanic subduction zones: A direct comparison between fossil petrological evidence (Rio San Juan Complex, Dominican Republic) and numerical simulation. *Lithos*, *103*(1), 106–137.

Krogh Ravna, E. J., & Terry, M. P. (2004). Geothermobarometry of UHP and HP eclogites and schists—An evaluation of equilibria among garnet–clinopyroxene–kyanite–phengite–coesite/quartz. *Journal of Metamorphic Geology*, *22*(6), 579–592.

Lapen, T. J., Johnson, C. M., Baumgartner, L. P., Mahlen, N. J., Beard, B. L., & Amato, J. M. (2003). Burial rates during prograde metamorphism of an ultra-high-pressure terrane: An example from Lago di Cignana, western Alps, Italy. *Earth and Planetary Science Letters*, *215*(1), 57–72.

Lázaro, C., García-Casco, A., Rojas Agramonte, Y., Kröner, A., Neubauer, F., & Iturralde-Vinent, M. (2009). Fifty-five-million-year history of oceanic subduction and exhumation at the northern edge of the Caribbean plate (Sierra del Convento mélange, Cuba). *Journal of Metamorphic Geology*, *27*(1), 19–40.

Leech, M. L., Singh, S., & Jain, A. K. (2007). Continuous metamorphic zircon growth and interpretation of U-Pb SHRIMP dating: An example from the Western Himalaya. *International Geology Review*, *49*(4), 313–328.

Li, J. L., Klemd, R., Gao, J., Jiang, T., & Song, Y. H. (2015). A common high-pressure metamorphic evolution of interlayered eclogites and metasediments from the 'ultrahigh-pressure unit' of the Tianshan metamorphic belt in China. *Lithos*, *226*, 169–182.

Liou, J. G., Tsujimori, T., Zhang, R. Y., Katayama, I., & Maruyama, S. (2004). Global UHP metamorphism and continental subduction/collision: The Himalayan model. *International Geology Review*, *46*(1), 1–27.

Ludwig, K. R. (2012). User's Manual for Isoplot 3.75, A Geochronological Toolkit for Microsoft Excel. Berkeley Geochronology Center Special Publication, *5*.

Mahar, E. M., Baker, J. M., Powell, R., Holland, T. J. B., & Howell, N. (1997). The effect of Mn on mineral stability in metapelites. *Journal of Metamorphic Geology*, *15*(2), 223–238.

Majka, J., Rosén, Å., Janák, M., Froitzheim, N., Klonowska, I., … Manecki, M., Yoshida, K. (2014). Microdiamond discovered in the Seve Nappe (Scandinavian Caledonides) and its exhumation by the "vacuum-cleaner" mechanism. *Geology*, *42*(12), 1107–1110.

Maldonado, R., Ortega-Gutiérrez, F., & Hernández-Uribe, D. (2016). Garnet–chloritoid–paragonite metapelite from the Chuacús Complex (Central Guatemala): New evidence for continental subduction in the North America-Caribbean plate boundary. *European Journal of Mineralogy*, *28*(6), 1169–1186.

Maresch, W. V., Kluge, R., Baumann, A., Pindell, J. L., Krückhans-Lueder, G., & Stanek, K. (2009). The occurrence and timing of high-pressure metamorphism on Margarita Island, Venezuela: A constraint on Caribbean-South America interaction. *Geological Society, London, Special Publications*, *328*(1), 705–741.

Martens, U. C., Brueckner, H. K., Mattinson, C. G., Liou, J. G., & Wooden, J. L. (2012). Timing of eclogite-facies metamorphism of the Chuacús complex, Central Guatemala: Record of Late Cretaceous continental subduction of North America's sialic basement. *Lithos*, *146*, 1–10.

Matte, P. (2006). The Southern Urals: Deep subduction, soft collision and weak erosion. *Geological Society, London, Memoirs*, *32*(1), 421–426.

McBirney, A. R. (1961). Geology of a part of the Central Guatemalan Cordillera. *California University Publications in Geological Sciences*, *38*, 177–242.

McDonough, W. F., & Sun, S. S. (1995). The composition of the Earth. *Chemical Geology*, *120*(3–4), 223–253.

Meyre, C., de Capitani, C., Zack, T., & Frey, M. (1999). Petrology of high-pressure metapelites from the Adula nappe (Central Alps, Switzerland). *Journal of Petrology*, *40*(1), 199–213.

Monteleone, B. D., Baldwin, S. L., Webb, L. E., Fitzgerald, P. G., Grove, M., & Schmitt, A. K. (2007). Late Miocene-Pliocene eclogite facies metamorphism, D'Entrecasteaux Islands, SE Papua New Guinea. *Journal of Metamorphic Geology*, *25*(2), 245–265.

Morán-Ical, S. D., Chiquín, L. G., & Requena, J. E. (2001). *Mapeo Geológico de superficie del cuadrángulo Granados, escala 1:50,000*. Unpublished report, Universidad de San Carlos de Guatemala, Centro Universitario del Norte.

Morimoto, N. (1988). Nomenclature of pyroxenes. *Mineralogy and Petrology*, *39*(1), 55–76.

Münker, C., Weyer, S., Scherer, E., & Mezger, K. (2001). Separation of high field strength elements (Nb, Ta, Zr, Hf) and Lu from rock samples for MC-ICPMS measurements. *Geochemistry, Geophysics, Geosystems*, *2*(12). https://doi.org/10.1029/2001gc000183

Neill, O. K., Mattinson, C. G., Donovan, J., Hernández-Uribe, D., & Sains, A. (2016). Increasing the efficiency of electron microprobe measurements of minor and trace elements in rutile. In *American Geophysical Union, Fall Meeting Abstracts*, V33D-3144.

Ortega-Gutiérrez, F., Solari, L. A., Solé, J., Martens, U., Gómez-Tuena, A., Morán-Ical, S., … Reyes-Salas, M. (2004). Polyphase, high-temperature eclogite-facies metamorphism in the Chuacús Complex, central Guatemala: Petrology, geochronology, and tectonic implications. *International Geology Review*, *46*(5), 445–470.

Ortega-Obregón, C., Solari, L. A., Keppie, J. D., Ortega-Gutiérrez, F., Solé, J., & Morán-Ical, S. (2008). Middle-Late Ordovician magmatism and Late Cretaceous collision in the southern Maya block, Rabinal-Salamá area, central Guatemala: Implications for North America-Caribbean plate tectonics. *Geological Society of America Bulletin*, *120*(5–6), 556–570.

Pindell, J. L. (1990). Geological evolution of the Caribbean region: A plate-tectonic perspective. *The Caribbean Region: Boulder, Colorado, Geological Society of America, the Geology of North America*, *H*, 339–374.

Pindell, J. L., & Kennan, L. (2009). Tectonic evolution of the Gulf of Mexico, Caribbean and northern South America in the mantle reference frame: An update. *Geological Society, London, Special Publications*, *328*(1), 1–55.

Pindell, J., Maresch, W. V., Martens, U., & Stanek, K. (2012). The Greater Antillean Arc: Early Cretaceous origin and proposed relationship to Central American subduction mélanges: Implications

for models of Caribbean evolution. *International Geology Review*, *54*(2), 131–143.

Ratschbacher, L., Franz, L., Min, M., Bachmann, R., Martens, U., Stanek, K., … López-Martínez, M. (2009). The North American-Caribbean plate boundary in Mexico-Guatemala-Honduras. *Geological Society, London, Special Publications*, *328*(1), 219–293.

Rojas-Agramonte, Y., García-Casco, A., Kröner, A., Herwartz, D., Ibis Despaigne, A., & Wilde, S. (2012). New geochronological ages (U-Pb/Lu-Hf) from high-pressure rocks of the Escambray terrane and Santa Clara serpentinite mélange, central Cuba. Regional correlations and geodynamic implications. *EGU General Assembly Conference Abstracts*, *14*, 14375.

Rubatto, D., & Hermann, J. (2003). Zircon formation during fluid circulation in eclogites (Monviso, Western Alps): Implications for Zr and Hf budget in subduction zones. *Geochimica et Cosmochimica Acta*, *67*(12), 2173–2187.

Sartini-Rideout, C., Gilotti, J. A., & McClelland, W. C. (2009). Reaction progress and timing of retrogression of eclogite-facies rocks, Danmarkshavn, North-East Greenland Caledonides. *European Journal of Mineralogy*, *21*(6), 1149–1172.

Schaaf, P., Weber, B., Weis, P., Gross, A., Ortega-Gutiérrez, F., & Kohler, H. (2002). The Chiapas Massif (Mexico) revised: New geologic and isotopic data and basement characteristics. *Neues Jahrbuch fur Geologie und Palaontologie-Abhandlungen*, *225*(1), 1–23.

Schertl, H. P., Maresch, W. V., Stanek, K. P., Hertwig, A., Krebs, M., Baese, R., … Sergeev, S. S. (2012). New occurrences of jadeitite, jadeite quartzite and jadeite-lawsonite quartzite in the Dominican Republic, Hispaniola: Petrological and geochronological overview. *European Journal of Mineralogy*, *24*(2), 199–216.

Sizova, E., Gerya, T., & Brown, M. (2014). Contrasting styles of Phanerozoic and Precambrian continental collision. *Gondwana Research*, *25*(2), 522–545.

Skora, S., Baumgartner, L. P., Mahlen, N. J., Johnson, C. M., Pilet, S., & Hellebrand, E. (2006). Diffusion-limited REE uptake by eclogite garnets and its consequences for Lu–Hf and Sm–Nd geochronology. *Contributions to Mineralogy and Petrology*, *152*(6), 703–720.

Smit, M. A., Scherer, E. E., Bröcker, M., & van Roermund, H. L. (2010). Timing of eclogite facies metamorphism in the southernmost Scandinavian Caledonides by Lu–Hf and Sm–Nd geochronology. *Contributions to Mineralogy and Petrology*, *159*(4), 521–539.

Smit, M. A., Scherer, E. E., & Mezger, K. (2013). Lu–Hf and Sm–Nd garnet geochronology: Chronometric closure and implications for dating petrological processes. *Earth and Planetary Science Letters*, *381*, 222–233.

Solari, L. A., García-Casco, A., Martens, U., Lee, J. K., & Ortega-Rivera, A. (2013). Late Cretaceous subduction of the continental basement of the Maya block (Rabinal Granite, central Guatemala): Tectonic implications for the geodynamic evolution of Central America. *Geological Society of America Bulletin*, *125*(3–4), 625–639.

Solari, L. A., Gómez-Tuena, A., Ortega-Gutiérrez, F., & Ortega-Obregón, C. (2011). The Chuacús Metamorphic Complex, central Guatemala: Geochronological and geochemical constraints on its Paleozoic-Mesozoic evolution. *Geologica Acta*, *9*(3–4), 329–350.

Song, S. G., Zhang, L. F., Niu, Y., Wei, C. J., Liou, J. G., & Shu, G. M. (2007). Eclogite and carpholite-bearing metasedimentary rocks in the North Qilian suture zone, NW China: Implications for Early Palaeozoic cold oceanic subduction and water transport into mantle. *Journal of Metamorphic Geology*, *25*(5), 547–563.

Sprung, P., Scherer, E. E., Upadhyay, D., Leya, I., & Mezger, K. (2010). Non-nucleosynthetic heterogeneity in non-radiogenic stable Hf isotopes: Implications for early solar system chronology. *Earth and Planetary Science Letters*, *295*(1), 1–11.

Sutter, J. F. (1979). Late Cretaceous collisional tectonics along the Motagua fault zone, Guatemala. *Geological Society of America, Abstracts with Programs*, *11*, 525–526.

Tomkins, H. S., Powell, R., & Ellis, D. J. (2007). The pressure dependence of the zirconium-in-rutile thermometer. *Journal of Metamorphic Geology*, *25*(6), 703–713.

Tsai, C. H., Iizuka, Y., & Ernst, W. G. (2013). Diverse mineral compositions, textures, and metamorphic *P–T* conditions of the glaucophane-bearing rocks in the Tamayen mélange, Yuli belt, eastern Taiwan. *Journal of Asian Earth Sciences*, *63*, 218–233.

Tsujimori, T., Liou, J. G., & Coleman, R. G. (2004). Comparison of two contrasting eclogites from the Motagua fault zone, Guatemala: Southern lawsonite eclogite versus northern zoisite eclogite. *Geological Society of America, Abstracts with Programs*, *36*(5), 136.

Tsujimori, T., Liou, J. G., & Coleman, R. G. (2005). Coexisting retrograde jadeite and omphacite in a jadeite-bearing lawsonite eclogite from the Motagua Fault Zone, Guatemala. *American Mineralogist*, *90*(5–6), 836–842.

Tsujimori, T., Sisson, V. B., Liou, J. G., Harlow, G. E., & Sorensen, S. S. (2006). Petrologic characterization of Guatemalan lawsonite eclogite: Eclogitization of subducted oceanic crust in a cold subduction zone. *Geological Society of America Special Papers*, *403*, 147–168.

van den Boom, G. (1972). Petrofazielle Gliederung des metamorphen Grungebirges in der Sierra de Chuacús, Guatemala. *Beihefte Geologisches Jahrbuch*, *122*, 5–49.

Watson, E. B., Wark, D. A., & Thomas, J. B. (2006). Crystallization thermometers for zircon and rutile. *Contributions to Mineralogy and Petrology*, *151*(4), 413.

Weber, B., Cameron, K. L., Osorio, M., & Schaaf, P. (2005). A Late Permian tectonothermal event in Grenville crust of the southern Maya terrane: U-Pb zircon ages from the Chiapas Massif, southeastern Mexico. *International Geology Review*, *47*(5), 509–529.

Weber, M., Cardona, A., Valencia, V., Altenberger, U., López-Martinez, M., Tobón, M., … Concha, A. E. (2011). Geochemistry and Geochronology of the Guajira Eclogites, northern Colombia: Evidence of a metamorphosed primitive Cretaceous Caribbean Island-arc. *Geologica Acta*, *9*(3–4), 425–443.

Weber, B., Scherer, E. E., Martens, U. K., & Mezger, K. (2012). Where did the lower Paleozoic rocks of Yucatan come from? AU–Pb, Lu–Hf, and Sm–Nd isotope study. *Chemical Geology*, *312*, 1–17.

White, R. W., Pomroy, N. E., & Powell, R. (2005). An in situ metatexite–diatexite transition in upper amphibolite facies rocks from Broken Hill, Australia. *Journal of Metamorphic Geology*, *23*(7), 579–602.

White, R. W., Powell, R., & Clarke, G. L. (2002). The interpretation of reaction textures in Fe-rich metapelitic granulites of the Musgrave Block, central Australia: Constraints from mineral equilibria calculations in the system K_2O-FeO-MgO-Al_2O_3-SiO_2-H_2O-TiO_2-Fe_2O_3. *Journal of Metamorphic Geology*, *20*(1), 41–55.

White, R. W., Powell, R., & Holland, T. J. B. (2007). Progress relating to calculation of partial melting equilibria for metapelites. *Journal of Metamorphic Geology*, *25*(5), 511–527.

White, R. W., Powell, R., Holland, T. J. B., & Worley, B. A. (2000). The effect of TiO_2 and Fe_2O_3 on metapelitic assemblages at greenschist and amphibolite facies conditions: Mineral equilibria calculations in the system K_2O-FeO-MgO-Al_2O_3-SiO_2-H_2O-TiO_2-Fe_2O_3. *Journal of Metamorphic Geology*, *18*(5), 497–512.

Whitney, D. L., & Evans, B. W. (2010). Abbreviations for names of rock-forming minerals. *American Mineralogist*, *95*(1), 185.

Yui, T. F., Maki, K., Usuki, T., Lan, C. Y., Martens, U., Wu, C. M., … Liou, J. G. (2010). Genesis of Guatemala jadeitite and related fluid characteristics: Insight from zircon. *Chemical Geology*, *270*(1), 45–55.

Yui, T. F., Maki, K., Wang, K. L., Lan, C. Y., Usuki, T., Iizuka, Y., … Liou, J. G. (2012). Hf isotope and REE compositions of zircon from jadeitite (Tone, Japan and north of the Motagua fault, Guatemala): Implications on jadeitite genesis and possible protoliths. *European Journal of Mineralogy*, *24*(2), 263–275.

Zack, T., Moraes, R., & Kronz, A. (2004). Temperature dependence of Zr in rutile: Empirical calibration of a rutile thermometer. *Contributions to Mineralogy and Petrology*, *148*(4), 471–488.

Zhang, G., Ellis, D. J., Christy, A. G., Zhang, L., & Song, S. (2010). Zr-in-rutile thermometry in HP/UHP eclogites from Western China. *Contributions to Mineralogy and Petrology*, *160*(3), 427–439.

Zhang, J., Meng, F., & Yang, J. (2004). Eclogitic metapelites in the western segment of the north Qaidam Mountains: Evidence on "in situ" relationship between eclogite and its country rock. *Science in China Series D: Earth Sciences*, *47*(12), 1102–1112.

Zheng, Y. F. (2012). Metamorphic chemical geodynamics in continental subduction zones. *Chemical Geology*, *328*, 5–48.

Zheng, Y., Ye, K., & Zhang, L. (2009). Developing the plate tectonics from oceanic subduction to continental collision. *Chinese Science Bulletin*, *54*(15), 2549–2555.

SUPPORTING INFORMATION

Additional Supporting Information may be found online in the supporting information tab for this article.

Appendix S1. Detailed description of analytical procedures.

Table S1. U-Pb isotopic data.

Table S2. Trace element data.

How to cite this article: Maldonado R, Weber B, Ortega-Gutiérrez F, Solari LA. High-pressure metamorphic evolution of eclogite and associated metapelite from the Chuacús complex (Guatemala Suture Zone): Constraints from phase equilibria modelling coupled with Lu-Hf and U-Pb geochronology. *J Metamorph Geol*. 2018;36:95–124. https://doi.org/10.1111/jmg.12285

Supporting information

APPENDIX S1. DETAILED DESCRIPTION OF ANALYTICAL PROCEDURES

Mineral chemistry

Major mineral compositions analyses with the CAMECA SX-100 electron microprobe at the CAMCOR facility, University of Oregon, were carried out employing an accelerating voltage of 15 kV, a beam current of 12 nA, and a beam diameter of 2 μm. Measurements of rutile compositions performed with the JEOL JXA-8500F field-emission electron microprobe at the GeoAnalytical Lab, Washington State University used an accelerating voltage of 15 kV, a beam current of 200 nA, and a beam diameter of 5 μm.

Mineral cations were calculated with the program AX (Holland, 2014), except for amphibole that was treated following the IMA 2012 recommendations (Hawthorne et al., 2012; Locock, 2014). Anhydrous mineral compositions were calculated to standard numbers of oxygen per formula unit (pfu); white mica analyses were calculated to a total of 11, staurolite to 23, chloritoid to 6, epidote to 12.5, and amphibole to 23 oxygens pfu.

U-Pb geochronology and trace element measurements

U-Pb and trace element data were acquired by laser ablation-inductively coupled plasma-mass spectrometry (LA-ICP-MS) using a Resonetics M-50 excimer laser ablation system coupled to a Thermo ICap Qc ICP-MS at the Laboratorio de Estudios Isotópicos (LEI), Centro de Geociencias, UNAM. Analyzed minerals were separated by routinely used techniques of crushing, sieving, magnetic and handpicking separation. All mineral separates, including garnet used for trace element measurements, were embedded in epoxy and then cut and polished down carefully to ensure the analysis of the central sections. Cathodoluminescence (zircon) and backscattered electron (monazite, titanite and garnet) images were used to select the best areas to be analyzed.

U-Pb zircon data was obtained employing a 23-μm analytical spot and an energy density of 6 J/cm^2. Zircon 91500 (Wiedenbeck et al., 1995) was used as the primary bracketing standard while Plešovice zircon (Sláma et al., 2008) was employed as a quality control reference. During the course of the analytical sessions, Plešovice yielded concordant results with a mean $^{206}Pb/^{238}U$ age of 338.9 ± 2.2 Ma (n=17, MSWD= 1.8), in agreement with its accepted age.

Titanite and monazite were analyzed using 44 and 13 μm spot sizes, respectively. The used primary standards were BLR for titanite (Aleinikoff et al., 2007) and 44069 for monazite (Aleinikoff et al., 2006). As secondary reference materials we employed homogeneous titanite and

monazite samples used internally at the LEI. Titanite is a large crystal dated by TIMS at 968 ± 9 Ma (Keppie et al., 2004), whereas monazite secondary standard belongs to the Acatlán Complex of southern Mexico and was previously dated at 442 ± 3.5 Ma (unpublished LA-ICP-MS data). The analyses performed in the course of the analytical sessions yielded 964 ± 8 and 435 ± 4.7 Ma, respectively, thus within error of the previously obtained values.

U-Pb isotopic data and error propagation were reduced offline using Iolite (Paton et al., 2011) and employing the VizualAge data reduction scheme of Petrus and Kamber (2012). Isoplot 3.75 (Ludwig, 2012) was used to calculate the mean ages, as well as to plot concordia diagrams. ^{204}Pb was not measured, because it is highly imprecise in a quadrupole-based mass spectrometer, and its signal is also swamped by the ^{204}Hg isobaric interference. For zircons, which normally do not incorporate common Pb at the moment of crystallization, no correction was employed, being the majority of the analyzed data concordant or nearly concordant. Titanite and monazite are instead discordant, probably due to the incorporation of common Pb at the moment of crystallization. In this case common Pb is evaluated, but not corrected, employing Tera-Wasserburg concordia diagrams.

Trace element concentrations in zircon were obtained employing the NIST 610 glass as a bracketing standard and using Si content as an internal standard. Trace element zoning profiles in garnet were measured employing a 60-μm spot. The NIST 612 glass was used as a reference material and Ca content as an internal standard. Element concentrations in both cases were calculated using reference values of Jochum et al. (2011). Interference resulting from micro-inclusions was monitored using several elements and the analyses were filtered to eliminate measurements that do not reflect pure compositions.

Lu-Hf geochronology

Sample processing for Lu-Hf geochronology were performed in PicoTrace clean lab facilities at Centro de Investigación Científica y de Educación Superior de Ensenada (CICESE), following procedures of Smit et al. (2010) and Estrada-Carmona et al. (2016), as well as methods modified from Münker et al. (2001) and Sprung et al. (2010) by González-Guzmán et al. (2016).

For mineral separation, samples were crushed and sieved in order to isolate as much as possible garnet crystals. To avoid mineral fractionation during separation, we did not use a magnetic separator to isolate garnet (e.g. Estrada-Carmona et al., 2016). Overall, the analyzed samples have unimodal grain-size distribution with relatively large euhedral garnet porphyroblasts (except for Grt_2 in sample CH60; see petrography for garnet denomination). Entire garnet crystals

(Grt_1 in the case of sample CH60) were separated by handpicking, crushed in an agate mortar and homogenized to prepare whole-garnet aliquots of ~100 mg. In addition, on the basis of a strong color/major-element zoning suggesting an abrupt change in the garnet rim-forming reaction, a garnet rim (Grt_2) fraction from the metapelite sample CH9 was separated from whole grains (Grt_{1-2}; 8-10 mm diameter) by combining micro sawing, crushing and handpicking. All garnet crystals used for Lu-Hf geochronology were analogous in size and morphology to the grains used for major and trace element measurements. Whole-rock aliquots were crushed and powdered in an agate mortar applying conventional processing techniques.

Garnet separates were cleaned in 3 M HCl at room temperature and then rinsed twice with deionized water. Garnet fractions, as well as whole-rock samples, were spiked with mixed ^{176}Lu-^{180}Hf isotope tracers (MS-Gt-1 for garnet and MS-WR-1 for whole-rock, respectively, both provided by the Institut für Mineralogie, Universität Münster, Germany) for isotope dilution determinations of ^{176}Lu/^{177}Hf. Garnet fractions were digested in Savillex screw-top PFA vials by sequential addition of concentrated HF-HNO_3-$HClO_4$ (4:2:1) and 6M HCl, both steps being followed by drying down on a hot plate. This digestion cycle was repeated until the addition of the HCl provided a clear solution, indicating that full digestion of the target phase was achieved. This method dissolves the target phases while leaving behind the more robust phases (e.g. zircon and rutile) that potentially harbor inherited Hf isotope signatures. Whole-rock aliquots were digested in PicoTrace DAS by addition of a HF-HNO_3-$HClO_4$ (4:2:1) mixture for one week at 210 ºC. Lu and Hf were separated from the matrix elements by two cation-exchange resin methods following a three-stage extraction scheme as described by González-Guzmán et al. (2016).

The determination of Lu and Hf isotope ratios was carried out on a Thermo Neptune Plus MC-ICP-MS installed at the LEI, Centro de Geociencias, UNAM. All masses were measured on Faraday cups in static mode following the procedure described by González-Guzmán et al. (2016). The sample solutions were introduced to the plasma via an Aridus desolvating sample introduction system using an Ar carrier gas and a blended Ar + N_2 sweep gas. The Hf fraction was taken up with 1 mL of 0.56 M HNO3–0.24 M HF solution and the Lu fraction from 0.6 mL of 0.1 M HNO3 solution. Data reduction was performed offline using the program IsotopeHf (González-Guzmán et al., 2016), and regressions of isochrons and ages were calculated with Isoplot 3.75 (Ludwig, 2012) using the ^{176}Lu decay constant of 1.867 x 10^{-11} (Scherer et al., 2001; Söderlund et al., 2004). Mass bias for spiked Lu was corrected by adding Re to every sample and normalizing to external Lu + Re standard solutions with known isotopic composition (e.g. González-Guzmán et al., 2016). Instrumental mass bias for Hf cannot be corrected by normalizing to the natural ^{179}Hf/^{177}Hf of 0.7325 in spiked samples. With the IsotopeHf software an empirical method is applied, first

obtaining the spike contribution on $^{179}Hf/^{177}Hf$, then using the spike-corrected $^{179}Hf/^{177}Hf$ to calculate the mass bias factor (β_{Hf}), and finally correcting the effects of both spike and mass bias on the $^{176}Hf/^{177}Hf$ (González-Guzmán et al., 2016). Isotope ratios are reported relative to the JMC-475 standard, which yielded an average $^{176}Hf/^{177}Hf$ value of 0.282148 ± 0.000018 (2σ, n = 5) during a single analytical session. Lu blank for this work is negligible, while Hf blanks range from 0.2 to 1.0 ng. Therefore, the $^{176}Hf/^{177}Hf$ values were corrected for 0.6 ± 0.4 ng blank using a typical $^{176}Hf/^{177}Hf$ of 0.2825 and the corresponding error propagation was added to the errors. For isochron calculations typical external reproducibilities (1σ) of 1% for $^{176}Lu/^{177}Hf$ and 0.003% for $^{176}Hf/^{177}Hf$, respectively, or the propagated errors were used, whichever is larger.

References

Aleinikoff, J. N., Schenck, W. S., Plank, M. O., Srogi, L., Fanning, C. M., Kamo, S. L., ... Bosbyshell, H. (2006). Deciphering igneous and metamorphic events in high-grade rocks of the Wilmington Complex, Delaware: Morphology, cathodoluminescence and backscattered electron zoning, and SHRIMP U-Pb geochronology of zircon and monazite. *Geological Society of America Bulletin*, *118*(1-2), 39-64.

Aleinikoff, J. N., Wintsch, R. P., Tollo, R. P., Unruh, D. M., Fanning, C. M., & Schmitz, M. D. (2007). Ages and origins of rocks of the Killingworth dome, south-central Connecticut: Implications for the tectonic evolution of southern New England. *American Journal of Science*, *307*(1), 63-118.

Estrada-Carmona, J., Weber, B., Scherer, E. E., Martens, U., & Elías-Herrera, M. (2016). Lu-Hf geochronology of Mississippian high-pressure metamorphism in the Acatlán Complex, southern México. *Gondwana Research*, *34*, 174-186.

González-Guzmán, R., Weber, B., Tazzo-Rangel, M. D., & Solari, L. (2016). Validation of digestion and element separation methods and a new data reduction program (IsotopeHf®) for Lu-Hf isotope dilution analysis by MC-ICP-MS. *Revista Mexicana de Ciencias Geológicas*, *33*(2).

Hawthorne, F. C., Oberti, R., Harlow, G. E., Maresch, W. V., Martin, R. F., Schumacher, J. C., ... Welch, M. D. (2012). Nomenclature of the amphibole supergroup. *American Mineralogist*, *97*(11-12), 2031-2048.

Holland, T. (2014). AX: a program to calculate activities of mineral endmembers from chemical analyses (usually determined by electron microprobe). Available at: http://www.esc.cam.ac.uk/research/research-groups/research-projects/tim-hollands-software-pages/ax.

Jochum, K. P., Weis, U., Stoll, B., Kuzmin, D., Yang, Q., Raczek, I., ... Günther, D. (2011). Determination of reference values for NIST SRM 610–617 glasses following ISO guidelines. *Geostandards and Geoanalytical Research*, *35*(4), 397-429.

Keppie, J. D., Solari, L. A., Ortega-Gutiérrez, F., Ortega-Rivera, A., Lee, J. K., Lopez, R., ... Hames, W. E. (2004). U-Pb and $^{40}Ar/^{39}Ar$ constraints on the cooling history of the northern Oaxacan Complex, southern Mexico: Tectonic implications. *Geological Society of America Memoirs*, *197*, 771-781.

Locock, A. J. (2014). An Excel spreadsheet to classify chemical analyses of amphiboles following the IMA 2012 recommendations. *Computers & Geosciences*, *62*, 1-11.

Ludwig, K. R. (2012). User's Manual for Isoplot 3.75, A Geochronological Toolkit for Microsoft Excel. Berkeley Geochronology Center Special Publication, *5*.

Münker, C., Weyer, S., Scherer, E., & Mezger, K. (2001). Separation of high field strength elements (Nb, Ta, Zr, Hf) and Lu from rock samples for MC-ICPMS measurements. *Geochemistry, Geophysics, Geosystems*, *2*(12).

Paton, C., Hellstrom, J., Paul, B., Woodhead, J., & Hergt, J. (2011). Iolite: Freeware for the visualisation and processing of mass spectrometric data. *Journal of Analytical Atomic Spectrometry*, *26*(12), 2508-2518.

Petrus, J. A., & Kamber, B. S. (2012). VizualAge: A novel approach to laser ablation ICP-MS U-Pb geochronology data reduction. *Geostandards and Geoanalytical Research*, *36*(3), 247-270.

Scherer, E., Münker, C., & Mezger, K. (2001). Calibration of the lutetium-hafnium clock. *Science*, *293*(5530), 683-687.

Sláma, J., Košler, J., Condon, D. J., Crowley, J. L., Gerdes, A., Hanchar, J. M., ... Schaltegger, U. (2008). Plešovice zircon—a new natural reference material for U–Pb and Hf isotopic microanalysis. *Chemical Geology*, *249*(1), 1-35.

Smit, M. A., Scherer, E. E., Bröcker, M., & van Roermund, H. L. (2010). Timing of eclogite facies metamorphism in the southernmost Scandinavian Caledonides by Lu–Hf and Sm–Nd geochronology. *Contributions to Mineralogy and Petrology*, *159*(4), 521-539.

Söderlund, U., Patchett, P. J., Vervoort, J. D., & Isachsen, C. E. (2004). The 176 Lu decay constant determined by Lu–Hf and U–Pb isotope systematics of Precambrian mafic intrusions. *Earth and Planetary Science Letters*, *219*(3), 311-324.

Sprung, P., Scherer, E. E., Upadhyay, D., Leya, I., & Mezger, K. (2010). Non-nucleosynthetic heterogeneity in non-radiogenic stable Hf isotopes: Implications for early solar system chronology. *Earth and Planetary Science Letters*, *295*(1), 1-11.

Wiedenbeck, M. A. P. C., Alle, P., Corfu, F., Griffin, W. L., Meier, M., Oberli, F. V., ... Spiegel, W. (1995). Three natural zircon standards for U-Th-Pb, Lu-Hf, trace element and REE analyses. *Geostandards and Geoanalytical Research*, *19*(1), 1-23.

Table S1. U-Pb isotopic data

				Isotope ratios									Apparent ages (Ma)						
Point	**U (ppm)**	**Th (ppm)**	**Th/U**	**$^{207}Pb/^{206}Pb$**	**±2σ abs**	**$^{207}Pb/^{235}U$**	**±2σ abs**	**$^{206}Pb/^{238}U$**	**±2σ abs**	**$^{208}Pb/^{232}Th$**	**±2σ abs**	**Rho**	**$^{206}Pb/^{238}U$**	**±2σ**	**$^{207}Pb/^{235}U$**	**±2σ**	**$^{207}Pb/^{206}Pb$**	**±2σ**	**% Disc.**
Zircon / Grt-Ky pelitic schist (CH9)																			
CH9-Zrn-031	884.0	3.5	0.004	0.0525	0.0038	0.0853	0.0060	0.0118	0.0003	0.0284	0.0068	0.03	75.4	1.8	82.9	5.6	407.0	65.0	9.0
CH9-Zrn-55	778.0	4.2	0.005	0.0517	0.0043	0.0796	0.0056	0.0117	0.0004	0.0465	0.0082	0.22	75.2	2.4	77.7	5.3	530.0	140.0	3.2
CH9-Zrn-042	731.0	3.8	0.005	0.0515	0.0049	0.0866	0.0083	0.0117	0.0004	0.0150	0.0200	0.47	74.7	2.5	85.8	8.4	387.0	79.0	12.9
CH9-Zrn-025	910.0	4.7	0.005	0.0578	0.0092	0.0870	0.0130	0.0116	0.0004	0.0760	0.0260	0.42	74.5	2.3	84.0	12.0	500.0	160.0	11.3
CH9-Zrn-69	672.0	2.7	0.004	0.0480	0.0041	0.0819	0.0077	0.0116	0.0004	0.0287	0.0070	0.21	74.5	2.4	79.9	7.2	360.0	100.0	6.8
CH9-Zrn-046	820.0	3.3	0.004	0.0507	0.0036	0.0779	0.0057	0.0116	0.0002	0.0393	0.0071	0.26	74.2	1.2	76.1	5.4	278.0	71.0	2.5
CH9-Zrn-64	695.0	3.1	0.004	0.0514	0.0057	0.0771	0.0081	0.0116	0.0004	0.0470	0.0140	0.18	74.2	2.6	75.3	7.7	560.0	180.0	1.5
CH9-Zrn-78	677.0	3.4	0.005	0.0640	0.0100	0.0810	0.0100	0.0115	0.0005	0.0740	0.0260	0.05	73.9	3.0	78.9	9.8	780.0	180.0	6.3
CH9-Zrn-039	695.0	4.9	0.007	0.0539	0.0056	0.0802	0.0087	0.0115	0.0004	0.0454	0.0093	0.14	73.5	2.5	78.2	8.2	480.0	130.0	6.0
CH9-Zrn-63	1001.0	3.7	0.004	0.0484	0.0034	0.0762	0.0055	0.0115	0.0002	0.0183	0.0054	0.16	73.5	1.5	74.4	5.2	346.0	79.0	1.2
CH9-Zrn-037	673.0	3.0	0.004	0.0526	0.0038	0.0773	0.0055	0.0114	0.0003	0.0318	0.0073	0.02	73.0	1.8	75.5	5.2	428.0	87.0	3.3
CH9-Zrn-040	667.0	3.3	0.005	0.0502	0.0048	0.0768	0.0068	0.0113	0.0003	0.0282	0.0086	0.13	72.7	2.0	75.0	6.4	308.0	70.0	3.1
CH9-Zrn-66	876.0	3.2	0.004	0.0515	0.0087	0.0850	0.0130	0.0113	0.0005	0.0580	0.0120	0.40	72.2	3.2	82.0	12.0	264.0	91.0	12.0
Zircon / Eclogite (CH56)																			
CH56-Zrn-048	404.0	249.0	0.616	0.0646	0.0040	0.9470	0.0690	0.1067	0.0034	0.0393	0.0028	0.55	653.0	20.0	674.0	35.0	817.0	55.0	3.1
CH56-Zrn-047	180.0	80.0	0.444	0.0629	0.0032	0.9000	0.0480	0.1031	0.0030	0.0385	0.0021	0.39	632.0	17.0	650.0	26.0	682.0	64.0	2.8
CH56-Zrn-004	612.0	510.0	0.833	0.0594	0.0019	0.8090	0.0300	0.0979	0.0023	0.0301	0.0010	0.61	602.0	13.0	601.0	17.0	572.0	72.0	-0.2
CH56-Zrn-031	670.0	172.0	0.257	0.0614	0.0025	0.8070	0.0340	0.0978	0.0033	0.0329	0.0017	0.41	601.0	19.0	599.0	19.0	658.0	39.0	-0.3
CH56-Zrn-123	1590.0	1010.0	0.635	0.0596	0.0026	0.7880	0.0400	0.0967	0.0021	0.0299	0.0008	0.25	595.0	12.0	590.0	23.0	576.0	72.0	-0.8
CH56-Zrn-113	1620.0	844.0	0.521	0.0593	0.0016	0.7650	0.0320	0.0938	0.0011	0.0320	0.0007	0.41	577.8	6.5	576.6	18.0	578.0	30.0	-0.2
CH56-Zrn-023	1630.0	2120.0	1.301	0.0595	0.0012	0.7660	0.0150	0.0937	0.0019	0.0282	0.0012	0.13	577.0	11.0	577.1	8.7	591.0	25.0	0.0
CH56-Zrn-001	385.0	118.0	0.306	0.0613	0.0031	0.7890	0.0450	0.0927	0.0021	0.0327	0.0021	0.02	571.0	12.0	589.0	26.0	684.0	71.0	3.1
CH56-Zrn-041	342.0	206.0	0.602	0.0641	0.0023	0.8220	0.0290	0.0926	0.0021	0.0304	0.0015	0.05	571.0	12.0	608.0	16.0	728.0	42.0	6.1
CH56-Zrn-110	439.0	341.0	0.777	0.0617	0.0025	0.7730	0.0430	0.0918	0.0020	0.0292	0.0010	0.30	566.0	12.0	580.0	25.0	631.0	45.0	2.4
CH56-Zrn-024	349.0	271.0	0.777	0.0602	0.0019	0.7490	0.0280	0.0914	0.0027	0.0297	0.0021	0.22	563.0	16.0	567.0	16.0	612.0	31.0	0.7
CH56-Zrn-033	690.0	710.0	1.029	0.0595	0.0031	0.7330	0.0590	0.0897	0.0036	0.0257	0.0032	0.86	554.0	21.0	557.0	34.0	580.0	110.0	0.5
CH56-Zrn-046	1150.0	1520.0	1.322	0.0580	0.0032	0.7150	0.0490	0.0895	0.0024	0.0266	0.0028	0.74	552.0	14.0	547.0	29.0	591.0	82.0	-0.9
CH56-Zrn-007	518.0	305.0	0.589	0.0593	0.0020	0.7270	0.0310	0.0892	0.0019	0.0270	0.0014	0.28	551.0	11.0	554.0	18.0	573.0	52.0	0.5
CH56-Zrn-022	1680.0	2370.0	1.411	0.0609	0.0009	0.7490	0.0160	0.0891	0.0020	0.0243	0.0039	0.59	550.0	12.0	567.3	9.3	636.0	20.0	3.0
CH56-Zrn-122	592.0	306.0	0.517	0.0590	0.0019	0.7310	0.0350	0.0891	0.0021	0.0299	0.0011	0.31	550.0	12.0	557.0	20.0	601.0	43.0	1.3
CH56-Zrn-012	1590.0	960.0	0.604	0.0589	0.0014	0.7190	0.0150	0.0885	0.0019	0.0255	0.0014	0.26	547.0	11.0	549.9	9.1	559.0	30.0	0.5
CH56-Zrn-120	1163.0	1300.0	1.118	0.0591	0.0021	0.7110	0.0320	0.0877	0.0015	0.0292	0.0004	0.05	541.6	8.7	547.0	20.0	598.0	46.0	1.0
CH56-Zrn-028	1350.0	1440.0	1.067	0.0654	0.0017	0.7800	0.0240	0.0876	0.0021	0.0253	0.0042	0.51	541.0	12.0	584.0	14.0	771.0	37.0	7.4
CH56-Zrn-055	130.2	65.4	0.502	0.0607	0.0039	0.7300	0.0490	0.0872	0.0029	0.0267	0.0019	0.26	539.0	17.0	554.0	29.0	667.0	75.0	2.7
CH56-Zrn-124	386.0	330.0	0.855	0.0580	0.0024	0.6870	0.0350	0.0863	0.0014	0.0282	0.0008	0.18	533.3	8.3	535.0	23.0	571.0	44.0	0.3
CH56-Zrn-125	205.3	126.1	0.614	0.0612	0.0037	0.7220	0.0480	0.0842	0.0023	0.0317	0.0015	0.05	521.0	13.0	550.0	28.0	637.0	75.0	5.3
CH56-Zrn-030	646.0	674.0	1.043	0.0587	0.0010	0.6770	0.0200	0.0840	0.0021	0.0250	0.0016	0.81	520.0	13.0	524.0	12.0	551.0	38.0	0.8
CH56-Zrn-005	274.0	165.0	0.602	0.0638	0.0030	0.7250	0.0350	0.0833	0.0028	0.0277	0.0019	0.18	516.0	16.0	553.0	21.0	808.0	65.0	6.7
CH56-Zrn-021	370.0	300.0	0.811	0.0634	0.0070	0.7270	0.0760	0.0833	0.0027	0.0265	0.0020	0.17	516.0	16.0	553.0	44.0	790.0	180.0	6.7
CH56-Zrn-025	133.0	86.6	0.651	0.0573	0.0015	0.6510	0.0370	0.0834	0.0031	0.0238	0.0024	0.83	516.0	18.0	508.0	23.0	502.0	60.0	-1.6
CH56-Zrn-129	250.9	168.0	0.670	0.0589	0.0028	0.6750	0.0370	0.0828	0.0015	0.0295	0.0012	0.10	512.7	9.0	522.0	22.0	564.0	53.0	1.8
CH56-Zrn-034	500.0	251.0	0.502	0.0584	0.0022	0.6550	0.0270	0.0826	0.0021	0.0307	0.0015	0.46	511.0	13.0	511.0	16.0	544.0	33.0	0.0

				Isotope ratios									Apparent ages (Ma)						
Point	**U (ppm)**	**Th (ppm)**	**Th/U**	**$^{207}Pb/^{206}Pb$**	**±2σ abs**	**$^{207}Pb/^{235}U$**	**±2σ abs**	**$^{206}Pb/^{238}U$**	**±2σ abs**	**$^{208}Pb/^{232}Th$**	**±2σ abs**	**Rho**	**$^{206}Pb/^{238}U$**	**±2σ**	**$^{207}Pb/^{235}U$**	**±2σ**	**$^{207}Pb/^{206}Pb$**	**±2σ**	**% Disc.**
CH56-Zrn-036	266.0	94.7	0.356	0.0574	0.0012	0.6500	0.0220	0.0821	0.0022	0.0216	0.0026	0.77	509.0	13.0	515.0	13.0	504.0	47.0	1.2
CH56-Zrn-131	257.0	109.0	0.424	0.0647	0.0070	0.7170	0.0780	0.0811	0.0023	0.0293	0.0025	0.12	503.0	13.0	554.0	36.0	760.0	90.0	9.2
CH56-Zrn-130	827.0	387.0	0.468	0.0604	0.0034	0.6490	0.0340	0.0796	0.0019	0.0264	0.0015	0.27	494.0	11.0	507.0	21.0	605.0	63.0	2.6
CH56-Zrn-117	235.0	144.0	0.613	0.0590	0.0025	0.6170	0.0360	0.0774	0.0017	0.0275	0.0011	0.34	480.3	10.0	486.0	22.0	537.0	56.0	1.2
CH56-Zrn-039	275.0	183.0	0.665	0.0642	0.0031	0.6850	0.0380	0.0771	0.0018	0.0260	0.0013	0.44	479.0	11.0	528.0	23.0	743.0	45.0	9.3
CH56-Zrn-027	613.0	490.0	0.799	0.0571	0.0010	0.5970	0.0200	0.0763	0.0019	0.0232	0.0012	0.77	474.0	11.0	475.0	13.0	490.0	41.0	0.2
CH56-Zrn-114	576.0	423.0	0.734	0.0613	0.0023	0.6420	0.0330	0.0761	0.0012	0.0276	0.0011	0.32	472.7	7.3	502.0	20.0	627.0	53.0	5.8
CH56-Zrn-109	304.8	211.0	0.692	0.0606	0.0027	0.6360	0.0330	0.0760	0.0014	0.0268	0.0010	0.23	472.3	8.3	499.0	20.0	607.0	65.0	5.4
CH56-Zrn-029	320.0	280.0	0.875	0.0578	0.0051	0.5770	0.0500	0.0718	0.0021	0.0262	0.0018	0.58	447.0	12.0	460.0	32.0	605.0	98.0	2.8
CH56-Zrn-026	84.0	43.0	0.512	0.0579	0.0011	0.5590	0.0440	0.0712	0.0041	0.0243	0.0075	0.96	443.0	25.0	456.0	27.0	523.0	41.0	2.9
CH56-Zrn-020	168.0	95.0	0.565	0.0582	0.0040	0.5510	0.0380	0.0699	0.0024	0.0236	0.0017	0.26	435.0	14.0	450.0	26.0	560.0	61.0	3.3
CH56-Zrn-042	216.0	112.0	0.519	0.0560	0.0029	0.5390	0.0250	0.0696	0.0015	0.0224	0.0014	0.36	433.7	9.2	437.0	16.0	417.0	61.0	0.8
CH56-Zrn-008	231.0	155.0	0.671	0.0585	0.0034	0.5570	0.0320	0.0690	0.0021	0.0213	0.0013	0.04	430.0	13.0	448.0	21.0	567.0	64.0	4.0
CH56-Zrn-054	194.0	90.8	0.468	0.0601	0.0028	0.5730	0.0250	0.0687	0.0018	0.0244	0.0024	0.06	428.0	11.0	462.0	16.0	647.0	67.0	7.4
CH56-Zrn-009	236.0	138.0	0.585	0.0568	0.0033	0.5490	0.0430	0.0684	0.0025	0.0209	0.0014	0.24	426.0	15.0	443.0	28.0	495.0	92.0	3.8
CH56-Zrn-014	238.0	132.0	0.555	0.0599	0.0064	0.5610	0.0530	0.0682	0.0025	0.0227	0.0016	0.04	425.0	15.0	451.0	34.0	600.0	140.0	5.8
CH56-Zrn-013	260.0	89.7	0.345	0.0574	0.0035	0.5350	0.0290	0.0680	0.0017	0.0242	0.0013	0.04	424.0	11.0	438.0	20.0	555.0	76.0	3.2
CH56-Zrn-050	221.0	143.0	0.647	0.0567	0.0037	0.5340	0.0350	0.0680	0.0020	0.0230	0.0013	0.06	424.0	12.0	432.0	23.0	511.0	67.0	1.9
CH56-Zrn-111	226.7	126.3	0.557	0.0546	0.0028	0.5070	0.0310	0.0677	0.0013	0.0216	0.0008	0.15	422.4	7.9	418.0	21.0	441.0	60.0	-1.1
CH56-Zrn-052	301.0	140.5	0.467	0.0557	0.0021	0.5190	0.0200	0.0676	0.0017	0.0210	0.0012	0.24	421.0	10.0	424.0	13.0	485.0	41.0	0.7
CH56-Zrn-018	197.0	71.0	0.360	0.0626	0.0066	0.5850	0.0610	0.0673	0.0019	0.0252	0.0019	0.00	420.0	11.0	466.0	39.0	670.0	110.0	9.9
CH56-Zrn-010	106.0	54.2	0.511	0.0592	0.0035	0.5480	0.0400	0.0671	0.0021	0.0257	0.0026	0.21	419.0	13.0	443.0	26.0	850.0	190.0	5.4
CH56-Zrn-015	179.0	89.9	0.502	0.0607	0.0046	0.5500	0.0430	0.0662	0.0018	0.0224	0.0014	0.32	413.0	11.0	444.0	29.0	651.0	80.0	7.0
CH56-Zrn-044	185.0	87.8	0.475	0.0610	0.0033	0.5500	0.0280	0.0656	0.0016	0.0231	0.0013	0.12	409.3	9.7	446.0	18.0	666.0	52.0	8.2
CH56-Zrn-106	118.6	61.9	0.522	0.0622	0.0059	0.5580	0.0520	0.0654	0.0020	0.0216	0.0016	0.20	408.0	12.0	447.0	34.0	691.0	98.0	8.7
CH56-Zrn-038	256.0	116.0	0.453	0.0571	0.0040	0.4700	0.0310	0.0598	0.0018	0.0211	0.0012	0.02	375.0	11.0	390.0	21.0	474.0	67.0	3.8
Zircon / Ky-bearing eclogite (CH60)																			
CH60-Zrn-067	52.1	17.5	0.336	0.0577	0.0061	0.5330	0.0530	0.0666	0.0029	0.0221	0.0021	0.10	416.0	18.0	428.0	37.0	510.0	240.0	2.8
CH60-Zrn-099	253.0	77.8	0.308	0.0642	0.0068	0.5310	0.0410	0.0648	0.0017	0.0256	0.0017	0.38	404.0	11.0	432.0	27.0	730.0	140.0	6.5
CH60-Zrn-071	172.6	44.0	0.255	0.0608	0.0020	0.5240	0.0460	0.0638	0.0042	0.0225	0.0017	0.07	404.0	25.0	437.0	24.0	605.0	63.0	7.6
CH60-Zrn-100	202.0	79.8	0.395	0.0613	0.0063	0.5020	0.0380	0.0638	0.0017	0.0219	0.0014	0.42	399.0	10.0	421.0	26.0	680.0	150.0	5.2
CH60-Zrn-109	426.0	22.3	0.052	0.0735	0.0063	0.3320	0.0360	0.0467	0.0030	0.0650	0.0270	0.03	294.0	19.0	286.0	28.0	970.0	130.0	-2.8
CH60-Zrn-050	40.0	16.0	0.400	0.0540	0.0110	0.2190	0.0430	0.0289	0.0014	0.0101	0.0016	0.01	183.6	8.8	195.0	35.0	260.0	350.0	5.8
CH60-Zrn-057	229.0	3.3	0.015	0.0505	0.0039	0.1950	0.0140	0.0278	0.0010	0.0096	0.0047	0.04	177.0	6.1	182.0	11.0	260.0	150.0	2.7
CH60-Zrn-052	70.9	3.5	0.049	0.0503	0.0055	0.1980	0.0220	0.0274	0.0011	0.0223	0.0057	0.05	174.3	6.6	181.0	18.0	260.0	220.0	3.7
CH60-Zrn-058	251.0	2.8	0.011	0.0513	0.0085	0.1910	0.0380	0.0273	0.0011	0.0180	0.0770	0.60	173.8	7.2	177.0	28.0	220.0	230.0	1.8
CH60-Zrn-73	78.8	1.1	0.014	0.0515	0.0066	0.1890	0.0250	0.0264	0.0011	0.0380	0.0110	0.27	167.9	6.8	172.0	21.0	220.0	270.0	2.4
CH60-Zrn-098	1230.0	26.4	0.021	0.0481	0.0016	0.1754	0.0053	0.0259	0.0006	0.0096	0.0054	0.70	164.7	3.4	164.1	4.6	101.0	77.0	-0.4
CH60-Zrn-094	2000.0	136.0	0.068	0.0526	0.0050	0.1770	0.0110	0.0258	0.0005	0.0096	0.0007	0.24	164.3	3.3	165.6	9.3	300.0	140.0	0.8
CH60-Zrn-113	877.0	17.8	0.020	0.0485	0.0009	0.1747	0.0066	0.0258	0.0007	0.0125	0.0074	0.72	164.0	4.1	163.4	5.7	126.0	45.0	-0.4
CH60-Zrn-118	628.0	111.8	0.178	0.0516	0.0053	0.1840	0.0140	0.0258	0.0007	0.0104	0.0014	0.28	164.0	4.6	171.0	12.0	300.0	120.0	4.1

				Isotope ratios							Apparent ages (Ma)					
Point	**U (ppm)**	**Th (ppm)**	**U/Th**	**$^{207}Pb/^{206}Pb$**	**±2σ abs**	**$^{207}Pb/^{235}U$**	**±2σ abs**	**$^{206}Pb/^{238}U$**	**±2σ abs**	**Rho**	**$^{206}Pb/^{238}U$**	**±2σ**	**$^{207}Pb/^{235}U$**	**±2σ**	**$^{207}Pb/^{206}Pb$**	**±2σ**
Monazite / Grt-Ky pelitic schist (CH9)																
CH9-Mnz-18	1685	19200	0.09	0.0918	0.0055	0.1577	0.0081	0.0127	0.0003	0.18	81.3	1.6	148.6	7.1	1464.0	71.0
CH9-Mnz-12	2810	32100	0.09	0.0820	0.0035	0.1387	0.0061	0.0123	0.0002	0.13	78.9	1.6	131.8	5.4	1242.0	38.0
CH9-Mnz-21	2583	27300	0.09	0.0898	0.0040	0.1498	0.0080	0.0124	0.0003	0.59	79.5	2.0	141.6	7.1	1424.0	64.0
CH9-Mnz-23	2200	23180	0.09	0.0705	0.0029	0.1138	0.0051	0.0120	0.0003	0.29	76.9	1.7	109.4	4.7	928.0	47.0
CH9-Mnz-3	3160	21100	0.17	0.0800	0.0037	0.1320	0.0077	0.0122	0.0003	0.47	77.8	1.6	127.2	6.5	1169.0	48.0
CH9-Mnz-17	2580	32300	0.08	0.0995	0.0072	0.1690	0.0100	0.0126	0.0003	0.11	80.7	1.9	158.2	8.8	1551.0	65.0
CH9-Mnz-4	2710	18890	0.15	0.0826	0.0030	0.1419	0.0050	0.0123	0.0003	0.01	78.6	1.8	134.7	4.5	1296.0	51.0
CH9-Mnz-11	2570	29200	0.09	0.0849	0.0032	0.1409	0.0047	0.0123	0.0003	0.01	78.7	1.7	133.8	4.2	1308.0	35.0
CH9-Mnz-10	2350	24200	0.10	0.0819	0.0043	0.1373	0.0060	0.0122	0.0003	0.09	78.3	1.9	130.5	5.3	1260.0	77.0
CH9-Mnz-25	2056	23800	0.08	0.0674	0.0053	0.1112	0.0086	0.0119	0.0003	0.19	75.9	2.1	107.0	7.9	888.0	77.0
CH9-Mnz-9	2080	24400	0.08	0.1028	0.0048	0.1789	0.0079	0.0125	0.0003	0.19	80.0	1.6	167.0	6.8	1697.0	62.0
CH9-Mnz-22	2513	28160	0.09	0.0956	0.0043	0.1653	0.0100	0.0123	0.0003	0.34	79.1	2.1	155.2	8.7	1572.0	60.0
CH9-Mnz-24	2450	27200	0.09	0.0766	0.0029	0.1246	0.0042	0.0119	0.0003	0.14	76.4	1.9	119.2	3.8	1121.0	34.0
CH9-Mnz-8	2162	24700	0.09	0.0983	0.0032	0.1680	0.0057	0.0124	0.0002	0.00	79.3	1.5	157.6	4.9	1605.0	36.0
CH9-Mnz-14	2799	35400	0.08	0.0910	0.0030	0.1536	0.0057	0.0122	0.0003	0.42	78.1	1.6	145.0	5.0	1437.0	38.0
CH9-Mnz-15	2560	28800	0.09	0.0679	0.0031	0.1127	0.0045	0.0119	0.0002	0.15	76.4	1.5	108.4	4.1	884.0	61.0
CH9-Mnz-6	2400	21000	0.11	0.0866	0.0029	0.1450	0.0048	0.0121	0.0002	0.19	77.5	1.2	137.4	4.2	1360.0	37.0
CH9-Mnz-20	2450	28800	0.09	0.0863	0.0027	0.1435	0.0045	0.0121	0.0002	0.06	77.7	1.4	136.7	3.8	1366.0	32.0
CH9-Mnz-19	2270	27700	0.08	0.0822	0.0026	0.1359	0.0040	0.0121	0.0002	0.01	77.4	1.5	129.4	3.6	1260.0	28.0
CH9-Mnz-16	2420	26900	0.09	0.0745	0.0026	0.1205	0.0040	0.0119	0.0003	0.05	76.1	1.6	115.5	3.6	1050.0	42.0
CH9-Mnz-5	3044	26900	0.12	0.0857	0.0036	0.1452	0.0067	0.0121	0.0004	0.25	77.2	2.6	137.6	5.9	1395.0	55.0
CH9-Mnz-7	3020	28900	0.10	0.0855	0.0027	0.1396	0.0048	0.0119	0.0003	0.37	76.4	1.8	132.6	4.3	1325.0	27.0
CH9-Mnz-2	2290	18500	0.14	0.0885	0.0026	0.1410	0.0046	0.0117	0.0002	0.20	75.2	1.3	133.9	4.1	1405.0	35.0

				Isotope ratios							Apparent ages (Ma)			
Point	**U (ppm)**	**Th (ppm)**	**Th/U**	**$^{207}Pb/^{206}Pb$**	**±2σ abs**	**$^{207}Pb/^{235}U$**	**±2σ abs**	**$^{206}Pb/^{238}U$**	**±2σ abs**	**Rho**	**$^{206}Pb/^{238}U$**	**±2σ**	**$^{207}Pb/^{235}U$**	**±2σ**
Titanite / Ky-bearing eclogite (CH60)														
CH60-Ttn-36	18.93	nd	-	0.8270	0.0370	24.2700	0.7500	0.2130	0.0140	0.78	1241.0	72.0	3278.0	30.0
CH60-Ttn-34	18.22	nd	-	0.8050	0.0130	23.9200	0.3900	0.2169	0.0032	0.26	1265.0	17.0	3264.0	16.0
CH60-Ttn-09-2	25.59	nd	-	0.7730	0.0180	14.6200	0.4300	0.1338	0.0030	0.60	809.0	17.0	2789.0	28.0
CH60-Ttn-14	13.69	nd	-	0.8090	0.0150	25.9400	0.8400	0.2327	0.0078	0.84	1347.0	41.0	3347.0	32.0
CH60-Ttn-35	8.55	nd	-	0.8400	0.0150	59.3200	0.9900	0.5140	0.0092	0.42	2672.0	39.0	4161.0	17.0
CH60-Ttn-24	16.77	nd	-	0.8170	0.0140	26.9000	0.3400	0.2397	0.0034	0.02	1385.0	18.0	3381.0	12.0
CH60-Ttn-33	15.17	nd	-	0.8210	0.0120	29.9800	0.3800	0.2661	0.0039	0.45	1521.0	20.0	3485.0	12.0
CH60-Ttn-23	11.45	nd	-	0.8430	0.0160	56.5000	1.3000	0.4790	0.0130	0.70	2519.0	57.0	4117.0	22.0
CH60-Ttn-04	28.71	nd	-	0.7880	0.0160	14.7300	0.2800	0.1353	0.0025	0.46	820.0	13.0	2799.0	18.0
CH60-Ttn-10	17.286	nd	-	0.8278	0.0090	34.8200	0.4600	0.3054	0.0048	0.66	1718.0	24.0	3633.0	13.0
CH60-Ttn-26-3	22.87	nd	-	0.8030	0.0160	19.7100	0.3200	0.1763	0.0035	0.48	1046.0	19.0	3078.0	15.0
CH60-Ttn-37-3	13.95	nd	-	0.8230	0.0160	36.3000	1.4000	0.3190	0.0120	0.84	1791.0	57.0	3676.0	38.0
CH60-Ttn-02	15.19	nd	-	0.8290	0.0130	38.6000	1.2000	0.3381	0.0085	0.80	1876.0	41.0	3732.0	31.0
CH60-Ttn-11	31.41	nd	-	0.7870	0.0260	11.5900	0.2400	0.1060	0.0029	0.10	650.0	17.0	2575.0	18.0
CH60-Ttn-06	19.77	nd	-	0.8040	0.0150	18.0100	0.2400	0.1623	0.0027	0.27	969.0	15.0	2989.0	13.0
CH60-Ttn-25-2	19.73	nd	-	0.8100	0.0150	22.9700	0.4500	0.2056	0.0035	0.54	1205.0	19.0	3223.0	19.0

				Isotope ratios							Apparent ages (Ma)			
Point	**U (ppm)**	**Th (ppm)**	**Th/U**	**$^{207}Pb/^{206}Pb$**	**±2σ abs**	**$^{207}Pb/^{235}U$**	**±2σ abs**	**$^{206}Pb/^{238}U$**	**±2σ abs**	**Rho**	**$^{206}Pb/^{238}U$**	**±2σ**	**$^{207}Pb/^{235}U$**	**±2σ**
CH60-Ttn-17	20.58	nd	-	0.8360	0.0140	42.0400	0.5500	0.3653	0.0060	0.43	2006.0	29.0	3819.0	13.0
CH60-Ttn-32	22.94	nd	-	0.8280	0.0130	33.3400	0.6900	0.2923	0.0063	0.65	1657.0	30.0	3591.0	21.0
CH60-Ttn-15	8.93	nd	-	0.8400	0.0150	46.8200	0.8400	0.4026	0.0076	0.49	2180.0	35.0	3928.0	17.0
CH60-Ttn-27	19.79	nd	-	0.8170	0.0180	22.0500	0.3700	0.1958	0.0036	0.36	1153.0	19.0	3184.0	16.0
CH60-Ttn-01	15.02	nd	-	0.8230	0.0140	29.5800	0.4500	0.2601	0.0040	0.38	1490.0	21.0	3471.0	15.0
CH60-Ttn-13	21.99	nd	-	0.8230	0.0110	26.1400	0.9400	0.2300	0.0074	0.89	1333.0	39.0	3349.0	35.0
CH60-Ttn-12	16.34	nd	-	0.8330	0.0140	35.4200	0.4000	0.3103	0.0046	0.29	1741.0	23.0	3650.0	11.0
CH60-Ttn-29	25.66	nd	-	0.8330	0.0120	30.3500	0.4500	0.2675	0.0030	0.47	1528.0	16.0	3497.0	15.0
CH60-Ttn-20	22.46	nd	-	0.8320	0.0130	29.1700	0.3200	0.2546	0.0035	0.26	1462.0	18.0	3459.0	11.0
CH60-Ttn-31	11.74	nd	-	0.8420	0.0150	49.2000	1.1000	0.4230	0.0100	0.64	2275.0	45.0	3973.0	22.0
CH60-Ttn-07	20.9	nd	-	0.8380	0.0140	30.2400	0.4800	0.2630	0.0051	0.66	1509.0	25.0	3493.0	16.0
CH60-Ttn-30	26.25	nd	-	0.8050	0.0260	17.6900	0.4500	0.1613	0.0038	0.35	964.0	21.0	2972.0	24.0
CH60-Ttn-03	27.22	nd	-	0.8080	0.0250	12.8600	0.2300	0.1143	0.0024	0.10	697.0	14.0	2673.0	19.0
CH60-Ttn-05	18.55	nd	-	0.8450	0.0110	41.7200	0.5300	0.3572	0.0047	0.42	1968.0	22.0	3812.0	13.0
CH60-Ttn-22	14.03	nd	-	0.8525	0.0095	80.7000	1.1000	0.6920	0.0100	0.63	3388.0	39.0	4471.0	13.0
CH60-Ttn-16	14.43	nd	-	0.8420	0.0130	34.0600	0.4500	0.2921	0.0046	0.43	1651.0	23.0	3613.0	13.0
CH60-Ttn-18	20.99	nd	-	0.8360	0.0160	22.7700	0.4500	0.1993	0.0038	0.57	1171.0	20.0	3218.0	19.0
CH60-Ttn-19	11.08	nd	-	0.8500	0.0120	60.2000	1.6000	0.5170	0.0140	0.85	2681.0	60.0	4176.0	27.0
CH60-Ttn-08-1	8.28	nd	-	0.8500	0.0130	80.6000	1.5000	0.6850	0.0150	0.77	3361.0	56.0	4468.0	19.0
CH60-Ttn-28	13.26	nd	-	0.8510	0.0120	47.4000	1.3000	0.4036	0.0093	0.85	2184.0	42.0	3935.0	26.0
CH60-Ttn-21	12.31	nd	-	0.8594	0.0094	82.5900	0.8900	0.7019	0.0088	0.47	3427.0	34.0	4493.0	11.0

Table S2. Trace element data

	Rare earth elements + Y (ppm)													
Point	**La**	**Ce**	**Pr**	**Nd**	**Sm**	**Eu**	**Gd**	**Tb**	**Dy**	**Ho**	**Er**	**Yb**	**Lu**	**Y**
Zircon / Grt-Ky pelitic schist (CH9)														
CH9-Zrn-031	0.000	1.35	0.013	0.06	0.19	0.28	3.5	0.9	6.3	1.5	6.5	27.2	9.1	49.6
CH9-Zrn-55	0.011	1.62	0.003	0.13	0.55	0.32	4.9	1.3	8.8	2.3	11.3	35.2	10.5	83.6
CH9-Zrn-042	0.000	1.53	0.010	0.06	0.32	0.26	3.3	1.1	6.7	1.8	8.2	27.5	7.7	60.5
CH9-Zrn-025	0.064	1.85	0.070	0.48	0.72	0.25	4.4	1.4	8.4	2.4	10.1	38.9	11.3	75.0
CH9-Zrn-69	0.000	1.01	0.000	0.03	0.10	0.32	2.7	0.9	5.4	1.3	5.4	22.1	6.7	41.4
CH9-Zrn-046	0.460	1.88	0.126	0.33	0.82	0.41	4.3	1.3	10.4	2.3	8.9	26.4	7.6	71.7
CH9-Zrn-64	0.000	1.41	0.014	0.03	0.31	0.34	3.2	1.0	6.1	1.7	7.3	28.7	8.5	54.8
CH9-Zrn-78	0.027	1.11	0.023	0.00	0.11	0.23	2.2	0.7	4.8	1.2	5.0	16.5	4.7	37.7
CH9-Zrn-039	0.000	1.63	0.027	0.15	0.61	0.37	4.4	1.6	11.6	2.9	13.4	41.3	11.9	97.9
CH9-Zrn-63	0.000	0.80	0.015	0.00	0.25	0.28	5.2	2.3	18.1	4.1	11.1	10.7	1.7	121.0
CH9-Zrn-037	0.000	1.31	0.005	0.04	0.24	0.19	2.5	0.7	5.0	1.1	5.5	21.5	6.4	39.4
CH9-Zrn-040	0.018	1.30	0.017	0.06	0.51	0.26	3.7	1.0	6.0	1.6	6.9	29.6	8.8	50.7
CH9-Zrn-66	0.043	1.63	0.037	0.00	0.80	0.68	6.7	1.7	11.8	3.4	14.2	50.8	15.8	110.0
Zircon / Eclogite (CH56)														
CH56-Zrn-048	0.031	39.40	0.257	4.50	8.60	2.99	43.0	16.1	200.0	77.2	355.0	688.0	137.0	2460.0
CH56-Zrn-047	0.000	9.10	0.038	0.56	1.18	0.50	8.2	3.1	39.8	16.0	81.0	176.0	38.7	532.0
CH56-Zrn-004	0.041	52.80	0.500	6.70	10.40	3.69	48.1	17.6	210.0	78.0	355.0	710.0	142.0	2510.0
CH56-Zrn-031	0.147	13.20	0.161	1.44	2.33	0.95	12.7	4.5	60.0	25.0	127.0	323.0	75.0	860.0
CH56-Zrn-123	0.015	43.00	0.084	2.15	3.90	1.94	28.9	11.4	151.0	63.0	318.0	730.0	159.0	2060.0
CH56-Zrn-113	0.124	32.80	0.167	2.05	2.92	1.72	20.3	7.7	107.8	44.7	240.0	622.0	139.3	248.0
CH56-Zrn-023	0.082	116.10	0.321	5.35	10.10	4.07	57.4	21.2	256.0	94.2	401.0	765.0	149.0	3010.0
CH56-Zrn-001	0.000	15.60	0.043	0.78	1.68	0.95	13.1	5.0	71.0	31.0	161.0	408.0	93.0	980.0
CH56-Zrn-041	0.000	26.40	0.139	2.65	4.90	1.78	25.9	9.6	115.0	46.2	217.0	444.0	93.0	1520.0
CH56-Zrn-110	0.078	39.70	0.228	4.20	6.20	2.85	37.5	13.3	163.0	63.4	286.0	578.0	113.8	1970.0
CH56-Zrn-024	0.012	23.60	0.091	1.48	3.58	1.54	18.6	6.9	85.0	31.6	141.0	287.0	59.1	154.0
CH56-Zrn-033	0.065	54.00	0.200	2.67	5.10	2.66	42.0	14.7	176.0	65.0	283.0	540.0	99.0	3220.0
CH56-Zrn-046	0.097	106.00	0.257	3.74	6.80	3.74	56.3	22.7	269.0	99.0	411.0	721.0	132.0	1640.0
CH56-Zrn-007	0.029	28.40	0.121	2.63	4.06	2.34	26.3	9.8	120.0	50.8	249.0	536.0	117.0	3590.0
CH56-Zrn-022	0.156	111.80	0.422	6.17	11.20	5.15	67.5	25.1	299.0	113.0	486.0	923.0	179.0	960.0
CH56-Zrn-122	0.000	19.40	0.084	1.16	2.13	1.10	13.2	5.3	74.0	31.3	151.0	370.0	83.1	1940.0
CH56-Zrn-012	0.032	35.30	0.076	1.09	2.95	1.03	22.3	9.1	128.0	57.5	297.0	649.0	135.0	2866.0
CH56-Zrn-120	0.063	68.40	0.332	5.32	9.88	4.53	54.6	19.6	236.8	89.5	397.0	800.0	157.9	2460.0
CH56-Zrn-028	0.350	79.00	0.332	3.81	7.30	3.22	41.2	16.2	196.0	73.7	333.0	673.0	140.0	301.0
CH56-Zrn-055	0.000	4.88	0.035	0.51	0.71	0.38	4.3	1.6	20.7	8.2	39.2	100.4	23.8	256.0
CH56-Zrn-124	0.003	24.70	0.145	2.17	3.68	1.65	20.5	7.5	94.0	36.8	178.0	377.0	78.6	1140.0
CH56-Zrn-125	0.000	15.83	0.105	1.81	3.02	1.28	18.6	6.5	78.9	31.8	143.6	290.0	61.6	1220.0
CH56-Zrn-030	0.093	41.50	0.335	4.79	6.24	3.02	34.8	12.3	143.0	54.9	243.0	502.0	105.4	158.0
CH56-Zrn-005	0.085	13.80	0.163	1.60	2.30	1.24	15.5	4.6	57.0	23.9	104.0	233.0	51.7	1740.0
CH56-Zrn-021	0.000	19.80	0.000	0.66	2.90	1.14	13.2	5.1	68.0	28.0	126.0	274.0	56.0	710.0
CH56-Zrn-025	0.000	3.69	0.000	0.10	0.33	0.21	2.2	1.2	15.4	6.5	32.9	84.3	20.1	222.0
CH56-Zrn-129	0.000	14.10	0.042	1.09	1.52	0.95	10.2	4.0	49.7	20.7	104.2	251.0	57.7	1630.0
CH56-Zrn-034	0.021	27.30	0.151	1.77	5.80	2.11	28.4	10.5	127.0	51.4	241.0	505.0	110.0	1040.0
CH56-Zrn-036	0.015	12.80	0.231	3.25	5.11	1.61	24.6	7.9	92.0	35.0	159.0	321.0	72.4	1342.0
CH56-Zrn-131	2.800	10.00	0.830	2.60	1.34	0.80	7.2	2.7	37.9	17.1	90.0	240.0	54.5	2360.0
CH56-Zrn-130	0.290	23.90	0.150	2.20	4.10	2.14	23.1	7.7	101.9	41.2	203.0	444.0	95.3	643.0
CH56-Zrn-117	0.004	15.40	0.029	0.53	1.17	0.88	8.6	3.6	47.8	19.3	95.0	225.0	48.4	1230.0
CH56-Zrn-039	0.000	8.20	0.040	0.20	0.62	0.33	5.0	1.8	26.4	10.4	54.1	142.0	32.2	950.0
CH56-Zrn-027	0.105	25.80	0.232	2.80	3.21	1.80	22.1	7.5	99.0	39.8	182.0	387.0	82.0	413.0
CH56-Zrn-114	0.000	24.20	0.059	0.85	1.99	1.12	14.1	5.4	73.4	29.2	147.0	311.0	63.7	126.0
CH56-Zrn-109	0.000	8.52	0.022	0.37	0.81	0.55	5.9	2.3	28.9	12.6	61.2	150.0	33.9	246.0
CH56-Zrn-029	0.015	19.20	0.000	0.95	3.00	0.85	14.6	4.7	65.0	25.3	116.0	258.0	53.0	121.0
CH56-Zrn-026	0.000	2.52	0.000	0.08	0.45	0.21	2.6	0.6	7.7	3.7	19.8	46.0	11.5	162.0
CH56-Zrn-020	0.000	3.26	0.013	0.05	0.36	0.14	1.6	0.6	8.4	3.7	19.9	53.2	13.1	219.0
CH56-Zrn-042	0.000	4.44	0.009	0.04	0.64	0.32	2.5	1.2	16.4	6.9	32.5	82.3	21.6	230.0
CH56-Zrn-008	0.430	4.50	0.075	0.48	0.79	0.23	2.7	1.2	14.3	6.0	31.3	82.1	20.8	218.0
CH56-Zrn-054	0.026	3.81	0.027	0.24	0.59	0.30	3.0	1.1	13.2	5.8	28.3	61.7	14.7	192.0
CH56-Zrn-009	0.007	4.40	0.010	0.22	0.55	0.33	4.1	1.3	16.9	7.3	37.6	98.0	24.8	181.0
CH56-Zrn-014	0.013	4.70	0.027	0.59	0.58	0.16	2.6	1.3	15.9	6.5	31.9	75.9	18.0	207.0
CH56-Zrn-013	0.026	4.26	0.031	0.32	0.41	0.28	2.7	1.1	14.3	5.9	29.8	68.1	18.3	116.0
CH56-Zrn-050	0.000	3.99	0.012	0.10	0.55	0.35	3.2	1.3	15.0	6.5	32.8	78.7	19.7	169.0
CH56-Zrn-111	0.000	4.08	0.000	0.00	0.33	0.26	2.6	1.1	14.4	6.4	33.4	86.7	22.0	163.0
CH56-Zrn-052	0.134	5.89	0.043	0.22	0.81	0.53	4.4	1.7	21.9	8.8	44.1	98.0	22.8	162.0
CH56-Zrn-018	0.000	3.69	0.028	0.19	0.47	0.40	3.5	0.9	13.6	5.8	28.7	66.0	16.0	208.0
CH56-Zrn-010	0.000	2.41	0.000	0.10	0.53	0.18	1.4	0.5	9.1	3.6	19.4	50.5	11.5	222.0
CH56-Zrn-015	0.000	3.75	0.021	0.07	0.46	0.16	3.0	1.0	12.9	5.0	27.1	73.5	17.9	190.3
CH56-Zrn-044	0.000	3.69	0.008	0.00	0.49	0.16	2.0	0.8	11.3	4.8	25.7	68.2	18.1	194.0
CH56-Zrn-106	0.000	4.10	0.000	0.00	0.51	0.15	2.6	0.9	13.0	5.7	29.0	75.0	19.7	182.0

	Rare earth elements + Y (ppm)													
Point	**La**	**Ce**	**Pr**	**Nd**	**Sm**	**Eu**	**Gd**	**Tb**	**Dy**	**Ho**	**Er**	**Yb**	**Lu**	**Y**
CH56-Zrn-038	0.230	6.20	0.164	0.88	1.01	0.47	4.2	1.6	21.5	8.8	41.7	93.0	21.1	268.0
Zircon / Ky-bearing eclogite (CH60)														
CH60-Zrn-067	0.000	6.38	0.050	0.72	1.42	0.81	7.7	2.4	29.8	11.9	58.5	142.9	34.7	386.0
CH60-Zrn-099	0.000	16.50	0.010	0.36	0.60	0.23	5.0	1.8	27.0	12.1	58.7	133.0	28.6	381.0
CH60-Zrn-071	0.000	12.05	0.000	0.14	0.19	0.20	3.5	1.5	17.7	8.3	37.7	83.6	17.3	242.0
CH60-Zrn-100	0.000	14.30	0.014	0.43	0.60	0.14	4.3	1.5	20.8	9.3	47.5	98.7	21.4	300.0
CH60-Zrn-109	0.009	0.94	0.020	0.00	0.03	0.10	1.1	0.5	6.8	3.0	18.2	55.1	14.8	105.0
CH60-Zrn-050	0.050	5.32	0.031	0.32	0.60	0.52	4.4	1.6	19.3	7.9	41.2	109.7	26.0	263.0
CH60-Zrn-057	0.000	1.87	0.000	0.09	0.35	0.42	3.0	1.2	17.7	8.3	46.0	146.0	36.6	278.0
CH60-Zrn-052	0.000	1.33	0.000	0.03	0.18	0.15	1.2	0.5	5.3	2.5	12.9	38.7	9.9	81.0
CH60-Zrn-058	0.000	2.85	0.000	0.19	0.70	0.65	5.6	2.3	37.2	16.5	93.0	297.0	72.4	570.0
CH60-Zrn-73	0.234	1.22	0.077	0.27	0.13	0.14	0.9	0.3	4.5	2.0	11.2	35.3	9.7	68.0
CH60-Zrn-098	0.095	2.13	0.047	0.05	0.83	0.45	4.1	1.8	24.3	10.7	60.4	186.0	49.0	387.0
CH60-Zrn-094	0.043	6.53	0.052	1.46	2.96	1.67	14.5	4.9	62.2	25.0	129.5	332.0	83.7	817.0
CH60-Zrn-113	0.018	2.89	0.019	0.07	0.21	0.17	2.5	1.1	13.2	6.2	35.3	100.6	25.9	218.0
CH60-Zrn-118	0.000	25.70	0.240	2.87	4.58	3.34	18.8	6.4	73.2	30.5	151.0	353.0	86.0	978.0
Garnet / Grt-Ky pelitic schist (CH9)														
CH9-Grt2	0.018	0.02	0.008	0.26	2.16	1.79	22.3	8.4	72.2	15.7	48.0	48.0	6.5	400.0
CH9-Grt2-1	0.000	0.01	0.014	0.28	2.52	1.98	23.1	7.5	56.6	10.7	29.0	24.8	3.1	283.0
CH9-Grt2-3	0.000	0.00	0.005	0.35	2.41	2.18	24.3	7.4	55.5	10.9	29.1	27.5	3.7	282.0
CH9-Grt2-4	0.000	0.00	0.006	0.29	2.57	2.00	23.6	6.9	49.3	9.4	26.3	24.9	3.2	251.0
CH9-Grt2-5	0.000	0.00	0.002	0.18	2.02	1.54	20.2	7.3	56.0	11.3	33.3	33.6	4.5	295.0
CH9-Grt2-8	0.000	0.00	0.004	0.06	0.45	0.41	6.3	3.2	31.4	7.0	21.6	23.0	3.4	172.4
CH9-Grt2-9	0.000	0.00	0.002	0.03	0.50	0.38	6.3	3.2	33.5	7.7	24.7	27.7	4.0	191.9
CH9-Grt2-10	0.000	0.00	0.002	0.05	0.39	0.39	6.5	3.6	40.5	9.7	30.6	34.6	5.1	234.2
CH9-Grt2-13	0.000	0.00	0.000	0.03	0.57	0.44	7.2	4.0	47.0	11.4	34.7	37.3	5.5	278.9
CH9-Grt2-14	0.000	0.00	0.000	0.05	0.51	0.44	6.7	3.7	43.7	10.5	30.8	32.4	4.8	258.9
CH9-Grt2-15	0.000	0.00	0.000	0.04	0.54	0.45	7.2	4.0	43.6	9.8	28.7	28.1	3.9	247.6
CH9-Grt2-17	0.035	0.09	0.017	0.14	0.44	0.40	6.0	3.3	40.7	9.9	32.0	35.8	5.5	245.0
CH9-Grt2-19	0.000	0.00	0.001	0.07	0.54	0.42	6.9	3.7	42.5	9.6	28.6	28.8	4.1	240.5
CH9-Grt2-21	0.000	0.00	0.000	0.03	0.62	0.52	7.7	3.9	42.7	9.3	26.9	25.7	3.7	234.1
CH9-Grt2-22	0.000	0.00	0.000	0.02	0.52	0.40	7.0	3.7	41.1	9.6	28.5	29.3	4.4	236.5
CH9-Grt2-23	0.000	0.00	0.000	0.03	0.40	0.37	6.2	3.4	37.5	9.0	28.1	31.3	4.7	219.7
CH9-Grt2-24	0.000	0.00	0.000	0.04	0.35	0.38	6.3	3.3	34.2	7.7	24.8	26.9	4.0	190.9
CH9-Grt2-25	0.000	0.00	0.003	0.04	0.50	0.38	7.0	3.6	37.2	8.7	26.4	28.7	4.1	212.9
CH9-Grt2-26	0.006	0.01	0.005	0.12	1.02	0.91	13.6	5.8	51.2	11.0	31.3	30.7	4.0	284.0
CH9-Grt2-27	0.000	0.01	0.004	0.25	2.16	1.64	20.8	6.7	50.0	9.9	30.6	32.0	4.4	260.0
CH9-Grt2-29	0.000	0.01	0.009	0.24	2.63	2.06	23.5	7.6	55.5	10.6	28.4	24.9	3.2	279.0
CH9-Grt2-30	0.074	0.19	0.042	0.44	2.70	2.13	24.4	7.9	58.8	10.6	28.1	21.5	2.5	283.0
CH9-Grt2-32	0.002	0.01	0.008	0.24	2.48	1.92	22.5	8.1	66.1	13.3	39.6	37.7	4.9	349.0
Garnet / Ky-bearing eclogite (CH60)														
CH60-Grt1	0.028	0.04	0.006	0.06	0.22	0.19	1.6	0.8	10.0	3.2	12.0	12.5	1.8	80.8
CH60-Grt1-1	0.013	0.02	0.003	0.05	0.27	0.20	1.8	0.7	9.1	2.8	10.4	12.8	2.0	74.4
CH60-Grt1-2	0.033	0.05	0.004	0.07	0.22	0.22	1.6	0.6	8.2	2.5	9.5	12.3	1.9	67.8
CH60-Grt1-3	0.004	0.01	0.002	0.04	0.23	0.19	1.7	0.6	8.3	2.6	9.8	12.8	1.9	71.5
CH60-Grt1-4	0.000	0.00	0.000	0.03	0.18	0.21	1.7	0.7	8.2	2.4	9.0	10.2	1.4	66.8
CH60-Grt1-6	0.074	0.12	0.012	0.07	0.20	0.19	1.4	0.6	7.3	2.2	7.9	7.7	1.0	61.1
CH60-Grt1-7	0.013	0.02	0.005	0.03	0.15	0.16	1.3	0.5	6.1	1.8	5.6	4.7	0.5	48.0
CH60-Grt1-8	0.000	0.00	0.000	0.02	0.17	0.22	1.3	0.5	6.4	1.8	5.7	4.1	0.5	48.2
CH60-Grt1-9	0.057	0.10	0.010	0.09	0.16	0.22	1.4	0.6	6.4	1.7	5.3	3.6	0.4	46.5
CH60-Grt1-10	0.044	0.08	0.008	0.04	0.24	0.35	1.6	0.6	5.7	1.3	3.2	1.8	0.2	34.6
CH60-Grt1-11	0.106	0.15	0.027	0.10	0.24	0.27	1.4	0.5	5.1	1.2	3.2	1.8	0.2	33.6
CH60-Grt1-12	0.118	0.16	0.029	0.08	0.21	0.29	1.9	0.6	6.1	1.2	3.2	1.7	0.2	33.2
CH60-Grt1-13	0.113	0.17	0.025	0.16	0.17	0.23	1.4	0.5	5.5	1.3	3.8	2.2	0.2	36.6
CH60-Grt1-14	0.036	0.10	0.015	0.07	0.20	0.24	1.5	0.6	5.6	1.3	3.5	2.1	0.2	35.7
CH60-Grt1-15	0.044	0.10	0.013	0.07	0.13	0.21	1.4	0.6	6.7	1.7	5.6	3.8	0.4	48.3
CH60-Grt1-16	0.056	0.09	0.013	0.11	0.17	0.20	1.2	0.5	6.3	1.8	6.0	5.1	0.6	49.2
CH60-Grt1-17	0.076	0.10	0.021	0.09	0.19	0.20	1.1	0.5	6.2	1.8	5.8	4.3	0.5	49.0
CH60-Grt1-18	0.069	0.11	0.016	0.06	0.14	0.17	1.1	0.5	6.5	1.8	6.0	4.8	0.6	49.1
CH60-Grt1-19	0.081	0.13	0.021	0.11	0.17	0.15	1.1	0.5	6.3	1.8	6.3	5.2	0.6	50.4
CH60-Grt1-20	0.039	0.06	0.004	0.05	0.19	0.21	1.3	0.6	7.3	2.2	7.0	5.5	0.6	58.3
CH60-Grt1-24	0.075	0.12	0.020	0.10	0.15	0.18	1.4	0.6	7.7	2.3	8.3	8.2	1.1	62.7
CH60-Grt1-25	0.030	0.06	0.007	0.04	0.23	0.17	1.5	0.6	7.9	2.5	9.2	11.9	1.8	67.5
CH60-Grt1-26	0.007	0.01	0.003	0.04	0.23	0.21	1.5	0.7	8.5	2.7	10.5	14.3	2.3	73.8
CH60-Grt1-27	0.000	0.00	0.003	0.03	0.25	0.19	1.7	0.6	8.1	2.6	9.8	12.7	2.0	68.7

Anexo

DATOS Y CONSIDERACIONES ADICIONALES

En este anexo se presenta una serie de datos petrográficos, geoquímicos y geocronológicos que complementan la información presentada en el Capítulo 3, sobre las rocas de composición básica (principalmente eclogita, pero también anfibolita) y pelítica (esquisto) del complejo Chuacús. En la Tabla A1 se presenta una síntesis de la información referente a cada muestra utilizada, incluyendo su localidad, sus características principales y el tipo de análisis llevado a cabo. Las muestras CH60 y CH56, descritas en la sección 4, son representativas de la variedad petrográfica observada en las muestras de eclogitas estudiadas en este anexo. En el caso de las metapelitas, la muestra CH3 es análoga a la muestra CH9, descrita también en la sección 4, mientras que las características de las muestras CH24 y CH35 fueron descritas en el Capítulo 2, sección 3.

Tabla A1. Muestras utilzadas para análisis químico de roca total y geocronológico

Muestra	Localidad	Tipo de roca	Mineralogía[1]	Mayores	Traza	U-Pb[2]	Lu-Hf[3]
Metabasita							
CH4	Palibatz	Eclogita con fengita	Cpx, Grt, Rt, Qz, Ph, Czo, Amp, Pl, Ttn, Bt, FeTi Ox, Zr	x	x		
CH16	Saltán	Eclogita con fengita	Cpx, Grt, Rt, Qz, Ph, Czo, Amp, Pl, Ttn, Bt, Ap, Zr	x	x		
CH23	Sur Rabinal	Anfibolita con granate	Amp, Pl, Grt, Rt, Ap, Zrn, ±Czo, ±FeTi Ox, ±Bt, ±Qz, ±Ph	x			
CH32	Sur Rabinal	Anfibolita con granate	Amp, Pl, Grt, Rt, Ap, Zrn, ±Czo, ±FeTi Ox, ±Bt, ±Qz, ±Ph	x			
CH45	El Chol	Eclogita con fengita	Cpx, Grt, Rt, Ph, Czo, Amp, Pl, Ttn, Bt, Ap, Zr, ±Qz	x	x	x	
CH51	El Chol	Eclogita con fengita	Cpx, Grt, Rt, Qz, Ph, Czo, Amp, Pl, Ttn, Bt, FeTi Ox, Ap, Zr	x	x		
CH53	El Chol	Eclogita con fengita	Cpx, Grt, Rt, Qz, Ph, Czo, Amp, Pl, Ttn, Bt, FeTi Ox, Ap, Zr	x			
CH56	Concul	Eclogita con fengita	Cpx, Grt, Rt, Qz, Ph, Czo, Amp, Pl, Ttn, Bt, FeTi Ox, Ap, Zr	x	x	x	
CH60a	Agua Caliente	Eclogita con cianita	Cpx, Grt, Rt, Qz, Czo, Amp, Pl, Ttn, FeTi Ox, Ap, Pg, Ky, Zr	x			
CH60b	Agua Caliente	Eclogita con cianita	Cpx, Grt, Rt, Qz, Ph, Czo, Amp, Pl, Ttn, FeTi Ox, Ap, Pg, Ky, Zr	x	x	x	x
CH62	Tres Cruces	Eclogita con fengita	Cpx, Grt, Rt, Qz, Ph, Czo, Amp, Pl, Ttn, Bt, FeTi Ox, Ap, Zrn	x	x	x	
CH63	Agua Caliente	Eclogita	Cpx, Grt, Rt, Qz, Czo, Amp, Pl, Ttn, FeTi Ox, Ap	x	x		
CH69	Las Anonas	Anfibolita con granate	Amp, Pl, Grt, Czo, Rt, Ap, Zrn, ±FeTi Ox, ±Bt, ±Qz, ±Ph	x	x		
CH76	Agua Caliente	Eclogita con fengita	Cpx, Grt, Rt, Ph, Czo, Amp, Pl, Ttn, Bt, Ap, Chl, ±FeTi Ox, ±Qz	x			
CH79	Agua Caliente	Para-piroxenita	Cpx, Grt, Ph, Cal, Qz, Rt, Ttn, Zrn	x		x	
Metapelita							
CH3	Palibatz	Esquisto pelítico	Qz, Ph, Grt, Ky, Rt, Ap, Zrn, Mnz, Ilm, ±Pg, ±Cld, ±St, ±Czo, ±Chl	x	x		
CH9	Pachajob	Esquisto pelítico	Qz, Ph, Grt, Ky, Rt, Ap, Zrn, Mnz, Ilm, ±Pg, ±Cld, ±St, ±Czo, ±Chl	x	x	x	x
CH24	Sur Rabinal	Esquisto pelítico	Qz, Ph, Grt, Pg, Cld, Rt, Czo, Ap, Zrn, Mnz, Ilm, ±Ky, ±Chl	x			
CH35	El Apazote	Esquisto pelítico	Qz, Ph, Grt, St, Pg, Ap, Zrn, Mnz, Ilm, ±Ky, ±Cld, ±Czo, ±Rt, ±Chl	x	x	x	

[1]Las abreviaturas minerales son de acuerdo a Whitney & Evans (2010). Ph: muscovita con Si>3.0 átomos por unidad de fórmula; Cpx: principalmente onfacita con presencia minoritaria de clinopiroxeno diopsídico bajo en Na, con excepción de la muestra CH79 que carece de onfacita; Amp: anfíbol cálcico a cálcico-sódico; Pl: plagioclasa rica en albita. [2]Los análisis de U-Pb se refieren en todos los casos a geocronología U-Pb en zircón por LA-ICP-MS, con excepción de las muestras CH9 y CH60, donde además se emplearon monacita y titanita, respectivamente. [3]Los análisis de Lu-Hf se refieren a geocronología por el método de isocrona empleando roca-total y granate.

Química de roca total

Las composiciones químicas de roca total fueron obtenidas por fluorescencia de rayos X utilizando un espectrómetro Rigaku ZSX Primus II en el Instituto de Geología, UNAM, siguiendo la metodología descrita por Lozano and Bernal (2005). Las composiciones de elementos traza fueron determinadas por

espectrometría de masas con plasma acoplado inductivamente (ICP-MS), usando un espectrómetro Thermo ICap Qc ICP-MS en el Laboratorio de Estudios Isotópicos (LEI), Centro de Geociencias, UNAM. Se siguieron métodos convencionales de trituración y molienda de las muestras de roca para obtener alícuotas de roca pulverizada de ~50 mg, las cuales fueron procesadas siguiendo los procedimientos descritos por Ferrari *et al*. (2014). Los resultados obtenidos se muestran en la Tabla A2.

Metabasitas

En el diagrama de álcalis total vs. sílice para rocas volcánicas (TAS, Fig. A1a), este grupo de rocas muestra composiciones que van de basalto a traquiandesita, así como un carácter equivalente entre las series tholeiítica y calcoalcalina de potasio alto (Le Maitre *et al*., 1989). Sin embargo, estos esquemas de clasificación química, basados en el contenido de elementos comúnmente móviles durante el metamorfismo, únicamente proporcionan una idea de la variabilidad química preservada luego del proceso metamórfico y no necesariamente son indicadores de las composiciones originales de los protolitos. Un esquema de clasificación química más apropiado se basa en el diagrama Zr/TiO_2 vs. Nb/Y mostrado en la Fig. A1b (Winchester & Floyd, 1977), el cual utiliza elementos inmóviles para discriminar entre series distintas de derivados magmáticos. De acuerdo a este diagrama, la mayoría de las metabasitas estudiadas poseen composiciones de basalto alcalino, mientras que tres muestras varían de andesita/basalto a basalto subalcalino.

En términos de la abundancia de los elementos traza, las metabasitas se agrupan en dos categorías con concentraciones contrastantes, principalmente de los elementos más incompatibles, de forma consistente con la variación observada en el diagrama Zr/TiO_2 vs. Nb/Y. En el diagrama de tierras raras (REE) normalizadas con respecto a la composición condrítica (McDonough & Sun, 1995), las muestras que grafican en el campo del basalto alcalino exhiben un enriquecimiento relativo en las REE ligeras, con valores $(La/Yb)_N$ = 3.7-8.0 y patrones similares al basalto de isla oceánica (OIB), con excepción de una ligera anomalía negativa en Eu (Fig. A1c). Por otro lado, dos de las muestras ubicadas en el campo subalcalino (Fig. A1b) muestran patrones planos con valores $(La/Yb)_N$ = 0.9-1.8, comparables con la composición del basalto enriquecido de dorsal oceánica (E-MORB). Los datos presentados por Solari *et al*. (2011) muestran patrones similares, con un dato que además se ajusta a la composición del basalto normal de dorsal oceánica (N-MORB). En el diagrama multi-elemental presentado en la Fig. A1d se observa que las metabasitas afines a la composición OIB muestran, en general, anomalías positivas de Ba, Ta, Nb y Pb, así como una pronunciada anomalía negativa en Sr y anomalías variables de Ti. Las muestras similares al E-MORB se caracterizan por una notable anomalía negativa en Th, además de anomalías ligeramente negativas de Ta y Nb, así como anomalías positivas de Pb, Hf y Zr.

Tabla A2. Análisis químicos de roca total

Muestra	CH4	CH16	CH23	CH32	CH45	CH51	CH53	CH56	CH60a	CH60b	CH62	CH63	CH69	CH76	CH79	CH3	CH9	CH24	CH35
Grupo	**Metabasita**															**Metapelita**			
% peso																			
SiO_2	49.83	50.55	48.79	48.76	51.86	48.16	50.82	45.93	43.78	45.99	47.26	54.80	49.32	45.72	50.09	57.08	51.68	49.92	52.88
TiO_2	3.39	1.82	2.29	2.20	2.22	4.07	1.85	3.52	3.80	2.78	4.18	2.38	4.13	2.35	0.45	0.94	1.34	0.97	1.25
Al_2O_3	13.73	15.48	12.86	12.07	16.36	12.60	14.99	14.20	15.62	15.88	13.76	15.68	11.62	13.69	5.18	22.60	25.62	26.27	24.15
Fe_2O_3t	13.56	11.17	14.99	16.69	10.75	15.56	12.57	16.39	16.98	17.00	16.69	8.42	16.04	15.44	7.25	9.11	9.89	9.54	10.24
MnO	0.22	0.21	0.24	0.28	0.18	0.23	0.18	0.25	0.31	0.26	0.30	0.14	0.24	0.21	0.62	0.09	0.18	0.25	0.15
MgO	4.53	5.55	6.86	5.92	3.38	4.57	5.41	5.76	6.00	5.20	4.29	3.65	4.84	5.16	11.20	2.07	1.97	1.74	1.84
CaO	8.71	11.33	10.91	9.95	7.06	8.96	7.57	9.21	9.13	8.75	8.90	6.90	9.19	12.13	20.62	0.49	0.96	1.01	1.02
Na_2O	3.25	2.17	1.76	2.87	4.88	4.49	3.47	2.78	3.44	3.44	3.28	6.77	2.53	3.15	1.89	1.09	1.12	1.74	1.31
K_2O	1.50	0.33	0.30	0.37	1.57	0.56	2.18	0.81	0.33	0.19	0.69	0.29	1.05	0.57	0.22	4.32	4.53	4.84	4.42
P_2O_5	0.44	0.20	0.15	0.21	0.85	0.49	0.52	0.55	0.20	0.13	0.59	0.54	0.53	1.12	0.02	0.13	0.18	0.22	0.21
LOI	0.76	1.03	0.72	0.56	0.78	0.35	0.68	0.55	0.38	0.26	0.12	0.36	0.45	0.36	2.46	2.21	2.57	3.27	2.58
TOTAL	99.9	99.8	99.9	99.9	99.9	100.0	100.2	99.9	100.0	99.9	100.1	99.9	99.9	99.9	100.0	100.1	100.0	99.8	100.0
ppm																			
Li	6.34	20.9	-	-	7.66	7.81	-	7.15	-	16.54	3.95	7.53	9.41	-	-	23.5	29.7	-	79.2
Be	4.37	0.64	-	-	1.45	1.90	-	1.20	-	0.85	2.12	3.45	2.14	-	-	3.98	3.77	-	4.75
B	2.51	5.96	-	-	2.38	2.13	-	2.36	-	2.30	2.05	2.24	2.56	-	-	37.9	15.47	-	15.67
P	0.46	0.20	-	-	0.86	0.48	-	0.54	-	0.12	0.58	0.56	0.53	-	-	0.14	0.19	-	0.21
Sc	21.9	31.6	-	-	22.3	30.5	-	28.6	-	21.9	32.6	15.46	35.1	-	-	16.67	18.90	-	16.19
Ti	3.07	1.66	-	-	2.20	3.85	-	3.41	-	2.37	3.99	2.19	3.92	-	-	0.90	1.06	-	1.20
V	231	302	-	-	165	336	-	300	-	287	226	153	400	-	-	112	108	-	97.7
Cr	111	352	-	-	167	60.6	-	108	-	54.4	78.2	2.30	111	-	-	240	220	-	224
Co	44.4	37.9	-	-	19.15	34.7	-	40.1	-	26.8	30.7	11.02	46.6	-	-	22.7	21.0	-	20.7
Ni	52.8	77.9	-	-	31.6	20.9	-	50.6	-	33.5	23.9	3.69	45.1	-	-	48.1	39.8	-	37.8
Cu	128	69.2	-	-	38.2	43.7	-	37.9	-	63.5	64.4	13.57	236	-	-	11.49	17.15	-	66.1
Zn	108	84.0	-	-	89.0	138	-	142	-	115	143	62.1	161	-	-	96.3	76.7	-	120
Ga	26.1	18.08	-	-	20.3	22.2	-	21.0	-	19.32	23.2	20.6	22.1	-	-	29.9	33.9	-	32.9
Rb	35.7	5.30	-	-	31.6	13.61	-	15.61	-	3.66	14.35	3.31	28.5	-	-	194	195	-	199
Sr	203	164	-	-	436	224	-	282	-	204	266	1008	265	-	-	116	156	-	180
Y	38.2	38.1	-	-	42.1	49.2	-	46.6	-	25.0	61.8	33.3	47.2	-	-	40.1	68.9	-	52.9
Zr	241	121	-	-	241	254	-	213	-	150	327	252	281	-	-	193	296	-	282
Nb	26.6	4.73	-	-	18.12	30.4	-	26.8	-	8.43	44.6	24.0	38.2	-	-	23.8	33.8	-	36.9
Mo	2.02	2.11	-	-	0.75	2.17	-	2.21	-	0.24	3.11	1.06	1.53	-	-	3.24	3.12	-	3.23
Sn	2.17	1.28	-	-	1.54	2.07	-	1.59	-	1.07	2.33	1.83	2.40	-	-	4.49	4.92	-	5.24
Sn	2.17	1.29	-	-	1.55	2.08	-	1.59	-	1.08	2.32	1.83	2.40	-	-	4.50	4.93	-	5.25
Sb	0.08	0.13	-	-	0.07	0.08	-	0.08	-	0.06	0.07	0.08	0.10	-	-	0.62	0.58	-	0.14
Cs	0.24	-	-	-	0.18	0.15	-	0.22	-	-	0.03	-	0.37	-	-	4.49	3.36	-	6.00
Ba	739	22.79	-	-	550	693	-	263	-	188	307	40.84	178	-	-	692	665	-	611
La	20.3	5.35	-	-	42.4	25.4	-	21.4	-	6.98	40.0	38.8	29.6	-	-	54.2	72.5	-	78.9
Ce	48.7	16.7	-	-	93.4	61.6	-	49.4	-	18.7	93.6	81.6	68.1	-	-	110	150	-	180
Pr	6.76	2.37	-	-	12.59	8.59	-	6.82	-	2.93	12.83	10.10	9.28	-	-	12.98	15.95	-	17.83
Nd	28.5	12.42	-	-	52.2	37.4	-	30.3	-	13.93	54.9	39.1	40.6	-	-	47.3	67.8	-	74.7
Sm	6.74	4.16	-	-	11.10	9.24	-	7.65	-	3.35	12.37	7.89	10.13	-	-	9.21	13.50	-	14.92
Eu	1.84	1.35	-	-	2.99	2.78	-	2.56	-	1.18	4.01	2.19	2.77	-	-	1.64	2.31	-	2.48
Tb	1.34	0.94	-	-	1.43	1.50	-	1.31	-	0.64	1.91	1.11	1.53	-	-	1.27	2.04	-	1.93
Gd	7.68	5.22	-	-	10.20	9.53	-	8.17	-	3.82	12.10	7.45	10.07	-	-	8.01	12.02	-	12.56
Dy	8.03	6.68	-	-	7.53	9.16	-	8.44	-	4.20	11.73	6.24	9.10	-	-	7.32	12.88	-	10.59
Ho	1.37	1.42	-	-	1.53	1.76	-	1.66	-	0.88	2.22	1.24	1.72	-	-	1.41	2.49	-	1.93
Er	3.35	4.01	-	-	4.19	4.70	-	4.44	-	2.54	5.87	3.54	4.55	-	-	4.05	6.82	-	5.36
Yb	2.73	3.97	-	-	3.70	4.10	-	3.94	-	2.64	4.99	3.30	3.96	-	-	3.77	6.02	-	5.20
Lu	0.40	0.58	-	-	0.54	0.58	-	0.57	-	0.39	0.71	0.51	0.56	-	-	0.53	0.85	-	0.78
Hf	5.71	2.99	-	-	5.74	6.30	-	5.01	-	3.58	7.40	5.41	6.64	-	-	5.03	7.85	-	7.44
Ta	1.55	0.32	-	-	0.90	2.02	-	1.41	-	0.33	2.46	1.35	2.43	-	-	1.59	2.55	-	2.63
W	2.13	4.14	-	-	0.29	2.34	-	3.60	-	0.18	0.78	0.24	0.33	-	-	7.62	9.89	-	7.64
Tl	0.20	0.02	-	-	0.17	0.06	-	0.08	-	0.03	0.09	0.02	0.19	-	-	1.06	1.00	-	1.12
Pb	5.57	1.17	-	-	6.02	2.31	-	2.80	-	2.37	7.67	12.33	9.70	-	-	16.72	21.9	-	29.8
Th	1.19	0.08	-	-	2.95	1.47	-	1.44	-	0.24	2.68	6.02	2.95	-	-	17.51	24.6	-	23.6
U	0.32	0.29	-	-	0.80	0.76	-	0.46	-	0.25	0.60	1.62	0.84	-	-	3.51	4.19	-	4.71

Los elementos mayores fueron analizados por FRX, mientras que los elementos traza por ICP-MS. LOI = pérdida por calcinación.

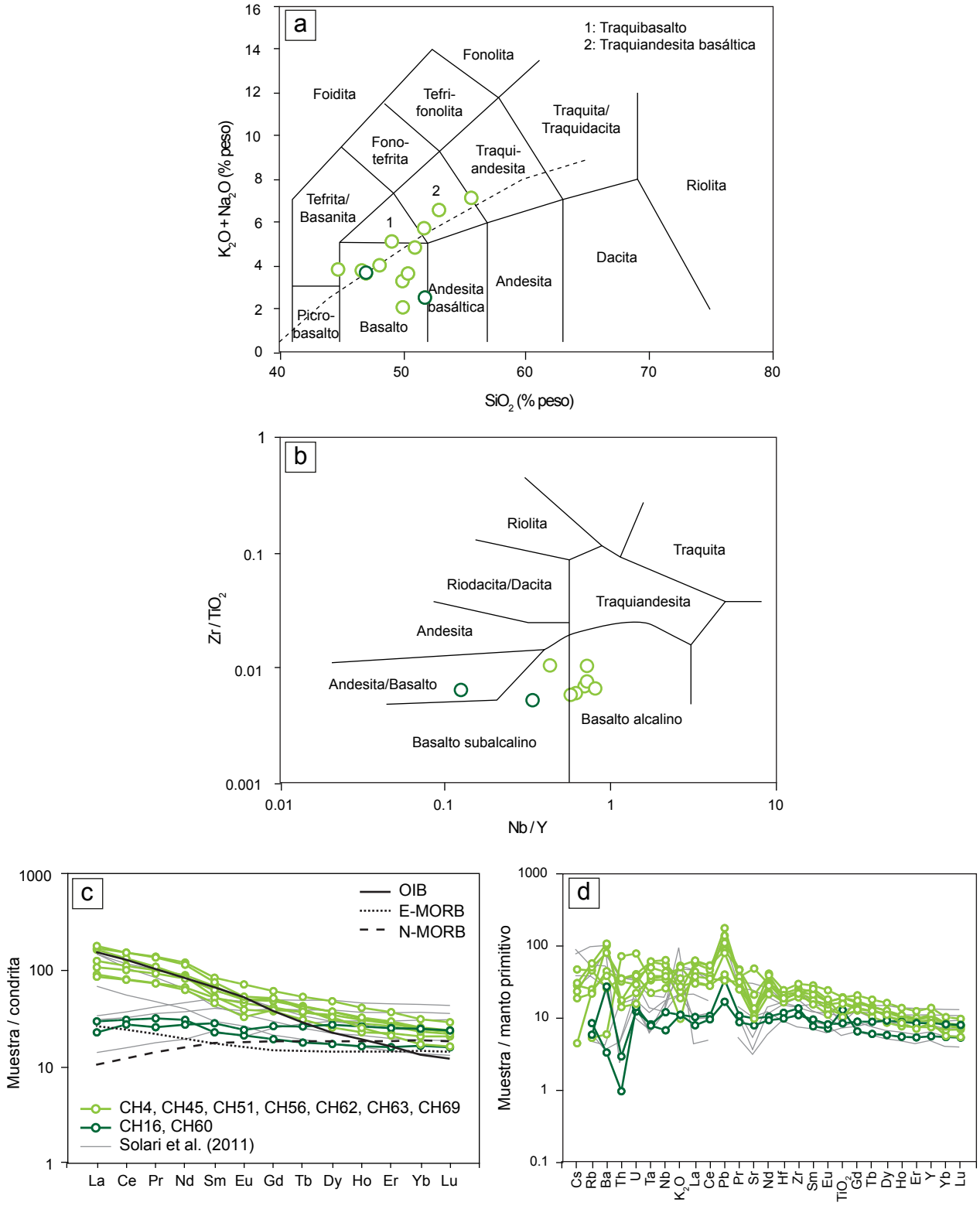

Figura A1. Química de roca total de las metabasitas. a) Diagrama de álcalis total vs. sílice (TAS) para rocas volcánicas. b) Diagrama Zr/TiO_2 vs. Nb/Y de Winchester & Floyd (1977). c) Diagrama de tierras raras (REE) normalizadas con respecto a los valores de la condrita de McDonough & Sun (1995). d) Diagrama de multi-elementos normalizados con respecto a los valores del manto primitivo de McDonough & Sun (1995).

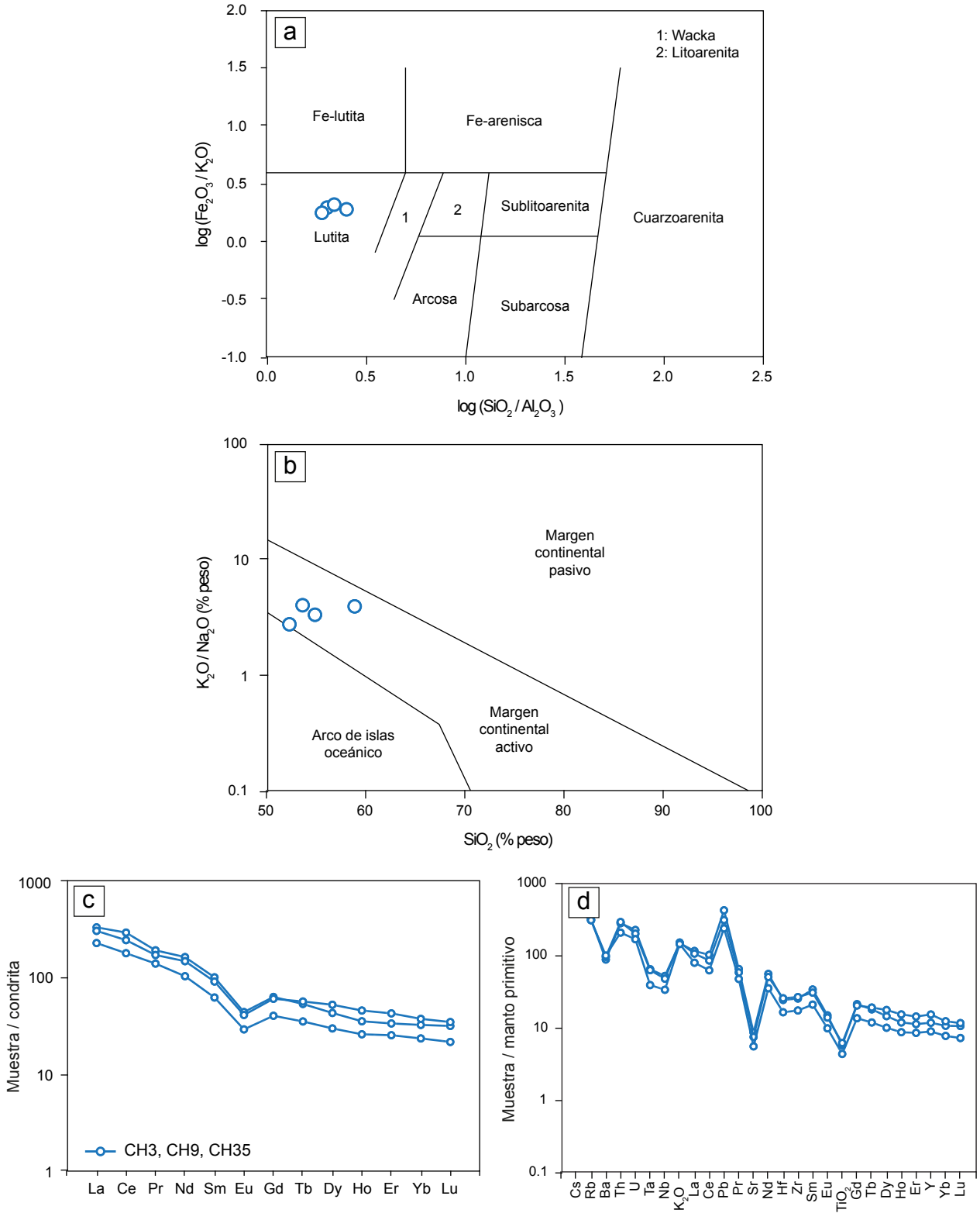

Figura A2. Química de roca total de las metapelitas. a) Diagrama de clasificación de las rocas terrígenas de Herron (1988). b) Diagrama de discriminación tectónica K_2O/Na_2O vs. sílice de Roser & Korsch (1986). c) Diagrama de tierras raras (REE) normalizadas con respecto a los valores de la condrita de McDonough & Sun (1995). d) Diagrama de multi-elementos normalizados con respecto a los valores del manto primitivo de McDonough & Sun (1995).

Metapelitas

Las muestras de metapelita poseen composiciones de lutita según el esquema de clasificación para rocas terrígenas de Herron (1988; Fig. A2a), mientras que quedan contenidas en el campo correspondiente a ambientes de margen continental activo del diagrama de discriminación tectónica K_2O/Na_2O vs. sílice (Roser & Korsch, 1986; Fig. A2b). En términos de los elementos traza, las muestras estudiadas muestran consistentemente un enriquecimiento en REE ligeras y patrones semiplanos en REE pesadas que resultan en valores $(La/Yb)_N$ = 9.8-10.3, así como una anomalía negativa en Eu (Fig. A2c). Los patrones de elementos incompatibles muestran anomalías negativas pronunciadas de Ba, Ta, Nb, Sr y Ti, así como una anomalía positiva acentuada de Pb (Fig. A2d). Estas características son similares a las que muestran las composiciones PASS y NARC (Condie, 1993), y pueden ser atribuidas a la presencia de productos de erosión de rocas ígneas ácidas y otras rocas de la corteza continental superior.

Geocronología U-Pb en zircón

Los análisis isotópicos U-Pb en zircón fueron obtenidos a través de ICP-MS por ablación laser (LA-ICP-MS) en el LEI, Centro de Geociencias, UNAM, siguiendo la metodología que se detalla en el *Appendix S1*. Los resultados obtenidos se presentan en la Tabla A3.

Eclogita con fengita (CH45)

Esta muestra contiene abundantes cristales prismáticos a redondeados de zircón de hasta 200 µm de longitud. En las imágenes de Cl se observan tanto núcleos heredados prismáticos como núcleos aparentemente corroídos, los cuales exhiben un zoneamiento variable de oscilatorio a heterogéneo, así como sobrecrecimientos con luminiscencia moderada que tienden a ser texturalmente más homogéneos (Fig. A3). Un conjunto de 33 análisis de los núcleos dio resultados concordantes a ligeramente discordantes con edades $^{206}Pb/^{238}U$ de entre ca. 1356 y 427 Ma, mientras que 14 mediciones en sobrecrecimientos con un ligero zoneamiento oscilatorio fueron concordantes, dando edades entre ca. 437 y 321 Ma (Fig. A4a) y valores Th/U de hasta 1.32. Una edad $^{206}Pb/^{238}U$ promedio de 432 +15/-16 Ma fue obtenida a partir de un grupo coherente de 14 análisis (Fig. A4b), utilizando el algoritmo TuffZirc (Ludwig, 2012). Adicionalmente, 5 análisis realizados en sobrecrecimientos idiomórficos con luminiscencia relativamente baja y homogénea resultaron en edades concordantes entre ca. 232 y 200 Ma, así como en valores Th/U significativamente menores de 0.03 a 0.01.

La variación en las edades obtenidas en los núcleos sugiere que algunos de los cristales analizados pudieran ser heredados (asimilados) o detríticos. Puesto que es más probable que tal variación sea el resultado de un aporte detrítico, se interpreta que la muestra CH45 pudiera tener un origen sedimentario, de forma similar a las interpretaciones de Solari *et al*. (2011) y Martens *et al*. (2012) en rocas similares. La edad promedio de ca. 432 Ma se interpreta como la edad de la fuente predominante de sedimento, la cual es análoga a la edad de protolito obtenida para la muestra CH56 (sección 6.1) y apenas más antigua, dentro de los errores, que la edad de protolito de la muestra CH62 (ver a continuación). Por último, las edades concordantes de entre 232 y 200 Ma se interpretan como edades de cristalización relacionadas con un evento metamórfico ocurrido durante el Triásico Tardío.

Eclogita con fengita (CH62)

Esta muestra se caracteriza por un contenido bajo de zircón, el cual se presenta como cristales de forma granular a prismática. En las imágenes de CL (no mostradas) se observan algunos núcleos heredados con luminiscencia baja, los cuales están sobrecrecidos por bordes predominantes que exhiben una luminiscencia moderada a alta y un ligero zoneamiento oscilatorio. Un grupo de 9 análisis de estos dominios externos dio como resultado edades concordantes a ligeramente discordantes en el intervalo de ca. 454 a 379 Ma (Fig. A4c) y valores Th/U = 0.02-0.53, definiendo una edad $^{206}Pb/^{238}U$ promedio de 398.4 ± 6.3 Ma (MSWD = 1.8; un dato descartado). Esta edad de ca. 400 Ma es interpretada como la edad de cristalización del protolito ígneo de esta roca.

Para-piroxenita (CH79)

Esta muestra contiene abundantes cristales redondeados a prismáticos de zircón de hasta 250 µm en longitud. Las imágenes de CL (no mostradas) revelan la presencia de núcleos heredados con morfología irregular y un zoneamiento aparentemente oscilatorio. Algunos de los cristales, sin embargo, son relativamente homogéneos en textura, al igual que los sobrecrecimientos que rodean los núcleos heredados. Un grupo de 11 puntos medidos tanto en núcleos como en bordes resultó en edades $^{206}Pb/^{238}U$ concordantes entre ca. 1017 y 924 Ma y valores Th/U = 0.2-0.9, lo que indica la presencia de zircón proterozoico de origen probablemente magmático. Por otro lado, un número de 5 análisis realizados en las zonas de borde define un grupo acotado concordante con edades entre ca. 475 y 387 Ma y valores Th/U significativamente bajos (0.001-0.04), el cual resulta en una edad $^{206}Pb/^{238}U$ promedio imprecisa de 420 ± 34 Ma (MSWD = 4.8).

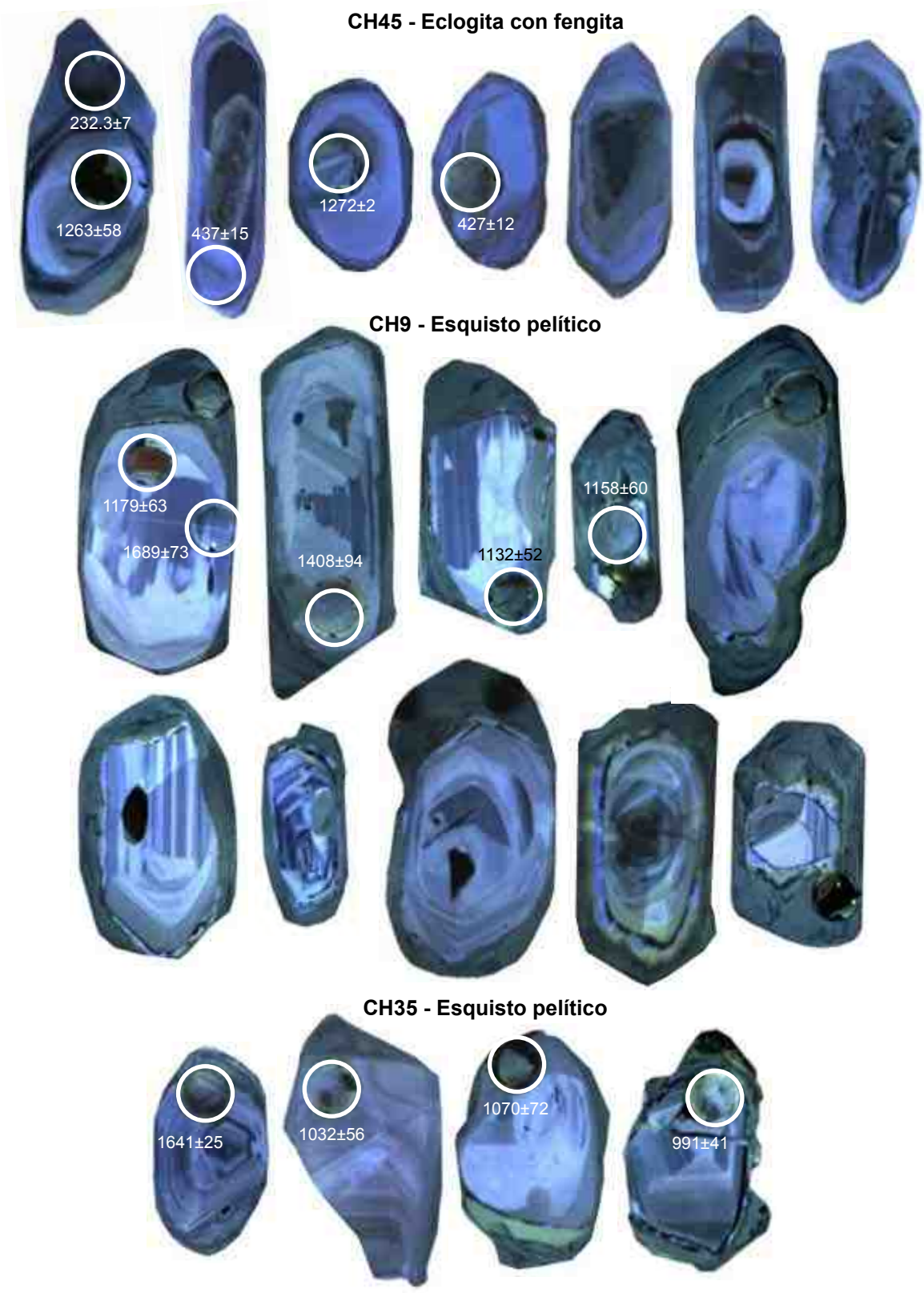

Figura A3. Imágenes de catodoluminiscencia (CL) de cristales representativos de zircón de tres de las muestras analizadas. Los círculos blancos indican las zonas analizadas, así como el diámetro (23 µm) del haz láser utilizado y sus edades $^{206}Pb/^{238}U$ (<1.0 Ga) y $^{207}Pb/^{206}Pb$ (>1.0 Ga) correspondientes.

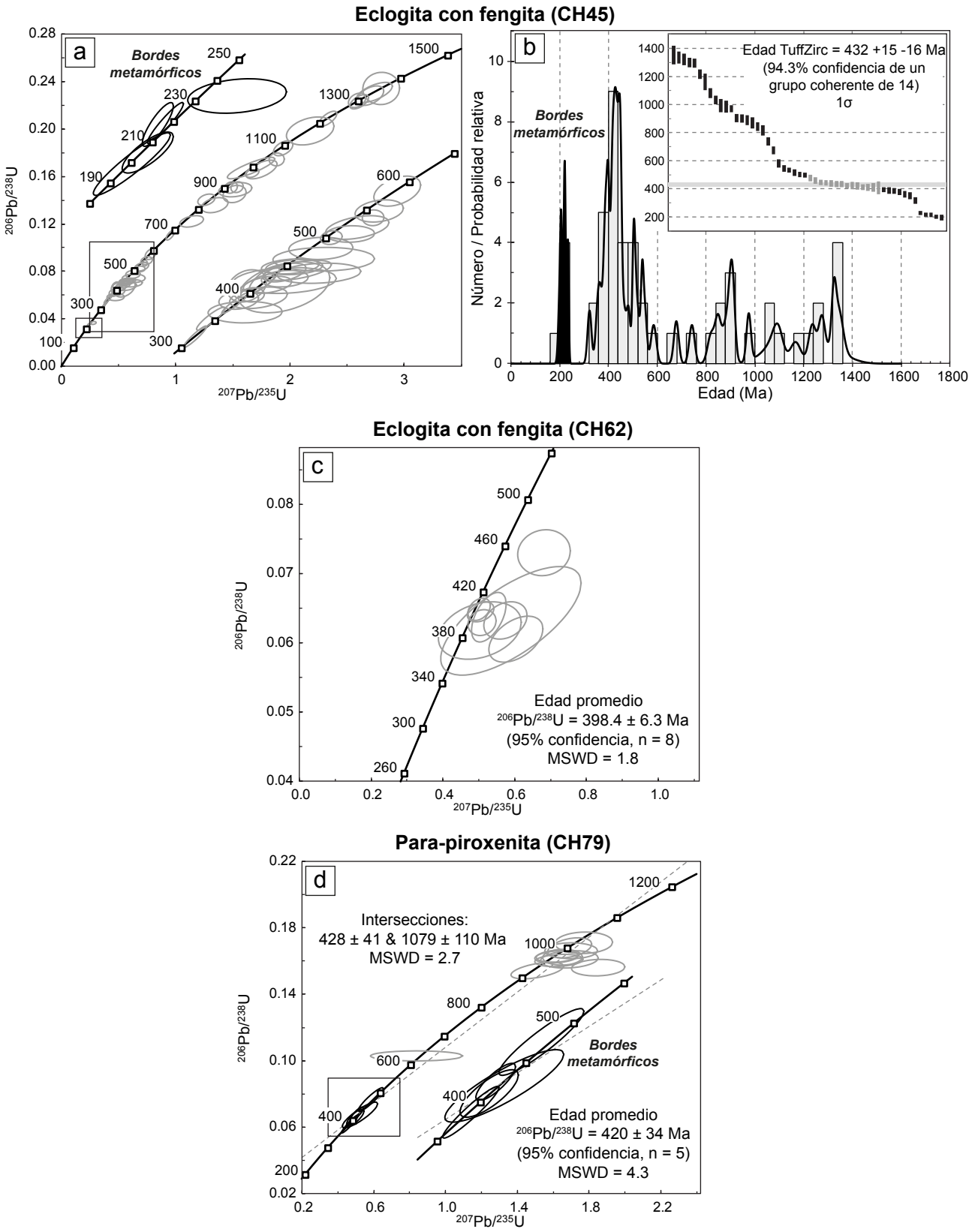

Figura A4. Resultados de los análisis geocronológicos U-Pb en zircón de las metabasitas. a) Diagrama de concordia y b) diagrama de frecuencia y probabilidad relativa de edades ($^{206}Pb/^{238}U$: <1.0 Ga; $^{207}Pb/^{206}Pb$: >1.0 Ga) para la eclogita CH45. c) y d) Diagramas de concordia para la eclogita CH62 y la para-piroxenita CH79, respectivamente.

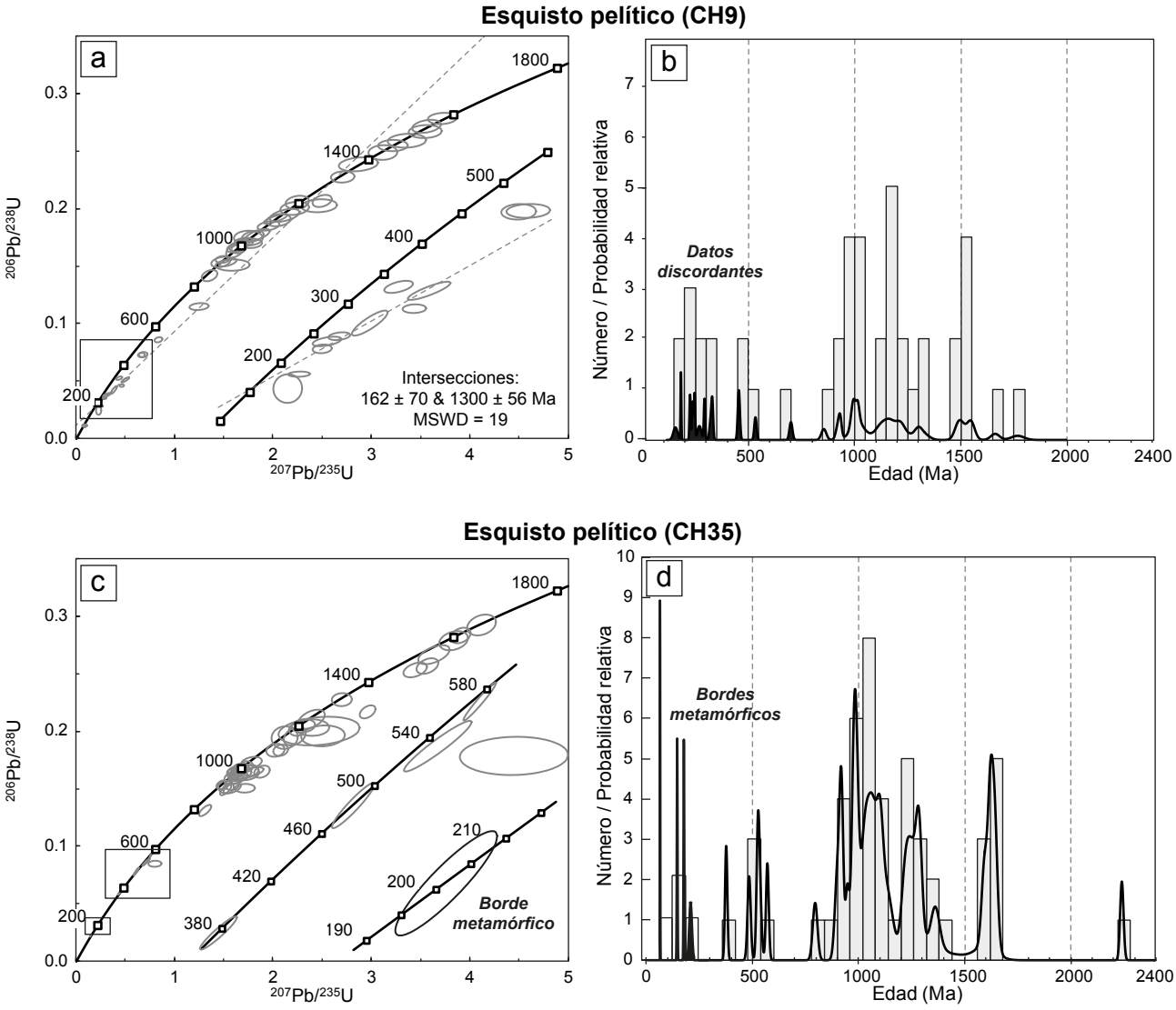

Figura A5. Resultados de los análisis geocronológicos U-Pb en zircón de las metapelitas. a), c) Diagramas de concordia y b), d) diagramas de frecuencia y probabilidad relativa de edades ($^{206}Pb/^{238}U$: <1.0 Ga; $^{207}Pb/^{206}Pb$: >1.0 Ga) para las metapelita CH9 y CH35, respectivamente.

A pesar de que esta roca se encuentra espacialmente relacionada con ortogneisses graníticos y otras rocas metaígneas, hay evidencias petrográficas y químicas que sugieren un protolito de origen sedimentario calcosilicatado (Tablas A1 y A2). Por lo tanto, las edades obtenidas de ca. 1.0 Ga pudieran representar un componente detrítico y no la edad del protolito. La edad promedio de ca. 420 Ma, en cambio, es interpretada como una edad de cristalización metamórfica, por lo que se sugiere que la edad del protolito estaría comprendida entre 1.0 Ga y 420 Ma.

Esquisto pelítico (CH9)

Esta roca contiene abundantes cristales prismáticos de zircón de hasta 300 μm en longitud. En las imágenes de CL se observan núcleos heredados tanto prismáticos como visiblemente corroídos, los cuales exhiben luminiscencia alta y un zoneamiento oscilatorio, a diferencia de los sobrecrecimientos metamórficos que los rodean (Fig. A3). Las edades y características de dichos sobrecrecimientos metamórficos fueron descritas en la sección 6.1. Un conjunto de 31 análisis de los núcleos resultó en una serie de datos que se extienden a lo largo de la línea de concordia con edades $^{206}Pb/^{238}U$ de entre ca. 1582 y 854 Ma (Figs. A5a-b) y valores Th/U entre 0.02 y 1.2. Un grupo menor de 13 análisis dio resultados discordantes (Disc. = 11-26 %) con edades $^{206}Pb/^{238}U$ entre ca. 700 y 155 Ma, los cuales definen una aparente línea de discordia con un intersección inferior imprecisa en 162 ± 70 Ma (MSWD = 19). Las edades $^{207}Pb/^{206}Pb$ correspondientes varían de manera aleatoria entre 1173 y 621 Ma, sugiriendo una pérdida de Pb variable e indicando únicamente las edades mínimas de las fuentes. Por lo tanto, la edad concordante de ca. 854 Ma (edad $^{207}Pb/^{206}Pb$ = 1132 Ma) es interpretada como una estimación conservadora de la edad máxima del depósito del protolito sedimentario y las edades discordantes se interpretan como el resultado de un episodio de pérdida de Pb que ocurriría probablemente durante el Cretácico.

Esquisto pelítico (CH35)

Esta muestra contiene abundantes cristales de zircón similares en morfología y tamaño a los de la muestra CH9 pero con sobrecrecimientos metamórficos menos prominentes (Fig. A3). Un grupo de 50 mediciones en núcleos con zoneamiento oscilatorio resultó en datos concordantes a moderadamente discordantes (Disc. < 12%) con edades $^{206}Pb/^{238}U$ de entre ca. 1654 y 795 Ma (Fig. A5c). Otras edades concordantes a ligeramente discordantes, obtenidas en sobrecrecimientos aparentemente metamórficos y con valores Th/U ≤ 0.1, definen picos de probabilidad relativa a ca. 500 y 400 Ma (Fig. A5d), sin embargo el análisis morfológico/textural no es concluyente sobre si estos sobrecrecimientos son intrínsecos de los granos

detríticos o si estos cristalizaron durante un evento metamórfico posterior. Por otro lado, algunas mediciones aisladas sobre crecimientos metamórficos que claramente carecen de un retrabajo típico del transporte sedimentario, resultaron en edades $^{206}Pb/^{238}U$ concordantes de ca. 203, 172, 140 y 60 Ma (Th/U = 0.01-0.04), revelando episodios múltiples de crecimiento metamórfico de zircón desde el Triásico Tardío hasta el Paleoceno. Por lo anterior, la edad de ca. 203 Ma se considera, de manera conservadora, una estimación de la edad mínima del protolito sedimentario de esta muestra.

Discusión y conclusiones

Origen de los protolitos básicos

La información química y geocronológica de las metabasitas de la Sierra de Chuacús es escasa, por lo cual resulta difícil plantear escenarios tectonomagmáticos-temporales para explicar el origen de sus protolitos. Sin embargo, como se mencionó en la sección 7.2, las edades de protolito U-Pb en zircón de ca. 425 Ma (CH56), 226 Ma (Martens *et al*., 2012; Solari *et al*., 2011) y 167 Ma (CH60), revelan que las metabasitas del área de estudio registran distintos episodios de magmatismo básico, ocurridos desde el periodo Silúrico hasta el Jurásico Medio. La edad U-Pb en zircón de 398.4 ± 6.3 Ma, obtenida en una eclogita adicional (CH62), es consistente con esta interpretación, confirmando la ocurrencia de un magmatismo Silúrico-Devónico Temprano (425-400 Ma) que no había sido documentado anteriormente. Los datos químicos de roca total indican que las metabasitas de esta edad (CH56, CH62) son equivalentes en composición al basalto alcalino y similares en sus abundancias de elementos traza a la composición del OIB (Fig. A1). Un número considerable de estudios previos han documentado la ocurrencia de rocas (meta) basálticas y graníticas del Ordovícico-Silúrico en el sur de México y Guatemala (e.g. Keppie *et al*., 2008; Ortega-Obregón *et al*., 2008; Ortega-Obregón *et al*., 2010; Estrada-Carmona *et al*., 2012), sin embargo, la evidencia de magmatismo Silúrico-Devónico Temprano es escasa y se restringe básicamente a los plutones graníticos de las Montañas Maya en Belice, los cuales poseen edades de cristalización de ca. 415-400 Ma y fueron probablemente originados en un ambiente magmático relacionado con subducción (Weber *et al*., 2012). Por lo tanto, estas unidades no son directamente correlacionables con las metabasitas contemporáneas de la Sierra de Chuacús, las cuales, en cambio, pudieron originarse en un ambiente de arco de islas o de rift continental durante un periodo de rompimiento incipiente del margen occidental de Gondwana. Las relaciones espacial y petrogenética de estas rocas máficas con los metagranitos del Ordovícico-Silúrico expuestos al norte de la Sierra de Chuacús (Solari *et al*., 2011) son ambiguas y se requieren estudios adicionales que permitan cotejarlas.

Las edades de ca. 226 Ma reportadas por Solari *et al*. (2011) y Martens *et al*. (2012) indican además un episodio de magmatismo básico durante el Triásico Tardío, pero desafortunadamente no hay datos químicos que permitan interpretar estas edades en términos de la petrogénesis de los protolitos. A pesar de ello, su relación espacio-temporal con metagranitos de ca. 224 Ma, aparentemente derivados de una fuente magmática no empobrecida (Capítulo 4), es indicativa de un episodio de magmatismo bimodal ocurrido probablemente en un ambiente intraplaca durante el rompimiento temprano de Pangea.

La muestra con edad de protolito del Jurásico Medio (CH60), es una de las muestras que mostró composiciones equivalentes al basalto subalcalino y características comparables con la composición del E-MORB. Esta edad es relativamente joven pero dentro del intervalo de la provincia volcanosedimentaria Nazas del noreste de México, en particular de su prolongación al suroeste del bloque Maya (Godínez-Urban *et al*., 2011), donde se han reportado principalmente rocas volcánicas ácidas a intermedias y flujos basálticos minoritarios probablemente relacionados a un ambiente extensional intraplaca, desarrollado durante la disgregación de Pangea (Martini & Ortega, 2016). Por lo tanto, la interpretación sobre el origen del protolito sería análoga, aunque en una etapa más avanzada, a la de los protolitos del Triásico Tardío.

No obstante esta diversidad cronológica, estudios previos han documentado que las eclogitas de las Sierra de Chuacús no derivan exclusivamente de protolitos de origen ígneo, sino que algunos horizontes máficos pudieron tener precursores sedimentarios (Solari *et al*., 2011; Martens *et al*., 2012). Esta interpretación se basa principalmente en el contenido de zircón aparentemente detrítico con edades U-Pb considerablemente variables, lo cuál es típico de las rocas metasedimentarias y, en algunos casos, de rocas graníticas originadas por anatexis (e.g. Helbig *et al*., 2012). Los datos U-Pb en zircón obtenidos en una eclogita con fengita (CH45) de la región de El Chol son consistentes con dicha interpretación, indicando una componente detrítica de entre 1.3 Ga y 321 Ma, así como un aporte predominante de ca. 432 Ma que es comparable con las edades de protolito del Silúrico-Devónico Temprano obtenidas a partir de las eclogitas CH56 y CH62. La edad concordante de ca. 321 Ma es interpretada como la edad máxima de depósito del protolito, mientras que la edad mínima de depósito estaría restringida por un borde de zircón metamórfico de ca. 232 Ma. Resulta relevante destacar que los datos químicos de roca total de ambos tipos de eclogita (metasedimentaria y metaígnea) indican una composición equivalente al basalto alcalino de afinidad OIB (Fig. A1), lo que lleva a tres posibles interpretaciones: (1) los cuerpos máficos metasedimentarios derivan mayoritariamente de la erosión y el depósito local de rocas ígneas de afinidad OIB con edad de cristalización del Silúrico-Devónico Temprano, y en menor medida de rocas continentales del Proterozoico medio-tardío; (2) dichas rocas metasedimentarias se originaron por el depósito de material volcanoclástico tipo OIB mezclado con sedimento derivado de una fuente continental con edad de hasta 1.3 Ga; y (3) una interpretación similar a la anterior pero con una mezcla detrítica tal que la afinidad OIB es ficticia e influenciada por detritos de distintas fuentes y composiciones. Con base

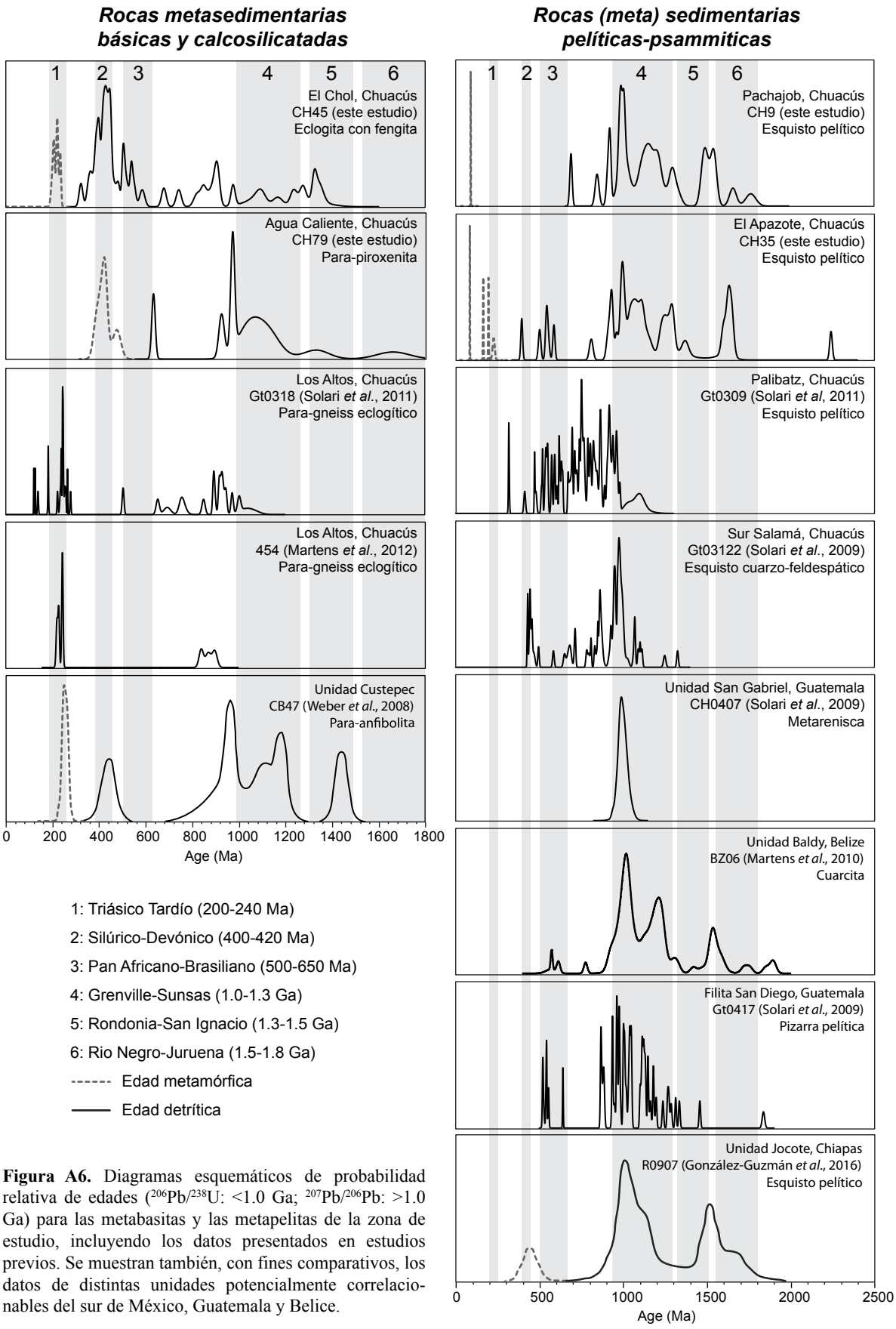

Figura A6. Diagramas esquemáticos de probabilidad relativa de edades ($^{206}Pb/^{238}U$: <1.0 Ga; $^{207}Pb/^{206}Pb$: >1.0 Ga) para las metabasitas y las metapelitas de la zona de estudio, incluyendo los datos presentados en estudios previos. Se muestran también, con fines comparativos, los datos de distintas unidades potencialmente correlacionables del sur de México, Guatemala y Belice.

en los datos de la eclogita CH45, la interpretación (3) es aparentemente más probable, en primer lugar porque el contenido de zircón en este tipo de metabasita es significativamente mayor, en comparación con lo comúnmente documentado en metabasitas de origen ígneo, y por otro lado, se observa un enriquecimiento relativo en Al_2O3, Na_2O y K_2O, así como anomalías negativas de Nb y Ta, lo que en su conjunto sugiere una influencia considerable de material félsico continental. Por lo anterior, se sugiere que la componente predominante de zircón de ca. 432 Ma pudiera provenir no solo de las metabasitas del Silúrico-Devónico Temprano, sino también de los (meta) granitoides contemporáneos expuestos en el norte del Complejo Chuacús (Solari *et al*., 2011) y en las Montañas Maya en Belice (Weber *et al*., 2012). En la Fig. A6 se observa que el área fuente de los metasedimentos básicos de la Sierra de Chuacús incluye además un aporte de tipo Pan Africana-Brasiliano (500-650 Ma), del Neoproterozoico, Grenvilliano-Sunsas (1.0-1.3 Ga) y en menor medida afín a la provincia Rondonia-San Ignacio (1.3-1.5 Ga), lo que es comparable con los patrones detríticos obtenidos en para-anfibolitas de la Unidad Custepec, en el Complejo Macizo de Chiapas (Weber *et al*., 2007; Weber *et al*., 2008).

Origen de los protolitos pelíticos

Los datos químicos de roca total en las metapelitas analizadas indican una composición típica de lutita, probablemente en un ambiente de margen continental activo a partir de sedimento derivado de una corteza continental félsica. El fechamiento U-Pb en zircón de dos muestras representativas (CH9, CH35) dio resultados similares, con una edad concordante de ca. 854 Ma (CH9) que se interpreta como la edad máxima de depósito del protolito. La edad mínima de depósito resulta de algún modo incierta por la presencia de crecimientos metamórficos de entre ca. 580-380 Ma que no son, de forma concluyente, atribuibles a un evento metamórfico post-diagenético. Por lo tanto, una edad concordante de ca. 203 Ma (CH35), obtenida en un crecimiento metamórfico claramente post-diagenético, es interpretada como la edad mínima de depósito. Los análisis U-Pb de zircón detrítico muestran que estas rocas están dominadas por un componente predominante tipo Grenville-Sunsas (1.0-1.3 Ga), así como también una población considerable de entre 1.4-1.7 Ma. El componente tipo Grenville-Sunsas, particularmente de 1.0-1.2 Ga, ha sido previamente documentado en rocas similares de la Sierra de Chuacús y también en otras localidades del sureste de México, Guatemala y Belice (Fig. A6), mientras que una población similar de 1.5 Ga ha sido reportada en las Unidades de Belice (Martens *et al*., 2010) y Jocote de Chiapas, México (González-Guzmán *et al*., 2016). Por otra parte, un componente detrítico de tipo Pan Africano-Brasiliano es aparentemente común en las rocas (meta) sedimentarias del bloque Maya (e.g. Weber *et al*., 2008), pero también se ha visto presente en la Filita San Diego del bloque Chortís, Guatemala (Solari *et al*., 2009). De resultar detríticas las edades de ca. 580 Ma obtenidas en la muestra CH35, es igualmente posible una

correlación con ambos bloques, sin embargo resulta evidente que los patrones detríticos de las muestras estudiadas son más afines con la Unidad Baldy de Belice (Fig. A6) y por lo tanto con el bloque Maya.

Evidencias de metamorfismo paleozoico

Estudios previos han reconocido, con base en edades U-Pb en zircón, dos posibles episodios de metamorfismo paleozoico en el complejo Chuacús (Ortega-Gutiérrez *et al*., 2004; Solari *et al*., 2011). En primer lugar, un grupo de edades de 348-324 Ma, obtenidas en un ortogneiss migmatítico de la región de El Chol, fueron interpretadas como el registro de un evento tectonotérmico ocurrido durante el Misisípico; sin embargo estas edades no han sido reportadas en otras localidades y esta interpretación no está suficientemente documentada. Por otro lado, Solari *et al*. (2011) documentan, en la misma muestra, un grupo de edades concordantes de entre 253 y 218 Ma, que ellos interpretan como la edad del evento anatéctico responsable de la migmatización. Este dato coincide con las edades de 243-220 Ma obtenidas en un gneiss migmatítico de la Sierra de las Minas (mismo trabajo), así como con una edad promedio de ca. 218 Ma obtenida en un gneiss migmatítico de la región de Huehuetenango, Guatemala (Ratschbacher *et al*., 2009). Las edades metamórficas de 232-200 Ma, obtenidas tanto en la eclogita CH45 como en la metapelita CH35 para equilibrios probablemente *subsolidus*, confirman adicionalmente la ocurrencia de este evento metamórfico del Triásico Tardío. Como lo sugieren Solari *et al*. (2011), la edad de este evento es consistente con la edad de un evento magmático de ca. 220 Ma, ampliamente reconocido en la Sierra de Chuacús (Solari *et al*., 2011; Martens *et al*., 2012; este trabajo). Por lo tanto, se interpreta que durante el Triásico Tardío, el basamento del complejo Chuacús experimentó un proceso combinado de magmatismo bimodal, metamorfismo de alto grado y anatexis, probablemente asociado con actividad ígnea intraplaca y relacionado con la fragmentación inicial de Pangea (Capítulo 4).

Por otra parte, los datos de U-Pb en zircón de la para-piroxenita CH79 proporcionan evidencia de un evento metamórfico adicional ocurrido en ca. 420 Ma. Esta edad es consistente con la edad del episodio magmático del Silúrico-Devónico Temprano (425-400 Ma) registrado por los protolitos básicos de afinidad OIB (CH56, CH62). Por lo tanto, de forma similar al evento tectonotérmico del Triásico Tardío, es probable que los episodios magmático y metamórfico del Silúrico-Devónico Temprano estén relacionados genéticamente y que en conjunto representen un evento tectonotérmico relacionado al desarrollo de un arco de islas o de un rift continental en el margen occidental de Gondwana, como se mencionó anteriormente.

Referencias

Condie, K. C. (1993). Chemical composition and evolution of the upper continental crust: contrasting results from surface samples and shales. *Chemical Geology*, *104*(1-4), 1-37.

Estrada-Carmona, J., Weber, B., Martens, U., & López-Martínez, M. (2012). Petrogenesis of Ordovician magmatic rocks in the southern Chiapas Massif Complex: relations with the early Palaeozoic magmatic belts of northwestern Gondwana. *International Geology Review*, *54*(16), 1918-1943.

Ferrari, L., Bergomi, M., Martini, M., Tunesi, A., Orozco-Esquivel, T., López-Martínez, M. (2014). Late Cretaceous-Oligocene magmatic record in southern Mexico: The case for a temporal slab window along the evolving Caribbean-North America-Farallon triple boundary. *Tectonics*, 33(9), 1738-1765.

Godínez-Urban, A., Lawton, T. F., Garza, R. S. M., Iriondo, A., Weber, B., & López-Martínez, M. (2011). Jurassic volcanic and sedimentary rocks of the La Silla and Todos Santos Formations, Chiapas: Record of Nazas arc magmatism and rift-basin formation prior to opening of the Gulf of Mexico. *Geosphere*, *7*(1), 121-144.

González-Guzmán, R., Weber, B., Manjarrez-Juárez, R., Cisneros de León, A., Hecht, L., & Herguera-García, J. C. (2016). Provenance, age constraints and metamorphism of Ediacaran metasedimentary rocks from the El Triunfo Complex (SE Chiapas, México): evidence for Rodinia breakup and Iapetus active margin. *International Geology Review*, *58*(16), 2065-2091.

Helbig, M., Keppie, J. D., Murphy, J. B., & Solari, L. A. (2012). U–Pb geochronological constraints on the Triassic–Jurassic Ayú Complex, southern Mexico: Derivation from the western margin of Pangea-A. *Gondwana Research*, *22*(3), 910-927.

Herron, M. M. (1988). Geochemical classification of terrigenous sands and shales from core or log data. *Journal of Sedimentary Research*, *58*(5).

Keppie, J.D., Dostal, J., Miller, B.V., Ramos-Arias, M.A., Morales-Gámez, M., Nance, R.D., Murphy, J.B., Ortega-Rivera, A., Lee, J.W.K., Housh, T. & Cooper, P., 2008. Ordovician–earliest Silurian rift tholeiites in the Acatlán Complex, southern Mexico: Evidence of rifting on the southern margin of the Rheic Ocean. *Tectonophysics*, *461*(1), 130-156.

Le Maitre, R.W.B., Dudek, P., Keller, A., Lameyre, J., Le Bas, J., Sabine, M.J., Schmid, P.A., Sorensen, R., Streckeisen, H., Woolley, A. & Zanettin, A.R., 1989. *A classification of igneous rocks and glossary of terms: Recommendations of the International Union of Geological Sciences, Subcommission on the Systematics of Igneous Rocks* (No. 552.3 CLA). International Union of Geological Sciences.

Ludwig, K. R. (2012). User's Manual for Isoplot 3.75, A Geochronological Toolkit for Microsoft Excel. Berkeley Geochronology Center Special Publication, *5*.

Lozano, R., Bernal, J. (2005). Characterization of a new set of eight geochemical reference materials for XRF major and trace element analysis. *Revista Mexicana de Ciencias Geológicas*, 22(3), 329-344.

Martens, U. C., Brueckner, H. K., Mattinson, C. G., Liou, J. G., & Wooden, J. L. (2012). Timing of eclogite-facies metamorphism of the Chuacús complex, Central Guatemala: record of Late Cretaceous continental subduction of North America's sialic basement. *Lithos*, *146*, 1-10.

Martens, U., Weber, B., & Valencia, V. A. (2010). U/Pb geochronology of Devonian and older Paleozoic beds in the southeastern Maya block, Central America: Its affinity with peri-Gondwanan terranes. *Geological Society of America Bulletin*, *122*(5-6), 815-829.

Martini, M., & Ortega-Gutiérrez, F. (2016). Tectono-stratigraphic evolution of eastern Mexico during the break-up of Pangea: A review. *Earth-Science Reviews*.

McDonough, W. F., & Sun, S. S. (1995). The composition of the Earth. *Chemical Geology*, *120*(3-4), 223-253.

Ortega-Gutiérrez, F., Solari, L. A., Solé, J., Martens, U., Gómez-Tuena, A., Morán-Ical, S., & Reyes-Salas, M. (2004). Polyphase, high-temperature eclogite-facies metamorphism in the Chuacús

Complex, central Guatemala: Petrology, geochronology, and tectonic implications. *International Geology Review*, *46*(5), 445-470.

Ortega-Obregon, C., Murphy, J. B., & Keppie, J. D. (2010). Geochemistry and Sm–Nd isotopic systematics of Ediacaran–Ordovician, sedimentary and bimodal igneous rocks in the western Acatlán Complex, southern Mexico: Evidence for rifting on the southern margin of the Rheic Ocean. *Lithos*, *114*(1), 155-167.

Ortega-Obregón, C., Solari, L. A., Keppie, J. D., Ortega-Gutiérrez, F., Solé, J., & Morán-Ical, S. (2008). Middle-Late Ordovician magmatism and Late Cretaceous collision in the southern Maya block, Rabinal-Salamá area, central Guatemala: implications for North America–Caribbean plate tectonics. *Geological Society of America Bulletin*, *120*(5-6), 556-570.

Ratschbacher, L., Franz, L., Min, M., Bachmann, R., Martens, U., Stanek, K., Stübner, K., Nelson, B.K., Herrmann, U., Weber, B. & López-Martínez, M., 2009. The North American-Caribbean plate boundary in Mexico-Guatemala-Honduras. *Geological Society, London, Special Publications*, *328*(1), 219-293.

Roser, B. P., & Korsch, R. J. (1986). Determination of tectonic setting of sandstone-mudstone suites using content and ratio. *The Journal of Geology*, *94*(5), 635-650.

Solari, L. A., Ortega-Gutiérrez, F., Elías-Herrera, M., Schaaf, P., Norman, M., Ortega-Obregón, C., & Chiquín, M. (2009). U-Pb zircon geochronology of Palaeozoic units in western and central Guatemala: Insights into the tectonic evolution of Middle America. *Geological Society, London, Special Publications*, *328*(1), 295-313.

Solari, L. A., Tuena, A. G., Gutiérrez, F. O., & Obregón, C. O. (2011). The Chuacús Metamorphic Complex, central Guatemala: geochronological and geochemical constraints on its Paleozoic-Mesozoic evolution. *Geologica Acta*, *9*(3-4), 329-350.

Weber, B., Iriondo, A., Premo, W. R., Hecht, L., & Schaaf, P. (2007). New insights into the history and origin of the southern Maya block, SE México: U–Pb–SHRIMP zircon geochronology from metamorphic rocks of the Chiapas massif. *International Journal of Earth Sciences*, *96*(2), 253-269.

Weber, B., Schaaf, P., Valencia, V. A., Iriondo, A., & Ortega-Gutiérrez, F. (2006). Provenance ages of late Paleozoic sandstones (Santa Rosa Formation) from the Maya Block, SE México: implications on the tectonic evolution of western Pangea. *Revista Mexicana de Ciencias Geológicas*, *23*(3), 262-276.

Weber, B., Scherer, E. E., Martens, U. K., & Mezger, K. (2012). Where did the lower Paleozoic rocks of Yucatan come from? AU–Pb, Lu–Hf, and Sm–Nd isotope study. *Chemical Geology*, *312*, 1-17.

Weber, B., Valencia, V. A., Schaaf, P., Pompa-Mera, V., & Ruiz, J. (2008). Significance of provenance ages from the Chiapas Massif Complex (southeastern Mexico): redefining the Paleozoic basement of the Maya Block and its evolution in a peri-Gondwanan realm. *The Journal of Geology*, *116*(6), 619-639.

Winchester, J. A., & Floyd, P. A. (1977). Geochemical discrimination of different magma series and their differentiation products using immobile elements. *Chemical Geology*, *20*, 325-343.

4

Origen y metamorfismo de alta presión del basamento continental granítico del Complejo Chuacús

---

Maldonado, R., Ortega-Gutiérrez, F., & Ortíz-Joya, G. A. (2018). Subduction of Proterozoic to Late Triassic continental basement in the Guatemala Suture Zone: A petrological and geochronological study of high-pressure metagranitoids from the Chuacús complex. *Lithos*, 308, 83-103.

CONTRIBUCIÓN DE LOS COAUTORES

Roberto Maldonado: planeación del proyecto, trabajo de campo, obtención, procesamiento e interpretación de los datos, redacción del artículo.

Fernando Ortega Gutiérrez: supervisión del trabajo, revisión del borrador del artículo.

Guillermo A. Ortíz Joya: trabajo de campo, procesamiento e interpretación de los datos, revisión del borrador del artículo.

Nota de error: los pies de figura en Fig. 7 y Fig. 8 están invertidos. El pie de figura en Fig. 7 describe la Fig. 8 y viceversa.

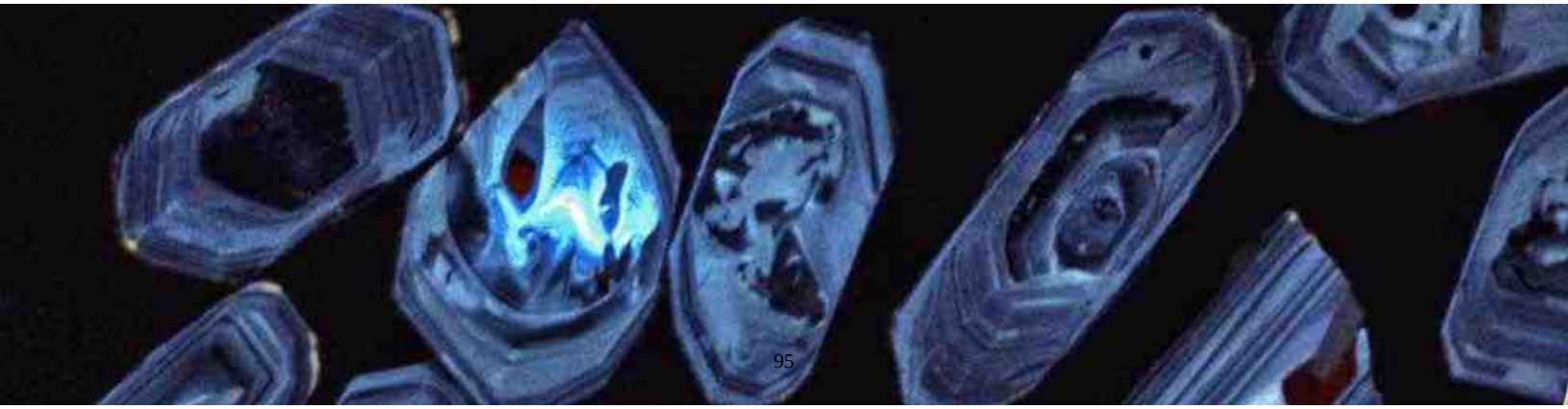

Lithos 308–309 (2018) 83–103

Contents lists available at ScienceDirect

Lithos

journal homepage: www.elsevier.com/locate/lithos

Subduction of Proterozoic to Late Triassic continental basement in the Guatemala suture zone: A petrological and geochronological study of high-pressure metagranitoids from the Chuacús complex

Roberto Maldonado [a,*], Fernando Ortega-Gutiérrez [a], Guillermo A. Ortíz-Joya [b]

[a] Instituto de Geología, Universidad Nacional Autónoma de México, D.F., Mexico
[b] Facultad de Ciencias, Universidad Nacional Autónoma de México, D.F., Mexico

ARTICLE INFO

Article history:
Received 17 November 2017
Accepted 26 February 2018
Available online 06 March 2018

Keywords:
Continental subduction
Guatemala suture zone
Chuacús complex
High-pressure metagranites
Thermobarometry
U-Pb geochronology

ABSTRACT

Many continental subduction complexes contain abundant granitic rocks coexisting with minor volumes of eclogite-facies rocks. Characterization of granitic protoliths is crucial to decipher the origin of subducted continental crust, whereas knowledge of its metamorphic evolution is required to constrain the mechanisms of burial and exhumation. In this work we present geochronological and petrological evidence that demonstrate the occurrence of a subducted Proterozoic to Late Triassic granitic basement in the Chuacús complex of central Guatemala. Metagranitoids exposed in this area are interlayered with eclogite and other high-pressure rocks, and their structure is considerably variable due to strain partitioning during deformation. Laser ablation-inductively coupled plasma-mass spectrometry U-Pb zircon data from two ferroan metagranites yield protolith crystallization ages of ca. 1.1 Ga and their trace-element abundances suggest an origin related to intraplate magmatism, while a high-silica, peraluminous metagranite is dated at 1.0 Ga and was probably originated by partial melting of a high-grade continental crust. On the other hand, two megacrystic to augen metagranitoids yield protolith crystallization ages of ca. 224 Ma, which are identical within errors to the protolith age of hosted eclogitic metabasites. Their high incompatible trace element abundances together with the observed spatial-temporal relationships with mafic protoliths suggest that Late Triassic bimodal magmatism in the Chuacús complex was probably originated in a within-plate setting. Regardless of their age or structure, the studied metagranites preserve evidences for high-pressure metamorphic equilibration, such as the occurrence of Ca-rich garnet (X_{Ca} up to 0.52) in association with phengite (Si contents of up to 3.4 pfu) and rutile. The integration of Zr-in-rutile thermometry and phengite barometry allows the peak metamorphic conditions to be constrained at ~640–680 °C and ~13 kbar. This pressure-temperature estimate indicates that metagranitoids underwent high-pressure metamorphism but equilibrated at significantly lower pressures than associated eclogite-facies rocks, and, therefore, they do not necessarily share a common high-pressure metamorphic evolution. The new data show that the Chuacús complex in the study area represents a Proterozoic (1.1–1.0 Ga) to Late Triassic (220 Ma) continental basement that was subducted, and consequently metamorphosed under high-pressure conditions, during the Cretaceous evolution of the North America-Caribbean plate boundary.

1. Introduction

Granitoids constitute an important part of the continental crust, being present in a variety of settings and along the geological time. Several studies in high-pressure (HP) and ultrahigh-pressure (UHP) terranes have shown that granitic crust is commonly involved in continental subduction processes (e.g. Carswell et al., 2000; Compagnoni and Rolfo, 2003; Le Goff and Ballèvre, 1990). In most cases, metagranitoids are volumetrically dominant and often closely related to minor volumes of eclogite and other HP rocks. Determining the age and nature of granitic protoliths is a crucial aspect to decipher the origin of subducted continental crust and establish plausible regional correlations (e.g. Hacker et al., 1998; Liu et al., 2004; Rowley et al., 1997). Petrological studies, in addition, allow comparison between the pressure-temperature (*P-T*) conditions experienced by both metagranites and hosted HP rocks, which provides insight into the mechanisms of burial and exhumation during subduction.

The Caribbean suture system delineates a continental-scale tectonic feature comprising both oceanic and continental subduction complexes. In the westernmost part of this system, the Chuacús complex (Ortega-Gutiérrez et al., 2004) of central Guatemala records continental subduction and collision of the North American plate beneath the

* Corresponding author at: Instituto de Geología, Universidad Nacional Autónoma de México, Ciudad Universitaria, 04510 México D.F., Mexico.
E-mail address: roberto_maldonado@ciencias.unam.mx (R. Maldonado).

https://doi.org/10.1016/j.lithos.2018.02.030
0024-4937/

Greater Antilles Arc during the Cretaceous (Maldonado et al., 2018; Martens et al., 2012). Recent studies have corroborated that the geological record of the Chuacús complex includes a prolonged magmatic activity, which is reflected by Ordovician, Silurian, Triassic and Jurassic protolith ages from both felsic and mafic metaigneous rocks (Maldonado et al., 2018; Martens et al., 2012; Ratschbacher et al., 2009; Solari et al., 2011), as well as an episode of HP subduction-zone metamorphism during the mid-Cretaceous, and a subsequent Late Cretaceous amphibolite-facies overprint (Maldonado et al., 2018; Martens et al., 2012). Furthermore, the available U-Pb zircon geochronological data not only from the Chuacús complex but also from other localities in Central America have revealed a pervasive Proterozoic inherited component in a diversity of rock types (e.g. Gomberg et al., 1968; Martens et al., 2012; Ortega-Gutiérrez et al., 2004; Ratschbacher et al., 2009; Solari et al., 2009; Solari et al., 2011), however the presence of an exposed basement of such age has not yet been confirmed.

The HP metamorphic event in the Chuacús complex is mostly documented on the basis of the occurrence of eclogite bodies hosted by a predominant gneissic sequence (e.g. Martens et al., 2017; Ortega-Gutiérrez et al., 2004). In addition, recent petrological studies have shown that the spatially associated metasedimentary rocks share a common HP metamorphic evolution (Maldonado et al., 2016; Maldonado et al., 2018). However, the metamorphic conditions experienced by other lithological units, including eclogite-hosting metagranitoid, are poorly constrained. The available U-Pb data show that this rock type underwent a Late Cretaceous thermal perturbation at ca. 74 Ma, which is equivalent to metamorphic U-Pb ages reported from hosted eclogite bodies (Martens et al., 2012; Ratschbacher et al., 2009). This indicates that felsic and mafic igneous protoliths have a primary structural relation predating this metamorphic event and, therefore, that the whole sequence share at least a common Late Cretaceous metamorphic history. Nevertheless, in view of recent petrochronological evidence indicating an earlier (pre-collisional) HP metamorphic stage (Maldonado et al., 2018), as well as the paucity of petrological data, it is still necessary to demonstrate if metagranitoids also experienced the same HP evolution.

In this study, we present new petrological, geochronological and geochemical data that contribute to enlarge the Caribbean zone database and that demonstrate that part of the subducted crust of the Chuacús complex represents a remnant of a Proterozoic granitic basement. We also discuss the significance and tectonic implications of bimodal Late Triassic magmatism recorded in this area, as well as its probable connections with other contemporary American granitic belts. Finally, we show that this Proterozoic to Late Triassic granitic basement experienced HP metamorphism, but the obtained *P-T* conditions considerably differ from those reported for eclogite and associated HP metasediments, an issue that is also discussed.

2. Geological background and field relations

The Chuacús complex is a medium- to high-grade metamorphic belt that extends ca. 220 km along the current North American-Caribbean plate boundary in Central America (Fig. 1a). This belt represents a fault-bounded block of continental crust in the Guatemala suture zone (Brueckner et al., 2009; Fig. 1b) and records subduction to >70 km depth of the passive continental margin of southern North America during the mid-Cretaceous (Maldonado et al., 2018; Martens et al., 2012; Ortega-Gutiérrez et al., 2004; Ratschbacher et al., 2009). A synthesis of the regional setting of the Guatemala suture zone has been recently presented in Flores et al. (2013), Maldonado et al. (2016) and Martens et al. (2017), so the reader is referred to these works for a detailed description of this region.

Most of the Chuacús complex is dominated by greenschist- to amphibolite-facies assemblages. The deepest portion of the belt is exposed in the Rabinal-Palibatz area of the Sierra de Chuacús (Fig. 1c), where a diversity of eclogite-facies rocks has been recognized (e.g. Maldonado et al., 2016; Martens et al., 2017; Ortega-Gutiérrez et al., 2004). The metamorphic sequence in this region is composed of: 1) a metaigneous unit, which comprises variably deformed metagranitoid, amphibolite, as well as subordinated eclogite and pyroxenite bodies, and 2) a metasedimentary unit, consisting of intercalated pelitic-psammitic schist, paragneiss, marble, quartzite and calcsilicate rocks, a sequence that denotes a passive continental margin origin (Maldonado et al., 2016; Maldonado et al., 2018; Martens et al., 2012; McBirney, 1963; Ortega-Gutiérrez et al., 2004; Ratschbacher et al., 2009). The predominant structural trend is defined by a NW-SE-striking, SW-dipping axial-plane foliation (S_{n+2}) produced largely by the tight-isoclinal folding of an earlier high-grade foliation (S_{n+1}). Locally developed high-strain shear zones (S_{n+3}) overprint S_{n+2} on the scale of meters to kilometers, indicating later NE-vergent folding-thrusting (Fig. 1c).

Metagranitoid make up the most abundant rock type in the Sierra de Chuacús. Available geochemical data show that whole-rock compositions are variable in terms of major element relations, probably reflecting a variety of granitoid protoliths, while trace-element patterns suggest an origin related to continental arc magmatism (Solari et al., 2011). U-Pb zircon ages indicate that granitic precursors mostly crystallized during a Late Triassic magmatic pulse (ca. 220 Ma; Ratschbacher et al., 2009; Solari et al., 2011; Martens et al., 2012; this work), but some older protolith ages from the Ordovician (ca. 450 Ma; Solari et al., 2011) to the Cambrian-Ediacaran (Ratschbacher et al., 2009), as well as from the Mesoproterozoic (this work) have also been reported. Mafic rocks (i.e. amphibolites and eclogites) occur as centimeter- to meter-scale bands and lenses concordantly hosted by both gneissic metagranitoids and metasedimentary rocks. These bodies are fairly homogeneous regarding their major element compositions, and their trace-element abundances indicate a MORB affinity (Solari et al., 2011). In addition, zircon U-Pb protolith ages of ca. 425, 227 and 167 Ma from eclogites indicate that mafic precursors in the Chuacús complex were originated at least in three different tectono-temporal settings during Silurian, Triassic, and Jurassic magmatic episodes (Maldonado et al., 2018; Martens et al., 2012).

Metasedimentary rocks are widely distributed in the Sierra de Chuacús, but the most prominent outcrops are exposed in the southwestern and northeastern zones of the studied area (Fig. 1c). These rocks cover a wide range of whole-rock compositions. In particular, semipelitic to pelitic levels are predominant and several localities (Fig. 1c) preserve diagnostic assemblages of HP metamorphism (Maldonado et al., 2016; Maldonado et al., 2018; Ortega-Gutiérrez et al., 2004). Their overall chemical features are typical of hemipelagic sedimentation, and the incompatible trace-element patterns suggest a mature upper crust provenance (Solari et al., 2011). Depositional ages of sedimentary protoliths are uncertain, but the available U-Pb detrital zircon age spectra suggest that sedimentary protoliths could have been formed during at least two different periods of sedimentation, an older one of pre-Ordovician age (Solari et al., 2009) and a younger period that occurred after the Late Triassic (Martens et al., 2012; Solari et al., 2011).

Recent garnet/whole rock Lu-Hf data indicates that HP, subduction-related metamorphism in the Chuacús complex occurred during the Albian-Cenomanian (ca. 100 Ma; Maldonado et al., 2018), while a medium-pressure overprint related to collision and partial exhumation took place from the Campanian (76–56 Ma; Sutter, 1979; Ortega-Gutiérrez et al., 2004; Ortega-Obregón et al., 2008; Ratschbacher et al., 2009; Solari et al., 2011; Martens et al., 2012; Maldonado et al., 2018). This metamorphic evolution was characterized by an early prograde stage of HP metamorphism at 19–20 kbar and 530–580 °C finally reaching minimum pressure-peak conditions of 23–25 kbar and 620–690 °C (Maldonado et al., 2018). After pressure peak, an initial stage of isothermal decompression produced metamorphic equilibration at 13 kbar and 660 °C (Ratschbacher et al., 2009). From this stage, the subduction-related regime was replaced by higher thermal conditions (ca. 20 °C/km) coeval with partial exhumation to shallow depths,

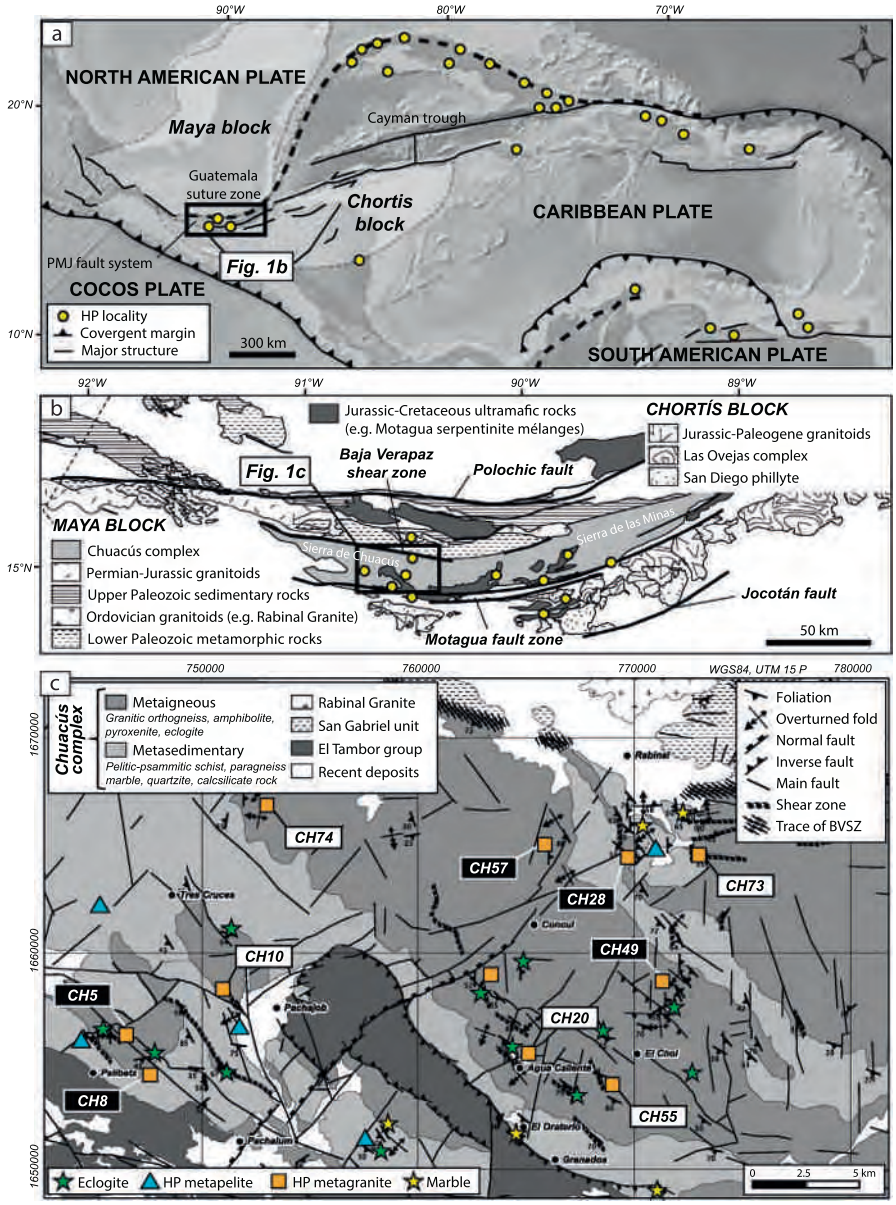

Fig. 1. (a) Tectonic setting of the Caribbean suture system modified from Martens et al. (2012). Circles and bold lines denote high-pressure localities and major fault zones, respectively. Notice the location of the Guatemala suture zone (rectangle). (b) Simplified geological map of the Guatemala suture zone (after Kesler et al., 1970; Anderson et al., 1973; Ratschbacher et al., 2009) showing the main high-pressure localities (after Harlow et al., 2004; Ortega-Gutiérrez et al., 2004; Tsujimori et al., 2006; Martens et al., 2012; Solari et al., 2013). (c) Simplified geological map of the study area in the Chuacús complex (modified from Morán-Ical et al., 2001; Ortega-Obregón et al., 2008). Color symbols highlight localities of relevant rock types. Locations of the studied samples are also shown; the white rectangles refer to samples used for U-Pb geochronology. BVSZ: Baja Verapaz shear zone. (For interpretation of the references to color in this figure legend, the reader is referred to the web version of this article.)

renewed tectonic burial with an amphibolite-facies overprint at 7–8 kbar and 450–600 °C, partial melting, pegmatite emplacement, and shortening deformation (Maldonado et al., 2016; Martens et al., 2012; Ortega-Gutiérrez et al., 2004; Ratschbacher et al., 2009; van den Boom, 1972), all of which marked the transition from a Pacific-type (accretionary) to an Alpine-type (collisional) subduction regime (Maldonado et al., 2018). Late syncollisional exhumation was characterized by sinistral-transpressive deformation resulting in N-S shortening by folding and reverse shear zones (e.g. Ratschbacher et al., 2009).

In the field, metagranitoids, metasedimentary rocks and eclogite/amphibolite bodies are interlayered (Figs. 1c, 2a–c). Locally, some primary intrusive contacts are partially preserved, but in most cases these relations are ambiguous. The structure of metagranitoids is considerably variable ranging from undeformed metagranitoids to banded granitic orthogneisses (Fig. 2). In fact, some massive, poorly foliated metagranitoid bodies (e.g. Agua Caliente River, Fig. 1c) gradually pass into augen gneiss or even into banded orthogneiss, which suggest that these weakly deformed bodies are meter-scale structural relicts preserved within the predominantly gneissic structure. Several lens-shaped bodies of relict metagranitoid, from tens to hundreds of meters in length, have been found in the study area. Isoclinal folding (S_{n+2}) with variable three-dimensional geometry, including sheath, oblique and rootless folds, is typically related to rotation of the high-grade (eclogite-facies?) S_{n+1} foliation planes in gneissic metagranitoids, but also probably to flattening and attenuation of pre-existing folds. Complex folding associated with migration and accumulation of anatectic melt in migmatized orthogneisses is characteristic of the central sector of the Sierra de Chuacús (e.g. El Chol zone).

Metagranitoids from the Chuacús complex not only display broad structural variations but also differences regarding to the extent of

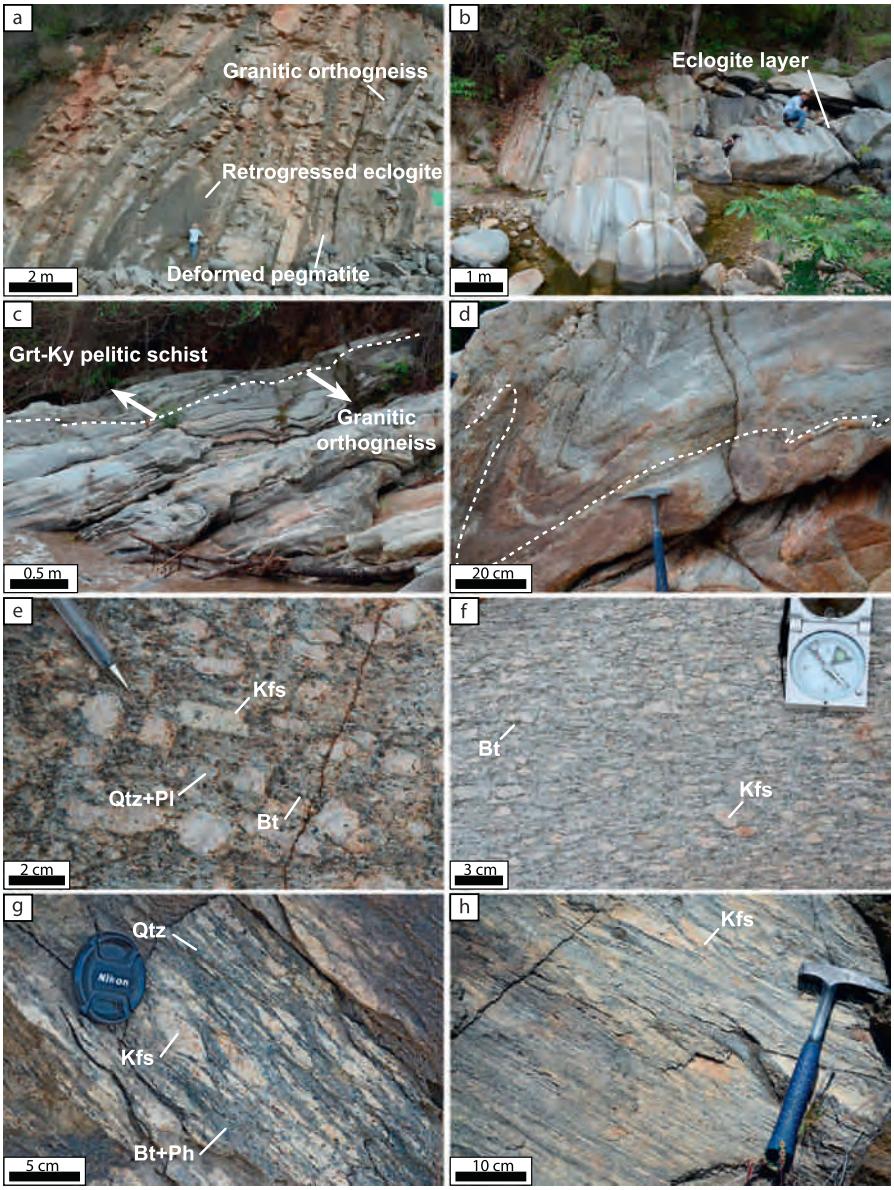

Fig. 2. Outcrop-scale photographs of metagranitoids showing different occurrences. (a) Granitic orthogneiss hosting a meter-sized boudin of retrogressed eclogite. (b) Banded orthogneiss. (c) Contact between migmatitic orthogneiss and Grt-Ky pelitic schist. (d) Folded granitic orthogneiss. (e) Detail of undeformed megacrystic metagranitoid. (f) Granitic augen gneiss showing K-feldspar porphyroclasts. (g) Detail of granitic orthogneiss showing stretched K-feldspar porphyroclasts and incipient layering. (h) Detail of banded granitic orthogneiss with still recognizable strongly flattened K-feldspar porphyroclasts.

retrograde overprint and the degree of late-stage partial melting. Thus, during fieldwork, we focused on sampling outcrops with only minor retrogression, and lacking evidence for later migmatization, because one of the purposes of this work is to investigate peak HP metamorphism. Twenty-two samples were collected for petrographic characterization in an area of ca. 40 × 20 km, of which a set of ten samples were chosen for additional analyses (Fig. 1c): electron microscopy (CH10, CH20 and CH74), U-Pb zircon geochronology (CH10, CH20, CH55, CH73 and CH74), and whole-rock chemistry (CH5, CH8, CH10, CH20, CH28, CH49, CH55, CH57, CH73 and CH74).

3. Analytical methods

Mineral compositions were analyzed with both a CAMECA SX-100 electron microprobe and a JEOL JXA-8900R Superprobe equipped with 5 wavelength dispersive spectrometers, at the CAMCOR facility, University of Oregon and at the Laboratorio Universitario de Petrología (LUP), Universidad Nacional Autónoma de México (UNAM), respectively. Operating conditions were in both cases an accelerating voltage of 15 kV, a beam current of 10–12 nA, and a beam diameter of 2–10 μm. The concentrations of Si, Ti, Al, Cr, Fe, Mn, Mg, Ca, Na and K were determined applying on-peak counting times of 30 s. Off-peak counting time was 5–30 s. Natural minerals (e.g. orthoclase MAD-10) and synthetic materials (e.g. synthetic TiO_2) were used as standards. The MAN background continuum absorption intensity correction was applied to Si, Al, Fe, Mg, Ca and Na (Donovan and Tingle, 1996). Matrix correction methods followed ZAF and $\phi\rho z$ procedures (Armstrong, 1988). Measurements of rutile compositions were carried out using a JEOL JXA-8500F field-emission electron microprobe equipped with 5 wavelength dispersive spectrometers at the GeoAnalytical Lab, Washington State University, applying the method of Neill et al. (2016). An accelerating voltage of 15 kV, a beam current of 200 nA, and a beam diameter of 5 μm were used. The concentrations of Nb, Si, Zr, Ti, Al, V, Cr and Fe were measured applying counting times of 400 s for Nb, 140 s for Si, 800 s for Zr, 10 s for

Ti, 240 s for Al, and 120 s for V, Cr, Fe. Natural minerals and synthetic oxides were used as standards. Counts for Zr were acquired on two spectrometers and aggregated (Donovan et al., 2011). Corrections for spectral interferences were made following the method of Donovan et al. (1993) to account for the overlap of the Ti Kβ on V Kα, Ti Kα (III) on Al Kα, and V Kβ on Cr Kα. Measurements were made using the combined MAN background/"blank" correction method for simple matrices outlined by Donovan et al. (2016). To ensure accuracy for Zr and Nb, a "blank" intensity correction (Donovan et al., 2011) was utilized, using the Sy synthetic rutile of Luvizotto et al. (2009), with published values of ~1 ppm Nb and 4.45 ppm Zr, as a blank standard. The R10 natural rutile (Luvizotto et al., 2009) was measured periodically during the analytical session to ensure measurement accuracy and internal consistency between analytical sessions. X-ray compositional maps of garnet were acquired on the JXA-8900R Superprobe at LUP, UNAM employing an accelerating voltage of 15 kV, a beam current of 50 nA and a dwell time of 20 ms. Backscattered electron (BSE) and cathodoluminescence (CL) imaging were acquired with a Zeiss EVO MA10 scanning electron microscope (SEM) at the Instituto de Geología, UNAM in high vacuum mode at 15 kV, and with a JEOL IT300 SEM coupled with a Gatan ChromaCL2 system at the Laboratorio de Microscopía Electrónica, Universidad Autónoma de Guerrero, respectively. Mineral cations were calculated with the AX program (Holland, 2016). Anhydrous mineral compositions were calculated to standard numbers of oxygen per formula unit (pfu); mica analyses were calculated to a total of 11, and epidote/clinozoisite to 12.5 oxygens pfu. Mineral abbreviations in figures and tables follow Whitney and Evans (2010).

Zircon trace element and U-Pb data were acquired by laser ablation-inductively coupled plasma-mass spectrometry (LA-ICP-MS) at the LEI, UNAM with a Resonetics M-50 excimer laser ablation system coupled to a Thermo ICap Qc ICP-MS. Zircon crystals were separated by routinely used techniques of crushing, sieving, magnetic and handpicking separation. Mineral separates were embedded in epoxy and then cut and polished down carefully to ensure the analysis of the central sections. A morphological/textural analysis based on CL images was carried out prior to U-Pb analysis in order to select the best areas to be ablated. Zircon 91500 (Wiedenbeck et al., 1995) was used as the primary bracketing standard with measurements at the beginning, end and twice each 10 unknown analyses, while Plešovice zircon (Sláma et al., 2008) was employed as a quality control reference, repeating its measurement each 10 unknown analyses. During the course of the analytical sessions, Plešovice yielded concordant results with a mean $^{206}Pb/^{238}U$ age in agreement with its accepted age. The isotope ^{204}Pb, which would be used for initial common Pb correction, was not measured because its determination is highly imprecise in a quadrupole-based mass spectrometer, and its signal is also swamped by the ^{204}Hg isobaric interference. Zircons normally do not incorporate common Pb at the moment of crystallization; hence, common Pb was evaluated, but not corrected, using the $^{207}Pb/^{206}Pb$ ratio through Tera-Wasserburg concordia diagrams. U-Pb isotopic data and error propagation were reduced offline using Iolite (Paton et al., 2011), employing the VizualAge data reduction scheme of Petrus and Kamber (2012). Isoplot 3.75 (Ludwig, 2012) was used to calculate the mean ages, as well as to plot concordia diagrams. In figures, tables, and results, $^{206}Pb/^{238}U$ ages are used for zircons younger than 1.0 Ga, whereas $^{207}Pb/^{206}Pb$ ages are referred for older grains, because $^{206}Pb/^{238}U$ ages older than 1.0 Ga become increasingly less precise in comparison with $^{207}Pb/^{206}Pb$ ages. U-Pb zircon methodology and instrumentation used at LEI are further described in Solari et al. (2010a).

Major element whole-rock compositions were determined by X-ray fluorescence analyses using a Rigaku ZSX Primus II spectrometer at the Instituto de Geología, UNAM, according to the procedures outlined in Lozano and Bernal (2005). Trace element compositions were measured by inductively coupled plasma-mass spectrometry (ICP-MS) using a Thermo ICap Qc ICP-MS at the Laboratorio de Estudios Isotópicos (LEI), Centro de Geociencias, UNAM. For this purpose, powdered rock aliquots of ~50 Mg were initially digested following the procedures described in Ferrari et al. (2014), and then were diluted to 1:2000 with an internal standard solution containing Ge (10 ppb), In (5 ppb), Tm (5 ppb) and Bi (5 ppb). Calibration was performed with the international rock standards AGV-2, BHVO-2, BCR-2, JB-2, and JR.

4. Results

4.1. Petrography and mineral compositions

Macroscopically, three rock types are distinguished on the basis of different degrees of strain with respect to S_{n+1}/S_{n+2} deformation: type I undeformed metagranitoid (e.g. Fig. 2e), type II augen orthogneiss (e.g. Fig. 2f) and type III banded orthogneiss (e.g. Fig. 2g, h). One representative sample of each structural type (CH74, CH20 and CH10, respectively) was chosen for detailed SEM study and mineral composition measurements. Representative electron microprobe analyses are given in Table 1.

4.1.1. Type I undeformed metagranitoid

Undeformed metagranitoids preserve, at the outcrop-scale, magmatic textures that range from coarse-grained, phaneritic (Fig. 3a) to porphyritic with phenocrysts (up to 5 cm in size) of K-feldspar (Fig. 2e). At thin-section scale, however, these rocks are seen to display different degrees of recrystallization, reflected by the occurrence of undulose extinction, subgrains and sutured boundaries in quartz, as well as polycrystalline quartz-plagioclase aggregates. Relict magmatic mineralogy consists of perthitic K-feldspar (e.g. Fig. 4a; 30–40 vol%) and quartz (20–30 vol%), with accessory apatite, allanite, zircon, monazite and Fe-Ti oxides. In most cases, both magmatic biotite and plagioclase were partially or completely consumed or recrystallized during subsequent metamorphic reactions. Metamorphic minerals occur either as fine-grained interstitial, mafic domains (Fig. 3b, c) or micrometer-scale pseudomorphs of plagioclase + white mica + epidote/clinozoisite after magmatic plagioclase (e.g. Fig. 4b–d). The peak-stage assemblage consists of plagioclase (20–30 vol%), white mica (<0.5 mm; 5–10 vol%) and garnet (<1 mm; <2 vol%), with accessory rutile and probably epidote/clinozoisite. A late-stage assemblage consists of brown-greenish biotite (<1 mm; 5–10 vol%) partially replacing garnet and white mica (Fig. 3c), titanite rimming both rutile and garnet (e.g. Fig. 4e) and epidote/clinozoisite-allanite as radial coronas surrounding magmatic apatite (e.g. Fig. 4f).

Sample CH74 is a type I metagranitoid with a coarse-grained phaneritic texture (Fig. 3a) that crops out ca. 7 km northeastward from the Tres Cruces village (Fig. 1c). In this sample, garnet (~1 vol%) displays slightly zoned compositional profiles with decreasing grossular (from 0.50 to 0.44), and increasing almandine (from 0.46 to 0.51) and pyrope (from 0.02 to 0.03) from core to rim (Figs. 5a–c, 6a). White mica (~5 vol%) is phengite with variable celadonite content due to concentric zoning, ranging in composition from Si = 3.40, Al = 2.01 and Fe^{2+} + Mg = 0.57 pfu in the cores to Si = 3.13, Al = 2.48 and Fe^{2+} + Mg = 0.35 pfu in the rims (Fig. 5d, e). Biotite (~8 vol%) replacing garnet and phengite is relatively Fe-rich with $X_{Mg} = Mg/Fe^{2+} + Mg = 0.29–0.33$, $Al^{VI} = 1.31–1.36$ pfu and Ti = 0.10–0.12 pfu (Fig. 5f). Epidote/clinozoisite (<3 vol%), in both plagioclase-rich pseudomorphs and coronas surrounding apatite, contains $X_{Fe} = Fe^{3+}/Fe^{3+} + Al = 0.20–0.34$ (Fig. 5g). Plagioclase (15–20 vol%) associated with phengite and epidote/clinozoisite is albite with anorthite contents below 0.02, and K-feldspar contains Ab = 0.06–0.11 (Fig. 5h, i).

4.1.2. Type II augen orthogneiss

Augen orthogneisses typically contain centimeter-sized (up to 10 cm) K-feldspar porphyroclasts set in a matrix of dynamically recrystallized aggregates of plagioclases and quartz, as well as aligned biotite-rich mafic domains (Fig. 3d). K-feldspar porphyroclasts host lenticular to patchy exsolution lamellae of plagioclase, and exhibit a variable degree of flattening. The relict protolith mineralogy comprises K-feldspar

Table 1
Representative mineral compositions for the studied samples. Cation totals were calculated with AX (Holland, 2016), which estimates the amount of ferric iron from stoichiometric criteria.

Sample	CH74	CH74	CH20	CH20	CH10	CH10	CH74	CH74	CH20	CH20	CH10	CH10	CH74	CH74	CH20
Mineral	Grt	Grt	Grt	Grt	Grt	Grt	Ph	Ph	Ph	Ph	Ph	Ph	Bt	Bt	Bt
Location	core	rim	core	rim	core	rim	matrix	matrix	matrix	matrix	matrix	matrix	matrix	matrix	matrix
Oxides (wt%)															
SiO_2	37.95	37.98	38.01	37.87	38.25	38.09	50.21	51.33	46.20	45.60	50.15	49.68	36.46	38.33	37.65
TiO_2	0.09	0.05	0.05	0.08	0.27	0.12	0.61	0.54	0.38	0.66	0.96	0.76	1.74	2.04	2.69
Al_2O_3	20.86	20.79	20.49	20.61	18.35	19.56	26.30	27.16	30.49	30.25	25.68	26.83	17.38	16.61	15.41
FeO	22.10	23.90	19.45	23.89	20.64	27.80	5.49	5.26	4.15	5.16	7.70	7.71	26.59	24.74	23.75
MnO	0.84	0.69	4.39	1.89	2.44	0.48	0.00	0.00	0.00	0.01	0.00	0.01	0.07	0.04	0.05
MgO	0.56	0.84	0.74	1.37	0.12	0.47	2.41	2.29	1.24	1.37	1.66	1.33	6.24	6.77	8.29
CaO	17.38	15.87	16.80	13.30	18.57	13.76	0.00	0.02	0.14	0.98	0.00	0.02	0.17	0.00	0.10
Na_2O	0.00	0.00	0.00	0.00	0.00	0.00	0.09	0.12	0.18	0.19	0.23	0.22	0.09	0.11	0.11
K_2O	0.00	0.00	0.00	0.00	0.00	0.00	11.04	11.23	10.83	10.69	11.00	10.92	9.53	9.70	9.66
Total	99.77	100.11	99.92	99.00	98.68	100.31	96.16	97.94	93.62	94.89	97.37	97.48	98.27	98.33	97.72
Cations (pfu)															
Si	3.00	3.00	3.00	3.03	3.08	3.04	3.38	3.40	3.19	3.13	3.37	3.33	2.78	2.88	2.85
Ti	1.94	1.94	0.00	1.94	0.02	0.01	0.03	0.03	0.02	0.03	0.05	0.04	0.10	0.12	0.15
Al	0.00	0.00	1.91	0.00	1.74	1.84	2.09	2.11	2.48	2.45	2.03	2.12	1.56	1.47	1.38
Fe^{3+}	0.05	0.06	0.08	0.00	0.08	0.07	0.03	0.00	0.01	0.02	0.06	0.09	0.00	0.00	0.00
Fe^{2+}	1.41	1.51	1.20	1.60	1.31	1.78	0.28	0.29	0.23	0.28	0.37	0.35	1.70	1.56	1.50
Mn	0.06	0.05	0.29	0.13	0.17	0.03	0.00	0.00	0.00	0.00	0.00	0.00	0.01	0.00	0.00
Mg	0.07	0.10	0.09	0.16	0.01	0.06	0.24	0.23	0.13	0.14	0.17	0.13	0.71	0.76	0.94
Ca	1.47	1.34	1.42	1.14	1.60	1.18	0.00	0.00	0.01	0.07	0.00	0.00	0.01	0.00	0.01
Na	0.00	0.00	0.00	0.00	0.00	0.00	0.01	0.02	0.02	0.03	0.03	0.03	0.01	0.02	0.02
K	0.00	0.00	0.00	0.00	0.00	0.00	0.95	0.95	0.95	0.94	0.94	0.93	0.93	0.93	0.93
Sum	8.00	8.00	8.00	8.00	8.00	8.00	7.01	7.01	7.04	7.08	7.02	7.01	7.81	7.74	7.78
Oxygens	12.00	12.00	12.00	12.00	12.00	12.00	11.00	11.00	11.00	11.00	11.00	11.00	11.00	11.00	11.00
X_{Mg}	0.04	0.06	0.07	0.09	0.01	0.03	–	–	–	–	–	–	–	–	–
Alm	0.47	0.50	0.40	0.53	0.42	0.58	–	–	–	–	–	–	–	–	–
Sps	0.02	0.02	0.10	0.04	0.05	0.01	–	–	–	–	–	–	–	–	–
Prp	0.02	0.03	0.03	0.05	0.00	0.02	–	–	–	–	–	–	–	–	–
Grs	0.49	0.45	0.47	0.38	0.52	0.39	–	–	–	–	–	–	–	–	–
Fe^{2+} + Mg	–	–	–	–	–	–	0.52	0.52	0.35	0.42	0.54	0.48	–	–	–
K/K + Na	–	–	–	–	–	–	0.99	0.98	0.98	0.97	0.97	0.97	–	–	–
X_{Mg}	–	–	–	–	–	–	–	–	–	–	–	–	0.29	0.33	0.38
Al^{VI}	–	–	–	–	–	–	–	–	–	–	–	–	1.34	1.36	1.23
X_{Fe3+}	–	–	–	–	–	–	–	–	–	–	–	–	–	–	–
Ab	–	–	–	–	–	–	–	–	–	–	–	–	–	–	–
An	–	–	–	–	–	–	–	–	–	–	–	–	–	–	–
Or	–	–	–	–	–	–	–	–	–	–	–	–	–	–	–

$X_{Mg} = Mg/(Mg + Fe^{2+})$; Alm $= Fe^{2+}/(Fe^{2+} + Mn + Mg + Ca)$; Sps $= Mn/(Fe^{2+} + Mn + Mg + Ca)$; Prp $= Mg/(Fe^{2+} + Mn + Mg + Ca)$; Grs $= Ca/(Fe^{2+} + Mn + Mg + Ca)$; $X_{Fe3+} = Fe^{3+}/(Fe^{3+} + (Al-2))$; Ab $= Na/(Na + Ca + K)$; An $= Ca/(Na + Ca + K)$; Or $= K/(Na + Ca + K)$
Note: Feldspar data correspond to energy-dispersive X-Ray spectroscopy (EDS) analyses

(25–30 vol%) and quartz (20–30 vol%), with accessory apatite, zircon, allanite, monazite and Fe-Ti oxides. The peak-stage metamorphic assemblage consists of plagioclase (20–30 vol%) and white mica (5–10 vol%), with minor amounts of garnet, epidote/clinozoisite and rutile, while the late-stage assemblage includes green biotite (5–10 vol%), epidote (<5 vol%) as well as accessory titanite and amphibole (Fig. 3e). Plagioclase occurs mainly as patchy to tabular poikiloblasts (pseudomorphs; <1 cm in size) associated with tiny white mica and epidote/clinozoisite (e.g. Fig. 4b–d). Fine- to medium-grained white mica (<2 mm) and garnet (<1 mm) are partially replaced by biotite (e.g. Fig. 3f), which instead displays mutual contacts with epidote-clinozoisite. Titanite is present as idioblastic porphyroblasts (<0.5 cm) that commonly contain rutile inclusions (Fig. 3f). Tabular intergrowths of green-bluish amphibole (<100 μm) + quartz are locally present and probably related to late infiltration of hydrous fluids.

Sample CH20 is a type II augen metagranitoid with up to 10 cm sized K-feldspar porphyroclasts (Fig. 2f) sampled at the Agua Caliente locality (Fig. 1c). Garnet (~1 vol%) from this rock is strongly zoned with a decrease in grossular (from 0.47 to 0.38) and spessartine (from 0.09 to 0.04), and increasing almandine (from 0.42 to 0.53) and pyrope (0.03–0.06; Figs. 5a–c, 6b) from core to rim. White mica (~5 vol%) is phengite with relatively low Si contents, varying in composition from Si = 3.13, Al = 2.37 and Fe^{2+} + Mg = 0.33 pfu to Si = 3.21, Al = 2.18 and Fe^{2+} + Mg = 0.42 pfu (Figs. 5d, e), but lacking any apparent chemical zoning. Green biotite (~10 vol%) replacing garnet and phengite has X_{Mg} = 0.37–0.39, Al^{VI} = 1.15–1.25 pfu and Ti = 0.15–0.20 pfu (Fig. 5f). Epidote/clinozoisite (~3 vol%) has X_{Fe} values between 0.19 and 0.29 (Fig. 5g). Plagioclase (~30 vol%) containing phengite and epidote-clinozoisite inclusions is albite with anorthite contents below 0.07, and K-feldspar (~30 vol%) is microcline with Ab = 0.05–0.12 (Fig. 5h, i).

4.1.3. Type III banded orthogneiss

Banded orthogneiss are medium- to coarse-grained rocks that display, at thin-section scale, either continuous or spaced foliations, ranging from disjunctive or S/C to striped fabrics (Fig. 3g). This rock type contains strongly flattened and dynamically recrystallized porphyroclasts of K-feldspar and plagioclase, which define millimeter-scale felsic layers alternating with both aligned mica-rich domains and quartz ribbons. K-feldspar (20–35 vol%) frequently contains flame-shaped exsolution lamellae of plagioclase (Fig. 4a). Plagioclase (15–25 vol%) is locally antiperthitic and often displays deformation twins. Quartz (25–35 vol%) occurs as polycrystalline aggregates and elongated subgrains. Inferred magmatic accessory phases are apatite, zircon, monazite and Fe-Ti oxides. Metamorphic phases include plagioclase, white mica (5–15 vol%), brown-greenish biotite (5–10 vol%) and epidote/clinozoisite (1–3 vol%), with accessory garnet, titanite, chlorite and (rarely) rutile, which are also associated as previously described. Although garnet is a common phase, it has

CH20	CH10	CH10	CH74	CH74	CH20	CH20	CH10	CH10	CH74	CH20	CH10	CH74	CH20	CH10
Bt	Bt	Bt	Ep	Ep	Ep	Ep	Ep	Ep	Pl	Pl	Pl	Kfs	Kfs	Kfs
matrix	matrix	matrix	matrix	matrix	matrix	matrix	matrix	matrix	matrix	matrix	matrix	matrix	matrix	matrix
37.21	34.86	35.30	38.37	38.12	38.67	39.22	37.71	37.47	67.51	66.76	65.16	64.75	64.13	64.46
2.72	3.05	3.11	0.10	0.17	0.06	0.09	0.16	0.23	0.00	0.00	0.00	0.00	0.00	0.00
15.36	15.54	15.87	24.18	24.25	24.28	23.01	22.78	22.41	20.19	20.66	21.30	19.49	19.62	19.32
24.09	30.40	29.63	10.24	12.38	9.97	11.37	11.67	11.70	0.00	0.00	0.00	0.00	0.00	0.00
0.08	0.24	0.23	0.00	0.03	0.04	0.01	0.14	0.10	0.00	0.00	0.00	0.00	0.00	0.00
7.92	3.29	3.26	0.04	0.36	0.03	0.06	0.03	0.05	0.00	0.00	0.00	0.00	0.00	0.00
0.14	0.01	0.01	24.00	21.47	23.51	22.81	22.97	22.70	0.00	0.61	2.01	0.00	0.00	0.00
0.10	0.08	0.06	0.00	0.00	0.00	0.00	0.00	0.00	12.30	11.97	11.53	1.07	0.54	0.95
9.77	9.65	9.75	0.00	0.00	0.00	0.00	0.04	0.01	0.00	0.00	0.00	14.68	15.71	15.26
97.38	97.12	97.22	96.93	96.77	96.57	96.58	95.51	94.67	100.00	100.00	100.00	99.99	100.00	99.99
2.84	2.77	2.78	3.03	3.02	3.06	3.10	3.04	3.04	2.96	2.93	2.88	2.97	2.96	2.97
0.16	0.18	0.18	0.01	0.01	0.00	0.01	0.01	0.01	0.00	0.00	0.00	0.00	0.00	0.00
1.38	1.45	1.48	2.25	2.26	2.26	2.15	2.16	2.14	1.04	1.07	1.11	1.05	1.07	1.05
0.00	0.00	0.00	0.67	0.73	0.65	0.75	0.78	0.79	0.00	0.00	0.00	0.00	0.00	0.00
1.54	2.02	1.96	0.01	0.09	0.01	0.01	0.01	0.01	0.00	0.00	0.00	0.00	0.00	0.00
0.01	0.02	0.02	0.00	0.00	0.00	0.00	0.01	0.01	0.00	0.00	0.00	0.00	0.00	0.00
0.90	0.39	0.38	0.01	0.04	0.00	0.01	0.00	0.01	0.00	0.00	0.00	0.00	0.00	0.00
0.01	0.00	0.00	2.03	1.82	1.99	1.93	1.98	1.97	0.00	0.03	0.10	0.00	0.00	0.00
0.02	0.01	0.01	0.00	0.00	0.00	0.00	0.00	0.00	1.05	1.02	0.99	0.10	0.05	0.09
0.95	0.98	0.98	0.00	0.00	0.00	0.00	0.00	0.00	0.00	0.00	0.00	0.86	0.92	0.90
7.80	7.82	7.79	8.00	7.98	7.98	7.95	7.99	7.98	5.05	5.05	5.07	4.98	5.00	5.00
11.00	11.00	11.00	12.50	12.50	12.50	12.50	12.50	12.50	8.00	8.00	8.00	8.00	8.00	8.00
–	–	–	–	–	–	–	–	–	–	–	–	–	–	–
–	–	–	–	–	–	–	–	–	–	–	–	–	–	–
–	–	–	–	–	–	–	–	–	–	–	–	–	–	–
–	–	–	–	–	–	–	–	–	–	–	–	–	–	–
–	–	–	–	–	–	–	–	–	–	–	–	–	–	–
–	–	–	–	–	–	–	–	–	–	–	–	–	–	–
–	–	–	–	–	–	–	–	–	–	–	–	–	–	–
0.37	0.16	0.16	–	–	–	–	–	–	–	–	–	–	–	–
1.22	1.22	1.26	–	–	–	–	–	–	–	–	–	–	–	–
–	–	–	0.23	0.24	0.22	0.26	0.26	0.27	–	–	–	–	–	–
–	–	–	–	–	–	–	–	–	1.00	0.97	0.91	0.10	0.05	0.09
–	–	–	–	–	–	–	–	–	0.00	0.03	0.09	0.00	0.00	0.00
–	–	–	–	–	–	–	–	–	0.00	0.00	0.00	0.90	0.95	0.91

not been observed in all studied orthogneisses. If present, garnet occurs as idioblastic to xenoblastic (e.g. Fig. 4g), as well as skeletal or atoll-shaped reddish grains (<1 mm in diameter) with variable replacement by biotite, epidote and chlorite (Fig. 3h). White mica occurs either as medium- to coarse-grained (<3 mm) aligned flakes or crenulated-fish porphyroclasts (Fig. 3h), and is partially replaced by biotite and chlorite (Figs. 3i, 4h). Late fine-grained white mica intergrowths associated with shear bands are also present. Epidote/clinozoisite (<1 mm in size) is commonly associated with biotite as retrograde phase, but its microstructural relations with garnet and white mica may be in some cases unclear.

Sample CH10 is a medium-grained, pinkish orthogneiss (Fig. 3g) that crops out near to the Pachajob village (Fig. 1c). In this sample, garnet (<1 vol%) displays a strong chemical zoning with a decrease in grossular (from 0.52 to 0.36) and spessartine (from 0.06 to 0.01), and an increase in almandine (from 0.45 to 0.60) and pyrope (from 0.00 to 0.02) from core to rim (Figs. 5a–c, 6c). Coarse-grained white mica (~5 vol%) porphyroclasts are zoned Fe-rich phengite (up to 8.6 wt% FeO_t) with maximum celadonite contents in cores (Si = 3.37, Al = 2.03, Fe^{2+} + Mg = 0.60 pfu) and a decrease in this component towards the rims (Si = 3.19, Al = 2.31, Fe^{2+} + Mg = 0.34 pfu; Fig. 5d, e). Brown-greenish biotite (~5 vol%) replacing phengite is relatively Fe-rich with X_{Mg} values between 0.15 and 0.16, as well as Al^{VI} = 1.22–1.43 and Ti = 0.15–0.19 pfu (Fig. 5f). Epidote/clinozoisite (<2 vol%), in textural equilibrium with biotite, contains $X_{Fe} = Fe^{3+}/Fe^{3+} + Al$ = 0.23–0.28 (Fig. 5g). Plagioclase (~20 vol%) is albite with anorthite contents below 0.09, meanwhile perthitic K-feldspar (~30 vol%) contains Ab = 0.05–0.11 (Fig. 5h, i).

A generalized scheme of the mineral assemblage evolution for the different types of metagranitoid is presented in Fig. 7, in order to summarize and integrate the above petrographic and chemical observations.

4.2. Pressure-temperature constraints

Despite structural differences among the studied samples, they share both petrographic and mineral chemical features suggestive of HP metamorphic equilibration, such as the occurrence of Ca-rich garnet (X_{Ca} up to 0.52) in association with phengite (Si contents of up to 3.4 pfu) and rutile. Even so, when using these phases to obtain *P-T* information it must be taken into account that, while garnet preserves an apparent growth zoning (Figs. 6 and 8a), phengite displays an inverse zoning suggestive of post-peak re-equilibration (Fig. 8b), and rutile is commonly replaced by titanite (Fig. 4e).

Several studies have been shown that the partitioning of Zr into rutile is strongly temperature dependent in assemblages containing rutile + zircon + quartz (e.g. Watson et al., 2006; Zack et al., 2004). Therefore, the Zr content in rutile from sample CH10 (type III metagranitoid) was used to calculate the temperature according to Tomkins et al. (2007). Measurements were performed in matrix rutile grains (50–100 μm in size) lacking reaction microstructures (e.g. replacement by titanite) and

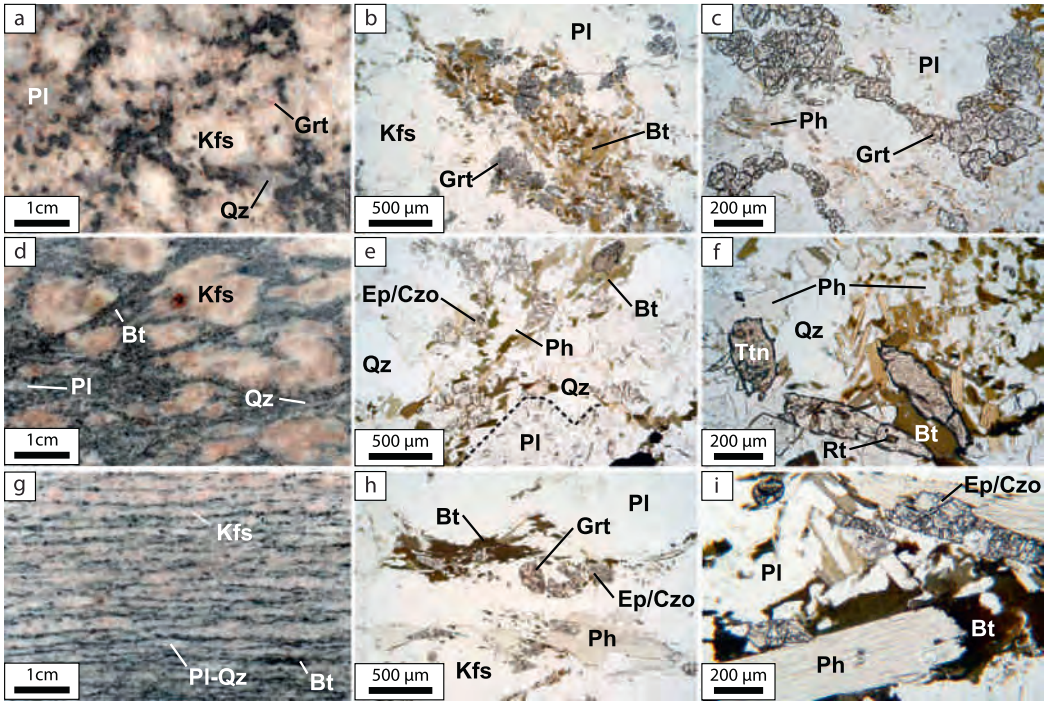

Fig. 3. Typical petrographic features of the studied samples. (a–c) Type I undeformed metagranitoid, (d–f) type II augen orthogneiss, and (g–i) type III banded orthogneiss. (a) Coarse-grained granitic microstructure. (b) Detail of (a) showing a typical interstitial, mafic domain mostly composed by garnet and biotite. (c) Interstitial garnet aggregates and fine-grained patches of white mica (Ph) within plagioclase. (d) Flattened K-feldspar porphyroclasts set in fine-grained matrix dominated by plagioclase, quartz and biotite. (e) Detail of a matrix domain showing typical microstructures and assemblages. (f) White mica partially replaced by biotite, and rutile inclusions in titanite. (g) Typical gneissic foliation with strongly flattened K-feldspar and biotite-rich mafic domains. (h) Biotite-epidote/clinozoisite intergrowth replacing garnet, and crenulated white mica porphyroclast. (i) Detail of a mafic domain showing white mica rimmed by biotite. All images are plane-polarized light views, except for (a), (d) and (g) that are scanned rock plates.

displaying equant-grain morphologies. Rutile grains were additionally analyzed for Si and Nb to account the possible interference of zircon micro-inclusions. Since the Tomkins et al. (2007) thermometer includes a pressure dependence for the substitution of Zr in rutile coexisting with quartz and zircon, a pressure range that encompasses previous barometric results in the study area was evaluated (e.g. Maldonado et al., 2016; Ratschbacher et al., 2009). Analytical results and calculated temperatures at 10 and 20 kbar are shown in Table 2. Zr concentrations in the analyzed rutile grains range between 256 and 289 ppm, which correspond to average temperatures ($\pm\ \sigma$) of 642 $\pm$ 3 and 684 $\pm$ 3 °C (n = 12), for 10 and 20 kbar respectively. Since temperatures obtained by this method are pressure-dependent, these values are, in principle, a first approximation to peak-stage temperature, which must be further constrained on the basis of reliable barometric data. However, it should be noted that even considering this relatively large pressure interval, the obtained Zr-in-rutile temperature variation range (~50 °C including errors) is comparable with typical uncertainties associated with conventional thermometry (Palin et al., 2016).

The studied metagranitoids contain K-feldspar + biotite + quartz, which corresponds to one of the limiting assemblages suitable for the application of the Si-in-phengite geobarometer of Massonne and Schreyer (1987). This method is based on the pressure dependence of the Si concentration in white micas, coexisting with K-feldspar, phlogopite/biotite, quartz, and a hydrous fluid, which was experimentally determined for a wide *P-T* range in the system K_2O-MgO-Al_2O_3-SiO_2-H_2O (KMASH). In general, the range of compositions obtained in phengite from three metagranitoid types (CH74, CH20 and CH10) is consistent with HP metamorphism. The resulting pressure employing phengite core compositions (Si = 3.35–3.40 pfu) from samples CH74 and CH10 is about 13 kbar at ~650 °C (Zr-in-rutile thermometry). However, the evident core-to-rim decrease in the celadonite content of phengite (Figs. 5d, e and 7b), observed in samples CH74 and CH10, suggests partial re-equilibration at pressures considerably lower than the one presumably attained during peak-stage metamorphism and hence the results of phengite barometry should be interpreted with caution.

4.3. U-Pb zircon geochronology

Zircon grains from samples CH74, CH20 and CH10, as well as those from three additional metagranitoid samples (see above), one of each structural type, were employed for LA-ICP-MS U-Pb geochronology. CL images of representative analyzed crystals are shown in Fig. 9 and the U-Pb results, plotted in Wetherill concordia diagrams, are displayed in Fig. 10. The analytical results are presented in Table A1 of the Supplementary material.

Sample CH55 is a type I undeformed metagranitoid with K-feldspar megacrysts (≤5 cm; Fig. 2e) cropping out ca. 3 km southwestward from the El Chol town (Fig. 1c). This sample contains abundant short to long prismatic zircons with aspect ratios up to 1:4. Some crystals have rounded inherited cores, but most show prismatic cores with overgrowths displaying magmatic oscillatory zoning (Fig. 9a). Thirty-one laser spots from overgrowths yielded $^{206}Pb/^{238}U$ apparent ages in the range of 273–213 Ma (Th/U = 0.54–1.47); nevertheless, a majority defines a concordant cluster at 230–220 Ma (Fig. 10a). A group of twenty-five analyses yielded a mean $^{206}Pb/^{238}U$ age of 224.2 $\pm$ 1.8 Ma (MSWD = 5.3; Fig. 10b), which is interpreted as the crystallization age of the granitic protolith. Two inherited cores with $^{206}Pb/^{238}U$ ages of 1052 and 984 Ma (Th/U = 0.42–0.49) indicate the assimilation of a country rock with a Proterozoic component.

In sample CH20, most zircon grains are relatively small (<200 µm long) and occur as elongated prisms with aspect ratios up to 1:5, displaying a dominant oscillatory magmatic zoning with minor inherited cores (Fig. 9b). A cluster of nineteen concordant analyses of the typical magmatic oscillatory zoning domains with Th/U = 0.6–1.89 yielded a mean $^{206}Pb/^{238}U$ age of 224.3 $\pm$ 1.5 Ma (MSWD = 1.6; Fig. 10d), which is identical to the protolith age of sample CH55. Locations of samples

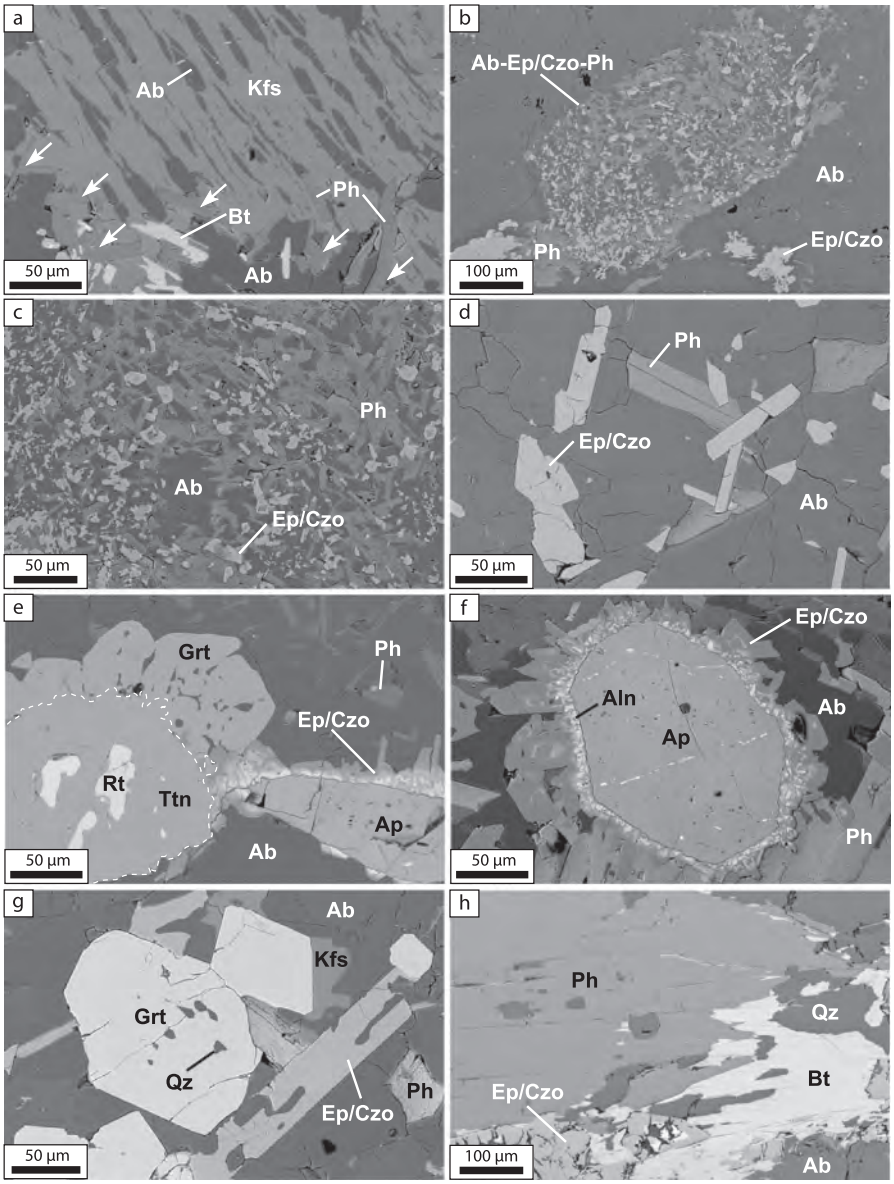

Fig. 4. BSE images showing microstructures related to different crystallization stages of the studied samples. (a) Flame-shaped exsolution lamellae of albite within a K-feldspar crystal. The K-feldspar boundary is replaced by phengite (arrows). (b) Fine-grained tabular pseudomorph of albite-epidote/clinozoisite-phengite within a groundmass of polycrystalline albite. (c) Detail of (b). (d) Albite-epidote/clinozoisite-phengite intergrowth. (e) Garnet and rutile partially replaced by titanite, and apatite rimmed by epidote/clinozoisite. (f) Complete radial allanite-epidote/clinozoisite corona around magmatic apatite. (g) Garnet porphyroblast and skeletal intergrowth of albite-epidote/clinozoisite. (h) Phengite porphyroblast partially replaced by a biotite-quartz intergrowth.

CH20 and CH55 are about 5 km from each other along the dominant NW-SE strike trend of the study area (Fig. 1c), therefore the coincidence in age and structural position of these samples is interpreted as reflecting the extension of the same, variably deformed Late Triassic megacrystic granitoid.

Zircon grains from CH74 have complex internal structures that reflect different stages of growth and recrystallization (Fig. 9c). Some zircon grains, for example, show irregular high-luminescence inherited cores surrounded by darker overgrowths with magmatic oscillatory zoning, and an outer high-luminescence rim. A total of forty-eight laser spots were performed, which spread along concordia between 930 and 1180 Ma (Fig. 10e). Although oscillatory zoning domains probably experienced partial Pb loss during post-magmatic alteration, the $^{207}Pb/^{206}Pb$ ages of a group of nineteen concordant analyses from these domains yielded a mean $^{207}Pb/^{206}Pb$ age of 1108 ± 13 Ma (MSWD = 2.6; Fig. 10f), which is the best estimate for the time of crystallization of the sample. Most laser spots from high luminescence rims (Fig. 9c) are concordant but some are clearly below the concordia line, suggesting secondary Pb loss (Fig. 10f). A group of nine concordant analyses from these zones yielded a concordia age of 1012 ± 6 Ma (Fig. 10e) of probably no geologic significance.

Sample CH73 is a type II augen- to lenticular orthogneiss (Fig. 2g) cropping out ca. 6 km southeastward from Rabinal (Fig. 1c). Zircon grains from this sample occur as stubby to elongated prisms with aspect ratios up to 1:4. CL images show that most zircon grains have prismatic cores with oscillatory to irregular zoning, and only some display apparent inherited cores. Overgrowths are characterized by an oscillatory zoning typical of magmatic crystallization, with no metamorphic rims detected (Fig. 9d). Thirty-nine laser spots from these overgrowths, which have U contents up to ~3100 ppm, yielded mostly discordant results that define a discordia line with upper- and lower-intercept ages of 1110 ± 20 Ma and 371 ± 35 Ma, respectively (MSWD = 0.67;

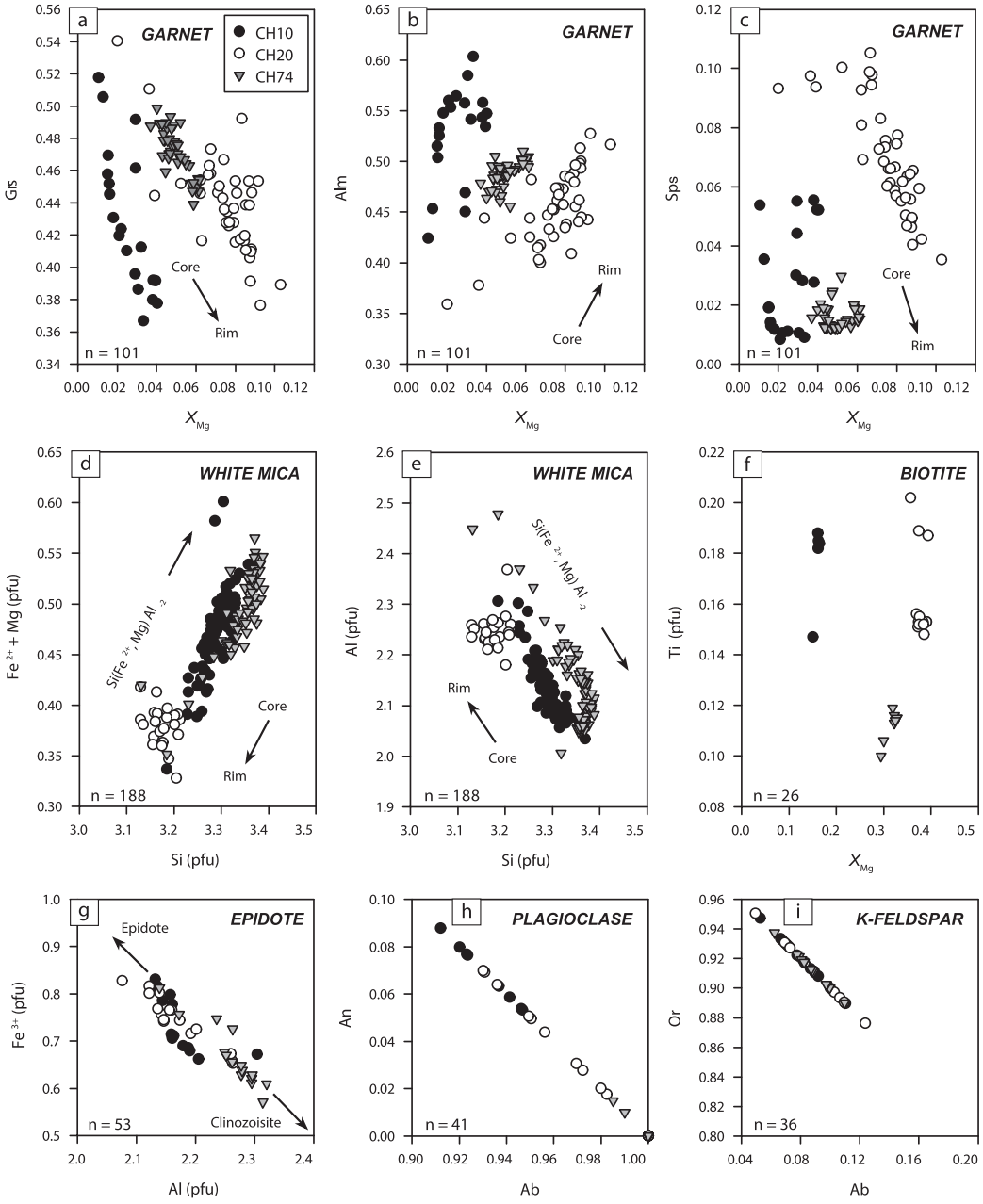

Fig. 5. Mineral composition of garnet (a–c), white mica (d–e), biotite (f), epidote/clinozoisite (g), and feldspar (h–i).

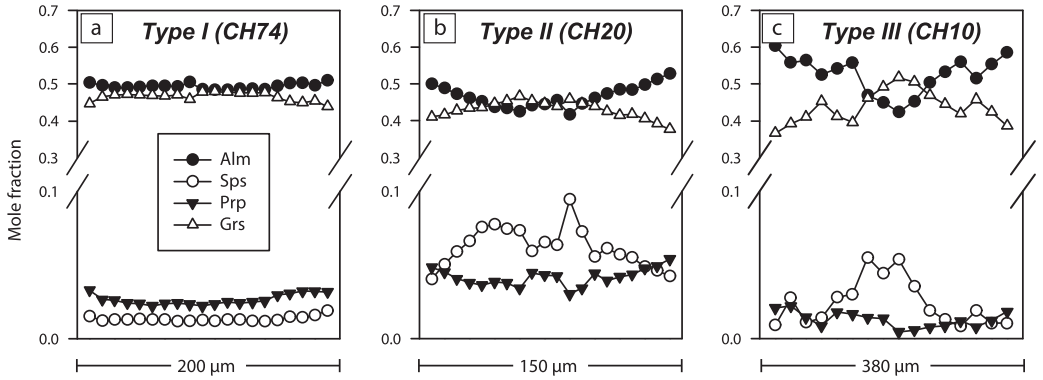

Fig. 6. Rim-to-rim compositional profiles of representative garnet porphyroblasts from the studied metagranitoids. The analyzed transects correspond closely to the central sections of the crystals.

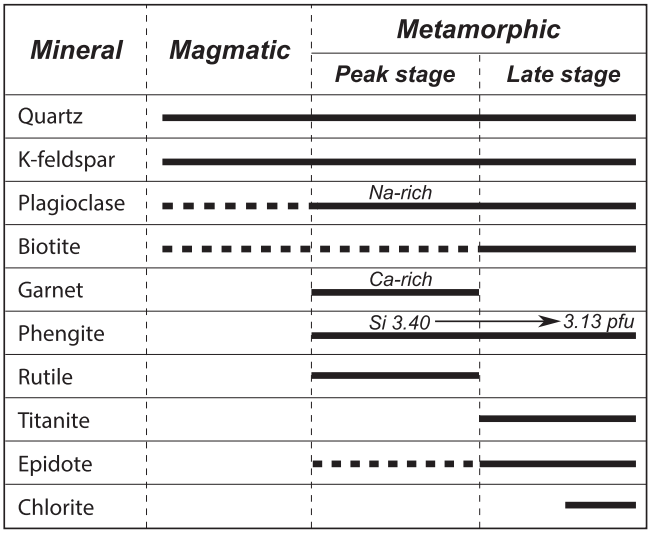

Fig. 7. (a) BSE image and X-ray compositional maps of representative garnet porphyroblasts. (b) BSE and pseudocolor images of a phengite porphyroblast displaying irregular compositional zoning due to chemical re-equilibration.

Fig. 10g). A coherent group of twenty-six measurements yielded a mean $^{207}Pb/^{206}Pb$ age of 1101 ± 13 Ma (MSWD = 5.5; Fig. 10h), which overlaps with the upper-intercept concordia age and, therefore, is interpreted to be the crystallization age of the granitic protolith. Three laser spots from inherited cores were discordant (4–8%; not plotted), but their $^{207}Pb/^{206}Pb$ ages of 1633 to 1235 Ma indicate that the minimum age of the inherited zircon is significantly older that the protolith crystallization. Although relatively imprecise, the lower-intercept age of ca. 371 Ma is equal within errors to previously reported lower-intercept and concordant ages obtained on a migmatized orthogneiss from the El Chol area (Fig. 1c; Ortega-Gutiérrez et al., 2004; Solari et al., 2011) and, therefore, it might be of geologic significance indicating a Late Devonian-Mississippian tectonothermal event recorded in the NE sector of the Sierra de Chuacús.

At CH10 sampling location, two structural/textural variations were sampled in the same, decameter-scale outcrop: CH10a, a leucocratic, fine-grained level with a poorly developed foliation, and CH10b, a medium-grained pinkish zone (see petrography). Zircon grains from both variations are relatively large (up to 400 μm long) and exhibit a variety of morphologies ranging from stubby to elongated prisms with aspect ratios up to 1:4. Unlike other samples, these grains commonly display rounded inherited cores with variable luminescence and zoning patterns (Fig. 9e, f). Overgrowths are also variable, ranging in brightness and zoning from medium-luminescence homogeneous to low-luminescence oscillatory. Some apparent metamorphic rims were not thick enough to be analyzed with the used 23-μm laser spot. Fifty-eight measurements from overgrowths, including homogeneous and oscillatory zoning domains in CH10a are characterized by Th/U values of up to ~1.8 and yielded mostly discordant results with a concordant cluster at ca. 1000 Ma. This data spread along a well-defined discordia line (MSWD = 3.2; Fig. 10i) with upper- and lower-intercepts at 1010 ± 11 Ma and 89 ± 50 Ma, respectively, which suggest variably strong Pb-loss during a Cretaceous thermal disturbance. A group of fifty-four laser spots yielded a mean $^{207}Pb/^{206}Pb$ age of 994 ± 9 Ma (MSWD = 1.08; Fig. 10j). However, as most of the analyses are discordant this date indicates only a minimum age and, therefore, the upper-intercept age is interpreted as the best approximation of the timing of granitic protolith crystallization. Only one point from a metamorphic rim (Th/U = 0.01) was measured giving a slightly discordant (8.3% discordance) result with a $^{206}Pb/^{238}U$ age of 72.2 ± 1.7 Ma, which is in agreement with the discordia lower-intercept, and suggest that a Late Cretaceous tectonothermal event resulted not only in partial Pb-loss but also in zircon neo-formation.

Forty-four laser spots from overgrowths (Th/U = 0.05–1.18) in CH10b yielded similar results with the data spread along a well-defined concordia chord (MSWD = 0.97; Fig. 10k) with upper- and lower-intercept ages of 1002 ± 13 Ma and 99 ± 36 Ma, respectively, and a mean $^{207}Pb/^{206}Pb$ age of 991 ± 12 Ma. These results allow an interpretation analogous to the previous one, where the upper-intercept age represents the best estimate of the crystallization age of the granitic protolith, and the lower-intercept age reflects a Cretaceous thermal event that promoted a strong Pb-loss. Two measurements of cores displaying magmatic

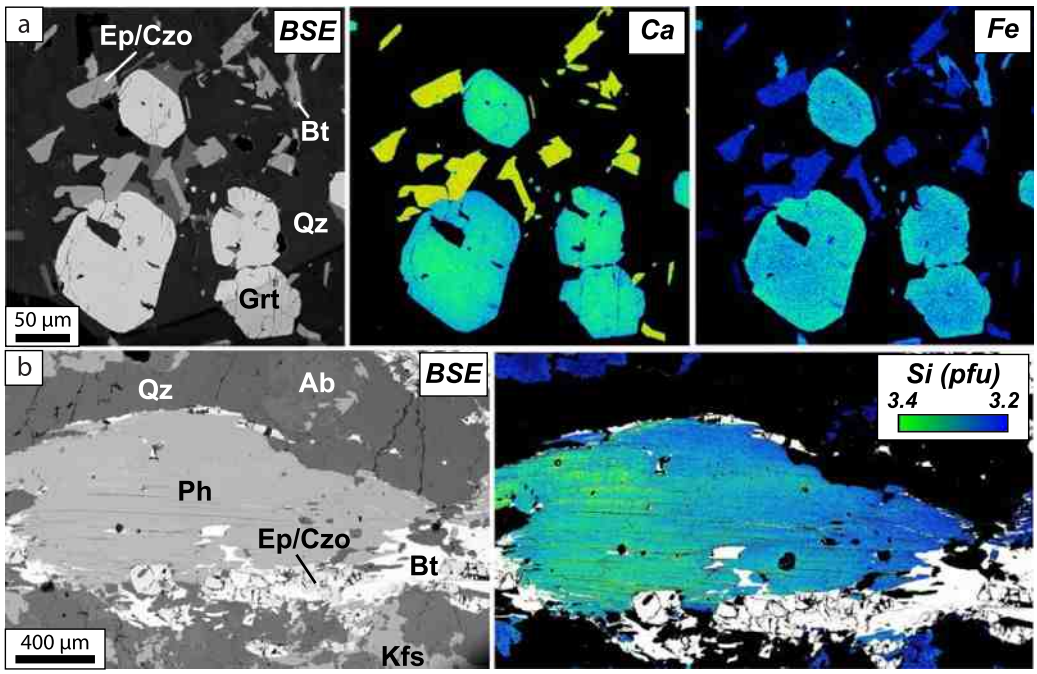

Fig. 8. Mineral assemblage evolution during the different stages of crystallization in the studied metagranitoids.

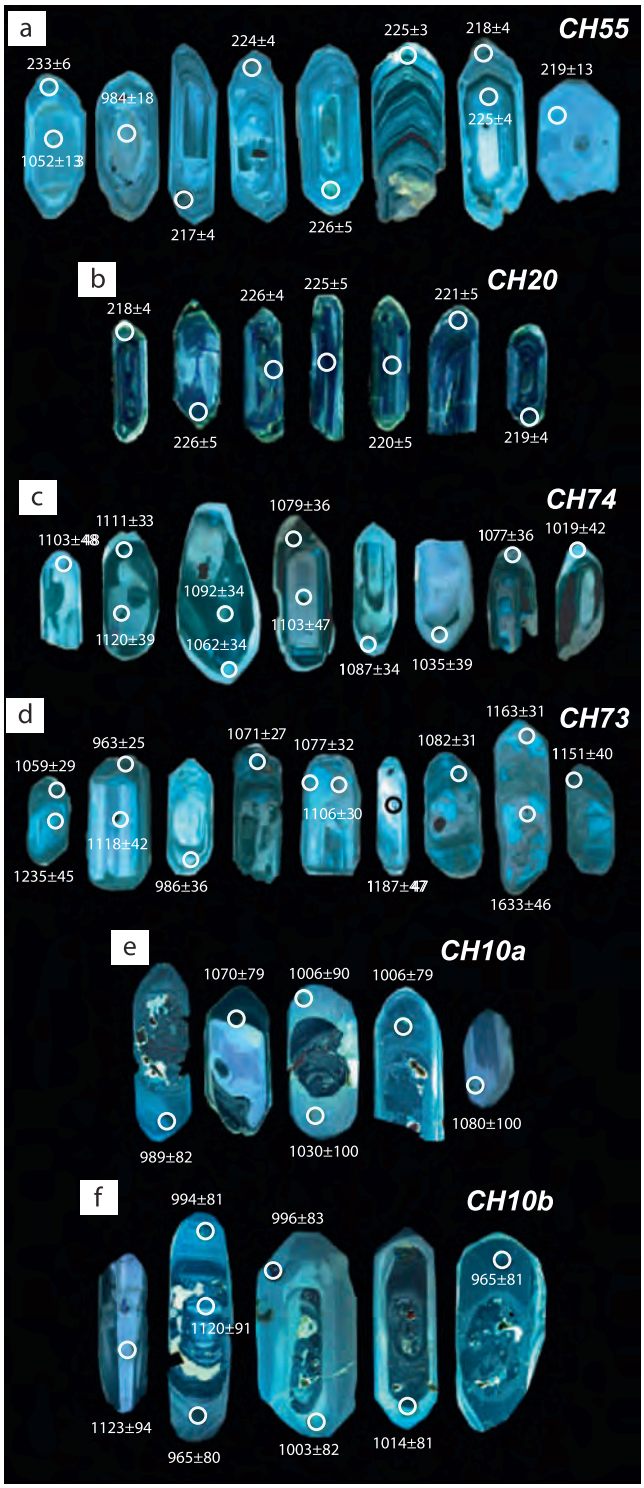

Fig. 9. CL images of representative zircon grains used for LA-ICP-MS geochronology. Circles indicate laser spot locations with their corresponding $^{206}Pb/^{238}U$ (a–b) and $^{207}Pb/^{206}Pb$ (c–f) ages.

zoning (Th/U = 0.3–0.4) were concordant- to slightly discordant (Fig. 9k) giving $^{207}Pb/^{206}Pb$ ages of ~1120 Ma, which indicates the inheritance of magmatic zircon with an age similar to the protolith ages of samples CH73 and CH74. No younger metamorphic ages can be reported from this sample.

4.4. Whole-rock compositions and constraints on protolith nature

Ten samples (Fig. 1c) were selected for major element analysis, whereas dated samples were additionally used for trace element measurements (Table 3). Most of the studied metagranitoids have SiO_2, Na_2O and K_2O contents that correspond to the granite composition according to the total alkali oxides-silica relation (Fig. 11). Furthermore, these rocks vary from ferroan to magnesian, alkalic to calcic, as well as metaluminous to peraluminous in composition (Fig. 11b–d). Samples with protolith ages of ca. 1.1 Ga (CH73, CH74) correspond to ferroan granite compositions with alkalic metaluminous- to alkalic-calcic peraluminous character. The ca. 1.0 Ga metagranitoid (CH10b) overlaps the boundary between ferroan and magnesian granites, and has an alkalic-calcic peraluminous nature. Metagranitoids with ca. 224 Ma protolith ages (CH20, CH55) range from syeno-diorite to granite and are distinguished by a magnesian (close to the ferroan-magnesian boundary), alkalic-calcic and metaluminous- to peraluminous character.

Primitive mantle normalized trace element abundances (Fig. 11e) reveal negative Nb, Ta and Ti anomalies, suggesting that a crustal component was incorporated into these rocks. In the same way as major elements, trace-element patterns show a correspondence with protolith age. Samples with ca. 1100 Ma protolith ages are relatively enriched in HFS elements, displaying a moderate negative Nb-Ta anomaly as well as moderate- to pronounced negative Ba, Sr and Eu anomalies. REE abundances normalized to CI chondrite reveal low $(La/Yb)_N$ values up to 5.2 with negative-slope HREE profiles (Fig. 11f). Zr contents in these samples range from 373 to 484 ppm and Ga/Al values are between 2.75 and 3.34, which together with major element compositions (ferroan type) and trace-element patterns suggest a magmatic source in an intraplate setting. In contrast, the ca. 990 Ma metagranitoid has low HFS element concentrations and displays more pronounced negative Ba, Nb, Ta, Sr and Ti anomalies. Its normalized REE abundances reveal a strongly fractionated pattern with a high $(La/Yb)_N$ value of 155 and a pronounced positive Eu anomaly, whereas the HREE contents result in a spoon-shaped profile (Fig. 11f). These features together with the marked negative Ta, Nb and Ti anomalies, as well as the high SiO_2 content (73 wt%) and the peraluminous character might reflect an origin related to (collisional?) anatexis, with garnet, amphibole and rutile as residual phases. On the other hand, ca. 224 Ma megacrystic metagranitoids also have relatively high HFS element abundances, giving moderate Nb, Ta and Ti anomalies as well as positive Zr anomaly. A positive Ba anomaly, negligible Eu anomaly, and less prominent negative Sr anomaly also characterize them. Their REE patterns result in $(La/Yb)_N$ values of 10 that are distinguished by flat HREE profiles. These samples have Zr contents ranging from 333 to 350 ppm and relatively low Ga/Al values of 2.1. High incompatible trace element contents suggest derivation from an undepleted mantle source, but the relatively low $(La/Yb)_N$ values could indicate a certain degree of contamination by an older continental crust.

Since there is a clear correlation between age and composition, including some of the most mobile elements, in spite of structural differences and metamorphic grade (see above), we interpret that both major and trace element compositions represent to a large degree the primary composition of the granitic protoliths.

5. Discussion and conclusions

5.1. Evidence for a Grenvillian-age basement and possible correlations

Although the available geochronological data from Central Guatemala reveal a ubiquitous Mesoproterozoic inherited/detrital component in both igneous and metamorphic rocks (e.g. Gomberg et al., 1968; Ratschbacher et al., 2009; Solari et al., 2009; Solari et al., 2010b; Solari et al., 2011), the actual presence of an exposed Precambrian basement has not been confirmed. The obtained U-Pb zircon protolith ages of 1.1

and 1.0 Ga are the first direct evidence that demonstrates the existence of a Grenvillian-age granitic basement in the Guatemala suture zone.

Geochemical data, on the one hand, suggest that protoliths of 1.1 Ga ferroan metagranitoids are related to intraplate magmatism, while the 1.0 Ga high-silica metagranite was probably originated by partial melting of a high-grade metamorphic continental crust in a collisional setting. Field and petrographic data, however, show that 1.1 Ga metagranitoids in the Sierra de Chuacús occur either as gneissic or undeformed bodies. In particular, sample CH74 preserves a magmatic appearance despite having equilibrated at HP conditions (Fig. 3a–c). It seems paradoxical that, if the 1.0 Ga metagranite was originated by anatexis of a necessarily older high-grade metamorphic continental crust, the spatially related 1.1 Ga metagranites (or at least sample CH74) lack any evidence of a former high-grade (e.g. granulitic) metamorphism. These considerations are particularly relevant because they preclude a direct correlation with the Grenvillian granulitic terranes from southern Mexico and northwestern South America. Nevertheless, geochronological similarities with recently published basement data from the northern Andes are still remarkable (e.g. Baquero et al., 2015; Ibanez-Mejia et al., 2011). For instance, zircon U-Pb crystallization ages of 1.1 Ga were obtained for an arc-related granitic augen gneiss from the Garzón Massif of Colombia, while anatectic leucogranite samples from exploratory wells in the Putumayo Basin yield 0.9–1.0 Ga ages (Cordani et al., 2005; Ibanez-Mejia et al., 2011; Fig. 12a).

The closest possibly Precambrian granitic basement in Central America occurs in the Sula Valley of Honduras (Chortís block). Massive to little deformed quartzofeldspathic rocks and chlorite-biotite-garnet metapelites are intruded by lineated granites that contain concordant 1.0 Ga zircons and yield a Nd model age of 1.4 Ga (Manton, 1996). Unfortunately these results published in abstract form have not been confirmed, and the dated granite could be much younger, perhaps contaminated by Grenvillian detrital zircons from the metamorphic country rocks. Additionally, recent U-Pb zircon data from felsic orthogneisses associated with amphibolite and massif-type anorthosite in the Chiapas Massif complex (southern Maya block) yield crystallization ages of ca. 1.0 Ga, indicating that granitic protoliths represent

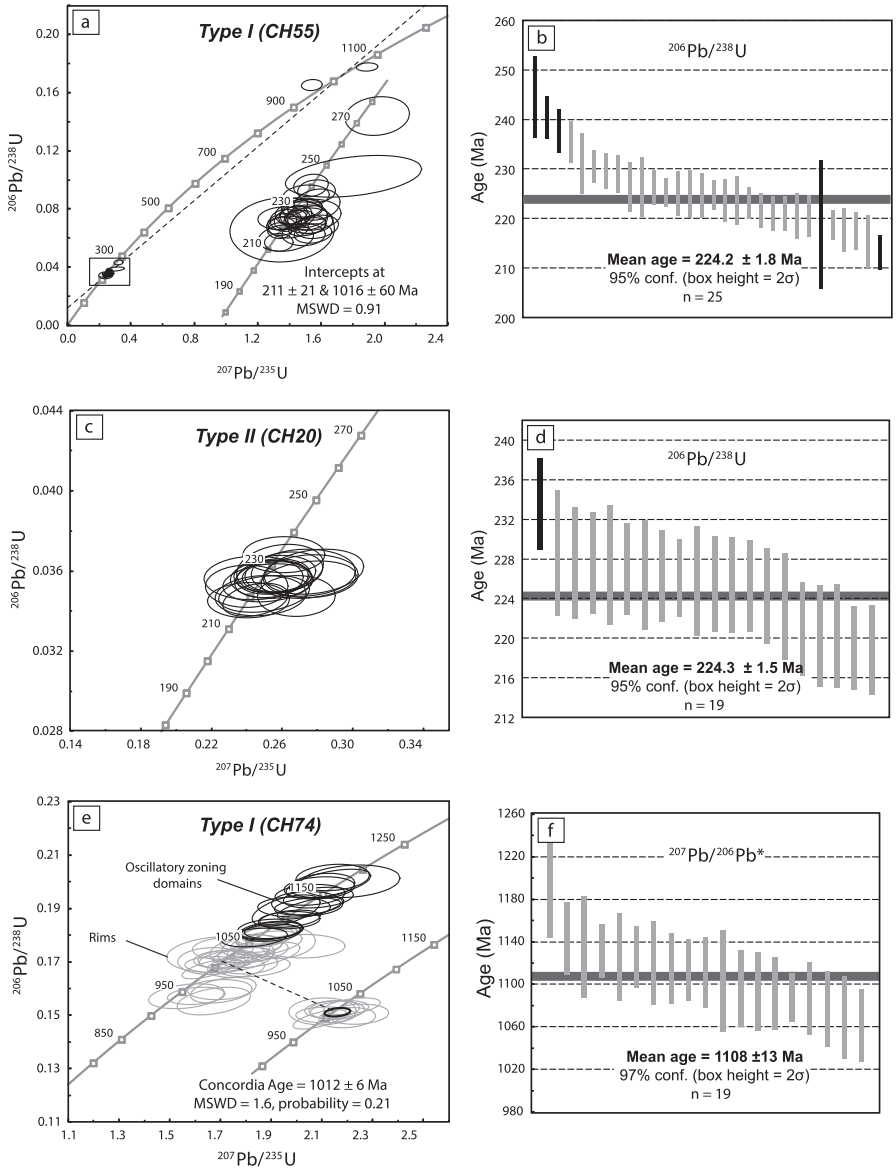

Fig. 10. Concordia diagrams (a, c, e, g, i, and k) and mean ages (b, d, f, h, j, and l) of LA-ICP-MS data from zircon grains of the studied metagranitoids. All uncertainties are shown at the 2σ level calculated with Isoplot (Ludwig, 2012).

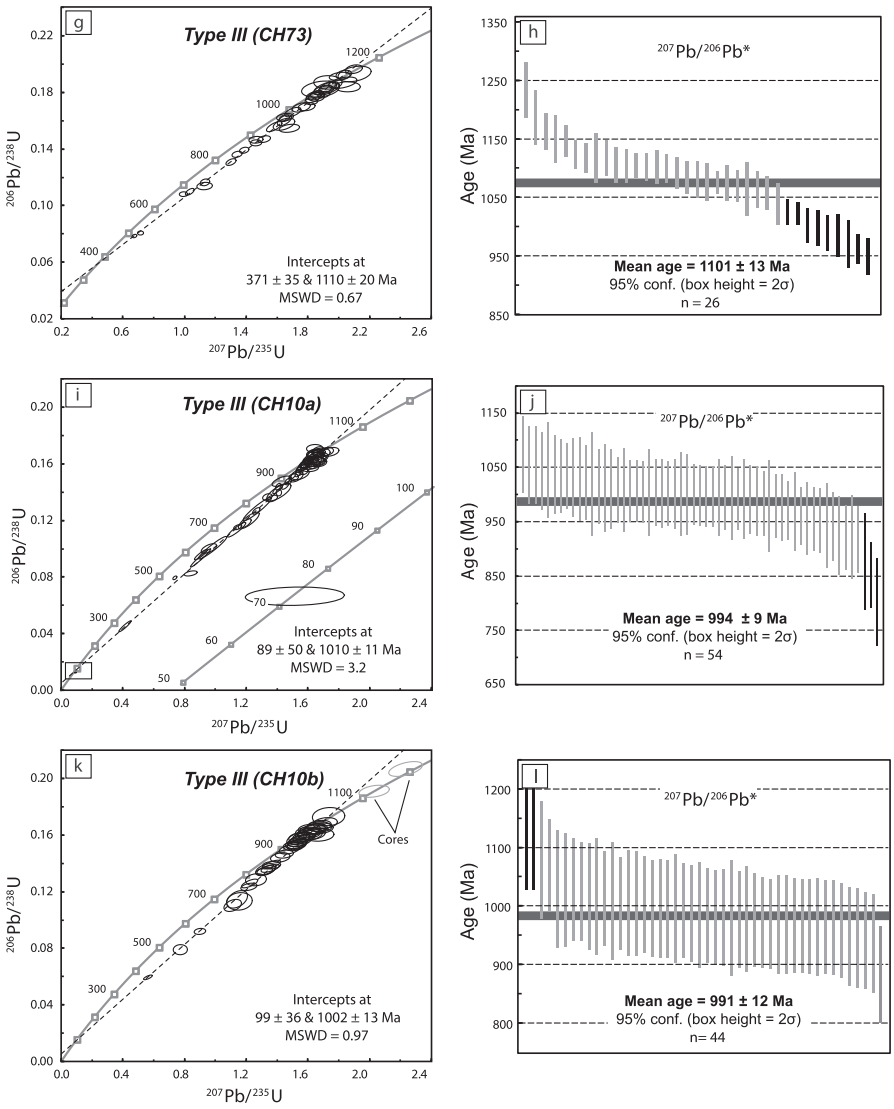

Fig. 10 (*continued*).

remnants of a Grenvillian basement that experienced amphibolite-facies metamorphism and anatexis at ca. 450 Ma (Weber et al., 2015; Cisneros de León et al., 2017; Fig. 12a). However, neither anorthositic bodies nor metamorphic ages of ca. 450 Ma have been reported in the Chuacús complex; therefore, with the available data it is not possible to consider a connection between both regions.

Stenian (1.1 Ga) granitic plutons intruding Laurentian crust are exposed north of the Ouachita-Marathon-Sonora (OMS) suture in northwestern Sonora (Yavapai-Mazatzal basement; e.g. Iriondo et al., 2004) and Texas (Grenville basement; e.g. Li et al., 2007; Barker and Reed, 2010), whereas south of the suture in the Coahuila block pebbles of banded and massive granites in conglomerate-bearing beds of the Paleozoic Las Delicias formation (McKee et al., 1999) yield zircon U-Pb crystallization ages of 1.2 Ga (Lopez et al., 2001; Fig. 12a). Correlations with Laurentian crust are however in conflict with the prevailing paleogeographic model that places southern Mexican and Middle American terranes south of the OMS suture in Pangea reconstructions (e.g. Dickinson and Lawton, 2001). Conversely, in spite of the 0.1 Ga age difference, a probable connection with the Coahuila block is more plausible due to the inferred adjacent position of the south Maya block before the breakup of Pangea.

5.2. Late Triassic magmatism: record of the initial breakup of western Pangea?

Even though current geochronological data indicates the existence of an older granitic basement in the Sierra de Chuacús (e.g. Ratschbacher et al., 2009; Solari et al., 2011; this work), Late Triassic igneous protoliths are apparently predominant. Previous studies reported zircon U-Pb mean ages between 213.5 ± 2.5 and 223 ± 4 Ma from granitic gneisses of the El Chol-Palibatz area (Martens et al., 2012; Ratschbacher et al., 2009; Solari et al., 2011), which are interpreted by Solari et al. (2011) to represent the time of protolith crystallization in a magmatic arc setting. Ratschbacher et al. (2009) also report a zircon U-Pb mean age of 217.7 ± 7.3 Ma from migmatitic gneisses from western Guatemala (Huehuetenango area). All these ages are equal within errors, or slightly younger, with the ages of ca. 224 Ma reported in this work from megacrystic/augen metagranitoids (samples CH20 and CH55). Analogous

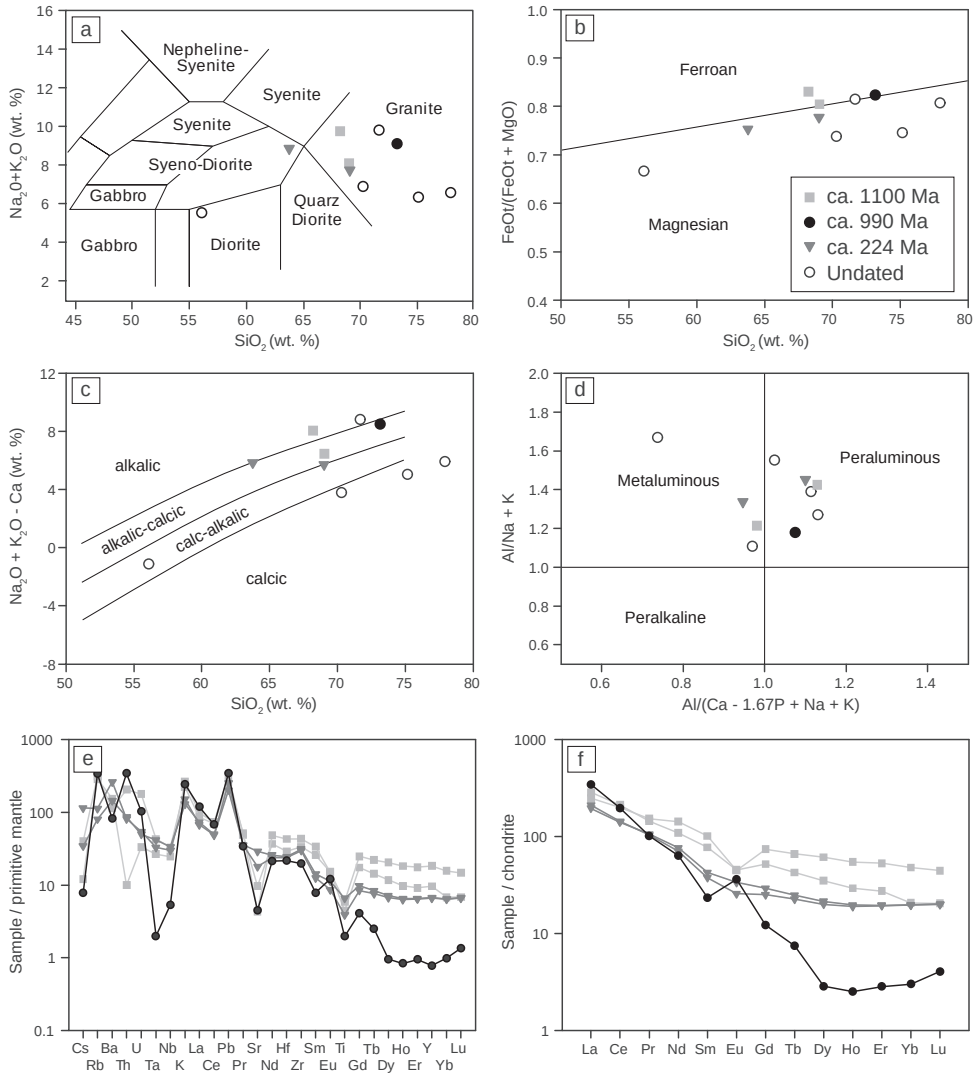

Fig. 11. Whole-rock compositions of the studied metagranitoids. (a) TAS diagram adapted for plutonic rocks (Wilson, 1989). (b) FeOt/(FeOt + MgO) vs SiO_2 diagram showing the boundary between ferroan and magnesian granitoids (Frost et al., 2001). (c) Modified alkali-lime index diagram (Frost et al., 2001). (d) Aluminum saturation index diagram with parameters modified by Frost et al., 2001. (e) Multi-element diagram normalized to Primitive Mantle values (Sun and McDonough, 1989). (f) REE diagram normalized to CI chondrite values (McDonough and Sun, 1995).

U-Pb crystallization ages of 226 ± 1 to 227 ± 19 Ma were obtained from basic rocks of the same region, including metagabbro and eclogite with tholeiitic signatures and isotopically juvenile compositions (Martens et al., 2012; Solari et al., 2011). This age correspondence among granitic and basic protoliths is indicative of Late Triassic bimodal magmatism recorded in the Sierra de Chuacús.

Geochemical features of Late Triassic metagranitoids include high incompatible trace element abundances and relatively low $(La/Yb)_N$ values, which suggest derivation from an undepleted mantle source, but with some degree of contamination by an older continental crust (also indicated by its Proterozoic zircon inheritance; Fig. 10a). We therefore suggest, on the basis of its geochemical character and spatial-temporal relationships with mafic protoliths, that Late Triassic granitic magmatism in the Sierra de Chuacús was probably originated in a within-plate setting instead of a magmatic arc environment. This bimodal association is more likely to have formed within a zone of elevated heat flow as is commonly observed in extending back-arc settings (Collins and Richards, 2008). However, more geochemical and geochronological data are still required to further support or discard this interpretation.

So far, Late Triassic magmatism (e.g. U-Pb crystallization ages) has not been documented in southern Mexico or Central America. Permian-Triassic magmatism is widely recognized in the Maya block of southern Mexico, but precise zircon U-Pb ages are not younger than 250.9 ± 2.3 Ma (lower intercept age; Weber et al., 2005), which contrasts with the restricted U-Pb ages of ca. 220 Ma found in the Sierra de Chuacús (Fig. 12a). Variably deformed metagranitoids within the Chiapas Massif complex crystallized since ca. 272 Ma and have been interpreted to represent Mid Permian arc magmatism linked to the amalgamation of Pangea (Weber et al., 2007). Trace element abundances in these rocks are variable but tend to display more fractionated REE patterns as well as strongest Nb and Ta anomalies with respect to Late Triassic metagranites from the Chuacús complex (Fig. 12b). On the other hand, granitic magmatism in other localities of the Maya block (e.g. Altos Cuchumatanes, Maya Mountains) seems to be entirely of Middle Ordovician to Lower Pennsylvanian age (Solari et al., 2010b; Weber et al., 2012). Therefore, in terms of Late Triassic magmatism, there is not an obvious correlation between the Chuacús complex and other localities within the Maya block such as the Chiapas Massif complex, the Altos Cuchumatanes and the Maya Mountains (Fig. 12a).

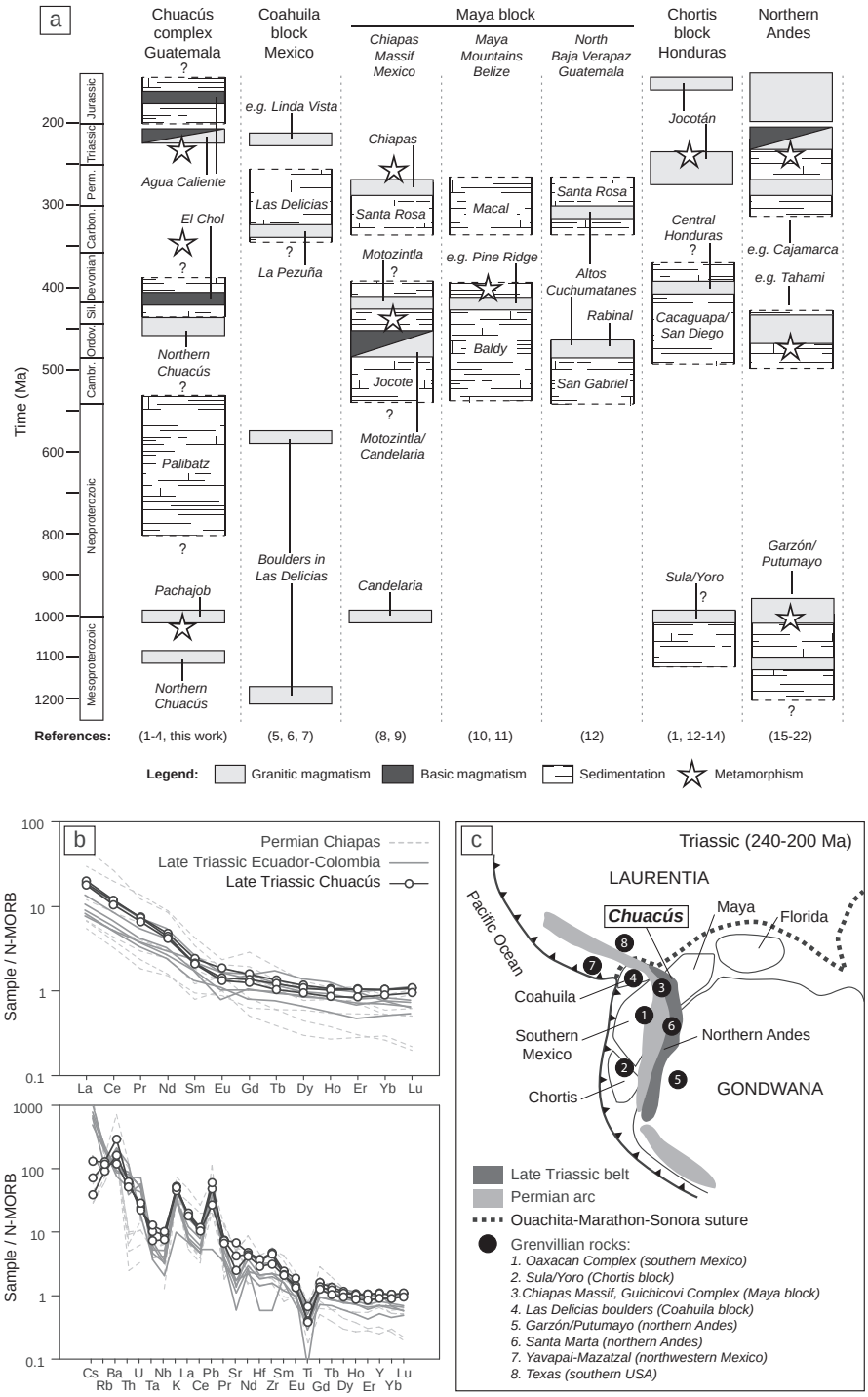

Fig. 12. (a) Temporal correlation scheme for the Chuacús complex, the Coahuila, Maya (Chiapas, Belize and Guatemala) and Chortis blocks, and the northern Andes (Ecuador, Colombia and Venezuela). All ages refer to available zircon U-Pb data. References for each region are numbered in the figure as follow figure. 1: Ratschbacher et al. (2009); 2: Solari et al. (2011); 3: Martens et al. (2012); 4: Maldonado et al. (2018); 5: Lopez (1997); 6: McKee et al. (1999); 7: Lopez et al. (2001); 8: Weber et al. (2005, 2007, 2008, 2015); 9: Estrada-Carmona et al. (2012); 10: Martens et al. (2010); 11: Weber et al. (2012); 12: Solari et al. (2009, 2010b, 2013); 13: Manton (1996); 14: Rogers et al. (2007 and references therein); 15: Litherland et al. (1994); 16: Cordani et al. (2005); 17: Vinasco et al. (2006); 18: Cardona et al. (2010); 19: Villagómez et al. (2011); 20: Ibanez-Mejia et al. (2011); 21: Cochrane et al. (2014); 22: Van der Lelij et al. (2016). (b) Trace element comparison between Permian and Late Triassic granitoids from the Chuacús complex, the Chiapas Massif complex (Maya block), and the Andes of Ecuador and Colombia. The data are normalized to N-MORB values (Sun and McDonough, 1989) and correspond to samples with available U-Pb crystallization ages. Data from the Chuacús complex: Solari et al. (2011); this work; Chiapas: Weber et al. (2005); Ecuador and Colombia: Cochrane et al. (2014). (c) Schematic reconstruction modified after Weber et al. (2007) and Cochrane et al. (2014) for western Pangea during 240–200 Ma, showing the proposed northward extension of the Late Triassic granitic belt exposed in the northern Andes. The locations of Grenvillian-age rocks, as well as other localities mentioned in the text are also shown.

Other possible correlative units are located in the Paleozoic terranes of northwestern South America. Late Triassic metagranites with comparable zircon U-Pb crystallization ages are found in the northern Andes of Colombia, Venezuela and Ecuador (Fig. 12a). Several concordant zircon U-Pb dates obtained from gneissic granitoids exposed in the Cordillera Central and the Guajira Peninsula in Colombia range between 222 ± 10

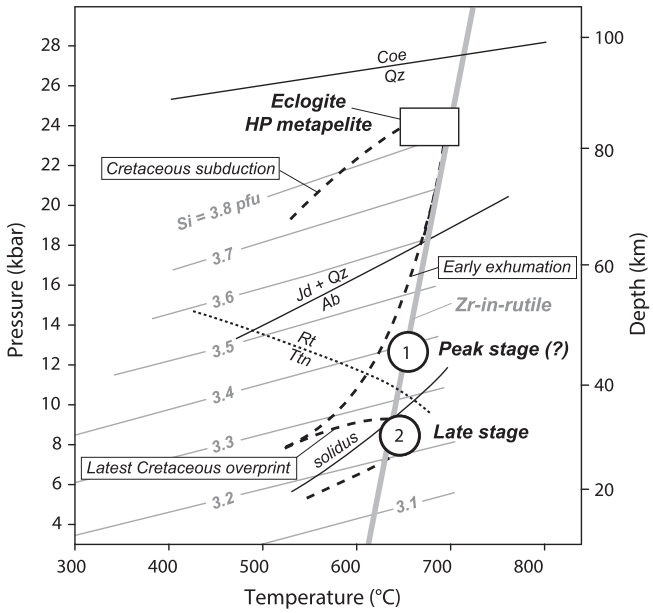

Fig. 13. Summary of the *P-T* estimates for the studied metagranitoids, showing some relevant reaction curves as reference. White circles represent: 1) the probable peak stage conditions obtained by combining Si-in-phengite barometry (Massonne and Schreyer, 1987) and Zr-in-rutile thermometry (Tomkins et al., 2007), and 2) the late stage conditions inferred from mineral assemblages. The dashed path indicates the Cretaceous subduction-zone evolution derived from associated eclogite and metapelite, where the white square represents the peak high-pressure conditions (Maldonado et al., 2018). The dotted line denotes the stability fields of rutile and titanite obtained experimentally in granitic compositions (Angiboust and Harlov, 2017).

and 247.6 ± 4.1 Ma (Cochrane et al., 2014; Restrepo et al., 2011; Villagómez et al., 2011; Vinasco et al., 2006). Undeformed granitoids from the Mérida Andes and the Sierra del Perijá in Venezuela yield similar concordant zircon U-Pb dates ranging between 211.2 ± 1.2 and 243.5 ± 3.4 Ma (Van der Lelij et al., 2016). These dates overlap with concordant zircon U-Pb dates obtained from metagranites in the Cordillera Real and the Amotape complex of Ecuador, which range between 207.6 ± 9.2 and 247.2 ± 4.3 Ma (Cochrane et al., 2014; Litherland et al., 1994). Apart from these age similarities, trace element abundances of Late Triassic granitoids from northern Andes and the Chuacús complex are almost identical (Fig. 12b).

While Permian granitoids reported in northern Colombia are interpreted to have formed during arc magmatism along the western margin of Pangea (Cardona et al., 2010), and thus have a direct correlation with the southern Maya block, Cochrane et al. (2014) suggest that Late Triassic bimodal magmatism in NW South America occurred during continental rifting at ca. 240–225 Ma, related to the initial disassembly of western Pangea. However, as Spikings et al. (2015) noted, a potential obstacle in conceiving southern Mexican terranes and NW Gondwana as probable conjugate margins regards to the lack of magmatic rocks in southern Mexico with crystallization ages spanning between 230 and 216 Ma. We suggest that Late Triassic bimodal magmatism in the Sierra de Chuacús formed within a similar extensional tectonic setting, and may represent the continuation of the Late Triassic belt exposed in northern Andes (Fig. 12c).

Additional probable correlations can be established with the Late Triassic granitic magmatism recorded in the Coahuila block of northeastern Mexico (Fig. 12a), where zircon U-Pb dates of ca. 220 Ma are reported by Lopez (1997). This probable correlation that includes the pre-Mississippian to late Paleozoic conglomerate-bearing Las Delicias formation (McKee et al., 1999), with granite boulders dated at 1.2 Ga (Lopez et al., 2001), could represent a potential piercing point between northeastern Mexico (Coahuila block) and the southern Maya block before the disassembly of western Pangea (Fig. 12c).

5.3. Subduction of Proterozoic to Late Triassic continental basement

The lithological association of the Chuacús complex and its metamorphic imprint suggest that a portion of continental lithosphere was subducted and eventually exhumed. Subduction-related metamorphism is primarily recognized by the presence of gneiss-hosted eclogite from the Sierra de Chuacús, which reached peak HP conditions close to the coesite stability field (Maldonado et al., 2018; Martens et al., 2012; Ortega-Gutiérrez et al., 2004). Associated metapelite attained similar *P-T* conditions of 23–25 kbar and 640–690 °C, and thus share a common HP evolution (Maldonado et al., 2018). Nevertheless, the metamorphism of granitic rocks, despite being the predominant lithology, has been scarcely documented and evaluated. Therefore, petrological constraints presented in this work, in combination with the geochronological results, provide important insights into the nature of the Chuacús complex and its implications for the evolution of the southern edge of the North American plate.

Regardless of their age or strain intensity, many of the studied granitic samples preserve, to a greater or lesser extent, evidence for HP metamorphic equilibration. Although it is commonly assumed that granitic compositions give only limited *P-T* information due to the lack of diagnostic assemblages, several studies in HP terranes have shown that the occurrence of Ca-rich garnet (X_{Ca} up to 0.72), in association with phengitic muscovite and rutile, represents a good indicator of HP metagranites (e.g. Carswell et al., 2000; Chopin et al., 2012; Compagnoni and Rolfo, 2003; Le Goff and Ballèvre, 1990; Massonne, 2015). In this work, the integration of Zr-in-rutile thermometry and phengite barometry in assemblages with Ca-rich garnet (X_{Ca} up to 0.52) allows the peak HP metamorphic conditions to be constrained at ~640–680 °C and ~13 kbar. This *P-T* estimate indicates that metagranitoids from the Sierra de Chuacús underwent HP metamorphism but equilibrated at least at 10 kbar below the pressure range of enclosed eclogite and adjoining metapelite (Fig. 13). Two possible scenarios could explain such pressure discrepancy: (1) metagranitoids did not follow the same *P-T* trajectory, or (2) they did, but not effectively register the *P-T* changes for kinetic reasons or, alternatively, the evidence for higher pressures was erased later during exhumation. Scenario (1) would imply that granitic rocks were buried to shallower crustal levels within the same subduction zone, and that, during exhumation, they were tectonically mixed with slices of eclogite and HP metapelite coming from deeper levels. This mechanism has been interpreted to occur in many collisional orogens, where eclogitic metamorphism may have occurred by pre-collisional oceanic subduction followed by syn-collisional continental subduction (e.g. Li and Massonne, 2016; Massonne, 2016, and references therein). On the other hand, scenario (2), which has also been invoked to argue the apparent lack of mineral

Table 2
Composition of rutile and temperatures from the Zr-in-rutile thermometer of Tomkins et al. (2007).

Label	Concentration (ppm)							Temperature (°C)	
	Nb	Si	Zr	Al	V	Cr	Fe	10 kbar	20 kbar
CH10-1	1130	35	262	41	366	3	4776	639	681
CH10-2	926	19	282	27	283	2	6264	645	688
CH10-3	1112	10	256	24	544	27	6320	637	679
CH10-4	1024	17	264	16	550	26	5594	640	682
CH10-5	1201	22	270	168	598	5	7105	641	684
CH10-6	1116	55	286	137	248	19	5389	646	689
CH10-7	1099	5	269	8	603	15	6398	641	684
CH10-8	1060	11	276	26	687	0	7844	643	686
CH10-9	1007	40	267	38	493	33	6556	640	683
CH10-10	1040	43	289	19	592	8	6100	647	690
CH10-11	1004	28	263	26	712	34	5705	639	682
CH10-12	1124	23	271	24	536	52	5054	642	684
Average ± σ			271 ± 10					642 ± 3	684 ± 3

Table 3
Whole-rock compositions.

Sample	CH5	CH8	CH10	CH20	CH28	CH49	CH55	CH57	CH73	CH74
Type	III	I	III	II	III	III	I	I	III	I
Major elements (wt%)										
SiO_2	74.47	77.23	72.58	62.95	70.99	55.18	68.13	69.83	67.95	67.53
TiO_2	0.50	0.14	0.26	0.86	0.32	2.56	0.51	0.25	0.77	0.58
Al_2O_3	13.08	12.74	13.57	16.48	13.31	14.39	15.64	16.83	14.18	14.80
Fe_2O_3t	2.61	1.55	2.78	5.20	3.24	9.73	3.91	1.94	5.13	4.09
MnO	0.04	0.02	0.03	0.09	0.04	0.16	0.05	0.03	0.06	0.06
MgO	0.80	0.34	0.54	1.53	0.66	4.39	1.01	0.62	1.12	0.75
CaO	1.37	0.69	0.64	3.02	1.00	6.58	2.03	3.11	1.57	1.72
Na_2O	4.52	5.21	3.00	5.00	2.63	4.82	4.42	6.04	2.42	3.03
K_2O	1.84	1.35	6.07	3.79	7.10	0.64	3.24	0.84	5.52	6.66
P_2O_5	0.13	0.01	0.05	0.34	0.10	0.89	0.21	0.05	0.22	0.20
LOI	0.52	0.68	0.49	1.03	0.43	0.56	0.99	0.70	1.26	0.52
Total	99.87	99.94	100.00	100.27	99.81	99.90	100.12	100.23	100.19	99.92
Trace elements (ppm)										
Li	–	–	4.02	13.4	–	–	3.14	–	8.14	9.03
Be	–	–	0.51	2.84	–	–	1.90	–	3.89	1.70
B	–	–	2.31	2.23	–	–	2.26	–	2.47	2.25
Sc	–	–	2.21	9.72	–	–	5.32	–	11.8	10.6
V	–	–	7.85	58.7	–	–	32.3	–	42.1	33.9
Cr	–	–	49.0	163	–	–	205	–	8.21	145
Co	–	–	2.80	7.47	–	–	6.20	–	8.62	5.83
Ni	–	–	1.48	5.69	–	–	5.05	–	3.98	5.76
Cu	–	–	0.97	10.1	–	–	16.8	–	7.22	5.26
Zn	–	–	34.2	53.7	–	–	28.2	–	76.5	58.3
Ga	–	–	24.7	18.7	–	–	17.1	–	25.1	21.5
Rb	–	–	215	72.1	–	–	51.0	–	200	182
Sr	–	–	94.6	611	–	–	379	–	91.4	204
Y	–	–	3.53	30.5	–	–	30.0	–	83.5	43.8
Zr	–	–	221	350	–	–	333	–	484	373
Nb	–	–	3.80	21.3	–	–	23.8	–	23.4	17.6
Mo	–	–	2.13	2.02	–	–	2.19	–	0.84	1.91
Sn	–	–	0.27	1.46	–	–	1.43	–	1.23	0.43
Sn	–	–	0.27	1.46	–	–	1.43	–	1.23	0.43
Sb	–	–	0.06	0.08	–	–	0.07	–	0.05	0.08
Cs	–	–	0.06	0.91	–	–	0.27	–	0.32	0.10
Ba	–	–	572	1836	–	–	1016	–	793	1085
La	–	–	81.8	46.5	–	–	50.0	–	59.0	67.8
Ce	–	–	121	86.4	–	–	88.3	–	123	130
Pr	–	–	9.42	9.85	–	–	9.64	–	14.2	13.4
Nd	–	–	28.9	35.0	–	–	32.2	–	65.3	49.8
Sm	–	–	3.47	6.34	–	–	5.58	–	15.0	11.5
Eu	–	–	2.03	1.90	–	–	1.45	–	2.51	2.56
Tb	–	–	0.27	0.90	–	–	0.82	–	2.40	1.54
Gd	–	–	2.44	5.85	–	–	5.01	–	14.8	10.3
Dy	–	–	0.70	5.29	–	–	4.93	–	15.0	8.63
Ho	–	–	0.14	1.07	–	–	1.03	–	2.99	1.60
Er	–	–	0.46	3.12	–	–	3.10	–	8.47	4.39
Yb	–	–	0.49	3.17	–	–	3.17	–	7.73	3.34
Lu	–	–	0.10	0.49	–	–	0.50	–	1.09	0.50
Hf	–	–	6.69	7.59	–	–	7.39	–	13.3	9.01
Ta	–	–	0.08	1.35	–	–	1.70	–	1.75	1.10
W	–	–	2.32	0.16	–	–	0.20	–	0.48	0.27
Tl	–	–	1.15	0.38	–	–	0.20	–	1.23	1.41
Pb	–	–	24.5	14.3	–	–	18.0	–	18.3	23.0
Th	–	–	29.2	6.95	–	–	7.41	–	17.5	0.85
U	–	–	2.15	1.13	–	–	1.04	–	3.76	0.70
Ga/Al	–	–	3.44	2.14	–	–	2.06	–	3.34	2.75

equilibration in granitic rocks from HP and UHP terranes (e.g. Chopin, 2003; Peterman et al., 2009; Proyer, 2003), would assume that the Chuacús complex was coherently subducted and exhumed. Ortega-Gutiérrez et al. (2004) and Ratschbacher et al. (2009) reported omphacite relics in granitic orthogneisses, demonstrating that some metagranitoids in the Sierra de Chuacús underwent eclogite-facies conditions. Although this finding could not be corroborated in this work, the possibility that retrogression has obliterated much of the HP features cannot be ruled out. In addition to this, we have emphasized the occurrence of contemporary granitic and basic protoliths in the Sierra de Chuacús, which suggests Late Triassic bimodal magmatism. Previous U-Pb zircon data, however, have shown that eclogite protoliths originated from the Silurian to the Jurassic (Maldonado et al., 2018). Therefore, this age variation of mafic precursors entails that the Chuacús complex may have subducted as a coherent, mostly pre-Jurassic, sequence, and that no (younger) oceanic crust component (e.g. Proto Caribbean crust) was tectonically incorporated later during exhumation. Further evidence for this latter interpretation is given by the fact that host metagranitoid and (centimeter- to meter-sized) eclogite lenses alternate at an outcrop scale and deformation localization in the host rock is far from representing meso-scale tectonic amalgamation. Accordingly, since we have indications of the two possible scenarios, the cause of the *P-T* discrepancy among

metagranitoids and other rock types in the Chuacús complex cannot be explained satisfactorily and must be further investigated.

The new data indicate that the Chuacús complex represents a Proterozoic (1.1–1.0 Ga) to Late Triassic (220 Ma) continental basement that was subducted, and consequently metamorphosed under HP conditions, during the Cretaceous evolution of the North America-Caribbean plate boundary. After subduction, part of this basement was exhumed as a relatively coherent sequence, allowing preservation of some primary structural relationships between protoliths and, in lesser degree, part of the textural features of granitic precursors. The local survival of undeformed, granitic bodies was promoted by strain partitioning from meso- to macro-scale during gneissic foliation development and it is the probable cause why previous interpretations have considered the Late Triassic magmatism to be younger than the HP metamorphism (e.g. Ratschbacher et al., 2009).

The age of HP metamorphism in the Sierra de Chuacús has recently been discussed in Maldonado et al. (2018). A garnet/whole-rock Lu-Hf date of 101.8 ± 3.1 from a kyanite-bearing eclogite is interpreted as indicating the time of garnet growth during subduction-zone metamorphism (pre-collisional stage), whilst zircon/monazite U-Pb dates between 73.6 ± 2.0 and 75.2 ± 2.2 Ma (Maldonado et al., 2018; Martens et al., 2012; Ratschbacher et al., 2009) are attributed to a subsequent amphibolite-facies overprint that occurred during a collisional stage. Zircon U-Pb geochronology presented in this work does not give further constraints on the timing of HP metamorphism due to the large uncertainty of lower-intercept dates (Fig. 10) as well as the paucity and thinness of metamorphic overgrowths in the analyzed grains (Fig. 9), which instead suggest that zircon growth in the studied metagranites must have been very limited during metamorphism. However, the U-Pb date of 72.2 ± 1.7 Ma obtained from only one laser spot on these zones is in agreement with other U-Pb ages probably related with the amphibolite-facies stage.

Supplementary data to this article can be found online at https://doi.org/10.1016/j.lithos.2018.02.030.

Acknowledgements

This work was funded by the Mexican "Programa de Apoyo a Proyectos de Investigación e Innovación Tecnológica, DGAPA-UNAM" grant IN104914. The first author acknowledges a Consejo Nacional de Ciencia y Tecología (CONACYT) PhD scholarship. M. C. Macías-Romo, A. M. Reyes-Salas, J. A. López-Díaz, C. Ortega-Obregón, and C. Linares-López are thanked for their technical support during the analytical procedures. D. Villanueva-Lascurain is thanked for his review of an early draft of the manuscript. Many thanks to Peter Schaaf, Luigi A. Solari, Sergio Morán-Ical and H. K. Brueckner for useful discussions. We are grateful to the reviewers H. J. Massonne and Samuel Angiboust, as well as to Lithos editor Marco Scambelluri for their constructive revision of the manuscript.

References

Anderson, T.H., Burkart, B., Clemons, R.E., Bohnenberger, O.H., Blount, D.N., 1973. Geology of the western Altos Cuchumatanes, northwestern Guatemala. Geological Society of America Bulletin 84 (3), 805–826.

Angiboust, S., Harlov, D., 2017. Ilmenite breakdown and rutile-titanite stability in metagranitoids: natural observations and experimental results. American Mineralogist: Journal of Earth and Planetary Materials 102 (8), 1696–1708.

Armstrong, J.T., 1988. Quantitative analysis of silicate and oxide minerals: comparison of Monte Carlo, ZAF and phi-rho-z procedures. Microbeam Analysis 23, 239–246.

Baquero, M., Grande, S., Urbani, F., Cordani, U., Hall, C., Armstrong, R., 2015. New evidence for Putumayo crust in the basement of the Falcon Basin and Guajira Peninsula, northwestern Venezuela. In: Bartolini, C., Mann, P. (Eds.), Petroleum Geology and Potential of the Colombian Caribbean Margin: AAPG Memoir. v108, pp. 103–136.

Barker, D., Reed, R., 2010. Proterozoic granites of the Llano Uplift, Texas: a collision–related suite containing rapakivi and topaz granites. Geological Society of America Bulletin 122, 253–264.

van den Boom, G., 1972. Petrofazielle Gliederung des metamorphen Grungebirges in der Sierra de Chuacús, Guatemala. Beihefte Geologisches Jahrbuch 122, 5–49.

Brueckner, H.K., Lallemant, H.G.A., Sisson, V.B., Harlow, G.E., Hemming, S.R., Martens, U., Tsujimori, T., Sorensen, S.S., 2009. Metamorphic reworking of a high pressure–low temperature mélange along the Motagua fault, Guatemala: a record of Neocomian and Maastrichtian transpressional. Earth and Planetary Science Letters 284 (1), 228–235.

Cardona, A., Valencia, V., Garzón, A., Montes, C., Ojeda, G., Ruiz, J., Weber, M., 2010. Permian to Triassic I to S-type magmatic switch in the northeast Sierra Nevada de Santa Marta and adjacent regions, Colombian Caribbean: tectonic setting and implications within Pangea paleogeography. Journal of South American Earth Sciences 29 (4), 772–783.

Carswell, D., Wilson, R., Zhai, M., 2000. Metamorphic evolution, mineral chemistry and thermobarometry of schists and orthogneisses hosting ultra-high pressure eclogites in the Dabieshan of central China. Lithos 52 (1), 121–155.

Chopin, C., 2003. Ultrahigh-pressure metamorphism: tracing continental crust into the mantle. Earth and Planetary Science Letters 212 (1–2), 1–14.

Chopin, F., Schulmann, K., Štípská, P., Martelat, J.E., Pitra, P., Lexa, O., Petri, B., 2012. Microstructural and metamorphic evolution of a high-pressure granitic orthogneiss during continental subduction (Orlica–Śnieżnik dome, Bohemian Massif). Journal of Metamorphic Geology 30 (4), 347–376.

Cisneros de León, A., Weber, B., Ortega-Gutiérrez, F., González-Guzmán, R., Maldonado, R., Solari, L., Schaaf, P., 2017. Grenvillian massif-type anorthosite suite in Chiapas, Mexico: magmatic to polymetamorphic evolution of anorthosites and their Ti-Fe ores. Precambrian Research 295, 203–226.

Cochrane, R., Spikings, R., Gerdes, A., Ulianov, A., Mora, A., Villagómez, D., Putlitz, B., Chiaradia, M., 2014. Permo-Triassic anatexis, continental rifting and the disassembly of western Pangaea. Lithos 190, 383–402.

Collins, W., Richards, S., 2008. Geodynamic significance of S-type granites in circum-Pacific orogens. Geology 36 (7), 559–562.

Compagnoni, R., Rolfo, F., 2003. UHPM units in the Western Alps. Ultrahigh Pressure Metamorphism. 5, pp. 13–49.

Cordani, U., Cardona, A., Jimenez, D., Liu, D., Nutman, A.P., 2005. Geochronology of Proterozoic basement inliers in the Colombian Andes: tectonic history of remnants of a fragmented Grenville belt. Geological Society, London, Special Publications 246 (1), 329–346.

Dickinson, W., Lawton, T., 2001. Carboniferous to Cretaceous assembly and fragmentation of Mexico. Geological Society of America Bulletin 113 (9), 1142–1160.

Donovan, J.J., Tingle, T.N., 1996. An improved mean atomic number background correction for quantitative microanalysis. Microscopy and Microanalysis 2 (1), 1–7.

Donovan, J.J., Snyder, D.A., Rivers, M.L., 1993. An improved interference correction for trace element analysis. Microbeam Analysis 2, 23–28.

Donovan, J.J., Lowers, H.A., Rusk, B.G., 2011. Improved electron probe microanalysis of trace elements in quartz. American Mineralogist 96 (2–3), 274–282.

Donovan, J.J., Singer, J.W., Armstrong, J.T., 2016. A new EPMA method for fast trace element analysis in simple matrices. American Mineralogist 101 (8), 1839–1853.

Estrada-Carmona, J., Weber, B., Martens, U., López-Martínez, M., 2012. Petrogenesis of Ordovician magmatic rocks in the southern Chiapas Massif Complex: relations with the early Palaeozoic magmatic belts of northwestern Gondwana. International Geology Review 54 (16), 1918–1943.

Ferrari, L., Bergomi, M., Martini, M., Tunesi, A., Orozco-Esquivel, T., López-Martínez, M., 2014. Late Cretaceous-Oligocene magmatic record in southern Mexico: the case for a temporal slab window along the evolving Caribbean-North America-Farallon triple boundary. Tectonics 33 (9), 1738–1765.

Flores, K.E., Martens, U.C., Harlow, G.E., Brueckner, H.K., Pearson, N.J., 2013. Jadeitite formed during subduction: in situ zircon geochronology constraints from two different tectonic events within the Guatemala Suture Zone. Earth and Planetary Science Letters 371, 67–81.

Frost, B.R., Barnes, C.G., Collins, W.J., Arculus, R.J., Ellis, D.J., Frost, C.D., 2001. A geochemical classification for granitic rocks. Journal of Petrology 42 (11), 2033–2048.

Gomberg, D., Banks, P., McBirney, A., 1968. Guatemela: preliminary zircon ages from Central Cordillera. Science 162 (3849), 121–122.

Hacker, B.R., Ratschbacher, L., Webb, L., Ireland, T., Walker, D., Shuwen, D., 1998. U/Pb zircon ages constrain the architecture of the ultrahigh-pressure Qinling-Dabie Orogen, China. Earth and Planetary Science Letters 161 (1–4), 215–230.

Harlow, G.E., Hemming, S.R., Lallemant, H.G.A., Sisson, V.B., Sorensen, S.S., 2004. Two high-pressure–low-temperature serpentinite-matrix mélange belts, Motagua fault zone, Guatemala: a record of Aptian and Maastrichtian collisions. Geology 32 (1), 17–20.

Holland, T., 2016. AX: A Program to Calculate Activities of Mineral Endmembers From Chemical Analyses (Usually Determined by Electron Microprobe). Available at:. http://www.esc.cam.ac.uk/research/research-groups/research-projects/tim-hollands-software-pages/ax.

Ibanez-Mejia, M., Ruiz, J., Valencia, V., Cardona, A., Gehrels, G.E., Mora, A.R., 2011. The Putumayo Orogen of Amazonia and its implications for Rodinia reconstructions: New U–Pb geochronological insights into the Proterozoic tectonic evolution of northwestern South America. Precambrian Research 191 (1), 58–77.

Iriondo, A., Premo, W.R., Martinez-Torres, L.M., Budahn, J.R., Atkinson, W.W., Siems, D.F., Guarás-González, B., 2004. Isotopic, geochemical, and temporal characterization of Proterozoic basement rocks in the Quitovac region, northwestern Sonora, Mexico: implications for the reconstruction of the southwestern margin of Laurentia. Geological Society of America Bulletin 116 (1–2), 154–170.

Kesler, S.E., Josey, W.L., Collins, E.M., 1970. Basement rocks of western nuclear Central America: the western Chuacús Group, Guatemala. Geological Society of America Bulletin 81 (11), 3307–3322.

Le Goff, E., Ballèvre, M., 1990. Geothermobarometry in albite-garnet orthogneisses: a case study from the Gran Paradiso nappe (Western Alps). Lithos 25 (4), 261–280.

van der Lelij, R., Spikings, R., Ulianov, A., Chiaradia, M., 2016. Palaeozoic to Early Jurassic history of the northwestern corner of Gondwana, and implications for the evolution of the Iapetus, Rheic and Pacific Oceans. Gondwana Research 31, 271–294.

Li, B., Massonne, H.J., 2016. Early Variscan P–T evolution of an eclogite body and adjacent orthogneiss from the northern Malpica-Tuy shear-zone in NW Spain. European Journal of Mineralogy 28 (6), 1131–1154.
Li, Y., Barnes, M., Barnes, C., Frost, C., 2007. Grenville-age A-type and related magmatism in southern Laurentia, Texas and New Mexico, USA. Lithos 97 (1), 58–87.
Litherland, M., Aspden, J., Jemielita, R., 1994. The metamorphic belts of Ecuador. British Geological Survey, Overseas Memoir. 11. British Geological Survey, Keyworth, p. 147.
Liu, F., Xu, Z., Xue, H., 2004. Tracing the protolith, UHP metamorphism, and exhumation ages of orthogneiss from the SW Sulu terrane (eastern China): SHRIMP U-Pb dating of mineral inclusion-bearing zircons. Lithos 78 (4), 411–429.
Lopez, R., 1997. The pre-Jurassic geotectonic evolution of the Coahuila terrane, northwestern Mexico: Grenville basement, a late Paleozoic arc. Triassic Plutonism, and the Events South of the Ouachita Suture. University of California, Santa Cruz, California, pp. 55–147 (PhD Dissertation).
Lopez, R., Cameron, K., Jones, N., 2001. Evidence for Paleoproterozoic, Grenvillian, and Pan-African age Gondwanan crust beneath northeastern Mexico. Precambrian Research 107 (3), 195–214.
Lozano, R., Bernal, J., 2005. Characterization of a new set of eight geochemical reference materials for XRF major and trace element analysis. Revista Mexicana de Ciencias Geológicas 22 (3), 329–344.
Ludwig, K.R., 2012. User's Manual for Isoplot 3.75, A Geochronological Toolkit for Microsoft Excel. Berkeley Geochronology Center Special Publication 5.
Luvizotto, G.L., Zack, T., Meyer, H.P., Ludiwg, T., Triebold, S., Kronz, A., Munker, C., Stockli, D.F., Prowatke, S., Klemme, S., Jacob, D.E., von Eynatten, H., 2009. Rutile crystals as potential trace element and isotope mineral standards for microanalysis. Chemical Geology 261, 346–369.
Maldonado, R., Ortega-Gutiérrez, F., Hernández-Uribe, D., 2016. Garnet–chloritoid–paragonite metapelite from the Chuacús Complex (Central Guatemala): new evidence for continental subduction in the North America–Caribbean plate boundary. European Journal of Mineralogy 28 (6), 1169–1186.
Maldonado, R., Weber, B., Ortega-Gutiérrez, F., Solari, L., 2018. High–pressure metamorphic evolution of eclogites and associated metapelites from the Chuacús complex (Guatemala suture zone): constraints from phase equilibria modeling coupled with Lu–Hf and U–Pb geochronology. Journal of Metamorphic Geology 36 (1), 95–124.
Manton, W., 1996. The Grenville of Honduras: Geological Society of America. Annual Meeting, Program With Abstracts A-493.
Martens, U., Weber, B., Valencia, V., 2010. U/Pb geochronology of Devonian and older Paleozoic beds in the southeastern Maya block, Central America: its affinity with peri-Gondwanan terranes. Geological Society of America Bulletin 122 (5–6), 815–829.
Martens, U.C., Brueckner, H.K., Mattinson, C.G., Liou, J.G., Wooden, J.L., 2012. Timing of eclogite-facies metamorphism of the Chuacús complex, Central Guatemala: record of Late Cretaceous continental subduction of North America's sialic. Lithos 146, 1–10.
Martens, U., Tsujimori, T., Liou, J., 2017. Eclogite varieties and petrotectonic evolution of the northern Guatemala Suture Complex. International Geology Review 59 (5–6), 721–740.
Massonne, H.J., 2015. Derivation of P–T paths from high-pressure metagranites — examples from the Gran Paradiso Massif, western Alps. Lithos 226, 265–279.
Massonne, H.J., 2016. Hydration of the lithospheric mantle by the descending plate in a continent–continent collisional setting and its geodynamic consequences. Journal of Geodynamics 96, 50–61.
Massonne, H.J., Schreyer, W., 1987. Phengite geobarometry based on the limiting assemblage with K-feldspar, phlogopite, and quartz. Contributions to Mineralogy and Petrology 96 (2), 212–224.
McBirney, A.R., 1963. Geology of a Part of the Central Guatemalan Cordillera. California University Publications in Geological Sciences 38 pp. 177–242.
McDonough, W.F., Sun, S.S., 1995. Composition of the Earth. Chemical Geology 120, 223–253.
McKee, J.W., Jones, N.W., Anderson, T.H., 1999. Late Paleozoic and early Mesozoic history of the Las Delicias terrane, Coahuila, Mexico. In: Bartolini, C., Lawton, T., Wilson, J.L. (Eds.), Mesozoic Sedimentary and Tectonic History of North-central Mexico. Geological Society of America Special Paper 340, pp. 161–190.
Morán-Ical, S.D., Chiquín, L.G., Requena, J.E., 2001. Mapeo Geológico de superficie del cuadrángulo Granados, escala 1:50,000. Unpublished report. Universidad de San Carlos de Guatemala, Centro Universitario del Norte.
Neill, O.K., Mattinson, C.G., Donovan, J., Hernández-Uribe, D., Sains, A., 2016. Increasing the efficiency of electron microprobe measurements of minor and trace elements in rutile. Abstract, AGU Fall Meeting, San Francisco, CA, USA.
Ortega-Gutiérrez, F., Solari, L., Solé, J., Martens, U., Gómez-Tuena, A., Morán-Ical, S., Reyes-Salas, M., 2004. Polyphase, high-temperature eclogite-facies metamorphism in the Chuacús Complex, central Guatemala: petrology, geochronology, and tectonic implications. International Geology Review 46 (5), 445–470.
Ortega-Obregón, C., Solari, L.A., Keppie, J.D., Ortega-Gutiérrez, F., Solé, J., Morán-Ical, S., 2008. Middle-Late Ordovician magmatism and Late Cretaceous collision in the southern Maya block, Rabinal-Salamá area, central Guatemala: implications for North America-Caribbean plate tectonics. Geological Society of America Bulletin 120 (5–6), 556–570.
Palin, R.M., Weller, O.M., Waters, D.J., Dyck, B., 2016. Quantifying geological uncertainty in metamorphic phase equilibria modelling; a Monte Carlo assessment and implications for tectonic interpretations. Geoscience Frontiers 7 (4), 591–607.
Paton, C., Hellstrom, J., Paul, B., Woodhead, J., Hergt, J., 2011. Iolite: freeware for the visualisation and processing of mass spectrometric data. Journal of Analytical Atomic Spectrometry 26 (12), 2508–2518.
Peterman, E.M., Hacker, B.R., Baxter, E.F., 2009. Phase transformations of continental crust during subduction and exhumation: Western Gneiss Region, Norway. European Journal of Mineralogy 21 (6), 1097–1118.
Petrus, J., Kamber, B., 2012. VizualAge: a novel approach to laser ablation ICP-MS U-Pb geochronology data reduction. Geostandards and Geoanalytical Research 36 (3), 247–270.
Proyer, A., 2003. The preservation of high-pressure rocks during exhumation: metagranites and metapelites. Lithos 70 (3–4), 183–194.
Ratschbacher, L., Franz, L., Min, M., Bachmann, R., Martens, U., Stanek, K., Stübner, K., Nelson, B.K., Herrmann, U., Weber, B., López-Martínez, M., Jonckheere, R., Sperner, B., Tichomirowa, M., Mcwilliams, M.O., Gordon, M., Meschede, M., Bock, P., 2009. The North American–Caribbean Plate boundary in Mexico–Guatemala–Honduras. In: James, K., Antonieta-Lorente, M., Pindell, J. (Eds.), The Geology and Evolution of the Region Between North and South America. Geological Society, London, Special Publications 328, pp. 219–293.
Restrepo, J., Ordóñez-Carmona, O., Armstrong, R., Pimentel, M., 2011. Triassic metamorphism in the northern part of the Tahamí Terrane of the central cordillera of Colombia. Journal of South American Earth Sciences 32 (4), 497–507.
Rogers, R.D., Mann, P., Emmet, P.A., 2007. Tectonic terranes of the Chortis block based on integration of regional aeromagnetic and geologic data. Geological Society of America Special Papers 428, 65–88.
Rowley, D.B., Xue, F., Tucker, R.D., Peng, Z.X., Baker, J., Davis, A., 1997. Ages of ultrahigh pressure metamorphism and protolith orthogneisses from the eastern Dabie Shan: U/Pb zircon geochronology. Earth and Planetary Science Letters 151 (3–4), 191–203.
Sláma, J., Košler, J., Condon, D., Crowley, J., Gerdes, A., 2008. Plešovice zircon–a new natural reference material for U–Pb and Hf isotopic microanalysis. Chemical Geology 249, 1), 1–35.
Solari, L.A., Ortega-Gutiérrez, F., Elias-Herrera, M., Schaaf, P., Norman, M., Ortega-Obregón, C., Chiquín, M., 2009. U-Pb zircon geochronology of Palaeozoic units in western and central Guatemala: insights into the tectonic evolution of Middle America. Geological Society, London, Special Publications 328 (1), 295–313.
Solari, L.A., Gómez-Tuena, A., Bernal, J., Pérez-Arvizu, O., Tanner, M., 2010a. U-Pb zircon geochronology with an integrated LA-ICP-MS microanalytical workstation: achievements in precision and accuracy. Geostandards and Geoanalytical Research 34 (1), 5–18.
Solari, L.A., Ortega-Gutiérrez, F., Elías-Herrera, M., Gómez-Tuena, A., Schaaf, P., 2010b. Refining the age of magmatism in the Altos Cuchumatanes, western Guatemala, by LA–ICPMS, and tectonic implications. International Geology Review 52 (9), 977–998.
Solari, L.A., Gómez-Tuena, A., Ortega-Gutiérrez, F., Ortega-Obregón, C., 2011. The Chuacús Metamorphic Complex, central Guatemala: geochronological and geochemical constraints on its Paleozoic-Mesozoic evolution. Geologica Acta 9 (3–4), 329–350.
Solari, L.A., García-Casco, A., Martens, U., Lee, J.K., Ortega-Rivera, A., 2013. Late Cretaceous subduction of the continental basement of the Maya block (Rabinal Granite, central Guatemala): tectonic implications for the geodynamic evolution of Central America. Geological Society of America Bulletin 125 (3–4), 625–639.
Spikings, R., Cochrane, R., Villagomez, D., Van der Lelij, R., Vallejo, C., Winkler, W., Beate, B., 2015. The geological history of northwestern South America: from Pangaea to the early collision of the Caribbean large igneous province (290–75 Ma). Gondwana Research 27 (1), 95–139.
Sun, S.S., McDonough, W.S., 1989. Chemical and isotopic systematics of oceanic basalts: implications for mantle composition and processes. Geological Society, London, Special Publications 42 (1), 313–345.
Sutter, J., 1979. Late Cretaceous collisional tectonics along the Motagua fault zone, Guatemala. Geological Society of America, Abstracts with Programs, p. 11.
Tomkins, H., Powell, R., Ellis, D., 2007. The pressure dependence of the zirconium-in-rutile thermometer. Journal of Metamorphic Geology 25 (6), 703–713.
Tsujimori, T., Sisson, V.B., Liou, J.G., Harlow, G.E., Sorensen, S.S., 2006. Petrologic characterization of Guatemalan lawsonite eclogite: eclogitization of subducted oceanic crust in a cold subduction zone. Geological Society of America Special Papers 403, 147–168.
Villagómez, D., Spikings, R., Magna, T., Kammer, A., Winkler, W., Beltrán, A., 2011. Geochronology, geochemistry and tectonic evolution of the Western and Central cordilleras of Colombia. Lithos 125 (3), 875–896.
Vinasco, C.J., Cordani, U.G., González, H., Weber, M., Pelaez, C., 2006. Geochronological, isotopic, and geochemical data from Permo-Triassic granitic gneisses and granitoids of the Colombian Central Andes. Journal of South American Earth Sciences 21 (4), 355–371.
Watson, E.B., Wark, D.A., Thomas, J.B., 2006. Crystallization thermometers for zircon and rutile. Contributions to Mineralogy and Petrology 151 (4), 413–433.
Weber, B., Cameron, K., Osorio, M., Schaaf, P., 2005. A Late Permian tectonothermal event in Grenville crust of the southern Maya terrane: U-Pb zircon ages from the Chiapas Massif, southeastern Mexico. International Geology Review 47 (5), 509–529.
Weber, B., Iriondo, A., Premo, W.R., Hecht, L., Schaaf, P., 2007. New insights into the history and origin of the southern Maya block, SE México: U–Pb–SHRIMP zircon geochronology from metamorphic rocks of the Chiapas massif. International Journal of Earth Sciences 96 (2), 253–269.
Weber, B., Valencia, V.A., Schaaf, P., Pompa-Mera, V., Ruiz, J., 2008. Significance of provenance ages from the Chiapas Massif Complex (southeastern Mexico): redefining the Paleozoic basement of the Maya Block and its evolution in a peri-Gondwanan realm. The Journal of Geology 116 (6), 619–639.
Weber, B., Scherer, E.E., Martens, U.K., Mezger, K., 2012. Where did the lower Paleozoic rocks of Yucatan come from? A U–Pb, Lu–Hf, and Sm–Nd isotope study. Chemical Geology 312, 1–17.

Weber, B., González, R., Cisneros, A., Manjarrez, R., Martens, U., 2015. The destruction and growth of lower continental crust along a Paleozoic active margin: an example from Chiapas, Mexico. Goldschmidt Abstracts.
Whitney, D., Evans, B., 2010. Abbreviations for names of rock-forming minerals. American Mineralogist 95 (1), 185–187.
Wiedenbeck, M., Alle, P., Corfu, F., Griffin, W.L., Meier, M., Oberli, F.V., von Quadt, A., Roddick, J.C., Spiegel, W., 1995. Three natural zircon standards for U-Th-Pb, Lu-Hf, trace element and REE analyses. Geostandards and Geoanalytical Research 19 (1), 1–23.
Wilson, M., 1989. Igneous Petrogenesis. Springer.
Zack, T.R., Moraes, R., Kronz, A., 2004. Temperature dependence of Zr in rutile: empirical calibration of a rutile thermometer. Contributions to Mineralogy and Petrology 148 (4), 471–488.

Supplementary material

PHASE EQUILIBRIA MODELING

We used a thermodynamic modeling approach in order to investigate mineral growth and obtain an estimate of peak metamorphic conditions. For this purpose, equilibrium phase diagrams were constructed over a range of pressure, temperature and bulk-rock H_2O conditions with the Gibbs free-energy minimization software Theriak-Domino (de Capitani and Brown, 1987; de Capitani and Petrakakis 2010), employing the thermodynamic data set of Holland and Powell (1998; upgraded to data set 5.5 in 2003 and translated readable for Theriak-Domino by D. K. Tinkham). The calculations were performed in the NCKFMASHTO (Na_2O-CaO-K_2O-FeO-MgO-Al_2O_3-SiO_2-H_2O-TiO_2-Fe_2O_3) system using the following *a-x* models: garnet, biotite and silicate melt from White *et al*., 2007, white mica from Coggon and Holland, 2002, epidote from Holland and Powell, 1998, ilmenite-hematite from White *et al*., 2000 and feldspar from Holland and Powell, 2003. Lawsonite, rutile, titanite, quartz, coesite, kyanite, jadeite and H_2O were considered as pure phases. Based on natural evidence pointing out garnet to be the major Ca-bearing stable phase during peak HP metamorphism (e.g. Proyer, 2003 and references therein), and in order to simplify the calculations, we have used pure jadeite instead an *a-x* model for Na-rich clinopyroxene (e.g. Green *et al*., 2007; Diener and Powell, 2012). The incorporation of *a-x* models for Na-rich clinopyroxene (not presented) favors the stability of omphacitic clinopyroxene over garnet, resulting in predicted mineral assemblages with low molar proportions of Fe-rich garnet (Fe (X) ≥ 0.85), which is inconsistent with the petrographic and mineral chemical data.

For the modeling, the whole-rock X-ray fluorescence analysis of sample CH10 was used (Table 3, Fig. A1). The effective bulk-composition was calculated by removing the total P_2O_5 and subtracting the appropriate amount of CaO to discard the apatite chemical contribution. MnO was neglected in the model due to its very low content in the sample. The Fe_2O_3 was set to be 2% of the total iron on the basis of the presence of peak-stage rutile, the occurrence of epidote/clinozoisite only as retrograde phase, and the low ferric iron content in garnet and phengite calculated by stoichiometric criteria. Higher ferric iron values of 10% have been used in similar study cases (e.g. Massonne, 2015), but such a values resulted in inconsistently high andradite contents in modeled garnet compositions. Fluid phase was considered to be pure water. The effect of chemical fractionation due to mineral zonation is inconsequential to the aim of the present study, thus bulk-composition fractionation calculations are not presented.

As a first approach a *P-H_2O* phase diagram was calculated to assess the effect of varying the water content on the predicted mineral assemblages and estimate the effective water amount to be considered in further calculations. A *P-H_2O* range of 10-25 Kbar and 0-4 mol. % at 650 ºC was set (Fig. A1a), which encompasses previous *P-T* results obtained for a structurally concordant garnet-kyanite-rutile bearing metapelite (Maldonado *et al*., 2018). The stability field of rutile in Fig. A1a constrains a lower pressure

limit of 11 kbar for mineral assemblages containing garnet, phengite and rutile, meanwhile the isopleth of phengite with maximum Si content (Si = 3.37 pfu) indicates pressure conditions of ~14 kbar (Fig. A1b). Garnet from sample CH10 shows a bell-shaped distribution of Mn indicative of a prograde growth zoning (Fig. 6c), such that the rim composition is interpreted to preserve the composition formed during peak-stage metamorphism. Fig. A1c shows that water content exerts a strong control over garnet composition at subsolidus conditions with increasing Ca and decreasing Fe as H_2O amount increases. The Ca (X) = 0.36 and Fe (X) = 0.60 isopleths, corresponding to garnet rim composition, overlap at relatively low water contents (~1-2 mol. %) within the (peak assemblage) field Grt-Bt-Kfs-Pl-Ph-Qz-Rt, between ~15-18 kbar (ellipse in Fig. A1c). On the other hand, suprasolidus equilibria is considerably extended to higher pressures for H_2O values >2 mol. %, but the sample lacks of evidence for the generation of granitic melt during peak-stage metamorphism. Consequently, an amount of 1.7 mol. % of H_2O was chosen to investigate phase equilibria in the *P-T* space.

A *P-T* phase diagram in a range of 10-25 Kbar and 500-750 ºC was performed (Fig. A1d), which involves mostly positive-slope boundaries with melt-bearing assemblages restricted to the relatively high-temperature, low-pressure corner. Phengite and quartz are predicted to be stable over the entire interval, meanwhile garnet and rutile are restricted to HP conditions above ~11 kbar. The Si = 3.37 pfu isopleth of phengite indicates equilibration pressures in the range of 16-17 kbar (Fig. A1e). However, as argued above, an evident decrease in the Si content of phengite during the post-peak metamorphic evolution suggest re-equilibration at pressures considerably lower than the presumably attained during peak-stage metamorphism. Therefore, isopleth barometry using phengite might provide only a minimum estimate of the pressure experienced by sample CH10, and higher-pressure conditions cannot be ruled out. On the other hand, garnet contours of Ca (X) and Fe (X) are almost parallel in the investigated *P-T* range (Fig. A1f), but the Ca (X) = 0.52 and Fe (X) = 0.45 isopleths representing garnet core composition overlap in a narrow area just above the Grt-in line at ~11 Kbar within the field Grt-Bt-Ilm-Kfs-Pl-Ph-Qz-Ttn, in agreement with the minor occurrence of titanite inclusions in garnet. The very low Mg (X) = 0.01 content in garnet core (not shown) indicates initial garnet growth temperatures of 450-500 ºC. *P-T* constrains on peak-stage metamorphism are given by the Ca (X) = 0.36 and Fe (X) = 0.60 isopleths for garnet rim composition that cross-cut at ~17-18 kbar and 600 ºC within the (peak assemblage) field Grt-Bt-Kfs-Pl-Ph-Qz-Rt, suggesting garnet rim crystallization slightly (~1 kbar) above the pressure range derived from Si-in-phengite barometry.

Additional constrains result from considering phengite and garnet rim compositions together with the Zr-in-rutile temperature line in Figs. A1e, f, which allows to define a *P-T* range of ~17 kbar and 630-660 ºC (ellipse in Fig. A1g) interpreted as the best approximation to peak-stage metamorphic conditions.

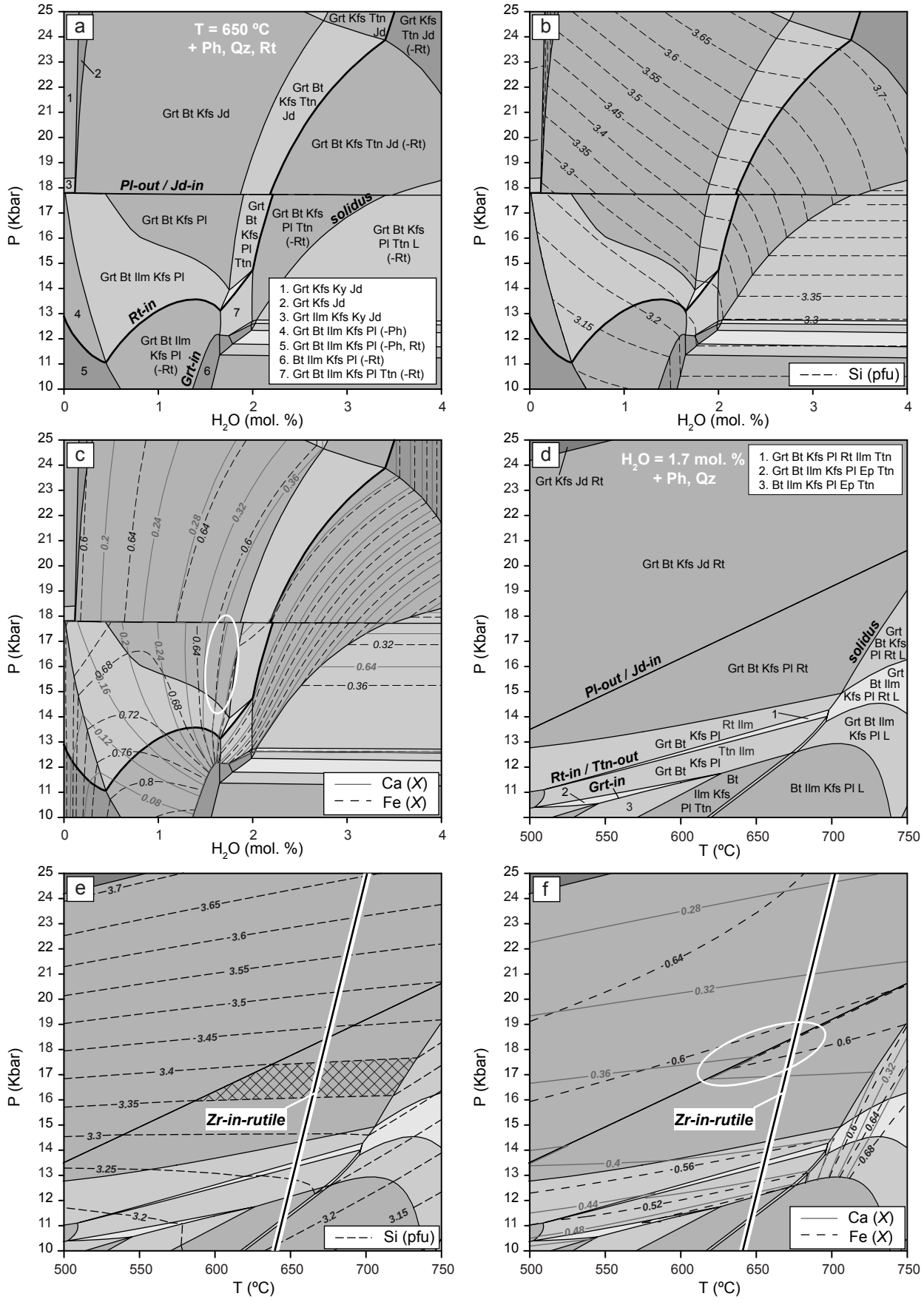
a
T = 650 ºC
+ Ph, Qz, Rt
Grt Kfs Ttn Jd
Grt Kfs Ttn Jd (-Rt)
Grt Bt Kfs Jd
Grt Bt Kfs Ttn Jd
Grt Bt Kfs Ttn Jd (-Rt)
Pl-out / Jd-in
Grt Bt Kfs Pl
Grt Bt Kfs Pl Ttn (-Rt)
solidus
Grt Bt Kfs Pl Ttn L (-Rt)
Grt Bt Ilm Kfs Pl
Rt-in
Grt Bt Ilm Kfs Pl (-Rt)
Grt-in
1. Grt Kfs Ky Jd
2. Grt Kfs Jd
3. Grt Ilm Kfs Ky Jd
4. Grt Bt Ilm Kfs Pl (-Ph)
5. Grt Bt Ilm Kfs Pl (-Ph, Rt)
6. Bt Ilm Kfs Pl (-Rt)
7. Grt Bt Ilm Kfs Pl Ttn (-Rt)
P (Kbar)
H2O (mol. %)
b
Si (pfu)
c
Ca (X)
Fe (X)
d
H2O = 1.7 mol. %
+ Ph, Qz
1. Grt Bt Kfs Pl Rt Ilm Ttn
2. Grt Bt Ilm Kfs Pl Ep Ttn
3. Bt Ilm Kfs Pl Ep Ttn
Grt Kfs Jd Rt
Grt Bt Kfs Jd Rt
Pl-out / Jd-in
Grt Bt Kfs Pl Rt
solidus
Grt Bt Kfs Pl Rt L
Grt Bt Ilm Kfs Pl Rt L
Grt Bt Ilm Kfs Pl L
Rt-in / Ttn-out
Grt-in
Bt Ilm Kfs Pl L
T (ºC)
e
Zr-in-rutile
f

Figure A1. Equilibrium phase diagrams for the modified bulk composition of sample CH10. (a-c) *P-H_2O* phase diagram at 650 ºC contoured with the calculated isopleths for phengite and garnet. (d-f) *P-T* phase diagram for the composition: SiO_2=73.04, TiO_2=0.26, Al_2O_3=13.65, Fe_2O_3=0.06, FeO=2.47, MgO=0.54, CaO=0.59, Na_2O=3.02, K2O=6.11, H_2O=0.46 (wt. %) and calculated isopleths for phengite and garnet. Ellipses in (c) and (f) indicate areas of *P-T* equilibration constrained by comparing predictions with petrographic and microchemical observations, but do not represent a formal assessment of uncertainty. Ca (*X*) and Fe (*X*) isopleths represent Ca and Fe compositions with respect to divalent cation *X*-site occupancy.

In consequence, assuming that sample CH10 was fully equilibrated during its HP evolution and that phase diagrams have not a significant topological change due to garnet chemical fractionation, the phase equilibria approach allows thus to constrain an approximate segment of the prograde *P-T* path from ~11 kbar and 450-500 ºC to ~17 kbar and 630-660 ºC.

References

Coggon, R., Holland, T., 2002. Mixing properties of phengitic micas and revised garnet-phengite thermobarometers. Journal of Metamorphic Geology 20(7), 683-696.

de Capitani, C., Brown, T., 1987. The computation of chemical equilibrium in complex systems containing non-ideal solutions. Geochimica et Cosmochimica Acta, 51(10), 2639-2652.

de Capitani, C., Petrakakis, K., 2010. The computation of equilibrium assemblage diagrams with Theriak/Domino software. American Mineralogist 95, 1006-1016.

Diener, J., Powell, R., 2012. Revised activity–composition models for clinopyroxene and amphibole. Journal of Metamorphic Geology 30(2), 131-142.

Green, E., Holland, T., Powell, R., 2007. An order-disorder model for omphacitic pyroxenes in the system jadeite-diopsidehedenbergite-acmite, with applications to eclogitic rocks. American Mineralogist 92(7), 1181-1189.

Holland, T., Powell, R., 1998. An internally consistent thermodynamic data set for phases of petrological interest. Journal of Metamorphic Geology 16(3), 309-343.

Holland, T., Powell, R., 2003. Activity-composition relations for phases in petrological calculations: an asymmetric multicomponent formulation. Contributions to Mineralogy and Petrology, 145(4), 492-501.

Maldonado, R., Weber, B., Ortega-Gutiérrez, F., Solari, L., 2018. High–pressure metamorphic evolution of eclogites and associated metapelites from the Chuacús complex (Guatemala suture zone): constraints from phase equilibria modeling coupled with Lu–Hf and U–Pb geochronology. Journal of Metamorphic Geology. 36(1), 95-124

Massonne, H., 2015. Derivation of P–T paths from high-pressure metagranites—Examples from the Gran Paradiso Massif, western Alps. Lithos 226, 265-279.

Proyer, A., 2003. Metamorphism of pelites in NKFMASH–a new petrogenetic grid with implications for the preservation of high-pressure mineral assemblages during exhumation. Journal of Metamorphic Geology 21(5), 493-509.

White, R. W., Powell, R., Holland, T. J. B., Worley, B. A., 2000. The effect of TiO_2 and Fe_2O_3 on metapelitic assemblages at greenschist and amphibolite facies conditions: mineral equilibria calculations in the system K_2O-FeO-MgO-Al_2O_3-SiO_2-H_2O-TiO_2-Fe_2O_3. Journal of Metamorphic Geology 18, 497-511.

White, R., Powell, R., Holland, T., 2007. Progress relating to calculation of partial melting equilibria for metapelites. Journal of Metamorphic Geology 25(5), 511-527.

Table A1. U-Pb isotopic data

				Isotope ratios										Apparent ages (Ma)						
Point	**U (ppm)**	**Th (ppm)**	**Th/U**	**$^{207}Pb/^{206}Pb$**	**±2σ abs**	**$^{207}Pb/^{235}U$**	**±2σ abs**	**$^{206}Pb/^{238}U$**	**±2σ abs**	**$^{208}Pb/^{232}Th$**	**±2σ abs**	**Rho**	**$^{206}Pb/^{238}U$**	**±2σ**	**$^{207}Pb/^{235}U$**	**±2σ**	**$^{207}Pb/^{206}Pb$**	**±2σ**	**% Disc.**
CH55 undeformed metagranitoid																			
CH55-Zrn-39	153	75	0.49	0.0772	0.0028	1.8910	0.0560	0.1773	0.0023	0.0548	0.0017	0.11	1052.0	13.0	1079.0	20.0	1124.0	44.0	2.5
CH55-Zrn-06	106	45	0.42	0.0685	0.0031	1.5410	0.0530	0.1650	0.0032	0.0496	0.0033	0.11	984.0	18.0	946.0	21.0	893.0	49.0	-4.0
CH55-Zrn-01	144	180	1.25	0.0548	0.0039	0.3220	0.0220	0.0433	0.0012	0.0132	0.0007	0.13	273.1	7.1	286.0	16.0	435.0	99.0	4.5
CH55-Zrn-15	64	55	0.87	0.0606	0.0094	0.3020	0.0470	0.0387	0.0013	0.0124	0.0013	0.35	244.7	8.2	264.0	37.0	720.0	160.0	7.3
CH55-Zrn-05	361	301	0.83	0.0507	0.0023	0.2660	0.0120	0.0380	0.0007	0.0134	0.0005	0.16	240.4	4.3	239.0	9.8	296.0	50.0	-0.6
CH55-Zrn-11	279	243	0.87	0.0539	0.0030	0.2710	0.0130	0.0376	0.0007	0.0122	0.0005	0.04	237.7	4.4	245.0	10.0	385.0	72.0	3.0
CH55-Zrn-17	314	266	0.85	0.0514	0.0032	0.2620	0.0160	0.0372	0.0007	0.0115	0.0004	0.12	235.5	4.2	235.0	13.0	371.0	68.0	-0.2
CH55-Zrn-03	233	260	1.12	0.0534	0.0038	0.2710	0.0160	0.0365	0.0010	0.0111	0.0005	0.17	231.3	6.1	242.0	13.0	401.0	84.0	4.4
CH55-Zrn-16	1097	1320	1.20	0.0503	0.0020	0.2520	0.0089	0.0364	0.0005	0.0119	0.0004	0.27	230.6	3.3	227.9	7.3	241.0	52.0	-1.2
CH55-Zrn-28	301	286	0.95	0.0526	0.0028	0.2610	0.0120	0.0363	0.0006	0.0116	0.0005	0.13	229.8	3.6	234.6	9.9	350.0	50.0	2.0
CH55-Zrn-14	244	218	0.89	0.0535	0.0029	0.2590	0.0140	0.0362	0.0006	0.0116	0.0004	0.12	229.1	3.8	238.0	11.0	400.0	68.0	3.7
CH55-Zrn-36	234	190	0.81	0.0523	0.0041	0.2580	0.0180	0.0358	0.0008	0.0115	0.0005	0.02	226.5	5.0	232.0	14.0	440.0	130.0	2.4
CH55-Zrn-13	228	126	0.55	0.0550	0.0049	0.2660	0.0210	0.0358	0.0010	0.0117	0.0007	0.11	226.4	6.0	238.0	17.0	551.0	73.0	4.9
CH55-Zrn-20	562	417	0.74	0.0512	0.0022	0.2510	0.0098	0.0357	0.0006	0.0113	0.0004	0.34	226.3	3.5	228.3	8.2	299.0	50.0	0.9
CH55-Zrn-08	804	771	0.96	0.0522	0.0020	0.2544	0.0087	0.0356	0.0005	0.0110	0.0003	0.13	225.3	2.9	229.9	7.1	283.0	44.0	2.0
CH55-Zrn-25	251	179	0.71	0.0543	0.0032	0.2630	0.0140	0.0356	0.0008	0.0114	0.0005	0.06	225.2	4.8	238.0	12.0	475.0	92.0	5.4
CH55-Zrn-26	296	436	1.47	0.0522	0.0028	0.2510	0.0130	0.0356	0.0007	0.0113	0.0004	0.37	225.2	4.5	227.0	11.0	311.0	57.0	0.8
CH55-Zrn-33	218	139	0.64	0.0487	0.0034	0.2420	0.0170	0.0355	0.0007	0.0111	0.0006	0.09	224.8	4.5	219.0	14.0	376.0	100.0	-2.6
CH55-Zrn-43	635	402	0.63	0.0527	0.0022	0.2568	0.0098	0.0355	0.0005	0.0117	0.0004	0.24	224.8	3.0	233.7	8.4	293.0	57.0	3.8
CH55-Zrn-35	320	185	0.58	0.0506	0.0026	0.2450	0.0110	0.0353	0.0007	0.0118	0.0005	0.03	223.8	4.3	222.1	9.1	328.0	64.0	-0.8
CH55-Zrn-44	295	176	0.60	0.0533	0.0036	0.2640	0.0170	0.0353	0.0008	0.0110	0.0006	0.05	223.7	4.9	237.0	14.0	408.0	80.0	5.6
CH55-Zrn-41	578	417	0.72	0.0502	0.0021	0.2417	0.0100	0.0352	0.0005	0.0116	0.0004	0.27	223.2	3.2	219.5	8.2	200.0	37.0	-1.7
CH55-Zrn-19	430	302	0.70	0.0561	0.0027	0.2664	0.0100	0.0350	0.0006	0.0113	0.0004	0.19	221.7	3.5	239.5	8.2	501.0	70.0	7.4
CH55-Zrn-18	389	349	0.90	0.0554	0.0027	0.2630	0.0130	0.0348	0.0006	0.0108	0.0004	0.37	221.2	3.5	236.0	10.0	430.0	56.0	6.3
CH55-Zrn-04	577	608	1.05	0.0506	0.0022	0.2410	0.0100	0.0349	0.0006	0.0109	0.0003	0.05	221.1	3.5	218.9	8.5	326.0	66.0	-1.0
CH55-Zrn-27	287	189	0.66	0.0531	0.0033	0.2470	0.0140	0.0348	0.0007	0.0114	0.0004	0.02	220.6	4.2	225.0	11.0	424.0	65.0	2.0
CH55-Zrn-29	234	126	0.54	0.0576	0.0038	0.2710	0.0150	0.0348	0.0007	0.0120	0.0006	0.22	220.6	4.6	243.0	12.0	539.0	86.0	9.2
CH55-Zrn-31	33	20	0.60	0.0503	0.0082	0.2420	0.0360	0.0346	0.0020	0.0096	0.0010	0.05	219.0	13.0	215.0	29.0	810.0	150.0	-1.9
CH55-Zrn-10	724	561	0.77	0.0507	0.0020	0.2397	0.0083	0.0345	0.0005	0.0111	0.0003	0.01	218.9	3.0	217.9	6.8	257.0	42.0	-0.5
CH55-Zrn-32	418	336	0.80	0.0542	0.0035	0.2600	0.0150	0.0343	0.0007	0.0108	0.0004	0.03	217.8	4.4	234.0	12.0	455.0	92.0	6.9
CH55-Zrn-21	461	384	0.83	0.0566	0.0033	0.2680	0.0130	0.0343	0.0006	0.0111	0.0004	0.18	217.6	3.8	240.0	11.0	466.0	65.0	9.3
CH55-Zrn-22	190	255	1.34	0.0530	0.0046	0.2450	0.0190	0.0340	0.0008	0.0113	0.0005	0.18	215.5	5.3	222.0	15.0	500.0	110.0	2.9
CH55-Zrn-42	397	350	0.88	0.0509	0.0026	0.2390	0.0100	0.0336	0.0006	0.0108	0.0004	0.02	213.3	3.5	216.9	8.4	354.0	51.0	1.7
CH20 augen metagranitoid																			
CH20-Zrn-006	457	377	0.82	0.0528	0.0054	0.2610	0.0190	0.0368	0.0007	0.0123	0.0005	0.01	233.6	4.6	235.0	15.0	390.0	130.0	0.6
CH20-Zrn-012	481	692	1.44	0.0551	0.0062	0.2590	0.0200	0.0361	0.0010	0.0115	0.0006	0.20	228.6	6.3	233.0	16.0	390.0	160.0	1.9
CH20-Zrn-005	419	348	0.83	0.0566	0.0055	0.2610	0.0180	0.0360	0.0008	0.0110	0.0006	0.22	227.7	5.1	235.0	15.0	490.0	120.0	3.1
CH20-Zrn-027	194	164	0.85	0.0557	0.0062	0.2780	0.0230	0.0360	0.0009	0.0119	0.0007	0.23	227.7	5.6	250.0	19.0	490.0	100.0	8.9
CH20-Zrn-013	180	133	0.74	0.0599	0.0072	0.2720	0.0240	0.0359	0.0010	0.0118	0.0007	0.07	227.4	6.0	244.0	19.0	670.0	120.0	6.8
CH20-Zrn-018	501	516	1.03	0.0531	0.0056	0.2560	0.0190	0.0359	0.0008	0.0116	0.0005	0.16	227.1	4.6	232.0	16.0	370.0	120.0	2.1
CH20-Zrn-026	198	231	1.17	0.0571	0.0065	0.2760	0.0220	0.0358	0.0009	0.0120	0.0006	0.07	226.4	5.5	247.0	17.0	530.0	130.0	8.3
CH20-Zrn-014	641	694	1.08	0.0535	0.0052	0.2550	0.0170	0.0357	0.0007	0.0117	0.0005	0.17	226.3	4.6	230.0	14.0	360.0	120.0	1.6

CH20-Zrn-004	743	995	1.34	0.0545	0.0052	0.2570	0.0160	0.0357	0.0006	0.0113	0.0004	0.06	226.1	3.9	232.0	13.0	420.0	110.0	2.5
CH20-Zrn-016	269	430	1.60	0.0598	0.0062	0.2440	0.0230	0.0357	0.0009	0.0115	0.0005	0.04	225.8	5.5	225.0	18.0	670.0	140.0	-0.4
CH20-Zrn-024	416	563	1.35	0.0521	0.0052	0.2540	0.0170	0.0356	0.0008	0.0118	0.0005	0.22	225.5	4.8	229.0	14.0	320.0	110.0	1.5
CH20-Zrn-010	428	370	0.86	0.0523	0.0054	0.2540	0.0190	0.0356	0.0008	0.0111	0.0005	0.02	225.4	4.8	229.0	15.0	370.0	140.0	1.6
CH20-Zrn-032	343	462	1.35	0.0548	0.0061	0.2750	0.0220	0.0356	0.0008	0.0110	0.0005	0.22	225.3	4.6	246.0	18.0	490.0	170.0	8.4
CH20-Zrn-028	351	617	1.76	0.0514	0.0057	0.2520	0.0210	0.0354	0.0008	0.0111	0.0005	0.19	224.3	4.8	229.0	17.0	320.0	160.0	2.1
CH20-Zrn-030	363	334	0.92	0.0577	0.0058	0.2400	0.0190	0.0352	0.0009	0.0115	0.0005	0.00	223.3	5.4	226.0	16.0	490.0	120.0	1.2
CH20-Zrn-017	406	451	1.11	0.0558	0.0059	0.2500	0.0210	0.0349	0.0008	0.0113	0.0005	0.27	221.0	4.7	226.0	16.0	560.0	110.0	2.2
CH20-Zrn-023	261	156	0.60	0.0595	0.0059	0.2680	0.0180	0.0348	0.0008	0.0129	0.0006	0.01	220.3	5.2	240.0	14.0	610.0	120.0	8.2
CH20-Zrn-025	287	344	1.20	0.0529	0.0058	0.2480	0.0210	0.0348	0.0008	0.0104	0.0005	0.12	220.3	5.1	224.0	17.0	360.0	130.0	1.7
CH20-Zrn-008	1011	1830	1.81	0.0538	0.0051	0.2450	0.0150	0.0346	0.0007	0.0106	0.0004	0.31	219.1	4.2	224.0	12.0	340.0	120.0	2.2
CH20-Zrn-015	623	1180	1.89	0.0530	0.0057	0.2410	0.0190	0.0345	0.0007	0.0106	0.0004	0.05	218.9	4.5	219.0	16.0	380.0	140.0	0.0
CH74 undeformed metagranitoid																			
CH74-Zrn-47	173	74	0.43	0.0760	0.0028	2.1430	0.0960	0.2016	0.0033	0.0616	0.0015	0.18	1184.0	18.0	1165.0	29.0	1135.0	48.0	-1.6
CH74-Zrn-24	135	60	0.44	0.0795	0.0038	2.2110	0.1300	0.2002	0.0040	0.0707	0.0030	0.19	1176.0	22.0	1182.0	40.0	1190.0	46.0	0.5
CH74-Zrn-07	277	140	0.51	0.0770	0.0026	2.1270	0.1100	0.1993	0.0036	0.0604	0.0019	0.55	1171.0	19.0	1160.0	34.0	1126.0	41.0	-0.9
CH74-Zrn-31	1800	457	0.25	0.0770	0.0021	2.1010	0.0850	0.1985	0.0030	0.0577	0.0015	0.21	1167.0	16.0	1149.1	28.0	1115.0	33.0	-1.6
CH74-Zrn-34	217	156	0.72	0.0760	0.0024	2.0920	0.0920	0.1977	0.0027	0.0603	0.0012	0.18	1163.0	15.0	1145.0	30.0	1096.0	36.0	-1.6
CH74-Zrn-33	556	437	0.79	0.0760	0.0025	2.0550	0.0910	0.1951	0.0026	0.0554	0.0008	0.20	1149.0	14.0	1137.0	32.0	1087.0	34.0	-1.1
CH74-Zrn-38	313	139	0.44	0.0778	0.0023	2.0860	0.0910	0.1940	0.0026	0.0558	0.0010	0.29	1143.0	14.0	1145.0	29.0	1144.0	34.0	0.2
CH74-Zrn-42	203	92	0.45	0.0772	0.0030	2.0430	0.0930	0.1919	0.0030	0.0572	0.0017	0.02	1131.0	16.0	1129.0	31.0	1103.0	48.0	-0.2
CH74-Zrn-27	392	220	0.56	0.0773	0.0022	2.0440	0.0870	0.1908	0.0022	0.0567	0.0010	0.33	1125.8	12.0	1129.0	29.0	1126.0	29.0	0.3
CH74-Zrn-40	234	262	1.12	0.0758	0.0028	1.9910	0.0950	0.1905	0.0025	0.0555	0.0009	0.01	1123.9	13.0	1113.0	33.0	1120.0	39.0	-1.0
CH74-Zrn-04	1006	131	0.13	0.0780	0.0021	2.0560	0.0870	0.1902	0.0027	0.0682	0.0031	0.69	1122.0	15.0	1134.0	29.0	1132.0	25.0	1.1
CH74-Zrn-23	465	151	0.32	0.0754	0.0022	1.9600	0.0880	0.1892	0.0039	0.0543	0.0013	0.53	1117.0	21.0	1103.0	29.0	1077.0	36.0	-1.3
CH74-Zrn-39	1737	377	0.22	0.0766	0.0018	1.9750	0.0790	0.1862	0.0021	0.0540	0.0007	0.34	1100.9	11.0	1106.9	27.0	1111.0	33.0	0.5
CH74-Zrn-19	999	173	0.17	0.0769	0.0019	1.9720	0.0800	0.1856	0.0022	0.0565	0.0011	0.18	1097.4	12.0	1107.1	26.0	1114.0	29.0	0.9
CH74-Zrn-08	549	142	0.26	0.0749	0.0024	1.8930	0.0830	0.1823	0.0025	0.0532	0.0014	0.19	1080.0	13.0	1081.0	31.0	1069.0	39.0	0.1
CH74-Zrn-20	1670	283	0.17	0.0757	0.0019	1.9120	0.0770	0.1818	0.0020	0.0539	0.0009	0.26	1077.0	11.0	1085.1	27.0	1087.9	23.0	0.7
CH74-Zrn-22	950	140	0.15	0.0762	0.0022	1.9010	0.0820	0.1817	0.0023	0.0544	0.0015	0.32	1076.1	12.0	1081.0	29.0	1092.0	34.0	0.5
CH74-Zrn-02	655	164	0.25	0.0755	0.0020	1.8980	0.0780	0.1810	0.0021	0.0570	0.0014	0.26	1072.5	11.0	1081.7	26.0	1094.0	37.0	0.9
CH74-Zrn-21	860	129	0.15	0.0744	0.0023	1.8660	0.0820	0.1801	0.0022	0.0547	0.0016	0.25	1067.6	12.0	1068.0	29.0	1062.0	34.0	0.0
CH74-Zrn-41	320	141	0.44	0.0760	0.0022	1.8820	0.0800	0.1798	0.0028	0.0530	0.0012	0.41	1066.0	15.0	1074.0	28.0	1087.0	34.0	0.7
CH74-Zrn-37	499	169	0.34	0.0763	0.0022	1.8800	0.0790	0.1795	0.0028	0.0526	0.0016	0.44	1064.0	16.0	1074.0	28.0	1112.0	47.0	0.9
CH74-Zrn-03	280	78	0.28	0.0735	0.0024	1.8350	0.0860	0.1791	0.0023	0.0547	0.0020	0.31	1062.0	12.0	1056.0	31.0	1035.0	39.0	-0.6
CH74-Zrn-16	112	83	0.73	0.0773	0.0034	1.9240	0.0990	0.1775	0.0042	0.0558	0.0017	0.05	1053.0	23.0	1086.0	35.0	1103.0	47.0	3.0
CH74-Zrn-05	362	112	0.31	0.0745	0.0025	1.8230	0.0820	0.1769	0.0023	0.0547	0.0014	0.01	1050.2	13.0	1052.0	30.0	1048.0	36.0	0.2
CH74-Zrn-18	192	68	0.36	0.0762	0.0027	1.8820	0.0930	0.1770	0.0030	0.0549	0.0017	0.39	1050.0	17.0	1075.0	32.0	1105.0	40.0	2.3
CH74-Zrn-43	112	49	0.44	0.0818	0.0040	2.0270	0.1100	0.1759	0.0029	0.0558	0.0022	0.02	1045.0	16.0	1121.0	37.0	1265.0	60.0	6.8
CH74-Zrn-45	1178	62	0.05	0.0756	0.0022	1.8250	0.0780	0.1759	0.0027	0.0536	0.0026	0.31	1044.0	15.0	1054.0	28.0	1087.0	27.0	0.9
CH74-Zrn-13	305	93	0.30	0.0696	0.0023	1.7110	0.0800	0.1750	0.0026	0.0549	0.0026	0.10	1039.0	14.0	1012.0	30.0	947.0	40.0	-2.7
CH74-Zrn-35	285	183	0.64	0.0732	0.0025	1.7770	0.0790	0.1744	0.0031	0.0488	0.0018	0.32	1036.0	17.0	1037.0	29.0	1030.0	28.0	0.1
CH74-Zrn-48	374	108	0.29	0.0757	0.0023	1.8470	0.0800	0.1740	0.0026	0.0532	0.0012	0.33	1034.0	14.0	1061.0	29.0	1099.0	37.0	2.5
CH74-Zrn-36	153	68	0.45	0.0719	0.0055	1.7000	0.1400	0.1727	0.0045	0.0548	0.0025	0.15	1027.0	25.0	1004.0	51.0	939.0	70.0	-2.3
CH74-Zrn-15	1032	271	0.26	0.0751	0.0019	1.8000	0.0720	0.1726	0.0020	0.0527	0.0009	0.14	1026.3	11.0	1045.3	26.0	1079.0	36.0	1.8
CH74-Zrn-26	198	157	0.79	0.0790	0.0037	1.8620	0.1000	0.1726	0.0031	0.0572	0.0025	0.56	1026.0	17.0	1065.0	36.0	1139.0	52.0	3.7

CH74-Zrn-17	781	73	0.09	0.0745	0.0020	1.7810	0.0740	0.1722	0.0021	0.0519	0.0015	0.44	1024.0	12.0	1040.0	28.0	1061.0	32.0	1.5
CH74-Zrn-44	568	240	0.42	0.0719	0.0021	1.7040	0.0720	0.1710	0.0021	0.0493	0.0008	0.18	1018.6	12.0	1011.0	28.0	991.0	36.0	-0.8
CH74-Zrn-49	616	298	0.48	0.0737	0.0021	1.7330	0.0760	0.1710	0.0022	0.0482	0.0009	0.32	1017.8	12.0	1022.0	29.0	1043.0	38.0	0.4
CH74-Zrn-11	277	214	0.77	0.0728	0.0022	1.7210	0.0720	0.1709	0.0023	0.0504	0.0008	0.08	1017.0	13.0	1018.0	28.0	1019.0	42.0	0.1
CH74-Zrn-09	231	116	0.50	0.0706	0.0032	1.6650	0.0880	0.1703	0.0033	0.0508	0.0015	0.05	1013.0	18.0	993.0	33.0	970.0	49.0	-2.0
CH74-Zrn-01	206	126	0.61	0.0771	0.0024	1.8060	0.0790	0.1693	0.0025	0.0569	0.0014	0.14	1008.0	14.0	1047.0	29.0	1120.0	48.0	3.7
CH74-Zrn-46	228	101	0.44	0.0716	0.0025	1.6780	0.0770	0.1690	0.0020	0.0518	0.0010	0.04	1006.6	11.0	999.0	29.0	982.0	46.0	-0.8
CH74-Zrn-32	188	88	0.47	0.0789	0.0032	1.8330	0.0940	0.1682	0.0024	0.0584	0.0023	0.27	1002.0	13.0	1059.0	32.0	1156.0	45.0	5.4
CH74-Zrn-06	455	142	0.31	0.0748	0.0022	1.7630	0.0740	0.1680	0.0025	0.0535	0.0012	0.18	1001.0	14.0	1031.0	27.0	1065.0	33.0	2.9
CH74-Zrn-14	1046	265	0.25	0.0713	0.0018	1.6550	0.0700	0.1672	0.0024	0.0520	0.0010	0.66	997.0	13.0	991.0	27.0	970.0	31.0	-0.6
CH74-Zrn-10	141	56	0.40	0.0768	0.0030	1.6980	0.0840	0.1596	0.0024	0.0497	0.0021	0.11	955.0	14.0	1006.0	31.0	1119.0	44.0	5.1
CH74-Zrn-30	182	47	0.26	0.0784	0.0031	1.7110	0.0860	0.1594	0.0032	0.0589	0.0021	0.39	953.0	18.0	1014.0	31.0	1168.0	54.0	6.0
CH74-Zrn-25	101	32	0.31	0.0728	0.0038	1.5670	0.0980	0.1572	0.0031	0.0506	0.0031	0.31	941.0	17.0	954.0	39.0	1069.0	59.0	1.4
CH74-Zrn-12	282	64	0.23	0.0737	0.0025	1.6040	0.0750	0.1572	0.0021	0.0520	0.0018	0.24	940.9	12.0	973.0	31.0	1032.0	43.0	3.3
CH74-Zrn-29	113	29	0.26	0.0772	0.0036	1.6750	0.0950	0.1553	0.0034	0.0569	0.0027	0.38	930.0	19.0	995.0	36.0	1113.0	57.0	6.5
CH73 augen-banded orthogneiss																			
CH73-Zrn-68	215	79	0.37	0.0995	0.0029	3.1890	0.0810	0.2318	0.0031	0.0623	0.0026	0.45	1344.0	16.0	1453.0	20.0	1633.0	46.0	7.5
CH73-Zrn-78	354	61	0.17	0.0969	0.0043	2.8400	0.1200	0.2141	0.0032	0.0890	0.0160	0.22	1250.0	17.0	1363.0	31.0	1561.0	67.0	8.3
CH73-Zrn-72	449	172	0.38	0.0770	0.0019	2.0990	0.0360	0.1964	0.0021	0.0610	0.0015	0.30	1155.9	11.0	1147.7	12.0	1147.0	27.0	-0.7
CH73-Zrn-62	173	93	0.54	0.0792	0.0027	2.1030	0.0720	0.1929	0.0036	0.0623	0.0025	0.34	1137.0	19.0	1148.0	24.0	1187.0	47.0	1.0
CH73-Zrn-54	594	222	0.37	0.0762	0.0018	2.0330	0.0320	0.1925	0.0020	0.0581	0.0019	0.27	1135.0	11.0	1126.3	11.0	1100.0	24.0	-0.8
CH73-Zrn-82	395	160	0.40	0.0763	0.0021	2.0060	0.0440	0.1914	0.0019	0.0574	0.0016	0.30	1129.0	10.0	1119.0	15.0	1103.0	28.0	-0.9
CH73-Zrn-67	273	110	0.40	0.0785	0.0024	2.0280	0.0610	0.1869	0.0026	0.0604	0.0019	0.46	1105.0	14.0	1127.0	20.0	1163.0	31.0	2.0
CH73-Zrn-70	88	37	0.43	0.0749	0.0029	1.9300	0.0620	0.1869	0.0032	0.0590	0.0025	0.01	1104.0	17.0	1089.0	22.0	1065.0	46.0	-1.4
CH73-Zrn-59	318	91	0.29	0.0809	0.0027	2.0570	0.0540	0.1839	0.0022	0.0706	0.0025	0.00	1088.0	12.0	1133.0	18.0	1235.0	47.0	4.0
CH73-Zrn-81	724	206	0.28	0.0774	0.0019	1.9320	0.0360	0.1837	0.0021	0.0573	0.0014	0.43	1087.2	12.0	1092.0	13.0	1118.0	30.0	0.4
CH73-Zrn-52	615	400	0.65	0.0770	0.0024	1.9210	0.0540	0.1826	0.0032	0.0558	0.0015	0.54	1081.0	17.0	1094.0	19.0	1119.0	25.0	1.2
CH73-Zrn-57	58	33	0.58	0.0749	0.0035	1.8820	0.0800	0.1823	0.0038	0.0536	0.0026	0.27	1079.0	21.0	1071.0	28.0	1118.0	42.0	-0.7
CH73-Zrn-83	847	265	0.31	0.0767	0.0019	1.9190	0.0340	0.1819	0.0017	0.0546	0.0015	0.27	1077.3	9.4	1087.3	12.0	1105.0	21.0	0.9
CH73-Zrn-63	797	260	0.33	0.0756	0.0019	1.8970	0.0380	0.1818	0.0022	0.0536	0.0015	0.53	1076.5	12.0	1080.0	13.0	1085.0	28.0	0.3
CH73-Zrn-74	871	263	0.30	0.0753	0.0017	1.8580	0.0280	0.1789	0.0017	0.0535	0.0015	0.32	1061.1	9.3	1066.1	9.8	1076.3	19.0	0.5
CH73-Zrn-51	917	333	0.36	0.0769	0.0017	1.9040	0.0270	0.1784	0.0016	0.0544	0.0013	0.41	1058.1	8.7	1083.5	9.2	1124.0	24.0	2.3
CH73-Zrn-61	607	176	0.29	0.0750	0.0019	1.8510	0.0390	0.1778	0.0020	0.0576	0.0017	0.41	1054.8	11.0	1063.0	14.0	1071.0	27.0	0.8
CH73-Zrn-55	477	139	0.29	0.0758	0.0020	1.8550	0.0340	0.1767	0.0019	0.0593	0.0016	0.13	1049.0	11.0	1065.0	12.0	1105.0	28.0	1.5
CH73-Zrn-89	754	300	0.40	0.0758	0.0019	1.8360	0.0340	0.1763	0.0023	0.0536	0.0015	0.49	1046.0	13.0	1058.0	12.0	1075.0	30.0	1.1
CH73-Zrn-64	891	278	0.31	0.0757	0.0018	1.8220	0.0270	0.1738	0.0016	0.0539	0.0013	0.11	1032.9	8.9	1053.0	9.6	1093.0	27.0	1.9
CH73-Zrn-66	325	118	0.36	0.0764	0.0021	1.7930	0.0370	0.1699	0.0019	0.0545	0.0016	0.25	1011.5	11.0	1044.0	13.0	1106.0	30.0	3.1
CH73-Zrn-65	469	154	0.33	0.0749	0.0021	1.7590	0.0390	0.1693	0.0023	0.0549	0.0018	0.42	1008.0	13.0	1030.0	14.0	1077.0	32.0	2.1
CH73-Zrn-90	870	328	0.38	0.0749	0.0019	1.7030	0.0350	0.1658	0.0022	0.0515	0.0017	0.56	989.0	12.0	1009.0	13.0	1064.0	31.0	2.0
CH73-Zrn-50	730	210	0.29	0.0738	0.0021	1.6530	0.0360	0.1624	0.0018	0.0497	0.0014	0.24	970.3	10.0	990.0	14.0	1039.0	36.0	2.0
CH73-Zrn-53	1315	347	0.26	0.0738	0.0016	1.6490	0.0220	0.1616	0.0016	0.0505	0.0013	0.35	965.7	8.9	989.0	8.3	1026.8	22.0	2.4
CH73-Zrn-87	868	295	0.34	0.0752	0.0019	1.6480	0.0310	0.1604	0.0025	0.0530	0.0014	0.55	959.0	14.0	989.0	12.0	1082.0	31.0	3.0
CH73-Zrn-86	344	168	0.49	0.0766	0.0022	1.6450	0.0460	0.1574	0.0027	0.0510	0.0016	0.47	942.0	15.0	990.0	19.0	1103.0	24.0	4.8
CH73-Zrn-79	995	335	0.34	0.0733	0.0018	1.5820	0.0330	0.1557	0.0023	0.0461	0.0013	0.69	933.0	13.0	963.0	13.0	1023.0	19.0	3.1
CH73-Zrn-69	1170	358	0.31	0.0792	0.0022	1.6820	0.0430	0.1545	0.0019	0.0555	0.0020	0.30	926.2	11.0	1001.0	16.0	1151.0	40.0	7.5
CH73-Zrn-58	1116	306	0.27	0.0749	0.0018	1.5170	0.0280	0.1470	0.0015	0.0468	0.0014	0.32	884.0	8.7	937.0	11.0	1059.0	29.0	5.7

CH73-Zrn-60	899	177	0.20	0.0719	0.0019	1.4650	0.0300	0.1466	0.0015	0.0495	0.0015	0.15	881.7	8.4	916.0	12.0	986.0	36.0	3.7
CH73-Zrn-49	1094	233	0.21	0.0731	0.0018	1.4640	0.0240	0.1445	0.0014	0.0471	0.0014	0.07	869.7	7.8	915.4	9.8	1004.0	29.0	5.0
CH73-Zrn-73	1204	190	0.16	0.0723	0.0016	1.3880	0.0210	0.1391	0.0014	0.0454	0.0014	0.30	839.6	7.9	883.5	8.8	991.0	30.0	5.0
CH73-Zrn-56	1135	212	0.19	0.0715	0.0017	1.3420	0.0220	0.1362	0.0015	0.0474	0.0014	0.29	823.2	8.5	864.0	9.5	963.0	25.0	4.7
CH73-Zrn-71	1550	390	0.25	0.0723	0.0017	1.3000	0.0220	0.1309	0.0016	0.0443	0.0016	0.50	793.2	9.1	845.3	9.6	998.0	30.0	6.2
CH73-Zrn-75	984	234	0.24	0.0708	0.0019	1.1330	0.0200	0.1164	0.0016	0.0397	0.0011	0.24	709.8	9.0	768.8	9.7	950.0	31.0	7.7
CH73-Zrn-80	444	46	0.10	0.0720	0.0023	1.1300	0.0340	0.1138	0.0017	0.0357	0.0021	0.13	694.6	9.6	767.0	16.0	971.0	41.0	9.4
CH73-Zrn-77	1686	541	0.32	0.0687	0.0017	1.0350	0.0190	0.1097	0.0015	0.0369	0.0011	0.62	671.0	8.7	721.0	9.7	891.0	26.0	6.9
CH73-Zrn-88	2081	515	0.25	0.0673	0.0017	0.9930	0.0170	0.1081	0.0011	0.0359	0.0010	0.07	661.5	6.3	700.0	8.5	846.0	30.0	5.5
CH73-Zrn-76	2870	379	0.13	0.0640	0.0017	0.7140	0.0130	0.0808	0.0010	0.0349	0.0010	0.03	500.6	6.0	547.0	7.6	747.0	31.0	8.5
CH73-Zrn-48	3160	330	0.10	0.0623	0.0014	0.6771	0.0100	0.0785	0.0007	0.0334	0.0010	0.29	487.2	4.2	524.9	6.2	686.0	34.0	7.2
CH10a granitic orthogneiss																			
CH10a-Zrn-141	164	91	0.55	0.0700	0.0026	1.6330	0.0430	0.1698	0.0024	0.0501	0.0027	0.06	1011.0	13.0	984.0	16.0	921.0	77.0	-2.7
CH10a-Zrn-105	584	251	0.43	0.0717	0.0022	1.6540	0.0320	0.1681	0.0024	0.0490	0.0025	0.34	1001.0	13.0	992.0	12.0	988.0	63.0	-0.9
CH10a-Zrn-092	372	300	0.81	0.0735	0.0025	1.7110	0.0380	0.1679	0.0024	0.0490	0.0025	0.24	1000.0	13.0	1014.0	15.0	1036.0	68.0	1.4
CH10a-Zrn-088	176	58	0.33	0.0749	0.0026	1.7370	0.0440	0.1675	0.0025	0.0520	0.0031	0.34	998.0	14.0	1021.0	16.0	1055.0	71.0	2.3
CH10a-Zrn-144	230	154	0.67	0.0724	0.0028	1.6770	0.0470	0.1670	0.0024	0.0496	0.0027	0.07	996.0	13.0	1007.0	16.0	1001.0	74.0	1.1
CH10a-Zrn-128	355	405	1.14	0.0722	0.0025	1.6600	0.0350	0.1668	0.0021	0.0499	0.0025	0.23	994.0	12.0	994.0	14.0	995.0	71.0	0.0
CH10a-Zrn-96	183	79	0.43	0.0729	0.0026	1.6430	0.0430	0.1664	0.0027	0.0505	0.0028	0.14	992.0	15.0	991.0	17.0	1008.0	77.0	-0.1
CH10a-Zrn-139	204	144	0.71	0.0714	0.0024	1.6330	0.0410	0.1661	0.0027	0.0495	0.0027	0.18	991.0	15.0	982.0	16.0	969.0	72.0	-0.9
CH10a-Zrn-120	195	101	0.52	0.0718	0.0028	1.6410	0.0450	0.1651	0.0025	0.0497	0.0027	0.03	985.0	14.0	984.0	17.0	980.0	84.0	-0.1
CH10a-Zrn-113	367	148	0.40	0.0737	0.0025	1.6770	0.0380	0.1641	0.0025	0.0487	0.0026	0.19	980.0	14.0	998.0	15.0	1037.0	72.0	1.8
CH10a-Zrn-135	1079	316	0.29	0.0710	0.0020	1.6100	0.0360	0.1640	0.0041	0.0458	0.0024	0.70	979.0	23.0	973.0	14.0	953.0	59.0	-0.6
CH10a-Zrn-124	198	161	0.81	0.0732	0.0028	1.6550	0.0430	0.1635	0.0028	0.0494	0.0026	0.04	976.0	16.0	995.0	16.0	1005.0	79.0	1.9
CH10a-Zrn-90	465	313	0.67	0.0728	0.0022	1.6230	0.0270	0.1629	0.0024	0.0493	0.0026	0.09	973.0	13.0	980.3	9.8	1003.0	63.0	0.7
CH10a-Zrn-136	1128	264	0.23	0.0723	0.0020	1.6130	0.0220	0.1618	0.0022	0.0493	0.0025	0.87	967.0	12.0	974.8	8.7	995.0	59.0	0.8
CH10a-Zrn-129	196	144	0.73	0.0721	0.0029	1.6290	0.0500	0.1614	0.0024	0.0483	0.0025	0.11	964.0	13.0	982.0	20.0	1013.0	81.0	1.8
CH10a-Zrn-145	238	123	0.52	0.0726	0.0026	1.6100	0.0400	0.1614	0.0023	0.0486	0.0026	0.12	964.0	13.0	972.0	16.0	992.0	73.0	0.8
CH10a-Zrn-110	313	558	1.78	0.0739	0.0026	1.6560	0.0350	0.1609	0.0023	0.0498	0.0025	0.11	962.0	13.0	991.0	13.0	1045.0	71.0	2.9
CH10a-Zrn-126	184	151	0.82	0.0734	0.0034	1.6290	0.0600	0.1608	0.0027	0.0485	0.0026	0.09	961.0	15.0	985.0	24.0	1021.0	95.0	2.4
CH10a-Zrn-089	1121	312	0.28	0.0726	0.0020	1.5970	0.0200	0.1606	0.0019	0.0482	0.0025	0.40	960.0	11.0	968.7	7.6	999.0	56.0	0.9
CH10a-Zrn-98	237	131	0.55	0.0738	0.0026	1.6130	0.0550	0.1604	0.0033	0.0518	0.0027	0.61	959.0	18.0	978.0	21.0	1032.0	72.0	1.9
CH10a-Zrn-114	222	114	0.51	0.0756	0.0027	1.6640	0.0390	0.1604	0.0025	0.0496	0.0026	0.12	959.0	14.0	994.0	15.0	1074.0	71.0	3.5
CH10a-Zrn-107	933	840	0.90	0.0727	0.0019	1.6010	0.0200	0.1594	0.0023	0.0480	0.0024	0.53	954.0	13.0	971.5	7.4	1007.0	57.0	1.8
CH10a-Zrn-95	564	175	0.31	0.0719	0.0022	1.5730	0.0300	0.1589	0.0023	0.0471	0.0025	0.45	951.0	13.0	962.0	12.0	977.0	62.0	1.1
CH10a-Zrn-140	340	226	0.66	0.0743	0.0026	1.6270	0.0350	0.1589	0.0025	0.0495	0.0026	0.22	950.0	14.0	979.0	14.0	1055.0	71.0	3.0
CH10a-Zrn-91	572	217	0.38	0.0717	0.0022	1.5680	0.0340	0.1581	0.0034	0.0481	0.0026	0.66	948.0	18.0	956.0	14.0	979.0	58.0	0.8
CH10a-Zrn-143	276	167	0.61	0.0726	0.0028	1.5950	0.0420	0.1582	0.0026	0.0490	0.0027	0.07	947.0	15.0	967.0	16.0	1011.0	73.0	2.1
CH10a-Zrn-146	1303	354	0.27	0.0724	0.0020	1.5840	0.0170	0.1582	0.0022	0.0471	0.0024	0.50	947.0	12.0	963.7	6.6	996.0	55.0	1.7
CH10a-Zrn-132	222	188	0.85	0.0741	0.0028	1.6010	0.0470	0.1564	0.0025	0.0490	0.0027	0.08	937.0	14.0	968.0	19.0	1029.0	77.0	3.2
CH10a-Zrn-99	721	235	0.33	0.0721	0.0021	1.5490	0.0280	0.1560	0.0023	0.0474	0.0025	0.61	936.0	13.0	949.0	11.0	985.0	59.0	1.4
CH10a-Zrn-102	581	440	0.76	0.0739	0.0022	1.5610	0.0220	0.1542	0.0020	0.0483	0.0024	0.14	924.0	11.0	954.3	8.5	1034.0	60.0	3.2
CH10a-Zrn-104	769	375	0.49	0.0726	0.0022	1.5350	0.0210	0.1538	0.0022	0.0472	0.0024	0.18	923.0	13.0	947.1	9.1	1002.0	59.0	2.5
CH10a-Zrn-116	2256	274	0.12	0.0725	0.0020	1.5270	0.0170	0.1527	0.0021	0.0460	0.0024	0.54	916.0	12.0	942.2	7.0	997.0	55.0	2.8
CH10a-Zrn-131	228	224	0.98	0.0725	0.0027	1.5390	0.0490	0.1517	0.0030	0.0484	0.0025	0.44	910.0	17.0	944.0	20.0	1016.0	69.0	3.6
CH10a-Zrn-100	450	285	0.63	0.0734	0.0024	1.5120	0.0370	0.1498	0.0029	0.0465	0.0024	0.50	900.0	16.0	936.0	15.0	1023.0	69.0	3.9

CH10a-Zrn-142	781	523	0.67	0.0722	0.0022	1.4970	0.0250	0.1496	0.0020	0.0471	0.0024	0.09	900.0	11.0	928.0	10.0	992.0	63.0	3.0
CH10a-Zrn-121	258	141	0.55	0.0703	0.0026	1.4210	0.0500	0.1466	0.0030	0.0470	0.0025	0.63	881.0	17.0	898.0	20.0	943.0	78.0	1.9
CH10a-Zrn-134	1012	504	0.50	0.0726	0.0020	1.4630	0.0190	0.1464	0.0019	0.0455	0.0023	0.43	881.0	11.0	915.0	7.9	1001.0	56.0	3.7
CH10a-Zrn-130	1841	291	0.16	0.0724	0.0020	1.4450	0.0200	0.1439	0.0021	0.0459	0.0024	0.66	867.0	12.0	907.5	8.5	1006.0	57.0	4.5
CH10a-Zrn-118	2507	337	0.13	0.0711	0.0019	1.3980	0.0150	0.1429	0.0019	0.0435	0.0022	0.46	861.0	11.0	888.8	6.3	961.0	53.0	3.1
CH10a-Zrn-109	2691	468	0.17	0.0716	0.0019	1.3940	0.0270	0.1412	0.0027	0.0433	0.0022	0.84	851.0	15.0	887.0	11.0	972.0	54.0	4.1
CH10a-Zrn-93	199	57	0.29	0.0724	0.0028	1.4020	0.0630	0.1391	0.0050	0.0498	0.0031	0.73	843.0	29.0	893.0	28.0	993.0	77.0	5.6
CH10a-Zrn-101	1891	331	0.18	0.0729	0.0020	1.4020	0.0150	0.1387	0.0019	0.0446	0.0023	0.04	837.0	11.0	889.7	6.4	1007.0	57.0	5.9
CH10a-Zrn-106	836	366	0.44	0.0707	0.0022	1.3260	0.0250	0.1357	0.0020	0.0424	0.0022	0.32	820.0	11.0	856.0	11.0	942.0	63.0	4.2
CH10a-Zrn-119	549	297	0.54	0.0726	0.0022	1.3580	0.0280	0.1347	0.0020	0.0427	0.0022	0.44	815.0	11.0	870.0	12.0	1002.0	64.0	6.3
CH10a-Zrn-115	1032	346	0.34	0.0711	0.0023	1.2620	0.0740	0.1270	0.0069	0.0442	0.0023	0.94	775.0	39.0	827.0	34.0	957.0	67.0	6.3
CH10a-Zrn-148	2603	340	0.13	0.0724	0.0020	1.2550	0.0190	0.1257	0.0019	0.0399	0.0021	0.63	763.0	11.0	825.0	8.4	993.0	57.0	7.5
CH10a-Zrn-97	371	163	0.44	0.0730	0.0027	1.2070	0.0550	0.1191	0.0049	0.0489	0.0027	0.81	725.0	28.0	800.0	26.0	1002.0	76.0	9.4
CH10a-Zrn-133	1355	225	0.17	0.0729	0.0022	1.1890	0.0280	0.1171	0.0026	0.0410	0.0022	0.68	714.0	15.0	794.0	13.0	1005.0	61.0	10.1
CH10a-Zrn-147	1456	174	0.12	0.0711	0.0020	1.1350	0.0210	0.1144	0.0016	0.0426	0.0023	0.52	698.1	9.5	769.3	9.7	956.0	58.0	9.3
CH10a-Zrn-103	885	377	0.43	0.0730	0.0022	1.1280	0.0470	0.1125	0.0043	0.0421	0.0027	0.91	686.0	25.0	770.0	24.0	1009.0	60.0	10.9
CH10a-Zrn-108	479	136	0.28	0.0699	0.0024	0.9730	0.0750	0.0998	0.0067	0.0440	0.0024	0.95	612.0	39.0	686.0	39.0	924.0	72.0	10.8
CH10a-Zrn-138	259	60	0.23	0.0687	0.0029	0.9490	0.0420	0.0994	0.0028	0.0494	0.0028	0.59	610.0	16.0	678.0	22.0	878.0	89.0	10.0
CH10a-Zrn-125	2176	151	0.07	0.0698	0.0020	0.8960	0.0330	0.0947	0.0029	0.0345	0.0021	0.90	583.0	17.0	650.0	17.0	917.0	61.0	10.3
CH10a-Zrn-127	2403	314	0.13	0.0697	0.0019	0.8950	0.0530	0.0927	0.0053	0.0318	0.0022	0.97	571.0	31.0	644.0	29.0	922.0	59.0	11.3
CH10a-Zrn-137	304	124	0.41	0.0742	0.0032	0.8310	0.0330	0.0814	0.0014	0.0488	0.0027	0.47	504.6	8.6	612.0	18.0	1045.0	88.0	17.6
CH10a-Zrn-123	4048	223	0.06	0.0674	0.0019	0.7270	0.0120	0.0783	0.0011	0.0292	0.0016	0.51	485.6	6.6	556.8	6.9	853.0	60.0	12.8
CH10a-Zrn-111	1062	47	0.04	0.0664	0.0025	0.4050	0.0320	0.0440	0.0031	0.0251	0.0019	0.94	277.0	19.0	342.0	23.0	803.0	80.0	19.0
CH10a-Zrn-112	700	5	0.01	0.0520	0.0041	0.0808	0.0059	0.0113	0.0003	0.0147	0.0039	0.18	72.2	1.7	78.7	5.6	250.0	170.0	8.3
CH10b granitic orthogneiss																			
CH10b-Zrn-033	178	73	0.41	0.0775	0.0035	2.2330	0.0900	0.2066	0.0042	0.0619	0.0017	0.52	1210.0	22.0	1190.0	30.0	1123.0	94.0	-1.7
CH10b-Zrn-041	196	58	0.30	0.0773	0.0034	2.0290	0.0800	0.1908	0.0036	0.0597	0.0016	0.34	1125.0	20.0	1127.0	26.0	1120.0	91.0	0.2
CH10b-Zrn-026	130	69	0.53	0.0752	0.0038	1.6700	0.0810	0.1601	0.0035	0.0513	0.0017	0.09	957.0	19.0	994.0	28.0	1080.0	100.0	3.7
CH10b-Zrn-029	165	195	1.18	0.0731	0.0035	1.6740	0.0740	0.1644	0.0031	0.0499	0.0011	0.19	983.0	17.0	997.0	29.0	1030.0	100.0	1.4
CH10b-Zrn-012	380	400	1.05	0.0735	0.0031	1.7130	0.0650	0.1684	0.0030	0.0506	0.0009	0.23	1003.0	16.0	1013.0	24.0	1028.0	87.0	1.0
CH10b-Zrn-019	177	94	0.53	0.0735	0.0035	1.7350	0.0850	0.1731	0.0052	0.0510	0.0015	0.09	1029.0	29.0	1024.0	33.0	1028.0	97.0	-0.5
CH10b-Zrn-035	261	151	0.58	0.0731	0.0031	1.6760	0.0640	0.1657	0.0029	0.0508	0.0012	0.00	988.0	16.0	999.0	24.0	1018.0	91.0	1.1
CH10b-Zrn-001	253	194	0.77	0.0730	0.0032	1.6740	0.0650	0.1666	0.0030	0.0498	0.0010	0.25	993.0	17.0	998.0	25.0	1005.0	89.0	0.5
CH10b-Zrn-021	767	765	1.00	0.0727	0.0029	1.6420	0.0560	0.1643	0.0028	0.0480	0.0008	0.29	981.0	15.0	986.0	22.0	1003.0	82.0	0.5
CH10b-Zrn-036	274	234	0.85	0.0721	0.0031	1.6490	0.0630	0.1643	0.0030	0.0500	0.0011	0.27	980.0	16.0	988.0	24.0	996.0	93.0	0.8
CH10b-Zrn-022	525	612	1.17	0.0716	0.0030	1.6090	0.0600	0.1638	0.0029	0.0479	0.0008	0.14	978.0	16.0	973.0	23.0	970.0	84.0	-0.5
CH10b-Zrn-044	236	184	0.78	0.0723	0.0035	1.6350	0.0720	0.1633	0.0030	0.0495	0.0011	0.23	975.0	17.0	985.0	27.0	981.0	98.0	1.0
CH10b-Zrn-046	242	204	0.84	0.0716	0.0033	1.5960	0.0630	0.1622	0.0029	0.0490	0.0009	0.18	969.0	16.0	972.0	26.0	979.0	90.0	0.3
CH10b-Zrn-020	820	800	0.98	0.0725	0.0030	1.6060	0.0610	0.1614	0.0027	0.0487	0.0009	0.09	964.0	15.0	973.0	24.0	996.0	83.0	0.9
CH10b-Zrn-028	189	198	1.05	0.0726	0.0033	1.6140	0.0670	0.1609	0.0035	0.0488	0.0012	0.17	962.0	19.0	974.0	27.0	1006.0	90.0	1.2
CH10b-Zrn-010	107	82	0.77	0.0731	0.0036	1.6260	0.0720	0.1605	0.0031	0.0491	0.0014	0.28	959.0	17.0	978.0	27.0	1017.0	99.0	1.9
CH10b-Zrn-011	770	351	0.46	0.0725	0.0029	1.5880	0.0570	0.1599	0.0029	0.0485	0.0009	0.26	956.0	16.0	965.0	22.0	997.0	82.0	0.9
CH10b-Zrn-015	1080	890	0.82	0.0723	0.0030	1.5750	0.0580	0.1586	0.0027	0.0476	0.0008	0.21	949.0	15.0	962.0	23.0	996.0	84.0	1.4
CH10b-Zrn-043	739	358	0.48	0.0705	0.0029	1.5450	0.0550	0.1582	0.0028	0.0479	0.0009	0.27	947.0	15.0	948.0	22.0	943.0	82.0	0.1
CH10b-Zrn-042	1150	225	0.20	0.0714	0.0028	1.5510	0.0540	0.1570	0.0026	0.0477	0.0010	0.56	940.0	14.0	952.0	22.0	967.0	81.0	1.3
CH10b-Zrn-018	319	138	0.43	0.0724	0.0032	1.5470	0.0700	0.1569	0.0042	0.0478	0.0012	0.39	939.0	23.0	948.0	27.0	986.0	90.0	0.9

CH10b-Zrn-014	1250	417	0.33	0.0718	0.0029	1.5460	0.0540	0.1567	0.0027	0.0462	0.0009	0.39	938.0	15.0	949.0	22.0	985.0	81.0	1.2
CH10b-Zrn-034	1930	421	0.22	0.0714	0.0028	1.5290	0.0520	0.1547	0.0026	0.0470	0.0008	0.29	927.0	15.0	942.0	21.0	965.0	81.0	1.6
CH10b-Zrn-004	1090	394	0.36	0.0731	0.0029	1.5340	0.0530	0.1538	0.0030	0.0458	0.0008	0.51	922.0	17.0	944.0	21.0	1014.0	81.0	2.3
CH10b-Zrn-032	1550	245	0.16	0.0722	0.0028	1.5320	0.0520	0.1536	0.0026	0.0476	0.0009	0.42	921.0	15.0	943.0	21.0	989.0	82.0	2.3
CH10b-Zrn-005	2150	295	0.14	0.0727	0.0028	1.5260	0.0530	0.1527	0.0026	0.0466	0.0010	0.37	916.0	14.0	941.0	21.0	1006.0	79.0	2.7
CH10b-Zrn-045	2170	323	0.15	0.0718	0.0028	1.5150	0.0510	0.1527	0.0025	0.0463	0.0009	0.09	916.0	14.0	936.0	21.0	978.0	80.0	2.1
CH10b-Zrn-023	1032	342	0.33	0.0722	0.0029	1.5040	0.0510	0.1519	0.0025	0.0451	0.0009	0.07	912.0	14.0	932.0	21.0	994.0	81.0	2.1
CH10b-Zrn-025	1220	426	0.35	0.0719	0.0029	1.4800	0.0540	0.1498	0.0026	0.0444	0.0008	0.39	900.0	15.0	922.0	22.0	979.0	82.0	2.4
CH10b-Zrn-027	1690	234	0.14	0.0715	0.0028	1.4490	0.0490	0.1463	0.0023	0.0444	0.0009	0.25	880.0	13.0	909.0	20.0	969.0	81.0	3.2
CH10b-Zrn-024	1223	269	0.22	0.0714	0.0029	1.4220	0.0510	0.1443	0.0027	0.0444	0.0010	0.28	869.0	15.0	898.0	21.0	965.0	80.0	3.2
CH10b-Zrn-013	2410	435	0.18	0.0713	0.0028	1.3650	0.0480	0.1389	0.0025	0.0453	0.0011	0.70	838.0	14.0	874.0	20.0	971.0	76.0	4.1
CH10b-Zrn-037	1630	339	0.21	0.0711	0.0028	1.3650	0.0470	0.1386	0.0022	0.0427	0.0009	0.17	837.0	13.0	876.0	20.0	959.0	81.0	4.5
CH10b-Zrn-003	3310	420	0.13	0.0720	0.0028	1.3560	0.0470	0.1365	0.0025	0.0422	0.0008	0.64	825.0	14.0	870.0	20.0	983.0	80.0	5.2
CH10b-Zrn-017	2270	220	0.10	0.0713	0.0028	1.3280	0.0540	0.1355	0.0033	0.0436	0.0010	0.47	819.0	19.0	858.0	23.0	973.0	77.0	4.5
CH10b-Zrn-038	1040	289	0.28	0.0708	0.0028	1.3300	0.0480	0.1350	0.0027	0.0430	0.0008	0.50	818.0	15.0	859.0	21.0	947.0	85.0	4.8
CH10b-Zrn-002	2880	297	0.10	0.0714	0.0028	1.3160	0.0450	0.1342	0.0022	0.0414	0.0008	0.41	812.0	12.0	853.0	19.0	968.0	80.0	4.8
CH10b-Zrn-039	1740	221	0.13	0.0719	0.0028	1.2630	0.0550	0.1285	0.0035	0.0418	0.0010	0.13	779.0	20.0	829.0	23.0	981.0	82.0	6.0
CH10b-Zrn-016	2080	195	0.09	0.0702	0.0028	1.2220	0.0440	0.1257	0.0024	0.0405	0.0009	0.70	763.0	14.0	810.0	20.0	937.0	84.0	5.8
CH10b-Zrn-040	1300	216	0.17	0.0716	0.0029	1.2170	0.0440	0.1233	0.0022	0.0416	0.0009	0.39	749.0	13.0	808.0	20.0	970.0	84.0	7.3
CH10b-Zrn-009	442	238	0.54	0.0728	0.0035	1.1410	0.0560	0.1146	0.0051	0.0496	0.0013	0.41	699.0	30.0	772.0	28.0	1010.0	100.0	9.5
CH10b-Zrn-031	1200	314	0.26	0.0751	0.0029	1.1560	0.0670	0.1130	0.0051	0.0411	0.0009	0.11	690.0	29.0	780.0	29.0	1070.0	79.0	11.5
CH10b-Zrn-030	1270	252	0.20	0.0733	0.0030	1.1140	0.0470	0.1104	0.0035	0.0474	0.0010	0.39	675.0	20.0	760.0	22.0	1026.0	84.0	11.2
CH10b-Zrn-006	3080	165	0.05	0.0714	0.0028	0.9010	0.0310	0.0919	0.0018	0.0334	0.0009	0.17	566.0	11.0	652.0	17.0	965.0	83.0	13.2
CH10b-Zrn-008	1350	206	0.15	0.0709	0.0029	0.7730	0.0380	0.0790	0.0028	0.0309	0.0012	0.03	490.0	17.0	581.0	21.0	949.0	84.0	15.7
CH10b-Zrn-007	1620	149	0.09	0.0685	0.0027	0.5630	0.0220	0.0596	0.0014	0.0161	0.0016	0.75	373.0	8.7	453.0	15.0	882.0	83.0	17.7

5

Conclusiones generales

5.1. ORIGEN DEL BASAMENTO

Los resultados geocronológicos de los metagranitos del Complejo Chuacús demuestran que al menos una parte de esta unidad representa un basamento mesoproterozoico (1.1-1.0 Ga). La evolución de dicho basamento comprende, además, diversos episodios de magmatismo ocurridos durante el Ordovícico (ca. 450 Ma; Solari *et al*., 2011), el Silúrico-Devónico (425-400 Ma), el Triásico Tardío (ca. 220 Ma; Martens *et al*., 2012; Solari *et al*., 2011; este trabajo) y, probablemente, el Jurásico Medio (ca. 170 Ma), así como periodos de sedimentación marina intermitentes (Solari *et al*., 2011; este trabajo).

5.1.1. Magmatismo mesoproterozoico

La ocurrencia de al menos tres localidades con edades de cristalización de entre 1.1-1.0 Ga en el área de estudio, implica la presencia de un basamento tipo Rodinia en el Complejo Chuacús. Por lo tanto, el descubrimiento de un fragmento cortical de tales características en Guatemala, representa un punto de referencia importante para la configuración de los basamentos proterozoicos del Sur de México y Centroamérica (Fig. 5.1a).

Dos metagranitos expuestos en el sector norte de la Sierra de Chuacús (Fig. 5.1b) poseen edades de cristalización de ca. 1.1 Ga, lo que indica que el origen de dichas rocas podría estar situado en el contexto del ensamblaje inicial del supercontinente Rodinia. Sin embargo, el carácter ferroano de dichas rocas y sus características geoquímicas, posiblemente atribuibles a un episodio de magmatismo intraplaca (además de la falta de evidencias de un metamorfismo granulítico previo), supondría que no hay una conexión directa con el basamento Precámbrico del sur de México (e.g. Oaxaquia y Complejo Guichicovi) u otras exposiciones de rocas similares en el noroeste de Sudamérica (e.g. Macizo Garzón), cuyo magmatismo Esténico estaría relacionado con un régimen tectónico convergente. Por otro lado, una correlación con el basamento Esténico de Laurencia (e.g. los basamentos Yavapai-Mazatzal y Grenville, al norte de la sutura Ouachita-Marathon-Sonora), donde se ha documentado un magmatismo granítico con

características similares (e.g. Li *et al*., 2007), podría ser plausible e implicaría una transferencia de fragmentos corticales de Laurencia a la margen de Amazonia antes de la separación de Rodinia. Sin embargo, el significado tectónico de este magmatismo debe de ser revisado de la mano de otros estudios adicionales, puesto que la interpretación tectónica basada puramente en datos geoquímicos (e.g. elementos mayores y traza) es riesgosa, ante la posibilidad de contaminación por asimilación, movilidad de elementos químicos durante el metamorfismo o, incluso, de un variabilidad química inherente de los procesos magmáticos que impidan una discriminación tectónica concluyente. Por lo tanto, las posibles correlaciones de este magmatismo deben de ser revisadas *a posteriori*.

Un metagranito hiperaluminoso alto en sílice (CH10), expuesto en el sector centro oriental de la Sierra de Chuacús (Fig. 5.1), resultó en una edad de cristalización de ca. 1.0 Ga y sus atributos geoquímicos sugieren un origen relacionado con fusión parcial de la corteza. Estas características son compatibles con el metamorfismo de alto grado y anatexis atribuidos a la consolidación final de Rodinia (colisión de Báltica con Amazonia) durante el Esténico-Tónico, lo cual se ha documentado ampliamente en diversas localidades de México (e.g. Lawlor *et al*., 1999; Keppie & Ortega-Gutiérrez, 2010; Ruiz *et al*., 1999; Solari *et al*., 2003; Weber & Kohler, 1999;) y el noroeste de Sudamérica (e.g. Baquero *et al*., 2015; Ibanez-Mejia *et al*., 2011; Van der Lelij *et al*., 2016).

Los metagranitos de 1.1-1.0 Ga del Complejo Chuacús representan la exposición más meridional de rocas mesoproterozoicas en el bloque Maya (Fig. 5.1b). En un trabajo reciente, Weber *et al*. (2018) documentan también la ocurrencia de un basamento de 1.0 Ga en el Macizo de Chiapas, México (Complejo el Triunfo), por lo que dicha localidad constituye *a priori* la correlación más cercana y plausible del Complejo Chuacús. Ambas localidades conforman, en su posición actual, una extensión aparente al sureste del complejo proterozoico Guichicovi (Weber & Köhler, 1999). Sin embargo, en el caso del Complejo Chuacús una simple continuidad espacial no puede ser justificada, debido a la interferencia del sistema de fallas Polochic-Motagua, cuya actividad durante el Cenozoico desplazaría a una distancia indeterminada los bloques corticales de la Zona de Sutura de Guatemala (e.g. Authemayou *et al*., 2011). Por otro lado, algunas peculiaridades del Complejo Chuacús son todavía contrastantes con respecto a lo documentado en el Complejo El Triunfo: 1) la ausencia de un metamorfismo granulítico en los granitoides de ca. 1.1-1.0 Ga, aunque a juicio del autor este debe ser todavía corroborado en el Complejo El Triunfo, 2) la ausencia de cuerpos de anortosita, 3) la ausencia de un magmatismo de arco Pérmico-Triásico y en su lugar 4) la ocurrencia de un magmatismo bimodal restringido al Triásico Tardío. Esta ultima característica junto con otras similitudes geocronológicas, como se verá más adelante, implican además una posible conexión con los terrenos andinos del noroccidente de Sudamérica.

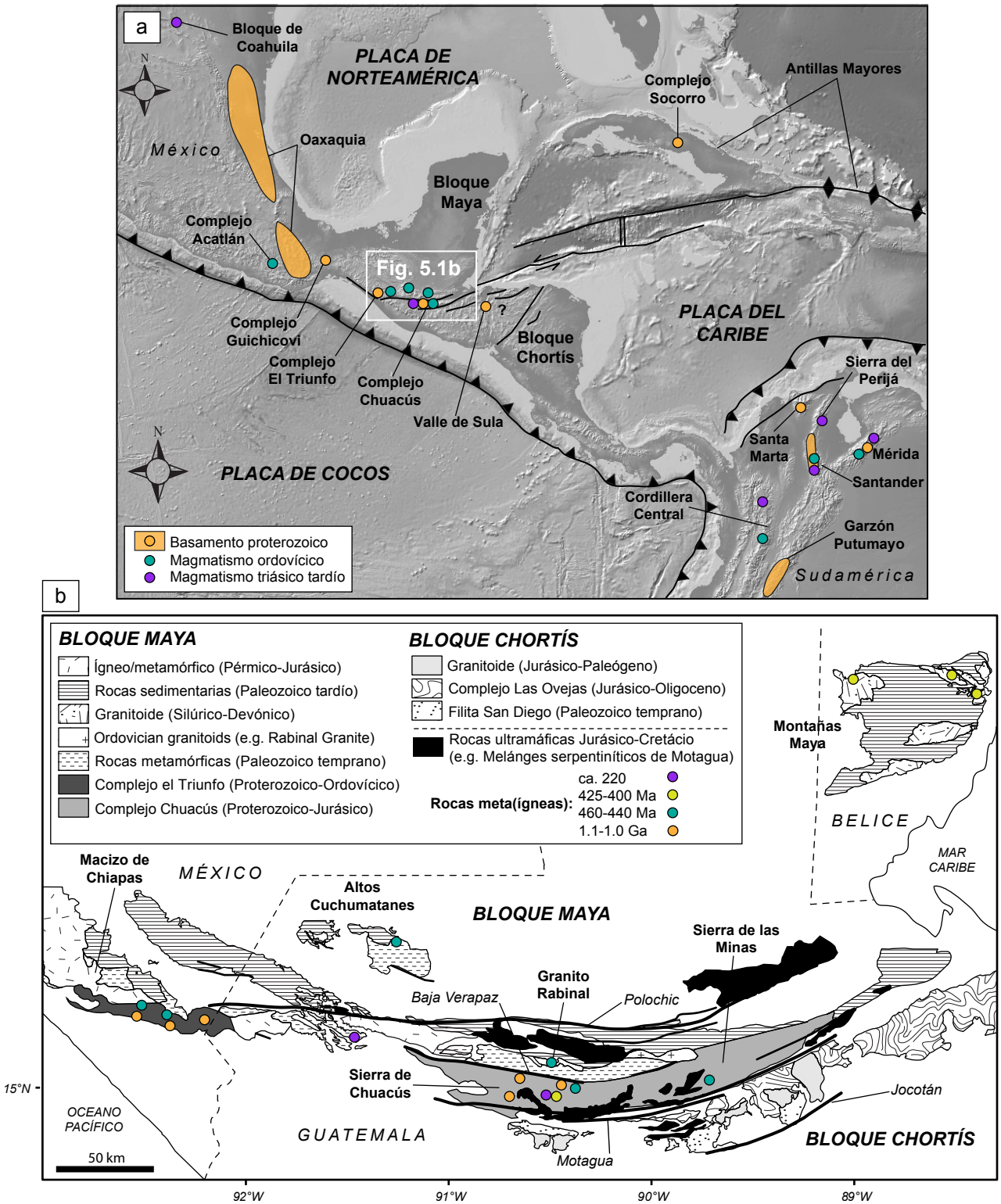

Figura 5.1. (a) Contexto tectónico de la zona del Caribe mostrando la ubicación de distintas unidades de basamento mesoproterozoico a paleozoico de México, las Antillas, Centroamérica y los Andes (ver referencias citadas en el texto). Se muestra también la ubicación de la Zona de Sutura de Guatemala (rectangulo). (b) Mapa geológico simplificado mostrando el contexto regional de la Zona de Sutura de Guatemala (modificado después de Kesler *et al*., 1970; Anderson *et al*., 1973; Ratschbacher *et al*., 2009 y Weber *et al*., 2018). Se señalan las fallas principales, así como la ubicación y el intervalo de edades de distintas localidades referidas en el texto.

5.1.2. Magmatismo ordovícico

Un episodio de magmatismo granítico de ca. 450 Ma fue documentado por Solari *et al*. (2011) no solo en el sector norte de la Sierra de Chuacús sino también en la Sierra de las Minas (Fig. 5.1b). A pesar de que en este trabajo no fue posible corroborar la ocurrencia de rocas ordovícicas en otros sectores, resulta oportuno revisar brevemente algunos aspectos referentes a dicho evento, con base en los nuevos datos presentados y en otros estudios recientes.

Un magmatismo ordovícico, en algunos casos de tipo bimodal, ha sido también documentado ampliamente en diversos fragmentos corticales peri-Gondwánicos; entre otras localidades (Fig. 5.1b), Los Altos Cuchumatanes y el Complejo Rabinal en Guatemala (Ortega-Obregón *et al*., 2008; Ratschbacher *et al*., 2009; Solari *et al*., 2010; Solari *et al*., 2013), los complejos Acatlán y El Triunfo en el sur de México (Estrada-Carmona *et al*., 2012; Miller *et al*., 2007; Ortega-Obregón *et al*., 2009; Weber *et al*., 2018) y la Cordillera Central, el Macizo de Santander y los Andes de Mérida en el noroccidente de Sudamérica (e.g. Van der Lelij *et al*., 2016; Villagómez *et al*., 2011). Actualmente no parece haber un consenso sobre el origen y el significado tectónico de dicho magmatismo Ordovícico en la mayoría de estos basamentos, en los cuales ha sido interpretado ya sea como el resultado de un magmatismo extensional a lo largo del margen sur del Océano Rheico (e.g. Estrada-Carmona *et al*., 2012; Keppie *et al*., 2008) o de un magmatismo de arco continental en el borde noroccidental de Gondwana (Solari *et al*., 2013; Van der Lelij *et al*., 2016; Vega-Granillo *et al*., 2009; Weber *et al*., 2018).

De todas estas localidades, la relación con el Complejo Rabinal es, sin duda, la de mayor relevancia, debido a su proximidad con el Complejo Chuacús. Las zona de cizalla de Baja Verapaz (ZCBV, Ortega-Obregón *et al*, 2008) separa las rocas en facies de esquisto verde del Complejo Rabinal de las rocas en facies de anfibolita-eclogita del Complejo Chuacús. El contraste en el grado metamórfico entre ambos complejos ha determinado que su posible correlación no sea obvia, a pesar de que en ambas unidades se han documentado edades de cristalización ordovícicas prácticamente iguales (450-470 Ma; Ortega-Obregón *et al*, 2008; Ratschbacher *et al*., 2009; Solari *et al*., 2011; Solari *et al*., 2013). Sin embargo, Solari *et al*. (2013) concluyen que el Granito Rabinal experimentó un metamorfismo de subducción cuya edad es equivalente a la edad de la ZCBV (ca. 70 Ma), lo que implica que dicha estructura no representa un límite fundamental que separe terrenos diferentes (e.g. Ortega-Gutiérrez *et al*. 2007), sino probablemente una estructura que yuxtapone niveles corticales distintos de un mismo basamento afectado por el evento caribeño.

Un aspecto relevante para otras posibles correlaciones del magmatismo ordovícico registrado en el Complejo Chuacús, tiene que ver con su relación espacial con rocas graníticas del Mesoproterozoico (Fig. 5.1b). Esta misma relación se ha documentado recientemente en otras unidades de basamento como el

Complejo El Triunfo en Chiapas, México (Weber *et al*., 2018) y los Andes de Mérida, Venezuela (Van der Lelij *et al*., 2016) (Fig. 5.1a).

5.1.3. Magmatismo silúrico-devónico temprano

Las edades de cristalización U-Pb en zircón de ca. 425-400 Ma, obtenidas en dos eclogitas de la parte central de la Sierra de Chuacús (Fig. 5.1b), implican la ocurrencia de un episodio de magmatismo básico del Silúrico-Devónico Temprano que no había sido documentado anteriormente. Dichas metabasitas son equivalentes en composición al basalto alcalino y similares en sus abundancias de elementos traza a la composición del basalto de isla oceánica (OIB). Por lo tanto, los precursores magmáticos de dichas rocas pudieron originarse en un ambiente de arco de islas o de rift continental. Su relación espacial con fragmentos de basamento continental más antiguo favorece esta última posibilidad, donde dicho magmatismo podría reflejar el rompimiento incipiente y la separación de terrenos individuales en el margen noroccidental de Gondwana. Sin embargo, aunque la mayoría de los cuerpos de eclogita estudiados muestran un carácter geoquímico similar, la información obtenida (tanto geoquímica como geocronológica) aún es insuficiente para argumentar sólidamente está hipótesis.

Un número considerable de estudios previos han documentado la ocurrencia de rocas (meta) basálticas y graníticas del Ordovícico-Silúrico en el sur de México y Guatemala (e.g. Ortega-Gutiérrez *et al*., 1999; Estrada-Carmona *et al*., 2012; Keppie *et al*., 2008; Ortega-Obregón *et al*., 2008; Ortega-Obregón *et al*., 2010; Weber *et al*., 2018), sin embargo, la evidencia de magmatismo Silúrico-Devónico Temprano es escasa y se restringe básicamente a los plutones graníticos de las Montañas Maya en Belice, los cuales poseen edades de cristalización de ca. 415-400 Ma y fueron probablemente originados en un ambiente magmático relacionado con subducción (Weber *et al*., 2012). Finalmente, las relaciones espacial y petrogenética de estas rocas máficas con los metagranitos del Ordovícico-Silúrico expuestos al norte de la Sierra de Chuacús (Solari *et al*., 2011) son ambiguas y se requieren estudios adicionales que permitan evaluarlas.

5.1.4. Magmatismo triásico tardío

Un episodio de magmatismo triásico tardío ha sido reconocido ampliamente en el Complejo Chuacús. Estudios previos han reportado edades U-Pb en zircón de entre 223 y 213 Ma en rocas gnéisicas de composición granítica de la región central de la Sierra de Chuacús, las cuales han sido interpretadas como la edad de cristalización de los protolitos ígneos (Martens *et al*., 2012; Ratschbacher *et al*., 2009; Solari *et al*., 2011). Esta interpretación es consistente con las edades magmáticas de ca. 224 Ma obtenidas

en este trabajo en metagranitos megacristalinos de la misma región (Fig. 5.1b). Adicionalmente, edades similares han sido reportadas también en rocas de composición básica, incluidos cuerpos de metagabro y eclogita con firmas tholeiíticas y composiciones isotópicamente juveniles (Martens *et al*., 2012; Solari *et al*., 2011). Esta equivalencia en edad entre los protolitos graníticos y básicos implica un magmatismo bimodal del Triásico Tardío en el Complejo Chuacús.

Las características químicas de los metagranitos, que incluyen una concentración alta de elementos incompatibles y valores relativamente bajos de $(La/Yb)_N$, sugieren que el magma original pudo haberse derivado de una fuente mantélica no empobrecida y quizá sufrido un cierto grado de contaminación durante su emplazamiento en la corteza continental (lo que también es sugerido por una componente heredada de zircón mesoproterozoico). Por lo tanto, con base en la composición química de ambos tipos de roca, así como en sus relaciones espacio-temporales, el magmatismo bimodal triásico tardío pudo haberse originado en un ambiente tectónico intraplaca, y no en contexto de arco continental como se sugirió previamente (Solari *et al*. 2011).

A la fecha, este periodo de magmatismo no ha sido reconocido en ningún otro lugar del sur de México o Centroamérica. Un magmatismo de arco voluminoso del Pérmico-Triásico Temprano (270-250 Ma) se encuentra bien documentado en el bloque Maya (e.g. Weber *et al*., 2007), pero dicho intervalo contrasta con las edades restringidas de ca. 220 Ma encontradas en el Complejo Chuacús. Por otro lado, el magmatismo registrado en otras localidades del bloque Maya (e.g. Los Altos Cuchumatanes, Las Montañas Maya, el Complejo Rabinal) parece ser enteramente del Ordovícico-Pensilvánico (Ortega-Obregón *et al*., 2008; Solari *et al*., 2010; Weber *et al*., 2012). Por lo tanto, en términos del magmatismo bimodal del Triásico Tardío, no existe una correlación obvia entre el Complejo Chuacús y otras unidades del bloque Maya.

Un magmatismo bimodal contemporáneo y con características químicas prácticamente idénticas ha sido documentado en los terrenos paleozoicos del noroccidente de Sudamérica (Fig. 5.1a). Un número considerable de edades U-Pb en zircón de entre 240 y 210 Ma han sido reportadas, sobre todo en rocas metagraníticas, en diversas localidades de la Cordillera Central y la Península de la Guajira en Colombia (Cochrane *et al*., 2014; Restrepo *et al*., 2011; Villagómez *et al*., 2011; Vinasco *et al*., 2006), los Andes de Mérida y la Sierra del Perijá en Venezuela (Van der Lelij *et al*., 2016) y en la Cordillera Real y el complejo Amotape de Ecuador (Cochrane *et al*., 2014; Litherland *et al*., 1994). Cochrane *et al*. (2014) sugieren que dicho magmatismo bimodal pudo haber ocurrido durante un evento de rifting continental entre 240-225 Ma que estaría relacionado con la fragmentación inicial del occidente de Pangea. Las características de las rocas metaígneas del Triásico Tardío en el Complejo Chuacús, son consistentes con esta interpretación y, por lo tanto, dichas rocas podrían representar la continuación del cinturón magmático del Triásico Tardío expuesto en el sector norte de los Andes.

Una posible correlación adicional se refiere al magmatismo triásico tardío registrado en el bloque de Coahuila (Fig. 5.1a), donde Lopez (1997) reporta edades U-Pb en zircón de ca. 220 Ma. Esta correlación resulta relevante porque podría representar un punto de referencia en la probable conexión entre el noreste de México y el sur del bloque Maya antes de la fragmentación de Pangea.

5.1.5. Magmatismo jurásico medio

La evidencia de un magmatismo básico del Jurásico Medio es escasa pues se deriva de una sola muestra de eclogita fechada en ca. 167 Ma. Esta roca, proveniente de la región central de la Sierra de Chuacús, mostró composiciones equivalentes al basalto subalcalino y características comparables con la composición del E-MORB. Su edad es relativamente joven pero dentro del intervalo de la provincia volcanosedimentaria Nazas del noreste de México, en particular de su prolongación al suroeste del bloque Maya (Godínez-Urban *et al*., 2011), donde se han reportado principalmente rocas volcánicas ácidas a intermedias y flujos basálticos minoritarios, probablemente relacionados con un ambiente extensional intraplaca, desarrollado durante la disgregación de Pangea (Martini & Ortega-Gutiérrez, 2016).

5.1.6. Sedimentación

El Complejo Chuacús incluye una variedad de rocas metasedimentarias cuyos protolitos son igualmente diversos, incluyendo caliza/dolomía, cuarzoarenita, arcosa, grauvaca y lutita, entre otros. Sin embargo, las conclusiones de esta sección se basan únicamente en los datos obtenidos en rocas con protolitos pelíticos y psammíticos.

Las metapelitas de la Sierra de Chuacús poseen una composición típica de lutita de acuerdo a la clasificación de Herron (1988) y sus protolitos probablemente se depositaron en un ambiente de margen continental activo, a partir de sedimento derivado de una corteza continental félsica, según el esquema de discriminación propuesto por Roser y Korsch (1986). Los datos geocronológicos U-Pb en zircón de dos localidades representativas de esquistos pelítico, una en el sector norte y otra en el sector suroccidental, dieron resultados similares con edades concordantes ≥854 Ma, la cual se interpreta como la edad máxima de depósito de los protolitos. Una edad de ca. 203 Ma, obtenida en un crecimiento metamórfico claramente post-diagenético, es interpretada de forma conservadora como la edad mínima de depósito. Sin embargo, otras edades concordantes de entre 580 y 380 Ma, aunque no son atribuibles de forma contundente a un evento metamórfico post-diagenético, implicarían un depósito probablemente anterior o durante el Ediacárico. En cuanto a su proveniencia, estas rocas están dominadas por componentes detríticos de 1.0-1.3 Ga (tipo Grenville-Sunsas) y 1.4-1.7 Ga (tipo Río Negro-Juruena). Un componente de

tipo Grenville-Sunsas, particularmente de 1.0-1.2 Ga, ha sido documentado previamente en rocas similares de la Sierra de Chuacús y también en otras localidades del bloque Maya en el sur de México (e.g. Unidad Jocote, Chiapas; González-Guzmán *et al*., 2016), Guatemala (e.g. Unidad San Gabriel; Solari *et al*., 2009) y Belice (e.g. Unidad Baldy; Martens *et al*., 2010), mientras que una población de tipo Río Negro-Juruena es particularmente distintiva de las unidades Jocote y Baldy. Por otro lado, de resultar detríticas, las edades de ca. 580 Ma implicarían una correlación igualmente posible con los bloques Maya y Chortís, donde un componente detrítico Pan Africano-Brasiliano es aparentemente común (e.g. Solari *et al*., 2009; Weber *et al*., 2008). Sin embargo los patrones detríticos de las muestras estudiadas son más afines al bloque Maya y de forma particular a la Unidad Baldy de Belice, cuyo depósito es pre-Devónico.

Las eclogitas del Complejo Chuacús no se derivan exclusivamente de protolitos de origen ígneo, sino también de precursores sedimentarios de composición básica, como lo sugiere su contenido de zircón aparentemente detrítico (e.g. Martens *et al*., 2012; Solari *et al*., 2011). Los datos U-Pb en zircón obtenidos en una localidad de eclogita en la región central de la Sierra de Chuacús son consistentes con dicha interpretación, indicando un componente detrítico de entre 1.3 Ga y 321 Ma, así como un aporte predominante de ca. 432 Ma que es comparable con las edades de protolito del Silúrico-Devónico Temprano obtenidas. Una edad concordante de ca. 321 Ma se interpreta como la edad máxima de depósito del protolito, mientras que la edad mínima de depósito estaría restringida por un borde de zircón metamórfico de ca. 232 Ma. El contenido de zircón detrítico y las características químicas de dicha eclogita sugieren que el protolito podría provenir no solo de la erosión de las metabasitas del Silúrico-Devónico Temprano, sino también probablemente de los metagranitos del Ordovícico-Silúrico expuestos en el norte del Complejo Chuacús (Solari *et al*., 2011) y en las Montañas Maya en Belice (Weber *et al*., 2012). Estos metasedimentos básicos muestran además un aporte de fuentes con edades tipo Pan Africano-Brasiliano (500-650 Ma) y Grenville-Sunsas (1.0-1.3 Ga), así como, en menor medida, afines a la provincia Rondonia-San Ignacio (1.3-1.5 Ga); lo cual es comparable con los patrones detríticos obtenidos en para-anfibolitas de la Unidad Custepec, en el Complejo Macizo de Chiapas (Weber *et al*., 2007; Weber *et al*., 2008).

En síntesis, la información geocronológica disponible revela al menos tres periodos de sedimentación en el Complejo Chuacús. El más antiguo ocurriría probablemente en el Neoproterozoico y sería correlacionable con las unidades Jocote y Baldy del bloque Maya. El segundo, que incluiría el depósito de horizontes de composición básica, estaría acotado entre 321 y 232 Ma, un intervalo que además sería consistente con un periodo de cese en la actividad ígnea, entre los pulsos magmáticos del Silúrico-Devónico Temprano (425-400 Ma) y Triásico Tardío (220 Ma). Un último periodo de sedimentación ocurriría probablemente después del Jurásico, de acuerdo a la interpretación de Solari *et al*. (2011).

5.2. METAMORFISMO PRE-CARIBEÑO

Estudios previos han mostrado evidencia de dos posibles episodios de metamorfismo paleozoico en el Complejo Chuacús (Ortega-Gutiérrez *et al*., 2004; Solari *et al*., 2011), el primero ocurrido probablemente durante el Misisípico (348-324 Ma) y el segundo en el Triásico (253-218 Ma). Sin embargo, la evidencia de un evento tectonotérmico del Misisípico es escasa y no ha sido corroborada en trabajos subsecuentes, por lo que esta interpretación permanece poco documentada. Los datos geocronológicos obtenidos en este trabajo, en cambio, proporcionan evidencia de un metamorfismo ocurrido en el Silúrico-Devónico Temprano y, adicionalmente, corroboran la interpretación de un segundo evento metamórfico del Triásico Tardío.

5.2.1. Metamorfismo del Silúrico-Devónico

Los datos de U-Pb en zircón obtenidos en una para-piroxenita de la región central de la Sierra de Chuacús implican un evento metamórfico de ca. 420 Ma. Esta edad coincide con el intervalo de edad del episodio magmático del Silúrico-Devónico Temprano (425-400 Ma), documentado en eclogitas con protolitos equivalentes al basalto alcalino y con probable afinidad OIB. Por lo tanto, se interpreta que ambos procesos están relacionados genéticamente y corresponden a un evento tectonotérmico extensional del Silúrico-Devónico Temprano que provocaría magmatismo de composición básica y metamorfismo probablemente relacionado con el aumento sustancial del flujo térmico, como es típico de los ambientes de extensión (e.g. Collins & Richards, 2008). Este evento podría estar relacionado con el desarrollo incipiente de un rift continental en el margen occidental de Gondwana, como se argumentó anteriormente.

5.2.2. Metamorfismo del Triásico Tardío

Sin duda el evento metamórfico del Triásico Tardío es el mejor documentado. Solari *et al*. (2011) reportan un grupo de edades concordantes de entre 253 y 218 Ma, en un gneiss migmatítico de área de El Chol, las cuales son interpretadas como la edad del evento anatéctico responsable de la migmatización. Este interpretación es consistente con las edades de 243-220 Ma obtenidas en otro gneiss migmatítico de la Sierra de las Minas (mismo trabajo), así como con una edad promedio de ca. 218 Ma obtenida también en un gneiss migmatítico de la región de Huehuetenango, Guatemala (Ratschbacher *et al*., 2009). Las edades metamórficas de 232-200 Ma, obtenidas en este trabajo para equilibrios probablemente *subsolidus*, corroboran la ocurrencia de este evento metamórfico del Triásico Tardío. Como lo sugieren Solari *et al*. (2011), la edad de este evento coincide con la edad del pulso magmático de ca. 220 Ma (Martens *et al*.,

2012; Solari *et al*., 2011; este trabajo), el cual ha sido interpretado en este trabajo como un episodio de magmatismo bimodal probablemente extensional. Por lo tanto se sugiere que, de forma similar al evento Silúrico-Devónico Temprano, durante el Triásico Tardío el basamento del Complejo Chuacús debió experimentar un proceso combinado de magmatismo bimodal, metamorfismo de alto grado y anatexis, que estaría probablemente relacionado con actividad ígnea intraplaca asociada a la fragmentación inicial de Pangea.

Resulta llamativo que ambos eventos, el del Triásico Tardío y el del Silúrico-Devónico, son respectivamente más jóvenes (20-30 Ma) que los eventos tectonotérmicos que afectaron al Macizo de Chiapas, México durante el Pérmico y el Ordovícico (Estrada-Carmona *et al*., 2012; González-Guzmán *et al*., 2016; Weber *et al*., 2008; Weber *et al*., 2018).

5.3. METAMORFISMO CARIBEÑO

5.3.1. Extensión del metamorfismo de alta presión

El metamorfismo de alta presión en el Complejo Chuacús no ha sido reconocido ni el extremo occidental de la Sierra de Chuacús ni en la Sierra de las Minas (Fig. 5.2a), donde las asociaciones minerales con sillimanita son características (e.g. Martens *et al*., 2016; Solari *et al*., 2011). En este trabajo se corrobora que, de representar un mismo basamento, su parte más profunda está expuesta en el sector central de la Sierra de Chuacús, en un área aproximada de 30 x 20 km (flechas punteadas en la Fig. 5.2b).

La presencia de rocas de alta presión en este sector se extiende en dirección noreste-suroeste (dirección del buzamiento dominante) desde Palibatz hasta unos 5 km al sur de la ZCBV (Fig. 5.2b), donde aflora un esquisto pelítico con la asociación diagnóstica de alta presión: granate + cloritoide + fengita + paragonita + rutilo, equilibrada a 20 kbar y 600 ºC. La extensión en dirección del rumbo de la foliación predominante (noroeste-sureste) es incierta; sin embargo, las observaciones de campo permitieron constatar que su continuidad al noroeste se encuentra aparentemente interrumpida por una estructura de tipo normal referida aquí como Falla Cubulco, mientras que al sureste su prolongación está trucada por el acoplamiento entre la zona de falla de Motagua y otra estructura normal referida como Falla Chuacusito (Fig. 5.2b).

Si bien la evidencia principal del metamorfismo de alta presión es la ocurrencia de cuerpos de eclogita (Martens *et al*., 2012; Ortega-Gutiérrez *et al*., 2004, Ratschbacher *et al*., 2009, Solari *et al*., 2011), en este trabajo se demuestra que otras tipos de roca experimentaron también un metamorfismo en condiciones *P-T* similares, como adelantaron Ortega-Gutiérrez *et al*. (2004) en un estudio preliminar. En particular, dicho metamorfismo está claramente registrado en las rocas metaígneas de composición

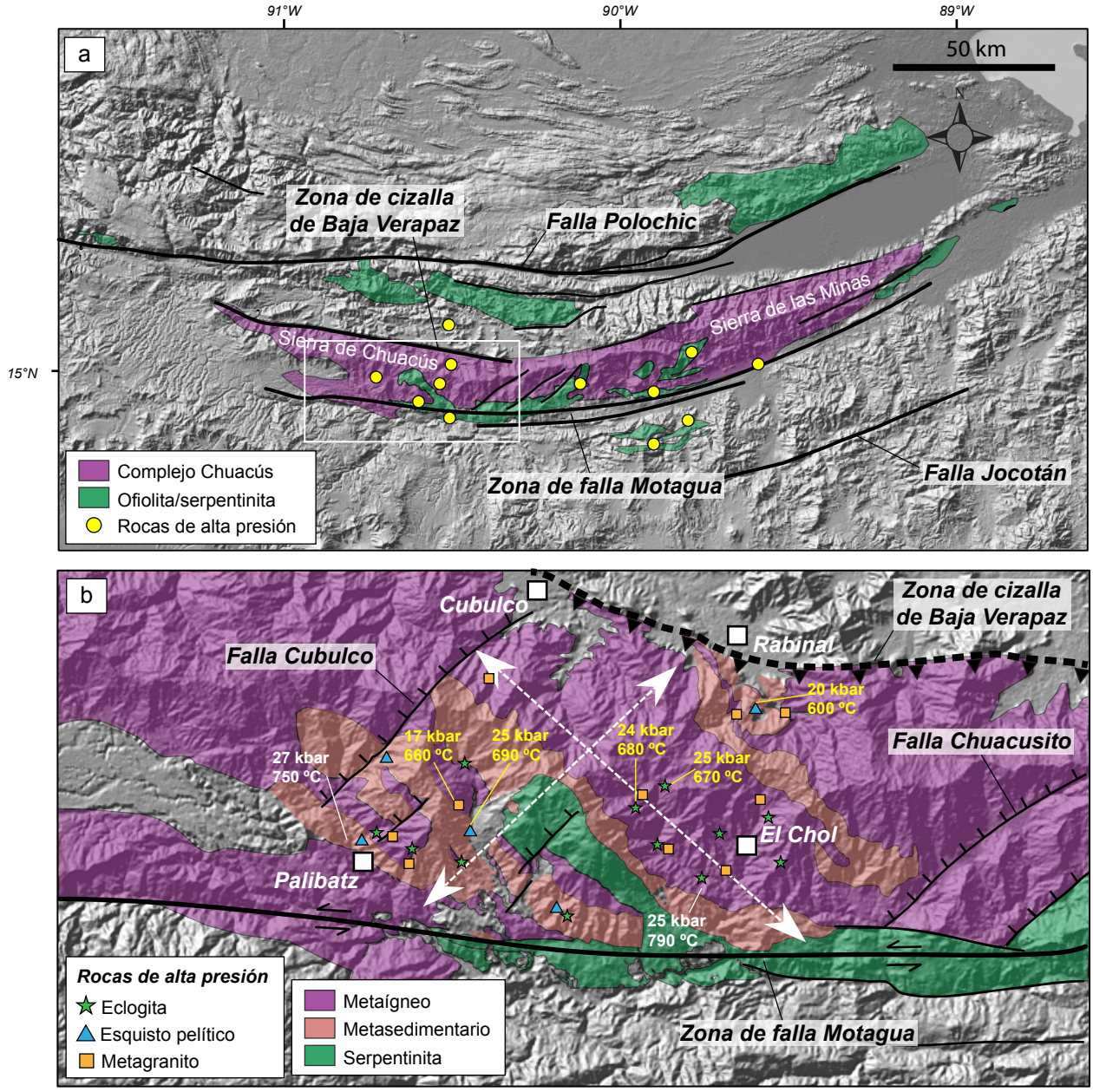

Figura 5.2. (a) Contexto tectónico simplificado de la Zona de Sutura de Guatemala mostrando las unidades principales con presencia de rocas metamórficas de alta presión y la ubicación de las localidades correspondientes después de Harlow *et al*. (2004); Ortega-Gutiérrez *et al*. (2004); Tsujimori *et al*. (2006); Martens *et al*. (2012); Solari *et al*. (2013). Se muestra también la ubicación de la Sierra de Chuacús (rectangulo). (b) Mapa geológico simplificado de la Sierra de Chuacús mostrando distintas localidades de rocas metamórficas de alta presión, así como las determinaciones termobarométricas obtenidas en este trabajo (texto amarillo) y por Marten *et al*. (2016) (texto blanco). Las flechas punteadas denotan la extensión del metamorfismo de alta presión, en dirección paralela y perpendicular al buzamiento predominante de la zona.

granítica y en los metasedimentos pelíticos, que en conjunto constituyen el volumen más significativo del complejo (Fig. 5.2b).

La información termobarométrica disponible no permite reconocer ningún tipo de gradiente *P-T* en la Sierra de Chuacús (Fig. 5.2b), pero las observaciones de campo y la ocurrencia de un esquisto pelítico equilibrado en condiciones *P-T* notoriamente contrastantes (20 kbar, 600 ºC), en el sector norte del complejo, sugieren que los posibles contrastes metamórficos en el complejo (e.g. McBirney, 1963; van den Boom, 1972) están posiblemente controlados por la presencia de zonas de cizalla que yuxtaponen en superficie bloques de profundidades diferentes y con un grado de retrogresión heterogénea. Esta hipótesis sería consecuente con los datos presentados por Solari *et al*. (2013), quienes documentan un metamorfismo de alta presión en el Granito Rabinal, el cual se encuentra separado del Complejo Chuacús por la ZCBV. Sin embargo, se requiere todavía un trabajo estructural-petrológico detallado al respecto para demostrar dicha hipótesis.

5.3.2. Evolución presión-temperatura

En este trabajo se llevó a cabo un estudio petrológico que incluyó el análisis no solo de localidades representativas de eclogita, algunas de ellas previamente descritas, sino también de localidades de metapelita y metagranito que no habían sido reconocidas o estudiadas a profundidad. La información petrológica obtenida a partir de esta variedad litológica indica que el metamorfismo caribeño en el Complejo Chuacús ocurrió a través de un gradiente geotérmico de ~7-9 °C/km, que es significativamente más bajo de lo que se suponía.

La etapa más temprana que se reconoce ocurrió probablemente a ~18-20 kbar y 530-580 ºC, apenas por encima de la temperatura de estabilidad de la lawsonita y dentro del campo de estabilidad de la jadeíta. La naturaleza y composición de las asociaciones relictas, incluidas jadeíta-cianita-paragonita (eclogita) y cloritoide-paragonita-rutilo (metapelita), son consistentes con esta estimación, implicando una trayectoria prógrada en condiciones metamórficas de alta presión y relativa baja temperatura. Condiciones similares, en este caso para el pico metamórfico, fueron obtenidas en un esquisto pelítico con granate + cloritoide + fengita + paragonita + rutilo del sector norte de la Sierra de Chuacús.

Las condiciones máximas de metamorfismo fueron estimadas en 23-25 kbar y 620-690 ºC. Estas condiciones fueron consistentes entre las muestras de eclogita y de esquisto pelítico estudiadas del sector central de la Sierra de Chuacús. Por lo tanto, con base en su equivalencia tanto en las condiciones prógradas como del pico metamórfico, se concluye que ambos tipos de roca debieron compartir una misma historia de inhumación. Sin embargo, estas condiciones discrepan considerablemente de las condiciones máximas estimadas en los metagranitos asociados, los cuales alojan comúnmente lentes de

eclogita, pero probablemente se equilibraron a ~17 kbar y 630-660 ºC (Fig. 5.2b); es decir, a una presión de hasta 7 kbar por debajo (fuera del campo de estabilidad del piroxeno onfacítico) de la presión alcanzada por las eclogitas y los esquistos pelíticos asociados. El significado de dicha discrepancia podría explicarse de acuerdo a los siguientes escenarios: (1) los metagranitos no experimentaron la misma historia de inhumación, (2) los metagranitos comparten la misma evolución pero no registraron eficientemente los cambios *P-T* por razones cinéticas o alternativamente (3) la evidencia de mayores presiones fue obliterada posteriormente durante la exhumación. El escenario (1) implica que los metagranitos habrían sido inhumados a una menor profundidad y que, durante la exhumación, se habrían mezclado tectónicamente con otros tipos de roca (e.g. eclogita, esquisto pelítico) provenientes de mayor profundidad. Los escenarios (2) y (3), en cambio, asumen que el complejo se habría inhumado (y exhumado) como una unidad coherente. Las evidencias de onfacita relicta en algunas rocas similares (Ortega-Gutiérrez *et al*., 2004, Ratschbacher *et al*., 2009), junto con la ocurrencia de un considerable reequilibrio químico en algunas fases (e.g. fengita), así como la falta de una estructura mesoscópica que demuestre un amalgamiento tectónico entre los distintos horizontes, favorecen en su conjunto la hipótesis de que el Complejo Chuacús se comportó como una secuencia relativamente coherente durante su inhumación en condiciones eclogíticas.

La evolución post-eclogítica incluyó una etapa de descompresión probablemente isotérmica con un reequilibrio a ~12 kbar y ~640 ºC en presencia de fluidos, como lo sugiere la formación de poikiloblastos de pargasita (Anf_2) y, posteriormente, simplectitas de clinopiroxeno diopsídico (Cpx_{3-4}) + albita (Pl_2) ± pargasita (Anf_3), reemplazando a la onfacita de pico metamórfico en las eclogitas. Subsecuentemente, un reequilibrio en condiciones de facies de anfibolita a 7-8 kbar y 590-620 °C, probablemente ocurrido durante un nuevo aumento en las condiciones *P-T*, está indicado por la cristalización de una segunda generación de granate (Grt_2) tanto en eclogitas como en esquistos pelíticos, así como de estaurolita y cianita (Ky_2) sobrecreciendo la paragénesis del pico metamórfico en las metapelitas.

5.3.3. Temporalidad del metamorfismo

La edad del metamorfismo caribeño fue evaluada empleando un enfoque isotópico multi-mineral, para lo cual se utilizaron un eclogita y un esquisto pelítico previamente investigados petrológicamente. Un grupo de datos concordantes U-Pb, obtenidos a partir del análisis de crecimientos metamórficos de zircón en el esquisto pelítico, resultaron en una edad promedio de 74.0 ± 0.5 Ma, la cual es consistente con una edad U-Pb de intersección inferior de 73.6 ± 2.0 Ma obtenida utilizando monacita de la misma muestra, y a su vez, es comparable, dentro de los errores, con una edad U-Pb de intersección inferior menos precisa

de 80 ± 13 Ma obtenida a partir de cristales de titanita (post-eclogítica) de la eclogita. Las edades Lu-Hf en granate/roca total fueron contrastantes, resultando en edades considerablemente más antiguas de 101.8 ± 3.1 Ma y 95.5 ± 2.1 Ma para la eclogita y el esquisto pelítico, respectivamente.

Las características morfológico-texturales y las abundancias de tierras raras de los crecimientos de zircón de ca. 74 Ma son típicos de un crecimiento metamórfico. Sin embargo, los patrones de tierras raras pesadas no muestran un perfil plano potencialmente indicativo de un crecimiento contemporáneo con granate (e.g. Harley *et al*., 2007; Rubatto & Hermann, 2003), mientras que sus valores extremadamente bajos de Th/U (0.004-0.007) sugieren un crecimiento relacionado con una interacción mineral-fluido tardía (e.g. Harley *et al*., 2007). Por lo tanto esta fecha se interpreta como la edad de precipitación del zircón en condiciones de relativa baja presión, posterior al metamorfismo eclogítico, y se sugiere que dicho proceso habría sido promovido por la desestabilización de fases ricas en Zr (e.g. rutilo) a relativa alta temperatura, probablemente durante el reequilibrio en facies de anfibolita. Esta conclusión está de acuerdo con los resultados previos obtenidos a partir de geocronómetros de temperatura intermedia, en el rango de 76-56 Ma (Martens *et al*., 2012; Ortega-Gutiérrez *et al*., 2004; Ortega-Obregón, *et al*., 2008; Ratschbacher *et al*., 2009; Solari *et al*., 2011; Sutter, 1979), así como con otras edades U-Pb en zircón idénticas, atribuidas a una etapa de retrogresión (Martens *et al*., 2012; Ratschbacher *et al*., 2009; Solari *et al*., 2011).

La eclogita contiene cristales de granate que experimentaron un ciclo de crecimiento en condiciones de alta presión y temperatura relativamente baja a intermedia, los cuales muestran un enriquecimiento en tierras raras pesadas hacia sus bordes. Por lo tanto, la edad Lu-Hf en granate/roca total de 101.8 ± 3.1 Ma es interpretada como el momento de la cristalización final del granate en condiciones de facies de eclogita y, en consecuencia, del metamorfismo de subducción en el Complejo Chuacús. Por su parte, el esquisto pelítico (que experimentó una misma historia de inhumación) contiene porfiroblastos de granate con núcleos cristalizados en condiciones eclogíticas y sobrecrecimientos que corresponden a una fase de crecimiento posterior en facies de anfibolita. De tal forma que la edad Lu-Hf en granate/roca total de 95.5 ± 2.1 Ma se interpreta como un promedio de la edad de crecimiento del granate, incluyendo una etapa tardía de crecimiento en condiciones de presión intermedia.

En síntesis, la integración de la información geocronológica previa con los datos obtenidos en este trabajo, permite sugerir que el proceso de subducción continental del Complejo Chuacús y, por tanto, su metamorfismo de alta presión ocurrieron durante el Albiano-Cenomaniano y que un reequilibrio en facies de anfibolita, probablemente durante un nuevo ciclo de metamorfismo prógrado, tuvo lugar en el Campaniano. Estas edades implican un lapso de tiempo de ca. 25 Ma entre el metamorfismo de subducción y el reequilibrio subsecuente en facies de anfibolita.

5.3.4. Implicaciones tectónicas y correlaciones

La información petrológica y geocronológica obtenida en este trabajo sugiere que el Complejo Chuacús experimentó un metamorfismo de subducción a través de un gradiente geotérmico bajo de ~7-9 °C/km, alrededor de 25 Ma antes de lo previamente documentado. Por lo tanto, se propone que la evolución tectónica del complejo durante el evento caribeño incluye: (1) una etapa pre-colisional, caracterizada por subducción y metamorfismo eclogítico, y (2) una etapa colisional subsecuente marcada por un reequilibrio en facies de anfibolita y una exhumación parcial simultánea.

La etapa pre-colisional habría iniciado con la activación de la subducción de la corteza oceánica proto-caribeña por debajo del Arco de las Antillas Mayores durante el Cretácico Temprano (ca. 140 Ma; Pindell *et al*., 2012), lo cual eventualmente llevaría a la subducción sucesiva del margen pasivo adelgazado de la placa de Norteamérica (e.g. una secuencia tipo Caribeana; García-Casco *et al*., 2008) y al consecuente metamorfismo eclogítico de su basamento continental (i.e. el Complejo Chuacús) durante el Albiano-Cenomaniano (ca. 100 Ma). La etapa colisional se habría consumado luego del arribo de una corteza continental más gruesa a la zona de subducción, lo que habría provocado la colisión entre la placa de Norteamérica (bloque Maya) y el Arco de las Antillas Mayores en el Campaniano (ca. 74 Ma). Durante este evento, el régimen térmico de subducción debió ser reemplazado por condiciones térmicas más altas (~20 °C/km), de forma simultánea con una exhumación parcial del complejo, una probable nueva inhumación con un reequilibrio en facies de anfibolita, fusión parcial, emplazamiento de pegmatitas y deformación compresiva (Martens *et al*., 2012; Ortega-Gutiérrez *et al*., 2004; Ratschbacher *et al*., 2009; Solari *et al*., 2011, este trabajo). Una fase de exhumación tardía sin-colisional (ca. 70 Ma) se habría caracterizado por un régimen de deformación transpresiva sinestral, provocando el desarrollo de zonas de cizalla con retrocabalgadura (e.g. la ZCVB; Ortega-Obregón *et al*., 2008; Ratschbacher *et al*., 2009). La ocurrencia de estos eventos habían marcado la transición entre una subducción de tipo Pacífico (acrecional) y una de tipo Alpino (colisional).

Si bien este modelo de subducción/colisión entre el bloque Maya y el Arco de las Antillas Mayores ha sido ampliamente referido en las reconstrucciones paleogeográficas de la zona del Caribe (y adoptado también por parsimonia en los artículos derivados de este trabajo), algunos de los datos presentados aquí, en conjunto con los resultados de otros trabajos recientes, sugieren que dicho modelo es insuficiente para explicar las características petrológicas y la temporalidad del metamorfismo del Complejo Chuacús. En la actualidad, parece haber consenso general en la interpretación de que el Arco de las Antillas Mayores habría migrado hacia el noreste desde el Cretácico Temprano hasta el Eoceno, consumiendo a su paso la corteza oceánica proto-caribeña (Fig. 5.3). Durante esta migración, el orógeno antillano, en particular el sector de Cuba, habría registrado un metamorfismo de alta presión relacionado

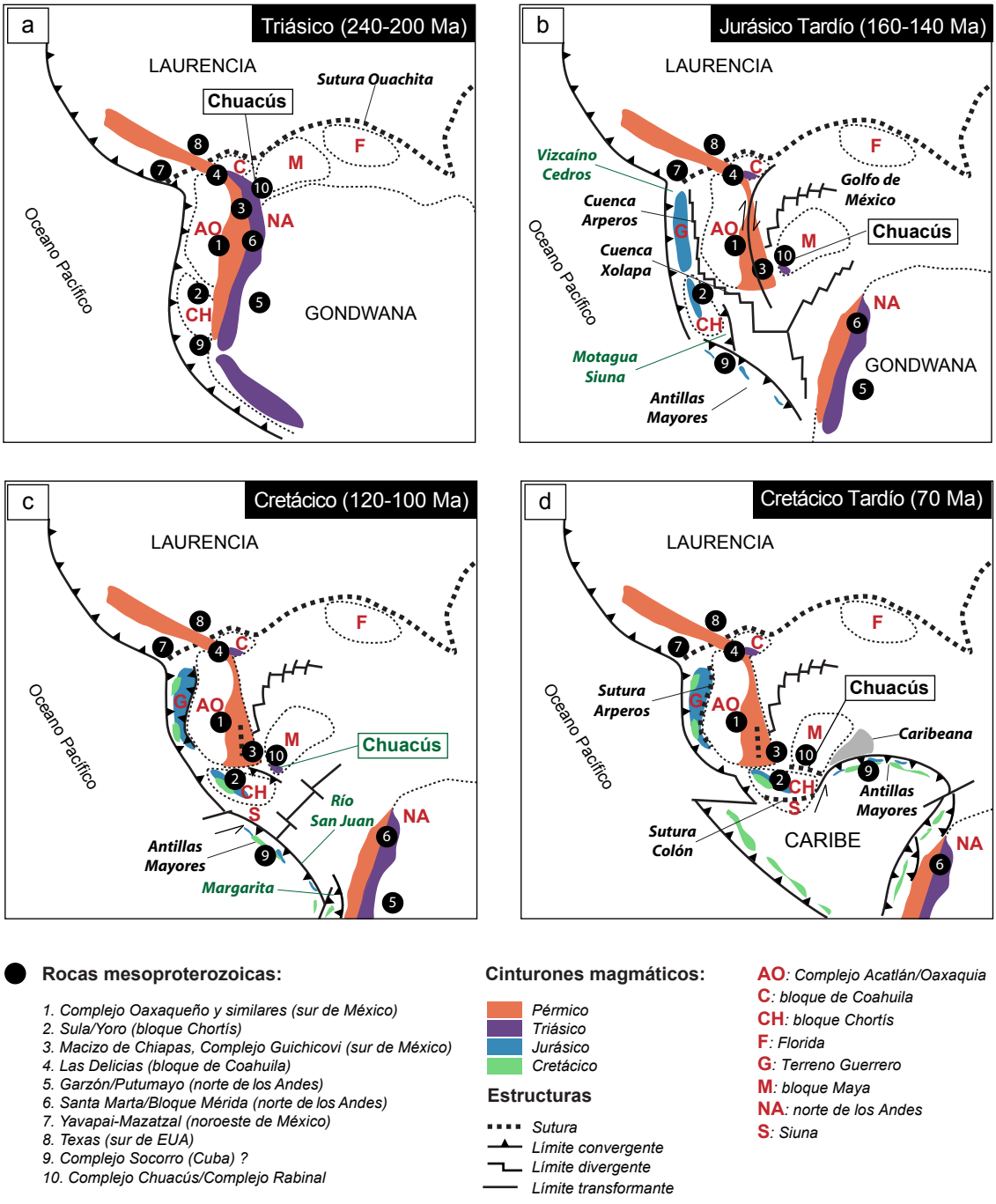

Figura 5.3. Reconstrucciones paleogeográficas esquemáticas modificadas de Cochrane *et al*. (2014), Pindell *et al*., (2012) y Weber *et al*. (2007) mostrando (a) la configuración del occidente de Pangea durante el Triásico (240-200 Ma) y (b) su eventual separación en el Jurásico Tardío (160-140 Ma) para dar lugar a la formación del Arco de las Antillas Mayores y la consolidación de la placa del Caribe durante el Cretácico (c, d). Se muestra la posición propuesta del Complejo Chuacús (y de su basamento precursor), así como la ubicación de distintas localidades de basamento mesoproterozóico, los cinturones magmáticos correspondientes y localidades relevantes de rocas metamórficas de alta presión (letra verde). En este modelo alternativo se atribuye el metamorfismo eclogítico del Complejo Chuacús a una posible subducción/colisión del bloque Maya por debajo del bloque Chortís. Ver discusión en el texto.

con la subducción de la litósfera oceánica proto-caribeña y del mismo arco volcánico entre ca. 120 y 80 Ma (e.g. Lázaro *et al*., 2016 y referencias citadas), seguido de un metamorfismo de alta presión derivado de la subducción/colisión de una parte del margen continental (i.e. secuencia Caribeana) de Norteamérica (bloque Maya) hace ca. 70 Ma y finalmente una sutura con la plataforma de las Bahamas hace ca. 45 Ma (e.g. Iturralde-Vinent *et al*., 2016). Por lo tanto, el metamorfismo eclogítico albiano-cenomaniano (ca. 100 Ma) documentado en el Complejo Chuacús implica un proceso de subducción continental anterior a la colisión del Arco de las Antillas Mayores con el promontorio Caribeana, ocurrida en el Campaniano-Maastrichtiano (ca. 70 Ma). Es decir, mientras que el orógeno antillano registra subducción oceánica entre ca. 120 y 80 Ma, en el sur del bloque Maya (Complejo Chuacús) ocurre la subducción de una litósfera continental que, a diferencia de la secuencia Caribeana, incluye además un basamento continental antiguo cuya edad se extiende hasta el Mesoproterozoico.

A pesar de que numerosos estudios han documentado la ocurrencia de metamorfismo de (ultra) alta presión en contextos de subducción y colisión arco-continente (ver Capítulo 3) podría suponerse más factible que el metamorfismo eclogítico del Complejo Chuacús correspondiera a un escenario de convergencia continente-continente y no al paso transversal del Arco de las Antillas Mayores. En este sentido, la opción más viable, si no la única, sería una hipotética subducción/colisión entre los bloques Maya y Chortís. La formación de la Cuenca Xolapa durante el Jurásico (Talavera *et al*., 2013), que representaría la extensión al sur de la Cuenca Arperos, implica una separación entre los terrenos proterozoicos-paleozoicos del sur de México y el bloque Chortís (Fig. 5.3b) y, en consecuencia, un proceso subsecuente de cierre oceánico para yuxtaponer ambas partes. Esta consideración supone una diferencia sustancial con respecto al modelo de Pindell *et al*. (2012) donde el bloque Chortís ocupa una posición adyacente al sur de México durante ese periodo y hasta el Mioceno. Por otro lado, la presencia de remanentes de corteza continental mesoproterozoica a triásica (Renne *et al*., 1989, Somin *et al*., 2006) en el sector occidental (Cuba) del Arco de las Antillas Mayores representa la evidencia de una probable cercanía o conexión de dicho arco con un basamento antiguo durante la etapa temprana de fragmentación de Pangea, como pudiera ser el caso del bloque Chortís (Figs. 5.3a, b). De este modo, la migración al noreste del Arco de las Antillas Mayores implicaría un movimiento similar del bloque Chortís, provocando el cierre de una cuenca oceánica proto-caribeña y la eventual subducción del basamento del bloque Maya durante el Cenomaniano (Figs. 5.3c, d). Un proceso análogo contemporáneo ha sido ampliamente documentado en el cierre de la Cuenca Arperos y la consecuente acreción del Terreno Guerrero en el occidente de México (e.g. Fitz-Díaz *et al*., 2017; Martini *et al*., 2014). Este modelo podría explicar no solo la temporalidad del metamorfismo eclogítico del Complejo Chuacús sino también la relación espacial que guarda con los mélanges serpentiníticos de la zona de Motagua, los cuales hospedan

bloques de eclogita con edades de entre 144 y 125 Ma y representarían fragmentos de la corteza oceánica subducida durante dicho proceso.

Varios estudios recientes han demostrado que el registro de un metamorfismo de alta presión pre-Campaniano (particularmente Albiano-Cenomaniano) es aparentemente común a lo largo de la zona de sutura del Caribe. La información geocronológica obtenida en distintas localidades de Guatemala (Flores *et al*., 2013; Yui *et al*., 2012), Cuba (Blanco-Quintero *et al*., 2011; Cárdenas-Párraga *et al*., 2012; García-Casco *et al*., 2002; Lázaro *et al*., 2009), República Dominicana (Escuder-Viruete *et al*., 2013; Krebs *et al*., 2008; Schertl *et al*., 2012) y el norte de Sudamérica (Maresch *et al*., 2009; Weber *et al*., 2011) revela un intervalo de edades metamórficas de entre 118 y 80 Ma. Resulta interesante que estas edades fueron obtenidas a partir de rocas de alta presión con una afinidad oceánica (e.g. subducción tipo Pacífico), con excepción del Complejo Chuacús y de Isla Margarita en Venezuela (Maresch *et al*., 2009), los cuales involucran corteza continental. Este hecho podría explicarse considerando las posiciones paleogeográficas inferidas de ambas zonas con respecto a la migración hacia el noreste del Arco de las Antillas Mayores durante el Cretácico (Pindell *et al*., 2012), lo cual probablemente llevaría a una subducción temprana de la corteza continental de las placas de Norteamérica y Sudamérica, respectivamente.

Referencias

Authemayou, C., Brocard, G., Teyssier, C., Simon-Labric, T., Guttiérrez, A., Chiquín, E. N., & Morán, S. (2011). The Caribbean–North America–Cocos Triple Junction and the dynamics of the Polochic–Motagua fault systems: Pull-up and zipper models. *Tectonics*, *30*(3).

Baquero, M., Grande, S., Urbani, F., Cordani, U., Hall, C., Armstrong, R. (2015). New Evidence for Putumayo Crust in the Basement of the Falcon Basin and Guajira Peninsula, Northwestern Venezuela. In Bartolini, C. and Mann, P. eds., *Petroleum geology and potential of the Colombian Caribbean Margin: AAPG Memoir*, 108, 103–136.

Blanco-Quintero, I. F., Rojas-Agramonte, Y., García-Casco, A., Kröner, A., Mertz, D. F., Lázaro, C., ... Renne, P. R. (2011). Timing of subduction and exhumation in a subduction channel: evidence from slab melts from La Corea Mélange (eastern Cuba). *Lithos*, *127*(1), 86-100.

Cárdenas-Párraga, J., García-Casco, A., Harlow, G. E., Blanco-Quintero, I. F., Rojas Agramonte, Y., & Kröner, A. (2012). Hydrothermal origin and age of jadeitites from Sierra del Convento Mélange (Eastern Cuba). *European Journal of Mineralogy*, *24*(2), 313-331.

Cochrane, R., Spikings, R., Gerdes, A., Ulianov, A., Mora, A., Villagómez, D., Putlitz B., Chiaradia, M. (2014). Permo-Triassic anatexis, continental rifting and the disassembly of western Pangaea. *Lithos*, 190, 383-402.

Collins, W., Richards, S. (2008). Geodynamic significance of S-type granites in circum-Pacific orogens. *Geology*, 36(7), 559-562.

Escuder-Viruete, J., Valverde-Vaquero, P., Rojas-Agramonte, Y., Gabites, J., Castillo-Carrión, M., & Pérez-Estaún, A. (2013). Timing of deformational events in the Río San Juan complex: Implications for the tectonic controls on the exhumation of high-P rocks in the northern Caribbean subduction–accretionary prism. *Lithos*, *177*, 416-435.

Estrada-Carmona, J., Weber, B., Martens, U., & López-Martínez, M. (2012). Petrogenesis of Ordovician magmatic rocks in the southern Chiapas Massif Complex: relations with the early Palaeozoic magmatic belts of northwestern Gondwana. *International Geology Review*, *54*(16), 1918-1943.

Fitz-Díaz, E., Lawton, T. F., Juárez-Arriaga, E., & Chávez-Cabello, G. (2017). The Cretaceous-Paleogene Mexican orogen: Structure, basin development, magmatism and tectonics. *Earth-Science Reviews*.

Flores, K. E., Martens, U. C., Harlow, G. E., Brueckner, H. K., & Pearson, N. J. (2013). Jadeitite formed during subduction: In situ zircon geochronology constraints from two different tectonic events within the Guatemala Suture Zone. *Earth and Planetary Science Letters*, *371*, 67-81.

García-Casco, A., Iturralde-Vinent, M. A., & Pindell, J. (2008). Latest Cretaceous collision/accretion between the Caribbean Plate and Caribeana: origin of metamorphic terranes in the Greater Antilles. *International Geology Review*, *50*(9), 781-809.

García-Casco, A., Torres-Roldán, R. L., Millán, G., Monié, P., & Schneider, J. (2002). Oscillatory zoning in eclogitic garnet and amphibole, Northern Serpentinite Melange, Cuba: a record of tectonic instability during subduction?. *Journal of Metamorphic Geology*, *20*(6), 581-598.

Godínez-Urban, A., Lawton, T. F., Garza, R. S. M., Iriondo, A., Weber, B., & López-Martínez, M. (2011). Jurassic volcanic and sedimentary rocks of the La Silla and Todos Santos Formations, Chiapas: Record of Nazas arc magmatism and rift-basin formation prior to opening of the Gulf of Mexico. *Geosphere*, *7*(1), 121-144.

González-Guzmán, R., Weber, B., Manjarrez-Juárez, R., Cisneros de León, A., Hecht, L., & Herguera-García, J. C. (2016). Provenance, age constraints and metamorphism of Ediacaran metasedimentary rocks from the El Triunfo Complex (SE Chiapas, México): evidence for Rodinia breakup and Iapetus active margin. *International Geology Review*, *58*(16), 2065-2091.

Harley, S. L., Kelly, N. M., & Möller, A. (2007). Zircon behaviour and the thermal histories of mountain chains. *Elements*, *3*(1), 25-30.

Herron, M. M. (1988). Geochemical classification of terrigenous sands and shales from core or log data. *Journal of Sedimentary Research*, *58*(5).

Ibanez-Mejia, M., Ruiz, J., Valencia, V., Cardona, A., Gehrels, G. E., Mora, A, R. (2011). The Putumayo Orogen of Amazonia and its implications for Rodinia reconstructions: New U–Pb geochronological insights into the Proterozoic tectonic evolution of northwestern South America. *Precambrian Research*, 191(1), 58-77.

Iturralde-Vinent, M. A., García-Casco, A., Rojas-Agramonte, Y., Proenza, J. A., Murphy, J. B., & Stern, R. J. (2016). The geology of Cuba: A brief overview and synthesis. *GSA Today*, *26*(10), 4-10.

Keppie, J. D., & Ortega-Gutiérrez, F. (2010). 1.3–0.9 Ga Oaxaquia (Mexico): remnant of an arc/backarc on the northern margin of Amazonia. *Journal of South American Earth Sciences*, *29*(1), 21-27.

Keppie, J.D., Dostal, J., Miller, B.V., Ramos-Arias, M.A., Morales-Gámez, M., Nance, R.D., Murphy, J.B., Ortega-Rivera, A., Lee, J.W.K., Housh, T. & Cooper, P., 2008. Ordovician–earliest Silurian rift tholeiites in the Acatlán Complex, southern Mexico: Evidence of rifting on the southern margin of the Rheic Ocean. *Tectonophysics*, *461*(1), 130-156.

Krebs, M., Maresch, W. V., Schertl, H. P., Münker, C., Baumann, A., Draper, G., ... Trapp, E. (2008). The dynamics of intra-oceanic subduction zones: a direct comparison between fossil petrological evidence (Rio San Juan Complex, Dominican Republic) and numerical simulation. *Lithos*, *103*(1), 106-137.

Lawlor, P. J., Ortega-Gutiérrez, F., Cameron, K. L., Ochoa-Camarillo, H., Lopez, R., & Sampson, D. E. (1999). U–Pb geochronology, geochemistry, and provenance of the Grenvillian Huiznopala Gneiss of Eastern Mexico. *Precambrian Research*, *94*(1-2), 73-99.

Lázaro, C., García-Casco, A., Rojas Agramonte, Y., Kröner, A., Neubauer, F., & Iturralde-Vinent, M. (2009). Fifty-five-million-year history of oceanic subduction and exhumation at the northern edge of the Caribbean plate (Sierra del Convento mélange, Cuba). *Journal of Metamorphic Geology*, *27*(1), 19-40.

Lázaro, C., Blanco-Quintero, I. F., Proenza, J. A., Rojas-Agramonte, Y., Neubauer, F., Núñez-Cambra, K., & Garcia-Casco, A. (2016). Petrogenesis and $^{40}Ar/^{39}Ar$ dating of proto-forearc crust in the Early

Cretaceous Caribbean arc: The La Tinta mélange (eastern Cuba) and its easterly correlation in Hispaniola. *International Geology Review*, *58*(8), 1020-1040.

Li, Y., Barnes, M., Barnes, C., Frost, C. (2007). Grenville-age A-type and related magmatism in southern Laurentia, Texas and New Mexico, USA. *Lithos*, 97(1), 58-87.

Litherland, M., Aspden, J., Jemielita, R. (1994). The metamorphic belts of Ecuador, British Geological Survey, Overseas Memoir 11. *British Geological Survey*, *Keyworth*, 147.

Lopez, R. (1997). The pre-Jurassic geotectonic evolution of the Coahuila terrane, northwestern Mexico: Grenville basement, a late Paleozoic arc. Triassic plutonism, and the events south of the Ouachita suture (PhD Dissertation). *Santa Cruz, California, University of California*, 55-147.

Maresch, W. V., Kluge, R., Baumann, A., Pindell, J. L., Krückhans-Lueder, G., & Stanek, K. (2009). The occurrence and timing of high-pressure metamorphism on Margarita Island, Venezuela: a constraint on Caribbean-South America interaction. *Geological Society, London, Special Publications*, *328*(1), 705-741.

Martens, U. C., Brueckner, H. K., Mattinson, C. G., Liou, J. G., & Wooden, J. L. (2012). Timing of eclogite-facies metamorphism of the Chuacús complex, Central Guatemala: record of Late Cretaceous continental subduction of North America's sialic basement. *Lithos*, *146*, 1-10.

Martens, U., Weber, B., & Valencia, V. A. (2010). U/Pb geochronology of Devonian and older Paleozoic beds in the southeastern Maya block, Central America: Its affinity with peri-Gondwanan terranes. *Geological Society of America Bulletin*, *122*(5-6), 815-829.

Martini, M., Solari, L., & López-Martínez, M. (2014). Correlating the Arperos Basin from Guanajuato, central Mexico, to Santo Tomás, southern Mexico: Implications for the paleogeography and origin of the Guerrero terrane. *Geosphere*, *10*(6), 1385-1401.

Martini, M., & Ortega-Gutiérrez, F. (2016). Tectono-stratigraphic evolution of eastern Mexico during the break-up of Pangea: A review. *Earth-Science Reviews*.

McBirney, A.R. (1963): Geology of a part of the central Guatemalan cordillera. *California University Publications in Geological Sciences*, 38, 177–242.

Miller, B. V., Dostal, J., Keppie, J. D., Nance, R. D., Ortega-Rivera, A., & Lee, J. K. (2007). Ordovician calc-alkaline granitoids in the Acatlán Complex, southern México: Geochemical and geochronologic data and implications for the tectonics of the Gondwanan margin of the Rheic Ocean. *Special papers Geological Society of America*, *423*, 465.

Ortega-Gutiérrez, F., Elías-Herrera, M., Reyes-Salas, M., Macías-Romo, C., & López, R. (1999). Late Ordovician–Early Silurian continental collisional orogeny in southern Mexico and its bearing on Gondwana-Laurentia connections. *Geology*, *27*(8), 719-722.

Ortega-Gutiérrez, F., Solari, L. A., Ortega-Obregón, C., Elías-Herrera, M., Martens, U., Morán-Icál, S., ... & Schaaf, P. (2007). The Maya-Chortís boundary: a tectonostratigraphic approach. *International Geology Review*, *49*(11), 996-1024.

Ortega-Gutiérrez, F., Solari, L. A., Solé, J., Martens, U., Gómez-Tuena, A., Morán-Ical, S., & Reyes-Salas, M. (2004). Polyphase, high-temperature eclogite-facies metamorphism in the Chuacús Complex, central Guatemala: Petrology, geochronology, and tectonic implications. *International Geology Review*, *46*(5), 445-470.

Ortega-Obregon, C., Keppie, J. D., Murphy, J. B., Lee, J. K. W., & Ortega-Rivera, A. (2009). Geology and geochronology of Paleozoic rocks in western Acatlán Complex, southern Mexico: Evidence for contiguity across an extruded high-pressure belt and constraints on Paleozoic reconstructions. *Geological Society of America Bulletin*, *121*(11-12), 1678-1694.

Ortega-Obregon, C., Murphy, J. B., & Keppie, J. D. (2010). Geochemistry and Sm–Nd isotopic systematics of Ediacaran–Ordovician, sedimentary and bimodal igneous rocks in the western Acatlán Complex, southern Mexico: Evidence for rifting on the southern margin of the Rheic Ocean. *Lithos*, *114*(1), 155-167.

Ortega-Obregón, C., Solari, L. A., Keppie, J. D., Ortega-Gutiérrez, F., Solé, J., & Morán-Ical, S. (2008). Middle-Late Ordovician magmatism and Late Cretaceous collision in the southern Maya block,

Rabinal-Salamá area, central Guatemala: implications for North America–Caribbean plate tectonics. *Geological Society of America Bulletin*, *120*(5-6), 556-570.

Pindell, J., Maresch, W. V., Martens, U., & Stanek, K. (2012). The Greater Antillean Arc: Early Cretaceous origin and proposed relationship to Central American subduction mélanges: implications for models of Caribbean evolution. *International Geology Review*, *54*(2), 131-143.

Ratschbacher, L., Franz, L., Min, M., Bachmann, R., Martens, U., Stanek, K., Stübner, K., Nelson, B.K., Herrmann, U., Weber, B. & López-Martínez, M., 2009. The North American-Caribbean plate boundary in Mexico-Guatemala-Honduras. *Geological Society, London, Special Publications*, *328*(1), 219-293.

Renne, P. R., Mattinson, J. M., Hatten, C. W., Somin, M., Onstott, T. C., Millán, G., & Linares, E. (1989). $^{40}Ar/^{39}Ar$ and U-Pb evidence for Late Proterozoic (Grenville-age) continental crust in north-central Cuba and regional tectonic implications. *Precambrian Research*, *42*(3-4), 325-341.

Restrepo, J., Ordóñez-Carmona, O., Armstrong, R., Pimentel, M. (2011). Triassic metamorphism in the northern part of the Tahamí Terrane of the central cordillera of Colombia. *Journal of South American Earth Sciences*, 32(4), 497-507.

Roser, B. P., & Korsch, R. J. (1986). Determination of tectonic setting of sandstone-mudstone suites using content and ratio. *The Journal of Geology*, *94*(5), 635-650.

Rubatto, D., & Hermann, J. (2003). Zircon formation during fluid circulation in eclogites (Monviso, Western Alps): implications for Zr and Hf budget in subduction zones. *Geochimica et Cosmochimica Acta*, *67*(12), 2173-2187.

Ruiz, J., Tosdal, R. M., Restrepo, P. A., & Murillo-Muñetón, G. (1999). Pb isotope evidence for Colombia-southern Mexico connections in the Proterozoic. *Special papers Geological Society of America*, 183-198.

Schertl, H. P., Maresch, W. V., Stanek, K. P., Hertwig, A., Krebs, M., Baese, R., ... Sergeev, S. S. (2012). New occurrences of jadeitite, jadeite quartzite and jadeite-lawsonite quartzite in the Dominican Republic, Hispaniola: petrological and geochronological overview. *European Journal of Mineralogy*, *24*(2), 199-216.

Solari, L. A., García-Casco, A., Martens, U., Lee, J. K., Ortega-Rivera, A. (2013). Late Cretaceous subduction of the continental basement of the Maya block (Rabinal Granite, central Guatemala): Tectonic implications for the geodynamic evolution of Central America. *Geological Society of America Bulletin*, 125(3-4), 625-639.

Solari, L. A., Keppie, J. D., Ortega-Gutiérrez, F., Cameron, K. L., Lopez, R., & Hames, W. E. (2003). 990 and 1100 Ma Grenvillian tectonothermal events in the northern Oaxacan Complex, southern Mexico: roots of an orogen. *Tectonophysics*, *365*(1-4), 257-282.

Solari, L. A., Ortega-Gutiérrez, F., Elías-Herrera, M., Gómez-Tuena, A. Schaaf, P. (2010). Refining the age of magmatism in the Altos Cuchumatanes, western Guatemala, by LA–ICPMS, and tectonic implications. *International Geology Review*, 52(9), 977-998.

Solari, L. A., Ortega-Gutiérrez, F., Elías-Herrera, M., Schaaf, P., Norman, M., Ortega-Obregón, C., & Chiquín, M. (2009). U-Pb zircon geochronology of Palaeozoic units in western and central Guatemala: Insights into the tectonic evolution of Middle America. *Geological Society, London, Special Publications*, *328*(1), 295-313.

Solari, L. A., Tuena, A. G., Gutiérrez, F. O., & Obregón, C. O. (2011). The Chuacús Metamorphic Complex, central Guatemala: geochronological and geochemical constraints on its Paleozoic-Mesozoic evolution. *Geologica Acta*, *9*(3-4), 329-350.

Somin, M. L. (2006). The El Guaybo Gneiss as a probable Fragment of sialic Basement for the Cretaceous Volcanic Arc in Western Cuba. In *Geophysical Research Abstracts* (Vol. 8, p. 03377).

Sutter, J. F. (1979). Late Cretaceous collisional tectonics along the Motagua fault zone, Guatemala. In *Geological Society of America, Abstracts with Programs*, 11, 525-526.

Talavera-Mendoza, O., Ruiz, J., Corona-Chavez, P., Gehrels, G. E., Sarmiento-Villagrana, A., García-Díaz, J. L., & Salgado-Souto, S. A. (2013). Origin and provenance of basement metasedimentary

rocks from the Xolapa Complex: New constraints on the Chortis–southern Mexico connection. *Earth and Planetary Science Letters*, *369*, 188-199.

van den Boom, G. (1972). Petrofazielle Gliederung des metamorphen Grungebirges in der Sierra de Chuacús, Guatemala. *Beihefte Geologisches Jahrbuch*, 122, 5–49.

van der Lelij, R., Spikings, R., Ulianov, A., Chiaradia, M. (2016). Palaeozoic to Early Jurassic history of the northwestern corner of Gondwana, and implications for the evolution of the Iapetus, Rheic and Pacific Oceans. *Gondwana Research,* 31, 271-294.

Vega-Granillo, R., Calmus, T., Meza-Figueroa, D., Ruiz, J., Talavera-Mendoza, O., & López-Martínez, M. (2009). Structural and tectonic evolution of the Acatlán Complex, southern Mexico: Its role in the collisional history of Laurentia and Gondwana. *Tectonics*, *28*(4).

Villagómez, D., Spikings, R., Magna, T., Kammer, A., Winkler, W., Beltrán, A. (2011). Geochronology, geochemistry and tectonic evolution of the Western and Central cordilleras of Colombia. *Lithos*, 125(3), 875-896.

Vinasco, C. J., Cordani, U. G., González, H., Weber, M., Pelaez, C. (2006). Geochronological, isotopic, and geochemical data from Permo-Triassic granitic gneisses and granitoids of the Colombian Central Andes. *Journal of South American Earth Sciences*, 21(4), 355-371.

Weber, B., & Köhler, H. (1999). Sm–Nd, Rb–Sr and U–Pb geochronology of a Grenville Terrane in Southern Mexico: origin and geologic history of the Guichicovi Complex. *Precambrian Research*, *96*(3-4), 245-262.

Weber, B., González-Guzmán, R., Manjarrez-Juárez, R., de León, A. C., Martens, U., Solari, L., ... & Valencia, V. (2018). Late Mesoproterozoic to Early Paleozoic history of metamorphic basement from the southeastern Chiapas Massif Complex, Mexico, and implications for the evolution of NW Gondwana. *Lithos*, *300*, 177-199.

Weber, B., Iriondo, A., Premo, W. R., Hecht, L., & Schaaf, P. (2007). New insights into the history and origin of the southern Maya block, SE México: U–Pb–SHRIMP zircon geochronology from metamorphic rocks of the Chiapas massif. *International Journal of Earth Sciences*, *96*(2), 253-269.

Weber, B., Scherer, E. E., Martens, U. K., & Mezger, K. (2012). Where did the lower Paleozoic rocks of Yucatan come from? AU–Pb, Lu–Hf, and Sm–Nd isotope study. *Chemical Geology*, *312*, 1-17.

Weber, B., Valencia, V. A., Schaaf, P., Pompa-Mera, V., & Ruiz, J. (2008). Significance of provenance ages from the Chiapas Massif Complex (southeastern Mexico): redefining the Paleozoic basement of the Maya Block and its evolution in a peri-Gondwanan realm. *The Journal of Geology*, *116*(6), 619-639.

Weber, M., Cardona, A., Valencia, V., Altenberger, U., López-Martinez, M., Tobón, M., ... Concha, A. E. (2011). Geochemistry and Geochronology of the Guajira Eclogites, northern Colombia: evidence of a metamorphosed primitive Cretaceous Caribbean Island-arc. *Geologica Acta*, *9*(3-4), 425-443.

Yui, T. F., Maki, K., Wang, K. L., Lan, C. Y., Usuki, T., Iizuka, Y., ... Liou, J. G. (2012). Hf isotope and REE compositions of zircon from jadeitite (Tone, Japan and north of the Motagua fault, Guatemala): implications on jadeitite genesis and possible protoliths. *European Journal of Mineralogy*, *24*(2), 263-275.